Informing Singlet Fission Chromophore Design via Photophysical Exploration of Tetracene and Tetracene-Inspired Covalent Dimers

by

Jasper Donald Cook

B.S., Chemistry, University of Oregon, 2011

A thesis submitted to the

Faculty of the Graduate School of the

University of Colorado in partial fulfillment

of the requirement for the degree of

Doctor of Philosophy

Department of Chemistry and Biochemistry

2017

This thesis entitled:

Informing Singlet Fission Chromophore Design via Photophysical Exploration of Tetracene and Tetracene-Inspired Covalent Dimers

written by:

Jasper Donald Cook

has been approved for the Department of Chemistry and Biochemistry by:

_____
Niels H. Damrauer

_____
Justin C. Johnson

Date _____

The final copy of this thesis has been examined by the signatories, and we find that both the content and the form meet acceptable presentation standards of scholarly work in the above mentioned discipline.

Cook, Jasper Donald (Ph.D., Physical Chemistry)

Informing Singlet Fission Chromophore Design via Photophysical Exploration of Tetracene and Tetracene-Inspired Covalent Dimers

Thesis directed by Associate Professor Niels Damrauer

Abstract

Singlet fission (SF) is a spin-allowed process wherein a singlet excited state on one molecule shares its energy with a neighbor to create a pair of spin-coupled triplet states. This process has the potential to significantly improve solar cell efficiency as part of a carrier multiplication cell, and thus deserves robust understanding. The factors which govern the efficiency and rate of SF are explored in three systems: polycrystalline tetracene (Tc); a rigid, tetracene-inspired covalent dimer (BT1); and its (triisopropylsilylethynyl)-substituted derivative (TIPS-BT1). For polycrystalline Tc, films of two different polymorphs are prepared with the complementary variable of grain size. Crystallite size affects SF in one polymorph but not the other, highlighting the complex interplay between chromophore coupling and large-scale effects in the solid phase. In BT1, the role of coupling is isolated from long-range effects by reduction of the problem to a covalent dimer. With unfavorable coupling due to symmetry and poor energetics, slow SF in BT1 is largely out-competed by other loss processes. In TIPS-BT1, improved stability and solubility allow for in-depth photophysical studies. In a nonpolar environment, the excited dimer relaxes emissively with no apparent singlet fission. In a polar environment, two distinct states emit—one monomer-like and one dimer-like—with the latter in equilibrium with a dark state. These findings provide a foundation of mechanistic details for contrasting with future dimers based on this molecular platform. There, through systematic changes to energetics and coupling, we expect significant improvements to SF accompanied by deep mechanistic insight.

Dedication

Science is an unending search for new mysteries.

Acknowledgements

To Niels: Your meticulous thinking, thoughtful questions, and frank, insightful critiques guided me to answers where I would have otherwise been lost in a pile of data and details. You helped me see the forest for the trees, and because of you I am a better scientist and thinker. I am glad to have had you as my mentor, and I will appreciate what you gave me for the rest of my life.

To My Labmates and Collaborators: Josh, your early mentorship and welcoming personality were huge when I was first getting started in the lab. Paul and Jamie, you laid the groundwork for this project, and my work would not have been possible without the foundation you built. Karen, you provided moral and intellectual support with a great attitude that livened up the lab. Steve, thanks for bringing your maturity and beard into the group, for helping me a ton with electrochemistry, and for calling out Sam's (repeated) fashion *faux pas*. Also: ganking. Sam, thanks for providing me with fun collaborative coding sessions (I am not saying that sarcastically) and for always being excited to talk/argue about science (or not science). Thomas, thank you for making a ton of molecules in a dark room for me to shoot with lasers, for doing it well, for not yelling at me when I destroyed them up sometimes, and for showing me that nobody knows anything about bonding. O**n**ion: your global fitting routine may be the single-most helpful piece of code I used in this lab, and you always had great input when I wanted to talk about science. You're the best kind of airplane. Renato, I had a ton of fun working with you on the 2D-electronic project (and just in general), and I'm glad you came to CU. Steven, Ryan, Alex, and Ethan, thank you for bringing your excitement, curiosity, self-motivation, and critical thinking into the group. It makes me happy to know the lab is in good hands (except for the cuvettes). Joe, Dylan, and Justin, thank you for the hours you spent working with me at NREL (and/or CU) to help with a variety of experiments

(many of which are in this dissertation). I appreciated every bit of help getting these molecules to teach me something. Also, Dylan, thanks a ton for teaching me how to use MATLAB and all the other random tricks in the laser lab. As a final comment to everyone: thank you for all of the conversations (arguments) we had about science (grammar and politics), and the fact that you were all *good people* to whom I could turn when something needed more brain power, or when it was hilarious and needed sharing.

To My Friends: Thank you for making Boulder a good place to be. I loved the pizza nights, noonch, League, bubble tea, homework tea, movies, bro camping, Broforce, sledding, disc golf, hiking, moral support, crosswords, building computers, adventuring in Chicago, conversations about the future of transportation (self-driving cars in 2064), and hiding under the kitchen sink. You have all brightened my life, and I couldn't have asked for better partners in whatever the opposite of crime is.

To My Family: I know it took a while, and that the timing was… not the best. Thanks for sticking with me for all these years, and for understanding every time when I had to disappear to do work late into the night. I love you, and will always appreciate the support that began long before graduate school. You're the people who have always been in my corner, and I can't put into words how much that means.

Table of Contents

Table of Tables

Table of Figures

Chapter 1. Introduction to Solar Energy and Singlet Fission Photophysics

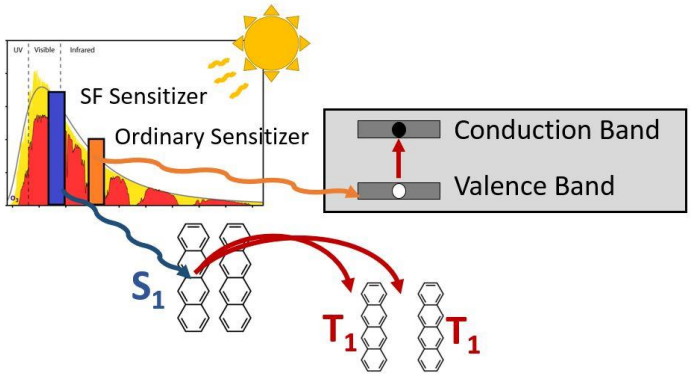

1.1 Solar Energy Conversion and Carrier Multiplication

The continued growth and development of humanity requires energy, and meeting our energy needs sustainably is increasingly crucial for environmental, economic, and political reasons.[1–3] Fortunately, the Earth is bathed in sunlight—which provides more than enough energy to meet future needs[3]—and humans are getting increasingly efficient at harvesting it. While solar energy is not the only form of sustainable energy (other examples include wind, hydroelectric, and geothermal), it is increasingly competitive, even when compared with traditional sources like coal. According to a 2016 report by the World Economic Forum, the unsubsidized, levelized* cost of utility-scale solar electricity was cheaper to deploy than any other form of energy in 30 countries.[4] Many of these 30 countries, however, are those who are experiencing rapidly increasing energy demands or whose exposure to sunlight is high. This latter point is significant when considering solar energy harvesting: sunlight is a fixed, and somewhat dilute, energy source.

In order to unambiguously reach cost parity with coal and other traditional energy generation methods, solar energy harvesting must drop in cost by cheaper manufacturing,

* Refers to the lifetime cost of building, operating, and maintaining an electricity source without inclusion of government or other artificial economic incentives.

increased efficiency, or both—even under suboptimal sunlight. While manufacturing is typically the domain of industry, the question of efficiency has been considered at length by the scientific community. For example, a 1961 paper on the topic by Shockley and Quiesser[5] has been cited more than 3400 times.[†] In their paper, Shockley and Queisser considered the thermodynamic limitations of a single-junction solar photovoltaic (PV) device and found that, under representative sunlight exposure (known as AM 1.5 solar irradiance[‡]), such devices can extract at most 1/3rd of incident solar power. This limitation is due to the nature of a single-junction device: sunlight with energy below the band gap of the absorbing material is not harnessed, while sunlight with energy exceeding the band gap of the material rapidly thermalizes (losing any excess energy as heat). Technologies that circumvent this limit constitute the so-called "third generation" of solar energy conversion,[6] and this is often accomplished by layering multiple solar cells (each with a different band gap) in series to give what is known as a tandem, or multi-junction cell. Figure 1.1 shows the higher efficiency associated with these cells in practice, as well as the general upward trend in efficiency over time (the contents of this chart in fact changed several times during preparation of this dissertation).

While multi-junction cells are in use today, they tend to be expensive due to production and material requirements, which hinders broad adoption. Fortunately, there is a subset of third-generation cells in which various motifs avoid increased cost while retaining efficiency gains. These cells utilize a process known as multiple-exciton generation (MEG) to achieve multiple effective junctions when combined with an ordinary sensitizer.[7,8] Some MEG cells avoid current matching (achieved by connecting cells in parallel), or are non-crystalline and therefore do not

[†] According to https://apps.webofknowledge.com.
[‡] Reference solar spectrum available at http://rredc.nrel.gov/solar/spectra/am1.5/

require lattice-matching. In an MEG cell, higher-energy photons from the sun are absorbed and "split" by the material into multiple lower-energy excited species before eventual carrier extraction, substantially increasing photocurrent and eventually efficiency relative to cells without MEG.[7,9] If the energy of the ordinary sensitizer is chosen correctly and a secondary MEG sensitizer is used (whose gap *after* multiplication matches that of the ordinary sensitizer, such that both can eventually be extracted at the same potential), the theoretical efficiency of an MEG cell is increased from the 33% value for a single-junction cell to between 44% and 48%, depending on configuration and MEG absorber type.[7,10] This is comparable to the limiting efficiency of an ordinary two-junction cell (46%[7]).

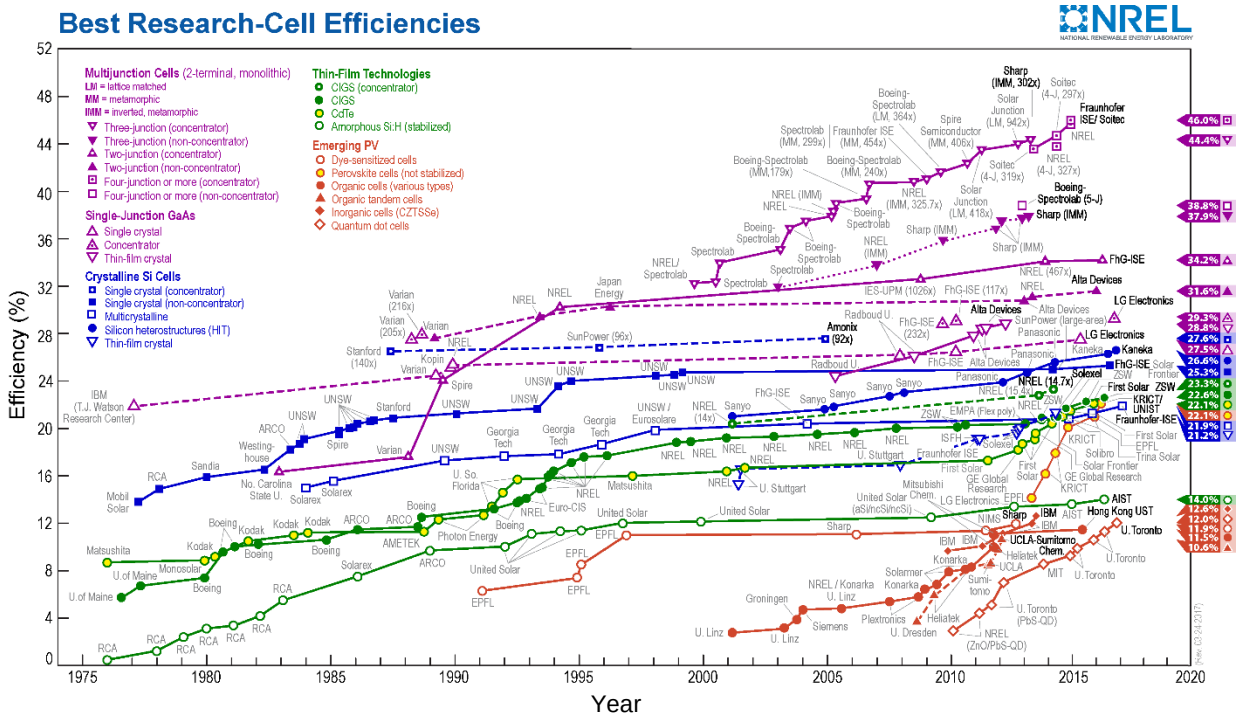

Figure 1.1. National Renewable Energy Laboratory research cell record efficiencies, as of April 2017.[§]

[§] This plot is courtesy of the National Renewable Energy Laboratory, Golden, CO.

1.2 Multiple Exciton Generation via Singlet Fission

Singlet fission (SF) is an MEG process found in organic materials that can be remarkably fast (less than a picosecond in some cases), promising increased efficiency when incorporated into a MEG solar cell.[7,10–15] The process occurs when a singlet excited state (S_1) molecule shares its energy with a singlet ground state (S_0) neighbor to give two triplet (T_1) excitons. SF is spin-allowed due to the nature of the initial product state triplets: they are spin-paired in the initially formed multi-exciton product state (^{1}TT) such that the net singlet spin is conserved. Equation 1 shows the basic photophysical reaction for SF, beginning with a single excited chromophore (and a ground state neighbor), and ending with two uncoupled triplet states as the product via breakdown of the multiexcitonic ^{1}TT intermediate.

$$S_1 + S_0 \rightleftharpoons {}^1TT \rightleftharpoons T_1 + T_1 \quad (1)$$

For SF to produce triplets at near 200% yield (i.e. two triplets formed per incident photon), there are a few important considerations:[10] (1) the energetics of the overall reaction ($\Delta E_{SF} = 2 \times E(T_1) - E(S_1)$) should be favorable, with a negative ΔE_{SF}; (2) the electronic coupling between the reactant S_1S_0 or S_0S_1 state (excitonic states composed of an S_1 and an S_0 chromophore; these may or may not be equivalent, depending on orientation and chromophore identity) and the product ^{1}TT should be large enough to enable SF to occur quickly (while being weak enough that the coupled molecules do not behave as a single chromophore).[11] The first consideration is important in so far as the equilibrium between S_1S_0/S_0S_1 and ^{1}TT will be determined in part by their relative energetics, with $E(^1TT) \approx 2\times E(T_1)$. The second is crucial if ^{1}TT formation is to compete with other S_1 loss pathways like fluorescence and intersystem crossing (enabled, for example, by a T_2 state proximal to S_1 as in tetracene[16]), which drain potentially fissile S_1 excited states.

1.3 Studying Polyacene-Inspired Systems

Given the discussion above regarding symmetry and energetics, it is perhaps unsurprising that identifying systems with efficient SF can be challenging and that relatively few are known to undergo efficient SF.[10,17] The most prominent of these include rylene–diimides,[18–20] 1,3-diphenylisobenzofuran,[21,22] and substituted[23–25] and un-substituted[26–29] polyacenes. This last system—polyacenes—is one with decades of foundational research,[10,29–36] and is the class of molecules in which SF was first proposed (invoked to explain fluorescence behavior in anthracene crystals[35]). Polyacenes are seminal SF systems due to this history and their energetics, with singlet and triplet energies that drop quickly with molecule size while approximately preserving the $S_1 \leftrightarrow T_1$ gap (a gap that is large in these elongated systems), such that ΔE_{SF} gets increasingly favorable (negative) as the number of rings is increased.[10,33] In thin films of the fourth and fifth linear polyacenes (tetracene, abbreviated Tc, and pentacene, abbreviated Pc), SF is highly efficient.[10] There are important differences between these two molecules however, with SF in Tc[26,28,37] slightly endoergic (approximately 70 meV uphill) and slower (its lifetime is ~30-100 ps), compared to SF that is exoergic (~100 meV downhill) and around a thousand times faster (<100 fs) in Pc[29,38]. From a practical standpoint, studying SF in either system comes with unique advantages: Pc offers insight into the nature of ultrafast SF, while Tc allows for more experimental accessibility and for the effects of perturbations (synthetic or optical, as in coherent control, *vide infra*) to be identified more readily. Both systems benefit from a large body of existing research efforts,[10] enabling detailed questions to be asked for which the groundwork has already been laid. For practical reasons, Tc is the system considered here, though future efforts on Pc are also underway in our group with the goal of providing a yet more complete picture of SF. Ideally, study

of both Tc and Pc in concert provides the most complete picture of the photophysics that determine SF efficiency in these types of systems.

For the reasons mentioned above, thesis considers three Tc-inspired systems: first, Tc itself is studied (as two different polymorphs); second, a Tc-derived covalently linked dimer (BT1); and third, a substituted derivative of that dimer (TIPS-BT1). A natural way to study these systems and their SF-relevant photophysics is through time-resolved electronic spectroscopies. These include photoluminescence (steady-state and time-resolved) and transient absorption (which probes states more directly), with interpretation aided by computational efforts from methods like time-dependent density functional theory (TD-DFT). Taken together, these methods allow experimentalists to watch and understand the evolution of molecules following excitation, and can provide deep insight into the quantum-mechanical nature of systems. Significant inspiration for this work also comes from earlier coherent control experiments in our group[39] on singlet fission in polycrystalline tetracene films. These experiments revealed the importance of coupling in SF using a technique called optical pulse shaping, where ultrafast pulses of light are tailored by altering their spectral phase or amplitude in order to control the behavior of systems after (or during) excitation.[40] In solid Tc, it was found that excitation with trains of pulses timed to a lattice mode of the crystal could enhance SF relative to a single pulse without changing the excitation fluence. The fact that coherent control can access vibrations and (in doing so) modulate coupling is an exciting prospect for gaining insight into the SF mechanism and allows us to test theoretical predictions about symmetry-breaking-enabled diabatic coupling[41]. These findings experimentally demonstrated the crucial role of interchromophore coupling in SF, and have shaped the thinking in our group with respect to accessing the microscopic details of SF. Accordingly, subsequent chapters discuss efforts to extend this work (first in different polymorphs of Tc in Chapter 2, then

in a covalent molecular dimer in Chapter 5) alongside an array of other in-depth photophysical studies, united in the goal of elucidating the mechanism of SF.

1.4 Intermolecular Coupling

For the acene systems considered in this thesis, SF is often described in the context of a set diabatic states that communicate through four-electron coupling pathways.[10] These pathways are termed direct coupling (which allows the initial singlet to communicate directly with the ^{1}TT product) and mediated coupling (in which communication occurs through a charge-transfer state), and are not true reaction mechanisms, since the charge-transfer intermediary states in the mediated pathway are not necessarily populated (and can instead participate virtually). These paths nonetheless provide a helpful conceptual framework in which to identify the couplings that are important for enabling SF. This framework is constructed in a simple dimeric (two molecule) frontier orbital picture that uses monomeric orbitals. These are the HOMO (highest occupied molecular orbital) and the LUMO (lowest unoccupied molecular orbital) of the separate chromophores, and those chromophores are in turn denoted A and B (taken hereafter to be identical molecules, though this is not required for SF in general). Representative electron configurations for the various dimer states (all diabatic excitonic states) are shown in Figure 1.2, and arrows show the coupling pathways leading to the product state (the multiexcitonic ^{1}TT). The other pictured states are the initially excited singlet (equivalently S_1S_0 or S_0S_1, depending upon where the S_1 excitation resides) and the two charge-transfer (CT) intermediary states (CA and AC, in which C denotes cation and A denotes anion). An equivalent configuration exists wherein all electron spins are flipped.

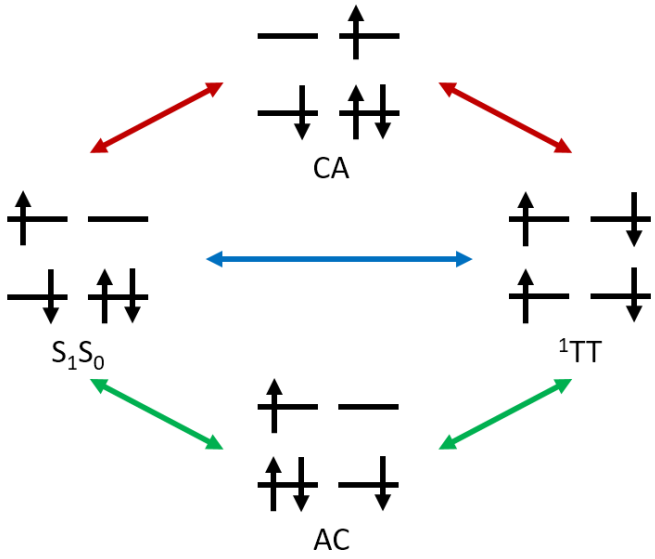

Figure 1.2. Two coupling mechanisms for SF: the direct coupling (blue arrow) pathway and the CT-mediated (electron transfer in red and hole transfer in green) pathways. In each configuration, the left chromophore is A and the right B, while lower orbitals are HOMO and upper are LUMO.

This set of states constitutes the diabatic basis (**Ψ**, Equation 2) in which SF couplings will be described in this thesis and for which the Hamiltonian, $\mathbf{H_{el}}$, (Equation 3) may be written to identify the important diabatic couplings.[10]

$$|\mathbf{\Psi}\rangle = \begin{pmatrix} |S_0S_0\rangle \\ |S_1S_0\rangle \\ |S_0S_1\rangle \\ |CA\rangle \\ |AC\rangle \\ |{}^1TT\rangle \end{pmatrix} \tag{2}$$

$\mathbf{H_{el}}$ =

$$\begin{pmatrix} E(S_0S_0) & \langle S_1S_0|\mathbf{H_{el}}|S_0S_0\rangle & \langle S_0S_1|\mathbf{H_{el}}|S_0S_0\rangle & \langle CA|\mathbf{H_{el}}|S_0S_0\rangle & \langle AC|\mathbf{H_{el}}|S_0S_0\rangle & \langle {}^1TT|\mathbf{H_{el}}|S_0S_0\rangle \\ \langle S_0S_0|\mathbf{H_{el}}|S_1S_0\rangle & E(S_1S_0) & \langle S_0S_1|\mathbf{H_{el}}|S_1S_0\rangle & \langle CA|\mathbf{H_{el}}|S_1S_0\rangle & \langle AC|\mathbf{H_{el}}|S_1S_0\rangle & \langle {}^1TT|\mathbf{H_{el}}|S_1S_0\rangle \\ \langle S_0S_0|\mathbf{H_{el}}|S_0S_1\rangle & \langle S_1S_0|\mathbf{H_{el}}|S_0S_1\rangle & E(S_0S_1) & \langle CA|\mathbf{H_{el}}|S_0S_1\rangle & \langle AC|\mathbf{H_{el}}|S_0S_1\rangle & \langle {}^1TT|\mathbf{H_{el}}|S_0S_1\rangle \\ \langle S_0S_0|\mathbf{H_{el}}|CA\rangle & \langle S_1S_0|\mathbf{H_{el}}|CA\rangle & \langle S_0S_1|\mathbf{H_{el}}|CA\rangle & E(CA) & \langle AC|\mathbf{H_{el}}|CA\rangle & \langle {}^1TT|\mathbf{H_{el}}|CA\rangle \\ \langle S_0S_0|\mathbf{H_{el}}|AC\rangle & \langle S_1S_0|\mathbf{H_{el}}|AC\rangle & \langle S_0S_1|\mathbf{H_{el}}|AC\rangle & \langle CA|\mathbf{H_{el}}|AC\rangle & E(AC) & \langle {}^1TT|\mathbf{H_{el}}|AC\rangle \\ \langle S_0S_0|\mathbf{H_{el}}|{}^1TT\rangle & \langle S_1S_0|\mathbf{H_{el}}|{}^1TT\rangle & \langle S_0S_1|\mathbf{H_{el}}|{}^1TT\rangle & \langle CA|\mathbf{H_{el}}|{}^1TT\rangle & \langle AC|\mathbf{H_{el}}|{}^1TT\rangle & E({}^1TT) \end{pmatrix} \tag{3}$$

The direct pathway (the blue arrow in Figure 1.2) relies on the direct coupling (off-diagonal) matrix elements between S_1S_0/S_0S_1 (here written only for S_1S_0) and ^{1}TT, which have the form $\langle ^1\text{TT}|\mathbf{H_{el}}|S_1S_0\rangle$, $\langle ^1\text{TT}|\mathbf{H_{el}}|S_0S_1\rangle$, and their Hermitian conjugates. These two-electron (see Figure 1.2) coupling terms may be small (this is thought to be the case in the polyacenes[41,42]), and SF may instead proceed using coupling derived from one of the mediated pathways (the green and red arrows in Figure 1.2). Each of those pathways relies on two diabatic couplings, consisting first of coupling between the initially excited singlet (S_1S_0/S_0S_1) and a CT state (either CA/AC), which is given by the matrix elements $\langle \text{CA}|\mathbf{H_{el}}|S_0S_1\rangle$ and $\langle \text{AC}|\mathbf{H_{el}}|S_0S_1\rangle$ (with equivalent couplings for S_0S_1, all with Hermitian conjugates). These pathways reach the product through coupling between CT and ^{1}TT; this is given by the matrix elements $\langle ^1\text{TT}|\mathbf{H_{el}}|\text{CA}\rangle$ or $\langle ^1\text{TT}|\mathbf{H_{el}}|\text{AC}\rangle$ (with their Hermitian conjugates). Depending on whether the electron or hole is transferred from the initially excited singlet (see Figure 1.2), the resulting pathway is referred to as the electron transfer or hole transfer pathway, respectively.

Calculating the values of these matrix elements allows for prediction of SF rates using simple (but powerful) models like Marcus theory. To achieve this, the above couplings are often approximated[10,41] in terms of the one-electron components of the Fock matrix ($\mathbf{F = H_1 + J + K}$, which includes Coulomb repulsion, **J,** and electron exchange, **K,** components perturbing the one-electron Hamiltonian $\mathbf{H}_1$) and two-electron Coulomb terms that are often neglected due to having small magnitude in the materials considered here.[10,42,43] The remaining elements (where A and B again denote the individual monomers) constitute electron transfer integrals, and are given in Equation 4. The involved orbitals are apparent from the pathways in Figure 1.2.

$$\langle CA|\mathbf{H_{el}}|S_1S_0\rangle \approx \langle LUMO_A|\mathbf{F}|LUMO_B\rangle = t_{LL}$$

$$\langle AC|\mathbf{H_{el}}|S_1S_0\rangle \approx -\langle HOMO_A|\mathbf{F}|HOMO_B\rangle = -t_{HH}$$

$$\langle CA|\mathbf{H_{el}}|S_0S_1\rangle \approx -\langle HOMO_A|\mathbf{F}|HOMO_B\rangle = -t_{HH}$$

$$\langle AC|\mathbf{H_{el}}|S_0S_1\rangle \approx \langle LUMO_A|\mathbf{F}|LUMO_B\rangle = t_{LL}$$

$$\langle {}^1TT|\mathbf{H_{el}}|CA\rangle \approx (3/2)^{1/2}\,\langle LUMO_A|\mathbf{F}|HOMO_B\rangle = (3/2)^{1/2}\,t_{LH}$$

$$\langle {}^1TT|\mathbf{H_{el}}|AC\rangle \approx (3/2)^{1/2}\,\langle HOMO_A|\mathbf{F}|LUMO_B\rangle = (3/2)^{1/2}\,t_{HL} \quad (4)$$

From these transfer integrals we can write the desired SF couplings, given by $H_{AB} = (3/2)^{1/2}(t_{LH}t_{LL} - t_{HL}t_{HH})/\Delta E_{CT}$ or $(3/2)^{1/2}(t_{HL}t_{LL} - t_{LH}t_{HH})/\Delta E_{CT}$ from second order perturbation theory (for the electron-transfer and hole-transfer pathways, respectively). Finally, it is possible to estimate the desired fission rate coefficient, $k_{fission}$, as shown in Equation 5. In this, λ is the reorganization energy, k_B is the Boltzmann constant, T is the temperature, and ΔG_{rxn} is the reaction free energy.

$$k_{fission} = \frac{2\pi}{\sqrt{4\pi\hbar^2\lambda k_B T}}|H_{AB}|^2 \exp\left(-\frac{(\Delta G_{rxn}+\lambda)^2}{4\lambda k_B T}\right) \quad (5)$$

As an important note (with implications throughout the latter chapters of this thesis), the transfer integrals (e.g. $\langle HOMO_A|\mathbf{F}|LUMO_B\rangle$) in Equation 4 scale[41,44,45] with the corresponding chromophore-to-chromophore orbital overlap integrals, (e.g. $\langle HOMO_A|LUMO_B\rangle$). From this, it is evident that under certain circumstances of orbital symmetry and monomer orientation where these integrals vanish, the accompanying SF-relevant couplings also vanish and $k_{SF} \approx 0$. This is a helpful metric as monomer frontier orbitals are relatively simple to obtain via techniques like density functional theory (and diabatization of dimer states may be used to obtain similar information in covalent dimers[41]). The limits of this assumption were considered in theoretical work on the covalent dimer known as BT1[41] (studied experimentally in Chapter 2) where it was proposed that nonzero couplings could still manifest due to vibrations that break this symmetry. With these considerations in mind, this dissertation aims to build a foundation upon which theoretical

understanding of these couplings (in conjunction with energetics) may be clearly observed controlling SF in real systems.

1.5 A Platform for Informing SF Chromophore Design

The work in this dissertation aims to inform chromophore design. The conceptual framework presented in this chapter guides thinking in subsequent chapters, where experimental results are interpreted in the context of coupling and energetics. This begins in Chapter 2 with an examination of four distinct polycrystalline films of the seminal SF chromophore Tc, including efforts at coherent control. The goal is to compare and contrast the roles of large-scale (e.g. crystallite domain size) and microscopic (e.g. electronic coupling) properties in determining SF rates. The concepts outlined therein are distilled to the fundamental subunit of SF—that of a dimer—for Chapter 3. In studying the molecule BT1 (a tetracene-inspired dimer), the microscopic parameters governing SF (energetics and electronic coupling) are accessed to show the importance of symmetry for SF electronics. A refinement to the BT1 platform is then considered in Chapter 4, where the improved stability and solubility of a BT1 derivative, TIPS-BT1, allows for detailed photophysical studies that reveal the role of charge-transfer states in a system that is otherwise similar to BT1. Chapter 5 then concludes with a brief exploration of solution-phase coherent control efforts targeted at symmetry-breaking in TIPS-BT1. Together, these chapters lay a foundation for future work that promises answers to difficult questions about the importance of symmetry, quantum mechanical coupling, and energetics in determining SF efficiency.

1.6 Bibliography

1. IPCC. *Climate Change 2013 - The Physical Science Basis*. (Cambridge University Press, 2014).
2. Cook, T. R., Dogutan, D. K., Reece, S. Y., Surendranath, Y., Teets, T. S. & Nocera, D. G. Solar Energy Supply and Storage for the Legacy and Nonlegacy Worlds. *Chem. Rev.* **110,** 6474–6502 (2010).
3. Lewis, N. S., Crabtree, G., Nozik, A. J., Wasielewski, M. R., Alivisatos, P., Kung, H., Tsao, J., Chandler, E., Walukiewicz, W., Spitler, M., Ellingson, R., Overend, R., Mazer, J., Gress, M., Horwitz, J., Ashton, C., Herndon, B., Shapard, L. & Nault, R. M. *Basic Research Needs for Solar Energy Utilization. Report of the Basic Energy Sciences Workshop on Solar Energy Utilization, April 18-21, 2005*. *Basic Energy Sciences Workshop on Solar Energy Utilization* (2005).
4. Bleich, K. & Guimaraes, R. D. *Renewable Infrastructure Investment Handbook: A Guide for Institutional Investors.* (2016).
5. Shockley, W. & Queisser, H. J. Detailed Balance Limit of Efficiency of p-n Junction Solar Cells. *J. Appl. Phys.* **32,** 510 (1961).
6. Green, M. A. Third generation photovoltaics: Ultra-high conversion efficiency at low cost. *Prog. Photovoltaics Res. Appl.* **9,** 123–135 (2001).
7. Hanna, M. C. & Nozik, A. J. Solar Conversion Efficiency of Photovoltaic and Photoelectrolysis Cells with Carrier Multiplication Absorbers. *J. Appl. Phys.* **100,** 74510 (2006).
8. Zhu, X. Exceeding the Limit in Solar Energy Conversion with Multiple Excitons. *Acc. Chem. Res.* **46,** 1239–1241 (2013).

9. De Vos, A. & Desoete, B. On the ideal performance of solar cells with larger-than-unity quantum efficiency. *Sol. Energy Mater. Sol. Cells* **51,** 413–424 (1998).

10. Smith, M. B. & Michl, J. Singlet Fission. *Chem. Rev.* **110,** 6891–6936 (2010).

11. Greyson, E. C., Stepp, B. R., Chen, X., Schwerin, A. F., Paci, I., Smith, M. B., Akdag, A., Johnson, J. C., Nozik, A. J., Michl, J. & Ratner, M. a. Singlet Exciton Fission for Solar Cell Applications: Energy Aspects of Interchromophore Coupling. *J. Phys. Chem. B* **114,** 14223–32 (2010).

12. Xia, J., Sanders, S. N., Cheng, W., Low, J. Z., Liu, J., Campos, L. M. & Sun, T. Singlet Fission: Progress and Prospects in Solar Cells. *Adv. Mater.* **28,** 1601652 (2016).

13. Jadhav, P. J., Mohanty, A., Sussman, J., Lee, J. & Baldo, M. a. Singlet Exciton Fission in Nanostructured Organic Solar Cells. *Nano Lett.* **11,** 1495–1498 (2011).

14. Congreve, D. N., Lee, J., Thompson, N. J., Hontz, E., Yost, S. R., Reusswig, P. D., Bahlke, M. E., Reineke, S., Van Voorhis, T. & Baldo, M. A. External Quantum Efficiency Above 100% in a Singlet-Exciton-Fission-Based Organic Photovoltaic Cell. *Science.* **340,** 334–337 (2013).

15. Pazos-Outón, L. M., Lee, J. M., Futscher, M. H., Kirch, A., Tabachnyk, M., Friend, R. H. & Ehrler, B. A Silicon–Singlet Fission Tandem Solar Cell Exceeding 100% External Quantum Efficiency with High Spectral Stability. *ACS Energy Lett.* **2,** 476–480 (2017).

16. Pavlopoulos, T. G. Measurement of the Triplet-Triplet Absorption Spectrum of Tetracene Using cw Argon Laser Excitation. *J. Chem. Phys.* **56,** 227 (1972).

17. Smith, M. B. & Michl, J. Recent Advances in Singlet Fission. *Annu. Rev. Phys. Chem.* **64,** 361–386 (2013).

18. Le, A. K., Bender, J. A. & Roberts, S. T. Slow Singlet Fission Observed in a Polycrystalline

Perylenediimide Thin Film. *J. Phys. Chem. Lett.* **7,** 4922–4928 (2016).

19. Margulies, E. A., Shoer, L. E., Eaton, S. W. & Wasielewski, M. R. Excimer formation in cofacial and slip-stacked perylene-3,4:9,10-bis(dicarboximide) dimers on a redox-inactive triptycene scaffold. *Phys. Chem. Chem. Phys.* **16,** 23735–23742 (2014).
20. Eaton, S. W., Miller, S. a., Margulies, E. a., Shoer, L. E., Schaller, R. D. & Wasielewski, M. R. Singlet Exciton Fission in Thin Films of tert -Butyl-Substituted Terrylenes. *J. Phys. Chem. A* **119,** 4151–4161 (2015).
21. Ryerson, J. L., Schrauben, J. N., Ferguson, A. J., Sahoo, S. C., Naumov, P., Havlas, Z., Michl, J., Nozik, A. J. & Johnson, J. C. Two Thin Film Polymorphs of the Singlet Fission Compound 1,3-Diphenylisobenzofuran. *J. Phys. Chem. C* **118,** 12121–12132 (2014).
22. Johnson, J. C., Akdag, A., Zamadar, M., Chen, X., Schwerin, A. F., Paci, I., Smith, M. B., Havlas, Z. Z., Miller, J. R., Ratner, M. A., Nozik, A. J. & Michl, J. Toward designed singlet fission: Solution photophysics of two indirectly coupled covalent dimers of 1,3-diphenylisobenzofuran. *J. Phys. Chem. B* **117,** 4680–4695 (2013).
23. Piland, G. B., Burdett, J. J., Kurunthu, D. & Bardeen, C. J. Magnetic field effects on singlet fission and fluorescence decay dynamics in amorphous rubrene. *J. Phys. Chem. C* **117,** 1224–1236 (2013).
24. Stern, H. L., Musser, A. J., Gelinas, S., Parkinson, P., Herz, L. M., Bruzek, M. J., Anthony, J., Friend, R. H. & Walker, B. J. Identification of a triplet pair intermediate in singlet exciton fission in solution. *Proc. Natl. Acad. Sci.* **112,** 7656–7661 (2015).
25. Walker, B. J., Musser, A. J., Beljonne, D. & Friend, R. H. Singlet exciton fission in solution. *Nat. Chem.* **5,** 1019–1024 (2013).
26. Burdett, J. J. & Bardeen, C. J. The Dynamics of Singlet Fission in Crystalline Tetracene and

Covalent Analogs. *Acc. Chem. Res.* **46,** 1312–1320 (2013).

27. Wan, Y., Guo, Z., Zhu, T., Yan, S., Johnson, J. & Huang, L. Cooperative singlet and triplet exciton transport in tetracene crystals visualized by ultrafast microscopy. *Nat. Chem.* **7,** 785–792 (2015).
28. Arias, D. H., Ryerson, J. L., Cook, J. D., Damrauer, N. H. & Johnson, J. C. Polymorphism influences singlet fission rates in tetracene thin films. *Chem. Sci.* **7,** 1185–1191 (2016).
29. Jundt, C., Klein, G., Sipp, B. & Moigne, J. Le. Exciton Dynamics in Pentacene Thin Films Studied by Pump-Probe Spectroscopy. *Chem. Phys. Lett.* **2614,** (1995).
30. Wright, G. Absolute Quantum Efficiency of Photofluorescence of Anthracene Crystals. *Proc. Phys. Soc. B* **241,** (1955).
31. Swenberg, C. E. & Stacy, W. T. Bimolecular radiationless transitions in crystalline tetracene. *Chem. Phys. Lett.* **2,** 327–328 (1968).
32. Tomkiewicz, Y., Groff, R. P. & Avakian, P. Spectroscopic Approach to Energetics of Exciton Fission and Fusion in Tetracene Crystals. *J. Chem. Phys.* **54,** 4504–4507 (1971).
33. Nijegorodov, N., Ramachandran, V. & Winkoun, D. P. The dependence of the absorption and fluorescence parameters, the intersystem crossing and internal conversion rate constants on the number of rings in polyacene molecules. *Spectrochim. Acta Part A Mol. Biomol. Spectrosc.* **53,** 1813–1824 (1997).
34. Lim, S.-H., Bjorklund, T., Spano, F. & Bardeen, C. J. Exciton Delocalization and Superradiance in Tetracene Thin Films and Nanoaggregates. *Phys. Rev. Lett.* **92,** 107402 (2004).
35. Singh, S., Jones, W. J., Siebrand, W., Stoicheff, B. P. & Schneider, W. G. Laser Generation of Excitons and Fluorescence in Anthracene Crystals. *J. Chem. Phys.* **42,** 330 (1965).

36. Johnson, R. & Merrifield, R. Effects of Magnetic Fields on the Mutual Annihilation of Triplet Excitons in Anthracene Crystals. *Phys. Rev. B* **1,** 896–902 (1970).

37. Wilson, M. W. B., Rao, A., Johnson, K., Gélinas, S., di Pietro, R., Clark, J. & Friend, R. H. Temperature-Independent Singlet Exciton Fission in Tetracene. *J. Am. Chem. Soc.* **135,** 16680–16688 (2013).

38. Wilson, M. W. B., Rao, A., Clark, J., Kumar, R. S. S., Brida, D., Cerullo, G. & Friend, R. H. Ultrafast dynamics of exciton fission in polycrystalline pentacene. *J. Am. Chem. Soc.* **133,** 11830–3 (2011).

39. Grumstrup, E., Johnson, J. & Damrauer, N. Enhanced Triplet Formation in Polycrystalline Tetracene Films by Femtosecond Optical-Pulse Shaping. *Phys. Rev. Lett.* **105,** 257403 1-4 (2010).

40. Brif, C., Chakrabarti, R. & Rabitz, H. Control of Quantum Phenomena: Past, Present and Future. *New J. Phys.* **12,** 75008 (2010).

41. Alguire, E. C., Subotnik, J. E. & Damrauer, N. H. Exploring Non-Condon Effects in a Covalent Tetracene Dimer: How Important Are Vibrations in Determining the Electronic Coupling for Singlet Fission? *J. Phys. Chem. A* **119,** 299–311 (2015).

42. Berkelbach, T. C., Hybertsen, M. S. & Reichman, D. R. Microscopic theory of singlet exciton fission. II. Application to pentacene dimers and the role of superexchange. *J. Chem. Phys.* **138,** 114103 (2013).

43. Teichen, P. E. & Eaves, J. D. A microscopic model of singlet fission. *J. Phys. Chem. B* **116,** 11473–81 (2012).

44. Vallett, P. J., Snyder, J. L. & Damrauer, N. H. Tunable electronic coupling and driving force in structurally well-defined tetracene dimers for molecular singlet fission: a computational

exploration using density functional theory. *J. Phys. Chem. A* **117,** 10824–38 (2013).

45. Ayed, O., Bernard, E. & Silvi, B. On the Mulliken approximation of multicentre integrals. *J. Mol. Struct. THEOCHEM* **135,** 159–168 (1986).

Chapter 2. Effects of Morphology and Grain Size on Singlet Fission in Polycrystalline Tetracene

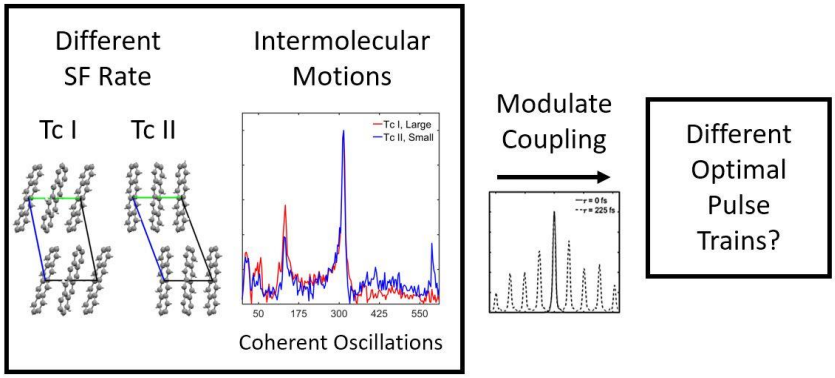

2.1 Polymorphism and Coupling

Efficiency and rate are crucial for determining the viability of different singlet fission (SF) moieties for solar energy applications. These properties may be dictated by large-scale phenomena (like grain boundaries, molecular packing, defects, and exciton diffusion)[1–8] that are present in bulk materials, or by small-scale effects like intermolecular coupling that appear relevant for all SF moieties (solids, covalent dimers, or otherwise).[5,9–13] Systems that allow for comparative studies of these factors (and their complex interactions with each other) are desirable, and polycrystalline films are well-suited to the task. Films can be modified via inducing formation of different crystallite polymorphs to give distinct couplings, defect densities, and exciton transport properties; they may also be modified through their crystallite sizes, changing the distance required to encounter grain boundaries (and defects).[4,5,8,14,15] It is therefore possible in films to examine the role of large-scale phenomena in controlling the efficiency and rate of SF. Given its status as a seminal and highly efficient SF chromophore,[9] this work considers polycrystalline tetracene (Tc) films for this purpose.

It is somewhat surprising that little work has been done to investigate the differences in SF behavior in different Tc polymorphs (though a recent study considered differences between polycrystalline films before and after annealing in comparison with single crystals[4]). The variety of fission lifetimes reported for Tc is surprising, with some experiments extracting singlet decays on a timescale as short as 25 ps at cold temperatures[16] despite other studies finding SF rates of 70–90 ps[4,17] (including work that found SF to be temperature independent with a lifetime of 90 ps[18]). The apparent disagreement of these findings may be due to uncontrolled variance in polymorph type and/or grain size. To rationalize these discrepancies and further investigate this complex problem, a set of polycrystalline films of two polymorphs of Tc,[19–24] with crystallite grain size as a complementary parameter, were synthesized and studied to find the rate of SF and, eventually, to investigate the role of interchromophore coupling in each system. Crystal structures for these two polymorphs, hereafter referred to as Tc I (the more common and thermodynamically stable polymorph at room temperature) and Tc II (more readily accessed at low temperatures and high pressures)[20] are shown in Figure 2.1.

When comparing the structures of Tc I[19] and Tc II,[24] a few differences are apparent. First, there is increased long-axis slipping for Tc molecules in Tc I as compared to Tc II. Specifically, Tc I has parallel Tc molecules that are translated by approximately one carbon-carbon bond along their long axes relative to their neighbors, as compared to a slip of around half of that distance in Tc II. Second, there is closer packing along the *c* crystallographic axis in Tc I (cell length of 13.0 Å in Tc I vs. 14.5 Å in Tc II), while its cell volume is slightly larger overall than that of Tc II (564 $Å^3$ for Tc I vs. 561 $Å^3$ for Tc II). Lastly, there is also a small constriction along the *a* and *b* crystallographic axes in Tc II (which brings the Tc π-systems slightly closer together). The overall

cell dimensions are *a* = 6.1 Å, *b* = 7.7 Å, and *c* = 13.0 Å for Tc I and *a* = 5.9 Å, *b* = 7.4 Å, and *c* = 14.5 Å for Tc II.

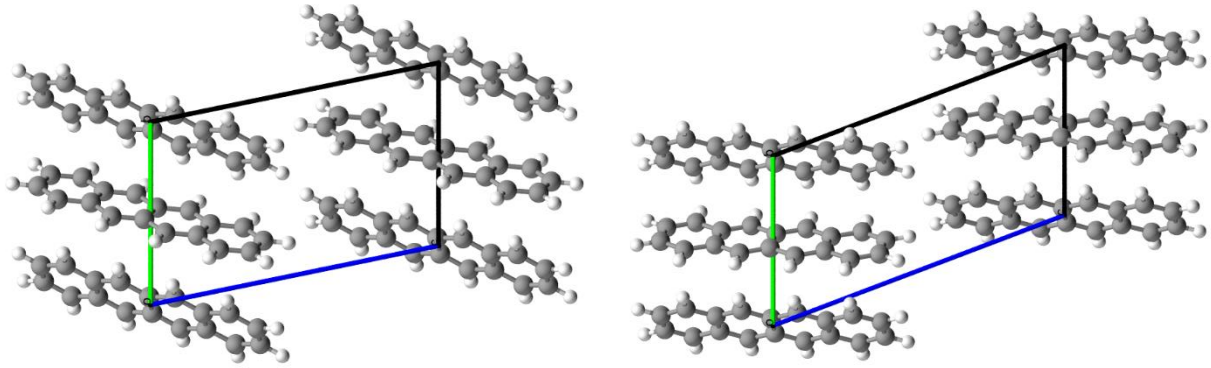

Figure 2.1. Crystal structures of Tc polymorphs Tc I (left) and Tc II (right) viewed along the *a* crystal axis. The increased slippage along the chromophore long axis in Tc I relative to Tc II is evident. The *b* (green) and *c* (blue) crystallographic axes are shown, along with the unit cell, for each crystal structure.

Electronic coupling is expected to differ in Tc I and Tc II as a result of their structural differences. The differences in packing along the *a* and *b* crystallographic axes in Tc II should influence the nearest-neighbor couplings between various chromophore pairs, but the aforementioned change in slipping along the long axis is not expected to have any effect due to it being perpendicular to the relevant HOMO → LUMO transition moment.[11] To provide a framework for discussing this coupling, various dimer interactions are defined here. These are labeled using translation vectors of the form [A B] which represent the separation between the two chromophores. Element A is the separation of the two chromophores along the *a* crystallographic axis, while B is their separation along the *b* crystallographic axis. Thus the [1 0] and [-1 0] vectors denote equivalent dimer pairs in which Tc subunits are separated by one unit cell length in the *a* direction but which share *b* coordinates (the chromophores in these pairs are connected by the red arrows in Figure 2.2). The remaining two dimer pairs are connected by yellow and purple arrows, and their vectors are given in the diagram below.

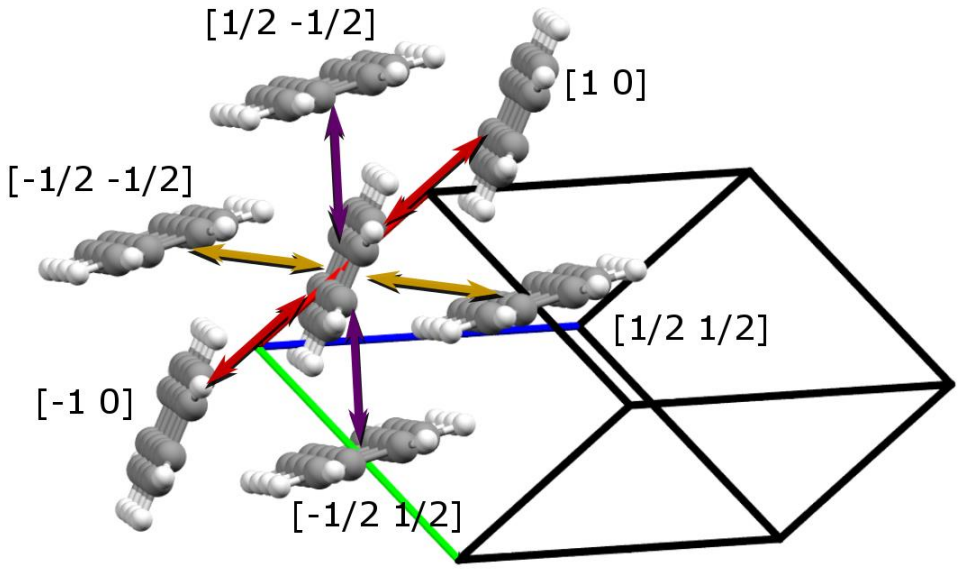

Figure 2.2. Nearest-neighbor pairs in Tc. Translation vectors are of the form [A B], where A represents translation along the *a* crystallographic axis (red) and B represents translation along the *b* crystallographic axis (green). A and B are normalized to the corresponding axis of the unit cell. Translation along the *c* crystallographic axis (blue, recedes into the plane) which gives end-to-end interactions, is not shown. Color-coded arrows (red, yellow, and purple) denote unique dimer interactions (same-color arrows denote equivalent interactions).

The interchromophore couplings considered for these dimer pairs are the same charge transfer (CT) mediated diabatic couplings discussed in Chapter 1. These couplings are the indirect (second order) links between the singly-excited dimer state S_1S_0 or S_0S_1, hereafter simply "S_1" (where one of the Tc molecules in the dimer pair, which are non-equivalent due to orientation, has been excited to its first singlet state) and ^{1}TT (the spin-paired multiexcitonic state created by SF). These couplings were calculated by our group according to Equations 1 and 2 (refer to Chapter 1 for the derivation of these diabatic coupling expressions).

$$\text{Diabatic Coupling } (S_1S_0 \rightarrow {}^1\text{TT}) = \frac{\left|\frac{\sqrt{3}}{2}(t_{LH}t_{LL} - t_{HL}t_{HH})\right|}{\Delta E_{CT}} \quad (1)$$

$$\text{Diabatic Coupling } (S_0S_1 \rightarrow {}^1\text{TT}) = \frac{\left|\frac{\sqrt{3}}{2}(t_{HL}t_{LL} - t_{LH}t_{HH})\right|}{\Delta E_{CT}} \quad (2)$$

This method assumes that the energy of the CT state (which enables communication between S_1 and ^1TT) lies above S_1 by $\Delta E_{CT} \approx 600$ meV (estimated based on CT and singlet energies from literature[1,25]). The value of ΔE_{CT} is not expected to vary substantially between Tc I and Tc II, and thus the same value was used for both systems. Finally, the one-electron coupling terms of the form t_{AB} are elements of the Fock matrix between frontier orbitals localized on chromophores A and B (in which H denotes highest occupied molecular orbital and L denotes lowest unoccupied molecular orbital) that were discussed in Chapter 1. Centroid distances for all dimer pairs (identified by their translation vector), along with diabatic couplings calculated by our group, are given in Table 2.1 for each nearest-neighbor dimer interaction in Tc I and Tc II. The largest diabatic coupling for each polymorph is additionally highlighted in bold.

Table 2.1. Interchromophore interactions in Tc I and Tc II, with largest couplings for each polymorph in bold

Dimer Pair [A B]	Centroid Distance /Å	Diabatic Coupling /meV ($S_1S_0 \rightarrow {}^1TT$, $S_0S_1 \rightarrow {}^1TT$)
Tc I [1 0]	6.1	0.5, 0.5
Tc II [1 0]	5.9	1.4, 1.4
Tc I [1/2 1/2]	5.1	0.6, **16**
Tc II [1/2 1/2]	4.8	**8.5**, 1.8
Tc I [-1/2 1/2]	4.7	4.5, 7.2
Tc II [-1/2 1/2]	4.7	3.4, 6.2

Based simply on the largest couplings (in both polymorphs, this is the [1/2 1/2] dimer pair given by the yellow arrows in Figure 2.2), one would predict that SF should be faster in Tc I than in Tc II, while larger grain sizes should slow SF[4] in both polymorphs substantially. The remainder of this chapter examines the experimental results, contrasting them with these predictions, from a

matrix of four Tc film types in which grain size and polymorph type have been independently varied. The goal is to address the role of coupling in discussions about SF in the solid-state and to work towards a better understanding of what truly governs efficiency in those materials.

2.2 Tc Film Preparation and Characterization

Tc films were created in collaboration with Joe Ryerson at the National Renewable Energy Laboratory using a thermal evaporator (Angstrom Engineering Nexdep) inside an inert-atmosphere glove box. Substrates (glass microscope cover slips) were washed with hexanes and acetone and subsequently plasma cleaned prior to deposition. Deposition was performed under high vacuum (<1 μTorr) by heating Tc (Sigma-Aldrich, used as received) to ~200 °C in an alumina crucible. During deposition, the substrates (in sets of ~10 cover slips) were rotated perpendicular to the growth axis while progress was monitored using a quartz crystal microbalance *in situ*. By varying substrate temperature and deposition rate it was possible to selectively control the Tc polymorph formed and the size of the crystallite domains in the resulting film. It was found that substrate temperature controlled polymorph type (Tc I was favored when depositing on heated substrates, and Tc II was favored when depositing onto cold substrates), while deposition rate determined grain size (with slower deposition yielding larger crystallites). After deposition was completed, films were sealed with matching cover slips in the inert atmosphere of the glove box prior to experimentation. This was accomplished by heating a DuPont Surlyn cutout frame on a clean cover slip to its melting point before placing a second cover slip (with deposited Tc film face-down) onto the first cover slip. The resulting films are air-tight.

The deposition parameters used and the resulting film properties are summarized in Table 2.2, and color coded according to film type (this color scheme is employed throughout the remainder of this chapter).

Table 2.2. Representative polycrystalline Tc film characteristics

Deposition Rate / Å/s	Substrate Temp. /°C	Crystallite Size /nm	Polymorph	Film Type
0.5–1	65	750–2000	Tc I	Tc I, Large
5	65	150–350	Tc I	Tc I, Small
0.5–1	-180	750–2000	Tc II	Tc II, Large
5	-180	150–350	Tc II	Tc II, Small

The film characterization by which these parameters were determined is summarized below, and consists of X-ray diffraction, which allowed for differentiation of polymorphs, and atomic force microscopy, which was used to determine film thickness and crystallite size.

2.2.1 X-Ray Diffraction

The polymorph purity of Tc film samples was determined using X-ray diffraction (XRD). XRD data was collected from a D2 Phaser X-Ray Diffraction Desktop system (Bruker) using Cu-Kα radiation. The substrate was rotated during acquisition, and diffraction patterns were detected with a LYNXEYE array detector at a resolution of 0.03 Å between 5–25°. Complementary XRD data for Tc II, Large films was collected from a Rigaku DMax 2500 X-ray diffractometer operating in Θ/2Θ mode using Cu-Kα radiation at a scan speed of 1°/min between 5–25°.

XRD results are shown in Figure 2.3 for the 001 diffraction peak of Tc I and Tc II corresponding to the 001 plane, which allows for simple differentiation between Tc I and Tc II.[21,22,24] Only 00*c* peaks are resolved by powder XRD due to the growth direction of crystals: Tc crystals grow with the crystallographic *c* axis normal to the surface and an otherwise random orientation of crystallite domains. The smaller angle found for Tc II is consistent with its larger *c* dimension. All films studied had Tc I or Tc II polymorph purity ~10:1, though on a timescale of

weeks, un-refrigerated Tc II films were found to convert to the more thermodynamically stable Tc I polymorph. Initial attempts to achieve the reverse process (conversion of Tc I films to Tc II films) by cooling films to cryogenic temperatures were unsuccessful, although it has been indicated in literature that irreversible (until subsequent annealing at 320–400 K) conversion of Tc I to Tc II is possible in this manner.[20]

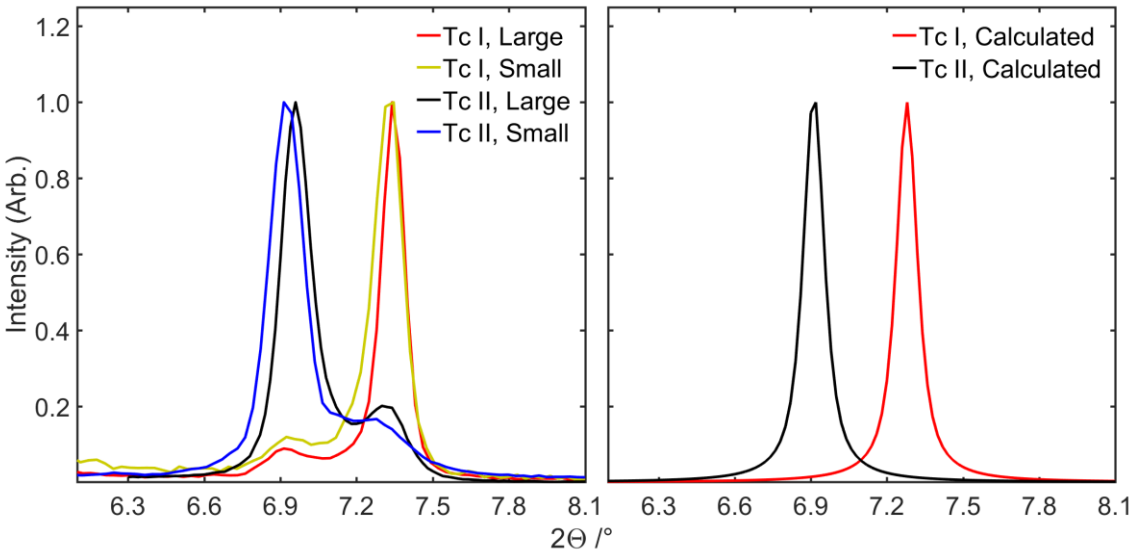

Figure 2.3. XRD spectra showing the 001 peak in Tc I and Tc II films of different grain sizes. Left: experimental data for representative films. Right: calculated XRD patterns for Tc I and Tc II based on the crystal structures.

2.2.2 Atomic Force Microscopy

AFM measurements were obtained from a Park Systems AFM XE-70 operating in tapping mode with a TAP-300G AFM tip. Film areas of 10 µm × 10 µm were scanned at a resolution of 256 × 256 pixels. Film thickness (~80 nm) was determined by scoring the film to the glass surface with a razor blade and measuring the depth of the resulting groove. Representative AFM data for Tc I and Tc II films used in these experiments is shown in Figure 2.4.

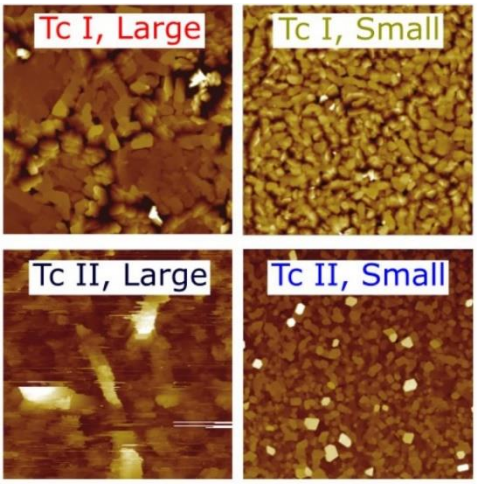

Figure 2.4. Representative AFM images of the Tc films studied. AFM images cover a 10 µm × 10 µm area. Film types are as labeled.

As indicated in Table 2.2, slower deposition rates were found to give large (750–2000 nm) crystallites, while faster deposition rates yielded smaller (150–350 nm) crystallites.

2.3 Time-Resolved Emission of Tc Films

The first time-resolved indication of differing SF rates in these films was provided by time-correlated single photon counting measurements (TCSPC), which provides insight into the emissive excited state population as a function of time. The instrument consists of an 82 MHz mode-locked Ti:sapphire oscillator (Tsunami, Spectra-Physics) stepped down to a repetition rate of 4.1 MHz using a NEOS Technologies pulse-picker. The second harmonic (395nm) of the laser is generated with a β-barium borate crystal and filtered to remove residual fundamental before exciting the sample (fluence ~2 µJ/cm^2) at ~20° from normal. Tc film emission was collected at magic angle (54.7°) polarization relative to excitation, passed through a monochromator (Oriel 77250, wavelength set to λ_{em} = 535 nm), detected with a Hamamatsu R3809U-50 microchannel plate detector, and analyzed with a Becker-Hickl time-correlated single photon counting card. The instrument response function (IRF) was measured in the same manner as the Tc films, but the

sample was replaced by a white card, scattering (attenuated) excitation light into the detector with the monochromator set to 395 nm.

TCSPC decays for Tc I and Tc II films of both grain sizes were fit to a sum of three exponentials convolved with the IRF as shown in Equation 3 to parameterize the emission decays.

$$\text{Fit(Time)} = \Sigma_{i=1,\,2,\,3}\,[\,A_i \times \exp(-\text{Time}/\tau_i) * \text{IRF}\,] \quad (3)$$

Each TCSPC decay, along with its accompanying fit, is shown in Figure 2.5. Differences between film types are readily evident at early times, and early fits accurately capture this despite the width of the IRF (pictured). A sum of three exponentials was necessary to fully reproduce the observed decay, with the fast component attributed to SF-driven loss of the emissive singlet, while the longer components are derived from delayed fluorescence upon triplet-triplet annihilation to recreate the emissive singlet.[1] We focus here only on the fastest component. A representative early time fit is shown for Tc I, Large with the accompanying IRF. Full fits to all film types are also shown, and accurately reproduce the observed decays for multiple lifetimes of the longest component. The results of this fitting (lifetimes τ_i and accompanying amplitudes A_i) are summarized in Table 2.3.

Table 2.3. Summary of TCSPC Lifetimes (τ_i) and accompanying amplitudes (A_i)

Film	τ_1 /ps (A_1)	τ_2 /ps (A_2)	τ_3 /ps (A_3)
Tc I, Large	88 (0.77)	440 (0.17)	2300 (0.06)
Tc I, Small	75 (0.82)	660 (0.14)	3500 (0.04)
Tc II, Large	38 (0.78)	300 (0.13)	1500 (0.09)
Tc II, Small	55 (0.82)	410 (0.12)	2000 (0.06)

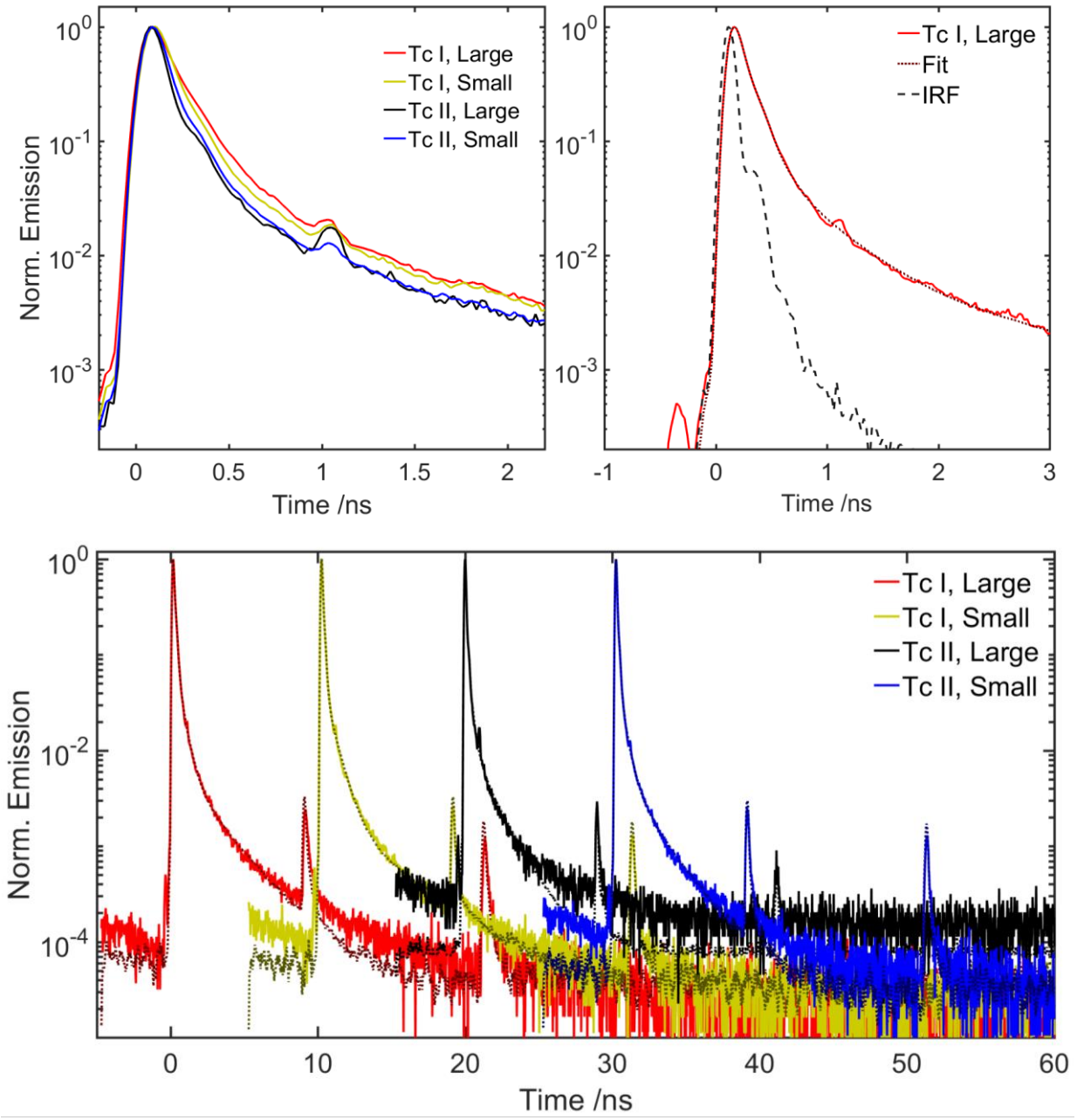

Figure 2.5. Measured TCSPC decays for all four film types. Top left: early-time behavior of all film types, showing differences in the fast decay component. Top right: data (solid line), IRF (dashed line) and fit (dotted line) for Tc I, Large film showing accurate fitting of early-time behavior through convolution. Bottom: full decays (solid lines) and corresponding fits (dotted lines) for all four film types, showing fit quality for all film types. The time axis has been arbitrarily shifted for clarity. The peaks at ~10 ns after the initial decay are due to re-excitation by imperfectly rejected oscillator pulses.

Examination of the fast decay component in the TCSPC data suggests that SF-driven loss of emissive S_1 occurs faster in Tc II films than in Tc I films, but that the effect of grain size is reversed between the two polymorphs. That is, larger grain size accelerates SF in Tc II, contrary to the expected behavior, while it slows SF in Tc I as expected.[4] Given that TCSPC does not directly observe triplet formation, and that the IRF temporal width is of the same order as the fastest decay component, these results are not sufficiently conclusive. Accordingly, transient absorption (TA) measurements were undertaken to provide a direct measurement of the SF rate in each film type.

2.4 Transient Absorption Spectroscopy: Polymorphism and Grain Size Dependence

The femtosecond TA spectroscopy (fsTA) results shown here were performed and modeled by collaborators Dylan Arias, Joe Ryerson, and Justin Johnson at the National Renewable Energy Laboratory (additional preliminary data acquisition and analysis was done in collaboration with Dylan Arias at the University of Colorado, Boulder, however these data are not presented here). This experiment provides access to SF in the different Tc films on an ultrafast timescale. Excitation pulses (400 nm, ~100 fs) were derived from a TOPAS-C optical parametric amplifier pumped with a Coherent Libra amplifier, and detection was achieved with an Ultrafast Systems LLC Helios TA Spectrometer (CaF_2-generated probe light; spectral range 350–800 nm). Due to fluence-dependence in the kinetics (known for Tc)[26] experiments were performed at a range of excitation densities (~10^{17}–10^{19} /cm^3), with the onset of fluence-dependent kinetics occurring near 10^{18} /cm^3. All results discussed here are in the low-fluence regime. Global fitting was performed using the kinetic model shown schematically in Figure 2.6 with basis spectra at ~1 ps (much less than the SF lifetime) and ~5 ns (well after the SF lifetime) chosen to represent singlet (S) and triplet (T) species associated spectra, respectively. Representative basis spectra for Tc II, Small are also

shown in Figure 2.6. The kinetic model used includes the following processes and rate constants: SF and its microscopic reverse (k_{sf}, k_{fus}); spontaneous and annihilation S losses (k^S_{sp}, k_{SS}); spontaneous and dissociative ^{1}TT losses (k^T_{sp}, k_{diss}); and spontaneous and recombinative T losses (k^T_{sp} and k_{TT}).

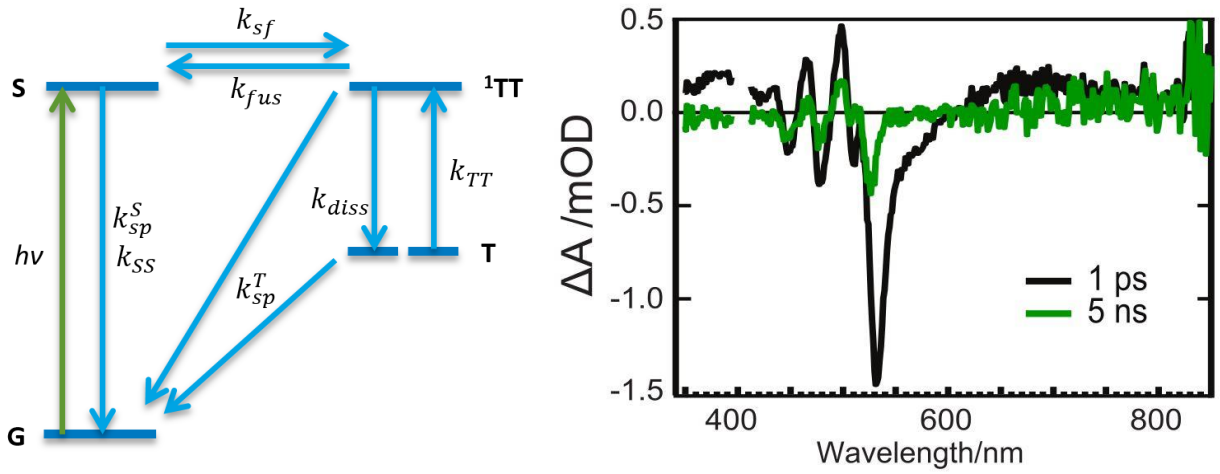

Figure 2.6. Left: kinetic model describing kinetics in Tc films. Right: example basis spectra used for fitting to determine population dynamics. Basis spectra are singlet (black) and triplet (green) for Tc II, Small.

Population dynamics were extracted based on fitting to a linear combination of S and T basis spectra, yielding the population kinetics in Figure 2.7 (after subtraction of signal derived from excitation of an acoustic mode in the high fluence data), and those kinetics were fitted globally according to the kinetic model above. The resulting SF lifetimes for each film type are listed in Table 2.2 along with the triplet yield determined from the population kinetics. Additional fit results and parameters are available elsewhere[27,28]. The results here are consistent with the TCSPC findings in that the rate of SF varies across film morphology and grain size. It is however more evident here that the dependence on grain size is significant for Tc I films but relatively unimportant for Tc II films (for which the SF rate is unchanged within experimental uncertainty

between the two grain sizes due to the signal-to-noise ratio of the data). The only obvious difference in triplet yield occurs for the Tc I, Large film, for which the yield appears smaller than the other films types; this is presumably related to its slower SF.

Table 2.4. Summary of extracted kinetic parameters by film type

Film Type	Fission Lifetime /ps	Triplet Yield /%
Tc I, Large	124	125
Tc I, Small	35	175
Tc II, Large	22	160
Tc II, Small	36	155

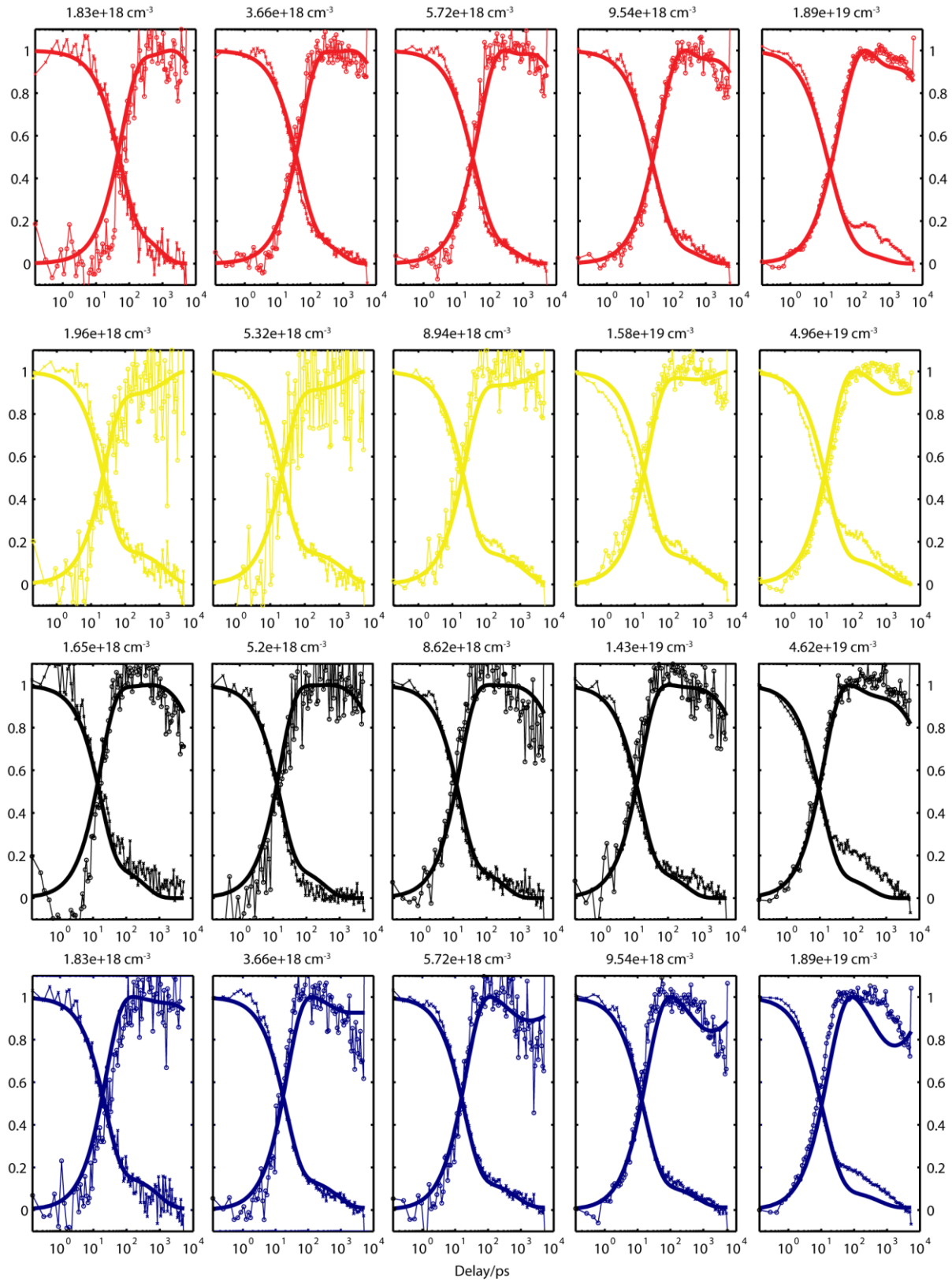

Figure 2.7. S decay and T rise kinetics for (top to bottom): Tc I, Large; Tc I, Small; Tc II, Large; and Tc II, Small films at the indicated excitation densities.

The observations from these experiments highlight the complexity of solid-phase systems, specifically with regards to the ability of dimer-pair diabatic couplings to accurately predict SF rates. For equivalent grain size, Tc II exhibits faster SF than Tc I in contrast with the coupling values predicted in Section 2.1. It is therefore hypothesized that large-scale effects (such as grain boundaries) play an important role here such that a dimer coupling picture discussed is inadequate for describing SF in polycrystalline Tc. Tc I behaves here in a manner consistent with the findings of Bardeen and co-workers[4] where SF was increasingly faster in single-crystals, annealed films and finally non-annealed films. This may be derived from increasing defect densities that act as traps for triplet excitations (this localization has been theoretically predicted to increase the rate of SF[3]), but the absence of this effect in Tc II suggests that the picture is still more complex. It is possible that defect densities are higher (or transport, which allows access to these defects, is faster) in Tc II. It is additionally possible that, despite inferior dimer-pair coupling, the closer-packing of chromophores in Tc II (due to constriction of the crystal *a* and *b* axes, which are 0.2 Å and 0.3 Å smaller in Tc II, respectively) facilitates better delocalization of the initial singlet excitations.

The findings here thus confirm the previously observed role of crystallinity[4] for Tc I, but newly highlight the importance of polymorphism in Tc as a whole. They also raise new questions about the role of coupling in solid Tc. In an attempt to disentangle the role of interchromophore coupling from transport and related phenomena, the remainder of this chapter considers attempts to control coupling-relevant intermolecular vibrations as an extension of previous work[29]. This begins with a brief examination of coherent oscillations in the TA data of two film types (accessed through ultrafast excitation) and concludes with preliminary efforts at controlling these accompanying intermolecular motions.

2.5 Towards Coherent Control of Polymorph-Dependent Vibrations

2.5.1 Experimental Methods

The fsTA experiment utilized in the following experiments differs from that described in Section 2.4. Here, the second harmonic of a CW Nd:YVO_4 laser (Coherent Verdi) is used to pump a Ti:sapphire oscillator (~800 nm, ~50 fs pulses at 94 MHz, K&M Labs), the output of which is directed into a multi-pass amplifier (Quantronix Odin, utilizing a Quantronix Darwin pump laser). Amplified ~800 nm pulses (~1 mJ/pulse at 1 kHz) are primarily directed (~80%) into a home-built non-collinear optical parametric amplifier (NOPA). NOPA output pulses (center wavelength near 530 nm, full-width at half-maximum (FWHM) of ~15 nm) are passed through a prism compressor to give pulses with 30–50 fs temporal FWHM, characterized using second-harmonic generation frequency resolved optical gating (SHG-FROG)[30]. Pump pulses are mechanically chopped at 500 Hz and directed through a home-built zero-dispersion 4-f grating compressor with a CRi 640 liquid-crystal spatial-light modulator (SLM) at its center in the frequency domain. The SLM was set during these experiments to provide no phase modulation (see Section 2.5.3 for a discussion of the pulse shaper). Excitation fluences were approximately matched to those used in previous, similar experiments[29] (60 nJ/pulse, ~200 μm spot diameter measured by translating a razor blade through the beam at its focus and fitting the resulting error function). All measurements were done at magic angle polarization (54.7°) relative to the probe, with mechanical chopping at 500 Hz.

White light is generated from a small portion of 800 nm amplifier output that is routed onto a delay stage before being focused into a sapphire crystal. Resulting white light is split into separate probe (overlapped with pump) and reference (passes through the sample at a location separate from the pump) beams. After exiting the sample, both the probe and the reference beams are coupled into an Acton 2300i monochromator set to 496 nm and detected using a Thor labs PDB210A

balanced photodiode detector. This allows for wavelength selectivity and high sensitivity of detected light. Additionally, the amplified photodiode output is coupled into a Stanford Research SR250 boxcar integrator and then a Stanford Research SR810 lock-in amplifier synced to the 500 Hz chopper frequency. This enables detection with high signal/noise between ~450–700 nm. This experiment is controlled using home-built software written in LabVIEW (National Instruments).

2.5.2 Observation of Coherent Oscillations

Clear oscillations are visible in the TA signal at 496 nm shown in Figure 2.8 (refer to the the S and T basis spectra in Figure 2.6 for the shape of this feature in both species). At early times, this excited state absorption (ESA) is derived from S, and after SF has occurred it is again present in T with a different magnitude (this ESA was initially assigned as a purely triplet feature in previous work[29], an assumption which is correct at times significantly longer than the SF time). It is believed that these oscillations are the result of broadband femtosecond laser pulses impulsively exciting coherent vibrational motions in the Tc crystal.[29] Raman studies in the literature[20,23] have assigned modes below ~140 cm^{-1} to intermolecular lattice vibrations; these are the modes we focus on for their potential to modulate interchromophore coupling, though there are a number of higher frequency modes present as well.

Figure 2.8 (left) shows single-wavelength kinetics for Tc I, Large and Tc II, Small films over the first 5 ps of the singlet decay. The coherent oscillations are readily apparent by eye, and a fast Fourier transform (FFT) of the residual (Figure 2.8, right; obtained after subtracting the pictured multiexponential fit from the data) shows peaks whose frequencies correspond to those from literature[20,23] and previously observed in fsTA coherent oscillations[29]. Additionally, there are subtle differences evident in the relative intensities between the two film polymorphs. The FFT

has been scaled to the strong (and presumably equivalent in both polymorphs) 313 cm^{-1} intramolecular[29,31,32] peak.

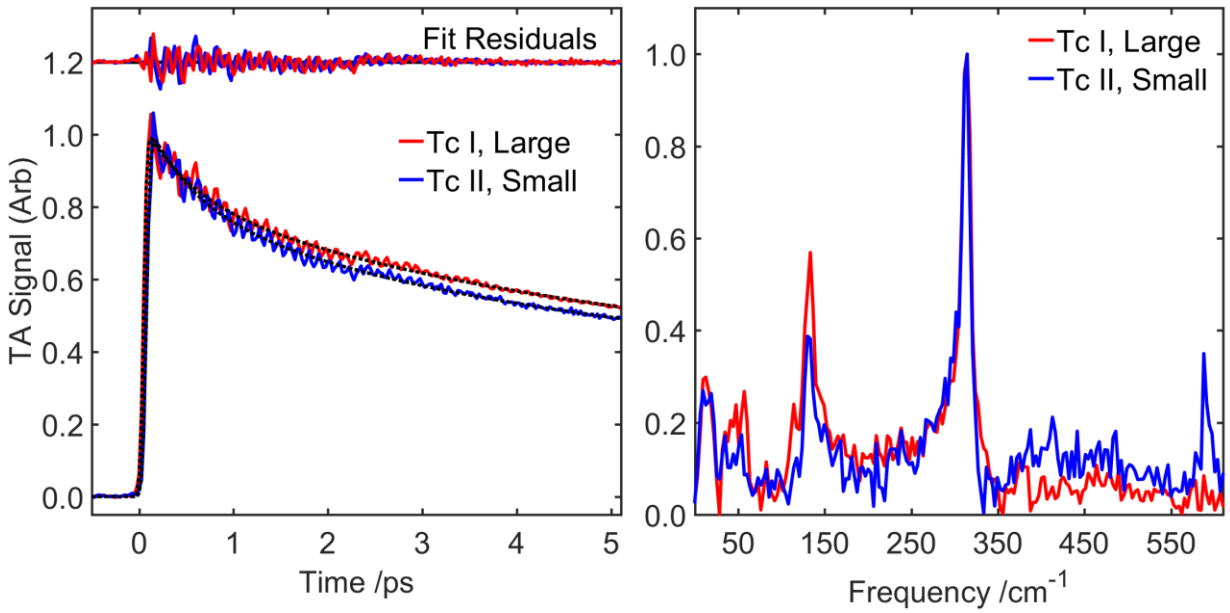

Figure 2.8. Measured early-time TA decays (left) for Tc I, Large and Tc II, Small films at 496 nm with fits and residuals (shown offset at top) and a fast Fourier transform of those residuals (right) showing known Tc Raman modes with different amplitudes and shapes.

There are differences evident in the FFT amplitudes, in particular the (most relevant) low frequency modes at ~50 cm^{-1} and 130 cm^{-1}, where the amplitudes differ significantly and (in the former case) the shape appears to be different. This is similar to behavior observed in literature[20,23] for the Raman modes of two polymorphs of Tc in which the amplitude of lattice vibrations was found to depend on Tc polymorph. These modes and their equivalent peaks from literature are summarized in Table 2.5.

Table 2.5. Observed intermolecular Raman modes in Tc I and Tc II compared with closest corresponding literature frequencies

Tc I, literature[a] × cm	Tc I, this work × cm	Tc II, literature[a] × cm	Tc II, this work × cm
129.8	133	130.4	131
58.5	42–58	57.4	53
47.8 & 42.3		38.3	34

[a]From Venuti et al.[20]

With coherent oscillations observable in both film types, it appears that fsTA can access the range of intermolecular vibrations that may be able to modulate diabatic couplings between Tc chromophores. In light of this observation (which was extended here to differentiate between Tc I and Tc II polymorphs), previous work in our group[29] sought to and succeeded in optically controlling these lattice modes to effect an enhancement of 20% in the fsTA signal of T at long times (this experiment is discussed below). While subtle, the differences between polymorphs observed here may give rise to differentially important frequencies for achieving this enhancement to SF or—perhaps more interesting—a situation where modulation of intermolecular modes (and thus diabatic coupling) is important in one polymorph but provides no benefit to the other. Efforts were therefore made to control these vibrations in Tc I and Tc II via femtosecond pulse shaping experiments.

2.5.3 Coherent Control Background

Manipulating the dynamics of chemical systems through tailoring excitation light fields is known as coherent control.[33,34] This can be done to effect specific physical or chemical events such as isomerization[35], energy flow,[36] or nuclear motions in a lattice,[29,37] and presents a powerful tool for interacting with the Hamiltonian of an arbitrarily complex system. Designing light fields capable of yielding the desired results, however, requires fulfilment of a number of challenging

requirements. First, one needs the ability to control the light field used to interact with the sample. Many control schemes accomplish this goal with a device known as a spatial light modulator (SLM)[33,38–40]. An SLM consists of one or more liquid crystal arrays ("masks") for which the index of refraction at individual points (pixels) may be manipulated electronically. When an ultrafast input pulse passes through an SLM in the frequency domain (as shown in the cartoon in Figure 2.9), it is possible to individually control the relative phase and amplitude of the frequencies within the pulse, often with a startling number of degrees of freedom (for instance, the SLM used in the experiments below uses ~200 active pixels, each with hundreds of degrees of individual phase control). This allows for extensive manipulation of the phase and/or amplitude of an input pulse. What remains is the second of the aforementioned tasks: designing this pulse to achieve the desired physical or chemical result. The Hamiltonian of a large molecule (or set of molecules, as in a crystal) may be quite complex, and it is thus challenging to identify the optimal pulse for a given task purely from theory. Thus shaping is often coupled with search algorithms designed to identify pulses from an otherwise massive search space; this is known as adaptive feedback control (AFC)[33,34,40,41]. To briefly summarize, AFC operates by interrogating a sample with a population of different pulses whose fitness (the extent to which they yield the desired control result) is monitored. Following evaluation of fitness, a new (improved) population is generated, and this process iteratively continues until an optimal excitation pulse is found.

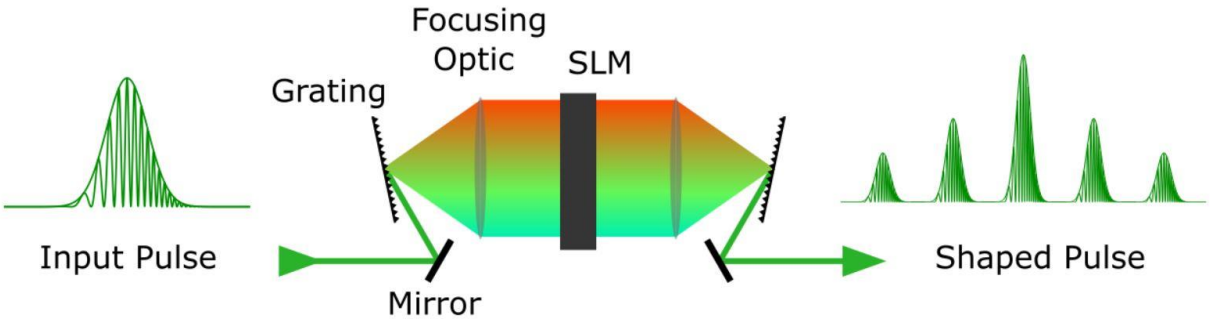

Figure 2.9. Cartoon illustrating the basic components of the 4f pulse shaper used in this work. The shaper consisting of a zero-dispersion 4f grating compressor with an SLM at its center. The focusing optic employed in practice is a curved mirror to minimize dispersion effects.

The search space for AFC may in principle consist of any arbitrary pulse shape accessible by the shaper (a "blind" optimization) or may be targeted at a specific subspace of pulse shapes (such as trains of pulses, which are the subject of the remainder of this chapter for reasons made clear below). Said subspace may additionally allow for amplitude shaping (wherein different frequencies may be removed from or attenuated in the pulse) or may be restricted to phase-only shaping (where only the relative delay of different frequencies within the pulse is changed).[33,34,40] The work in this chapter is based on previous collaborative control experiments in our group[29] that used a phase-only search space of sinusoidal phase functions. The frequency-dependent phase that is applied to the SLM, $\Phi(\omega_i)$, for these phase functions is given in Equation 4.

$$\Phi(\omega_i) = A \cos(\omega_i \tau + \phi) \tag{4}$$

The resulting shaped pulse is in fact a train of sub-pulses, each replicas of the input pulse. An example of this is shown in Figure 2.10 alongside an input (near-transform-limited, or TL), pulse in the SHG-FROG. In this pulse train, the parameter A determines the amplitude and number of sub-pulses (the envelope), τ determines the interpulse spacing (the separation in time between each sub-pulse), and ϕ determines their relative temporal phase. The frequency ω_i is discretized due to the pixelated nature the shaper (that is, the i^{th} pixel will provide a single phase to a region

of the otherwise continuous spectrum centered about frequency ω_i). This choice of a search sub-space was chosen previously[29] and has the benefit that pulse trains are intuitively related to molecular motions (timing pulses to vibrational periods may be thought of as akin to pushing a child on a swing[37]) and that other control efforts have implicated control of vibrations as successfully controlling product yields in a variety of systems.[35,36,42]

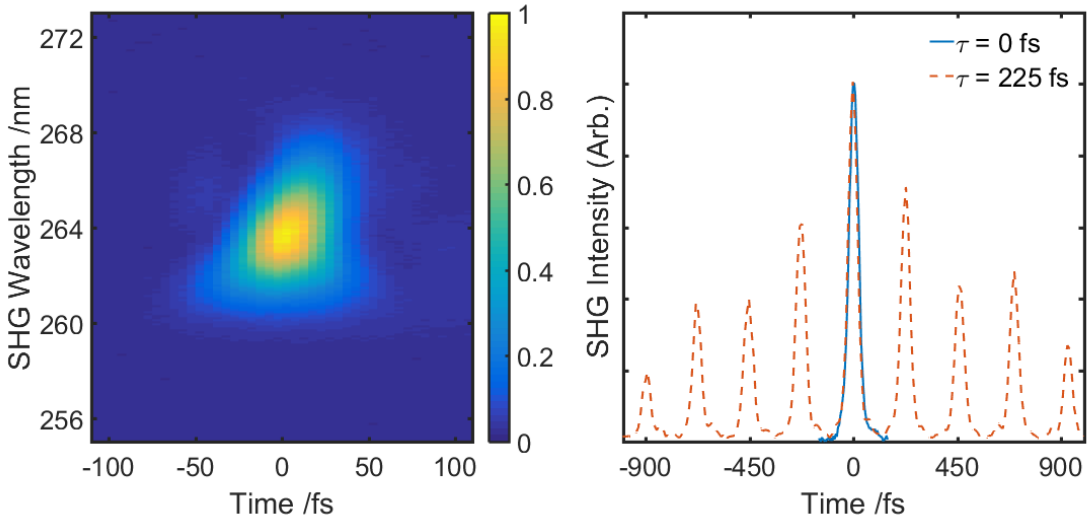

Figure 2.10. SHG-FROG of an unshaped pulse (left) and the resulting time autocorrelation (right, blue line) obtained by summing the SHG-FROG surface along the wavelength dimension. The time autocorrelation for a pulse train, generated using a sinusoidal phase function with τ = 225 fs, is shown as a red dashed line at right.

The coherent control work upon which the following experiments are based[29] examined SF in a Tc film that should approximate the Tc I, Small films discussed above. A 20% increase in the transient T signal (fixed at 1.5 ns after excitation) was found upon excitation with pulse trains whose frequencies matched or approximately matched those of the coherent oscillations discussed above. Specifically, pulse trains with period τ = 225 fs or 450 fs were found algorithmically to give enhancement, while applying a pulse train matched to a coherent oscillation period (270 fs

for the 123 cm^{-1} oscillation found in that work) gave results comparable to the algorithmically determined pulse trains. These results were achieved with fixed excitation fluence, and without substantial changes to co-monitored fluorescence. The findings were thus attributed to modulation of the interchromophore coupling between Tc subunits due to stimulation of lattice modes via coherent control. Given the differences found here between Tc I and Tc II (both in terms of intermolecular vibrations observed in coherent oscillations and the apparent breakdown of dimer-driven assumptions about diabatic coupling), extension of those findings to the case of polymorphism and grain size in Tc should provide new mechanistic insight into SF in Tc. For example, a difference in susceptibility of Tc I and Tc II to control would be equally if not more informative than a difference in optimal interpulse spacing (the latter was hinted at by the differences in observed coherent oscillations). If control is unable to effect an increase in SF for Tc II but is able to do so in Tc I (as observed previously), it could suggest that intermolecular vibrations that modulate coupling (and thus the diabatic couplings themselves) are less important for that polymorph.

2.5.4 Experimental Methods

The control experiment uses the fsTA instrument described in Section 2.5.1 with the SLM (dual-mask CRi SLM-640 with 640 pixels) active and calibrated using a homebuilt calibration procedure. The SLM is interposed in the Fourier plane between the two halves of a 4f grating compressor as shown in the cartoon in Figure 2.9 (with an important difference being that curved mirrors are used in place of lenses to minimize dispersion). The pump pulse had a bandwidth of 530 ± 15 nm and covered ~150 pixels for a spectral resolution near 0.3 nm/pixel. The phase sent to the shaper was constrained to vary between 0 and 2π followed the phase function in Equation 4. The TA signal was monitored in an identical manner to Section 2.5.1, with the pump-probe delay

fixed at 400 ps and the probe wavelength at 496 nm. The power was monitored simultaneously by directing a pump beam reflection (from a glass cover slip) onto an amplified photodiode coupled to a second Stanford Research SR810 lock-in amplifier synced to the 500 Hz chopper frequency.

2.5.5 Results of Manual and Algorithmic Searches

Initial investigation of Tc films covered a single-parameter search in the interpulse spacing τ, with the remaining two parameters (A and ϕ) fixed at values determined previously to give optimal pulses (the value of A was set to 2.5, while ϕ was set to zero as it was previously found to be uncorrelated with observations)[29]. The results from a set of these single-parameter control optimizations are shown in Figure 2.11. In these experiments, the interpulse spacing τ was varied between 0 (giving a TL pulse) and 700 fs. This τ range should encompass oscillations with frequencies as low as 47 cm^{-1}, though other measurements out to 800 fs were also attempted with similar results. The pump power was separately varied to include measurements at 40, 60, 80, 100, and 120 nJ/pulse to check for power-dependence in the measurement. TA signal (after normalization to the pump power) is shown in red (darker colors are higher powers) and the concurrent power measurements shown in blue (darker colors are again higher powers).

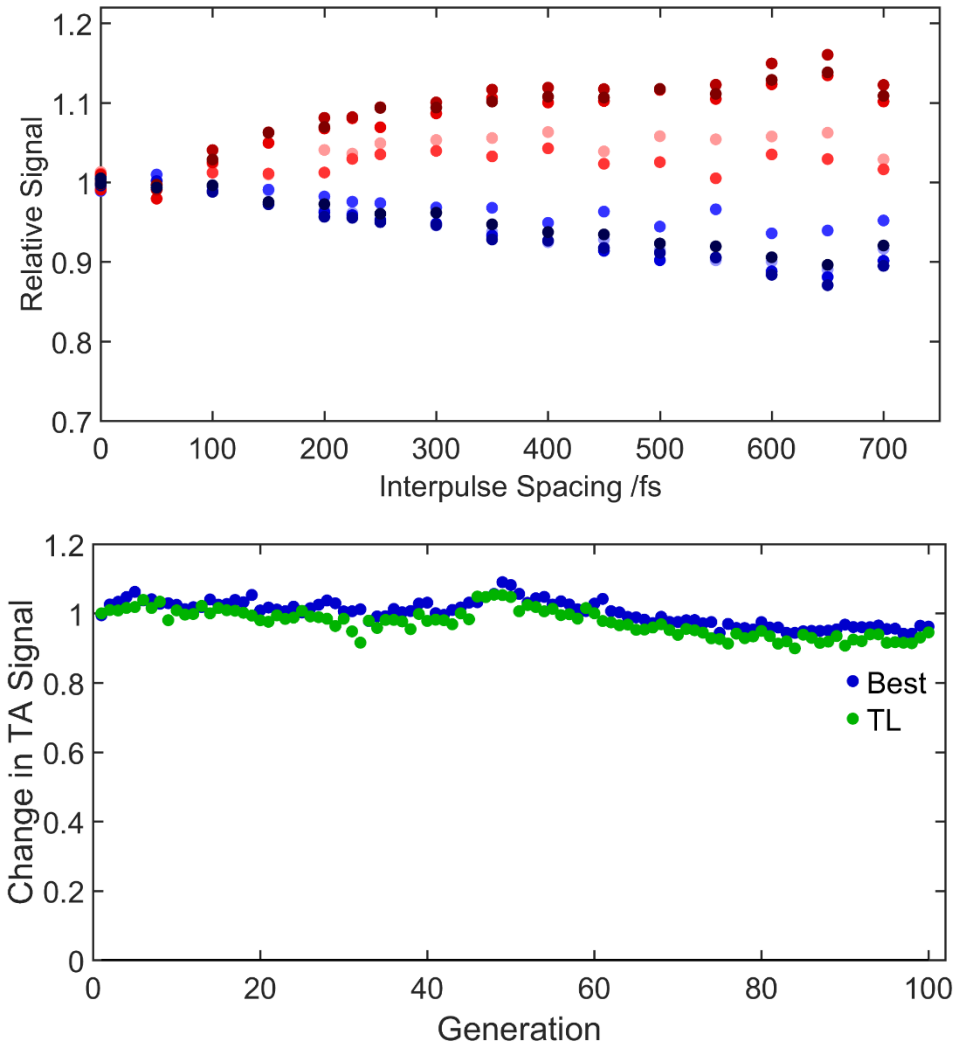

Figure 2.11. Attempted sinusoidal control of SF in polycrystalline Tc films. Top: single-parameter optimization of 496 nm TA signal at A = 2.5, ϕ = 0, and τ varied between 0 and 700 fs. Pump energies are between 40 and 120 nJ/pulse (darker colors are higher fluences). TA signal is shown in red and concurrently measured power is shown in blue. Bottom: control optimization in a search space of sinusoids showing no convergence on an optimal pulse after 100 generations.

A shaping-dependent change in the pump power is immediately apparent, and gives rise to a systematic reduction in pump power of 10-15% as interpulse spacing is increased. The structure observed in the TA signal (specifically, the slow overall growth and apparent peaks near 400 fs and 650 fs in some measurements) over that same range appears to be largely derived from the

power measurements, though its exact origin remains unclear (see below). Meanwhile, separate experiments that included a broadened parameter search space (where A, τ, and ϕ were allowed to vary) proved unsuccessful at identifying an optimal pulse after many generations (one such optimization is shown in Figure 2.11), even when normalizing the fitness parameter to the pump power during the experiment. Attempts within different control search spaces (including blind optimizations using pixels in blocks whose phase is randomly determined as a parameter) on different films gave similarly unsuccessful results.

These experiments did not find evidence of control in any power regime, and instead raised questions about the role of amplitude shaping in our pulse shaper when attempting ostensibly phase-only control. This led us to discover a problematic change in the shape of the pump beam with changing SLM phase. This is depicted in a series of photographs in Figure 2.12 (a). As a higher frequency phase function is sent to the shaper (that is, as τ is increased) the beam becomes wider along the horizontal dimension. Similarly problematic (and possibly related) behavior may be seen in Figure 2.12 (b), which shows a photo of a laser beam immediately after exiting the shaper, where the periodic phase function has generated a "grating" within the spectrum. These lines were observed independent of light source (CW light and an incandescent lamp were also tested) or phase function (square waves gave the same result), and appeared with and without polarizers in place on the SLM.

The resulting shaped excitation light does in fact have the desired phase, confirmed through SHG-FROG autocorrelation measurements such as the one shown in Figure 2.10 (c), but the aforementioned pump-beam distortions result in an indeterminate spot size that (in addition to the aforementioned power effects) causes fluence to vary in a manner that is uncorrectable by simple normalization using pump power measurements.

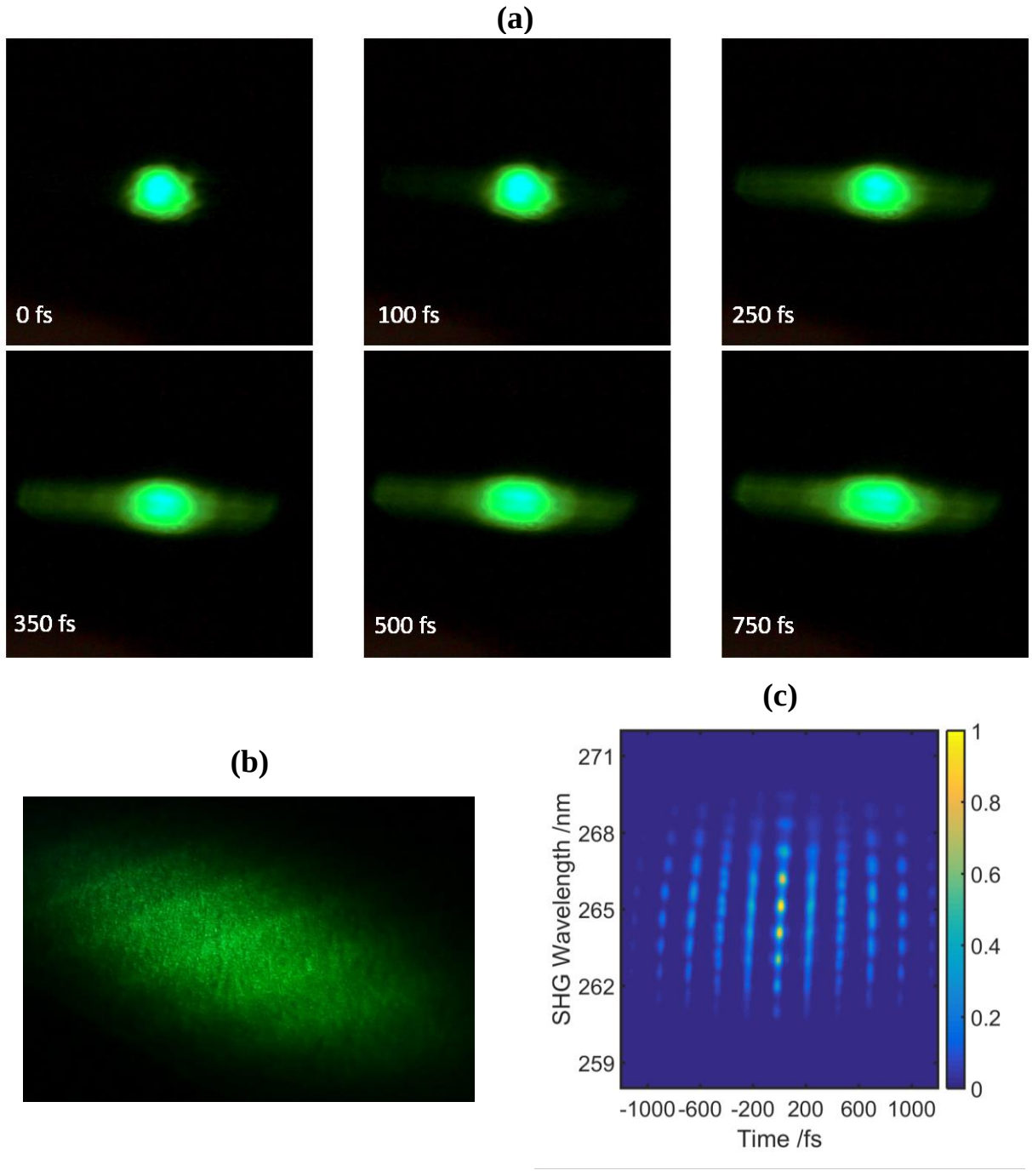

Figure 2.12. Behavior of pump light upon phase-only shaping. (a) Pump beam after going through shaper and immediately before focusing into the sample, with τ value indicated in white. (b) Dispersed light immediately after exiting the SLM, showing the origin of the beam distortions (shown for $\tau = 250$ fs; similar behavior is evident for other τ values). (c) SHG-FROG of a shaped pulse ($\tau = 225$ fs), showing generation of a pulse train despite the effects described in (a) and (b).

After lengthy discussions with the manufacturer, this problem could not be resolved and, since TA signal is spot size dependent, these control experiments were halted. The questions brought up at the outset about differential controllability of Tc I and Tc II thus remain unanswered and interesting. However, measurements that are strictly power dependent (that is, measurements that do not depend on spot size) may still prove fruitful using this instrument in the limit that the observable for control may be corrected by power measurement alone. This subject is therefore revisited in Chapter 5 with attempts to control emission quantum yield in a solution-phase dimer.

2.6 Conclusion

Though coherent control ultimately proved unsuccessful here, an experiment that is able to mitigate or avoid the discussed beam distortion problems (through, for example, use of an alternative shaper) should in principle be able to address the question of controllability in the array of film types discussed in this chapter. This work nonetheless demonstrated that morphology plays a substantial role in deciding the rate of SF in Tc, an otherwise very thoroughly studied system. The finding that Tc II undergoes faster SF than Tc I, with crystallite size having essentially no effect in Tc II (but a substantial effect in Tc I), highlights the complexity inherent in describing bulk systems. This is further shown in the apparent disconnect between SF rates predicted through dimer-pair couplings and those observed in experiment. The subsequent chapters of this thesis consider systems in which this complexity is reduced through the removal of bulk effects through the study of covalent dimers. These provide an alternate perspective on the electronic processes relevant to SF.

2.7 Bibliography

1. Burdett, J. J., Müller, A. M., Gosztola, D. & Bardeen, C. J. Excited state dynamics in solid and monomeric tetracene: The roles of superradiance and exciton fission. *J. Chem. Phys.* **133,** 144506 (2010).
2. Berkelbach, T. C., Hybertsen, M. S. & Reichman, D. R. Microscopic theory of singlet exciton fission. III. Crystalline pentacene. *J. Chem. Phys.* **141,** 0–12 (2014).
3. Teichen, P. E. & Eaves, J. D. Collective aspects of singlet fission in molecular crystals. *J. Chem. Phys.* **143,** 44118 (2015).
4. Piland, G. B. & Bardeen, C. J. How Morphology Affects Singlet Fission in Crystalline Tetracene. *J. Phys. Chem. Lett.* **6,** 1841–1846 (2015).
5. Ryerson, J. L., Schrauben, J. N., Ferguson, A. J., Sahoo, S. C., Naumov, P., Havlas, Z., Michl, J., Nozik, A. J. & Johnson, J. C. Two Thin Film Polymorphs of the Singlet Fission Compound 1,3-Diphenylisobenzofuran. *J. Phys. Chem. C* **118,** 12121–12132 (2014).
6. Wan, Y., Guo, Z., Zhu, T., Yan, S., Johnson, J. & Huang, L. Cooperative singlet and triplet exciton transport in tetracene crystals visualized by ultrafast microscopy. *Nat. Chem.* **7,** 785–792 (2015).
7. Hartnett, P. E., Margulies, E. A., Mauck, C. M., Miller, S. A., Wu, Y., Wu, Y.-L., Marks, T. J. & Wasielewski, M. R. Effects of Crystal Morphology on Singlet Exciton Fission in Diketopyrrolopyrrole Thin Films. *J. Phys. Chem. B* **120,** 1357–1366 (2016).
8. Kolata, K., Breuer, T., Witte, G. & Chatterjee, S. Molecular Packing Determines Singlet Exciton Fission in Organic Semiconductors. *ACS Nano* **8,** 7377–7383 (2014).
9. Smith, M. B. & Michl, J. Singlet Fission. *Chem. Rev.* **110,** 6891–6936 (2010).
10. Greyson, E. C., Stepp, B. R., Chen, X., Schwerin, A. F., Paci, I., Smith, M. B., Akdag, A.,

Johnson, J. C., Nozik, A. J., Michl, J. & Ratner, M. a. Singlet Exciton Fission for Solar Cell Applications: Energy Aspects of Interchromophore Coupling. *J. Phys. Chem. B* **114,** 14223–32 (2010).

11. Smith, M. B. & Michl, J. Recent Advances in Singlet Fission. *Annu. Rev. Phys. Chem.* **64,** 361–386 (2013).

12. Johnson, J. C., Nozik, A. J. & Michl, J. The Role of Chromophore Coupling in Singlet Fission. *Acc. Chem. Res.* **46,** 1290–1299 (2013).

13. Alguire, E. C., Subotnik, J. E. & Damrauer, N. H. Exploring Non-Condon Effects in a Covalent Tetracene Dimer: How Important Are Vibrations in Determining the Electronic Coupling for Singlet Fission? *J. Phys. Chem. A* **119,** 299–311 (2015).

14. Eaton, S. W., Miller, S. a., Margulies, E. a., Shoer, L. E., Schaller, R. D. & Wasielewski, M. R. Singlet Exciton Fission in Thin Films of tert -Butyl-Substituted Terrylenes. *J. Phys. Chem. A* **119,** 4151–4161 (2015).

15. Dillon, R. J., Piland, G. B. & Bardeen, C. J. Different Rates of Singlet Fission in Monoclinic versus Orthorhombic Crystal Forms of Diphenylhexatriene. *J. Am. Chem. Soc.* **135,** 17278–17281 (2013).

16. Voigt, M., Langner, a, Schouwink, P., Lupton, J. M., Mahrt, R. F. & Sokolowski, M. Picosecond time resolved photoluminescence spectroscopy of a tetracene film on highly oriented pyrolytic graphite: dynamical relaxation, trap emission, and superradiance. *J. Chem. Phys.* **127,** 114705 (2007).

17. Burdett, J. J. & Bardeen, C. J. The Dynamics of Singlet Fission in Crystalline Tetracene and Covalent Analogs. *Acc. Chem. Res.* **46,** 1312–1320 (2013).

18. Wilson, M. W. B., Rao, A., Johnson, K., Gélinas, S., di Pietro, R., Clark, J. & Friend, R. H.

Temperature-Independent Singlet Exciton Fission in Tetracene. *J. Am. Chem. Soc.* **135,** 16680–16688 (2013).

19. Holmes, D., Kumaraswamy, S., Matzger, A. J. & Vollhardt, K. P. C. On the Nature of Nonplanarity in the [N]Phenylenes. *Chem. Eur. J.* **5,** 3399–3412 (1999).

20. Venuti, E., Della Valle, R. G., Farina, L., Brillante, A., Masino, M. & Girlando, A. Phonons and structures of tetracene polymorphs at low temperature and high pressure. *Phys. Rev. B* **70,** 104106 (2004).

21. Milita, S., Santato, C. & Cicoira, F. Structural investigation of thin tetracene films on flexible substrate by synchrotron X-ray diffraction. *Appl. Surf. Sci.* **252,** 8022–8027 (2006).

22. Milita, S., Servidori, M., Cicoira, F., Santato, C. & Pifferi, A. Synchrotron X-ray investigation of tetracene thin films grown at different deposition fluxes. *Nucl. Instruments Methods Phys. Res. Sect. B Beam Interact. with Mater. Atoms* **246,** 101–105 (2006).

23. Brillante, A., Bilotti, I., Della Valle, R. G., Venuti, E. & Girlando, A. Probing polymorphs of organic semiconductors by lattice phonon Raman microscopy. *CrystEngComm* **10,** 937 (2008).

24. Schatschneider, B., Monaco, S., Tkatchenko, A. & Liang, J.-J. Understanding the Structure and Electronic Properties of Molecular Crystals Under Pressure: Application of Dispersion Corrected DFT to Oligoacenes. *J. Phys. Chem. A* **117,** 8323–8331 (2013).

25. Sebastian, L., Weiser, G. & Bässler, H. Charge transfer transitions in solid tetracene and pentacene studied by electroabsorption. *Chem. Phys.* **61,** 125–135 (1981).

26. Burdett, J. J., Gosztola, D. & Bardeen, C. J. The dependence of singlet exciton relaxation on excitation density and temperature in polycrystalline tetracene thin films: kinetic evidence for a dark intermediate state and implications for singlet fission. *J. Chem. Phys.*

135, 214508 (2011).

27. Arias, D. H., Ryerson, J. L., Cook, J. D., Damrauer, N. H. & Johnson, J. C. Polymorphism influences singlet fission rates in tetracene thin films. *Chem. Sci.* **7,** 1185–1191 (2016).
28. Ryerson, J. L. Structural and photophysical considerations of singlet fission organic thin films for solar photochemistry. (University of Colorado, Boulder, 2016).
29. Grumstrup, E., Johnson, J. & Damrauer, N. Enhanced Triplet Formation in Polycrystalline Tetracene Films by Femtosecond Optical-Pulse Shaping. *Phys. Rev. Lett.* **105,** 257403 1-4 (2010).
30. Trebino, R. *Frequency-Resolved Optical Gating: The Measurement of Ultrashort Laser Pulses*. (Springer US, 2000).
31. Lehnig, R. & Slenczka, A. Spectroscopic investigation of the solvation of organic molecules in superfluid helium droplets. *J. Chem. Phys.* **122,** 244317 (2005).
32. Weinberg-Wolf, J. R., McNeil, L. E., Liu, S. & Kloc, C. Evidence of low intermolecular coupling in rubrene single crystals by Raman scattering. *J. Phys. Condens. Matter* **19,** 276204 (2007).
33. Weiner, A. M. Ultrafast optical pulse shaping: A tutorial review. *Opt. Commun.* **284,** 3669–3692 (2011).
34. Brif, C., Chakrabarti, R. & Rabitz, H. Control of Quantum Phenomena: Past, Present and Future. *New J. Phys.* **12,** 75008 (2010).
35. Prokhorenko, V. I., Nagy, A. M., Waschuk, S. a, Brown, L. S., Birge, R. R. & Miller, R. J. D. Coherent control of retinal isomerization in bacteriorhodopsin. *Science* **313,** 1257–61 (2006).
36. Herek, J. L., Wohlleben, W., Cogdell, R. J., Zeidler, D. & Motzkus, M. Quantum control of

energy flow in light harvesting. *Nature* **417,** 533–5 (2002).

37. Weiner, A. M., Leaird, D. E., Wiederrecht, G. P. & Nelson, K. A. Femtosecond Pulse Sequences Used for Optical Manipulation of Molecular Motion. *Science (80-.).* **247,** 1317–1319 (1990).

38. Weiner, A. M. Femtosecond optical pulse shaping and processing. *Prog. Quantum …* **19,** 161–237 (1995).

39. Weiner, A. M. Femtosecond pulse shaping using spatial light modulators. *Rev. Sci. Instrum.* **71,** 1929 (2000).

40. Monmayrant, A., Weber, S. & Chatel, B. A newcomer's guide to ultrashort pulse shaping and characterization. *J. Phys. B At. Mol. Opt. Phys.* **43,** 103001 (2010).

41. Judson, R. S. & Rabitz, H. Teaching lasers to control molecules. *Phys. Rev. Lett.* **68,** 1500–1503 (1992).

42. Brüggemann, B., Organero, J. A., Pascher, T., Pullerits, T. & Yartsev, A. Control of Electron Transfer Pathways in a Dye-Sensitized Solar Cell. *Phys. Rev. Lett.* **97,** 208301 (2006).

Chapter 3. A Dimer Framework: Solution-Phase Singlet Fission in the Conformationally-Restricted Molecule BT1

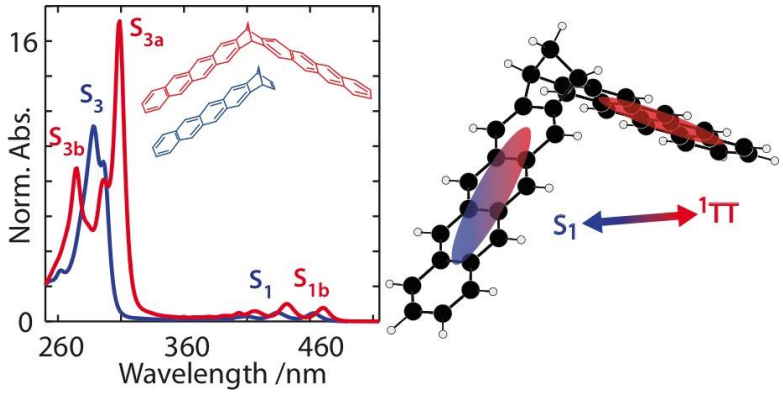

3.1 Arguments for a Dimer Framework

Though many condensed-phase materials undergo efficient singlet fission (SF),[1–10] these systems tend to be highly complex. With many chromophores in close proximity, factors like exciton diffusion rates, grain boundaries, and even excitation fluence can have marked effects on SF rates and yields.[8,10–21] It is correspondingly difficult to tease out detailed causal relationships between subtle modifications to parent chromophores and SF observables. One or multiple SF-relevant parameters in the solid may be sensitive to chromophore modifications (e.g. atom substitution or functionalization) in ways that are coupled and/or opaque. Focused efforts to identify the relative importance of factors like symmetry, energetics, and through-space vs. through-bond coupling benefit from avoiding this complexity, and molecular dimers are a promising avenue to accomplish this. In dimer studies, SF-relevant interactions are reduced to their simplest subunit: two coupled chromophores. The benefits of this simplicity are manifold: improved computational accessibility (consideration of two chromophores instead of many); straightforward interpretation of chemical modifications (such as atom substitution or changes to connectivity) without the need to consider crystal packing; and applicability to simple devices like

dye-sensitized solar cells.[22–24] In short, molecular dimers are an excellent chemical foundation for detailed exploration of SF.

All present photophysical studies of dimers consider systems with structural flexibility. This manifests due to covalent linkages occurring through single points of attachment[25–37] or from chromophore subunits being altogether unbound (with coupling coming from transient associations in concentrated solution).[38,39] This presents difficulty when attempting to experimentally probe the role of interchromophore coupling, which is known to depend heavily on the geometry of the chromophores and bridge.[3,40–42] Understanding intermolecular vibrations is likewise complicated when the geometry is indeterminate. The importance of vibrations is exemplified by the coherent control experiments discussed in the previous chapter[43] where shaped laser pulses targeted at stimulating lattice vibrations in tetracene (Tc) were able to enhance SF. This enhancement was explained as modulating interchromophore coupling, and highlights the usefulness of preserving orientation (mimicking a crystal) in an effective dimer platform.

In addition to conformational concerns, most studies of SF in dimers have utilized pentacene-derived molecules,[29–31,33,34] with a few exceptions where Tc[25,28,32] or other molecules[26,27] are considered. Pentacene, however, is known to have an substantially exoergic driving force for SF (ΔE_{SF}, defined as $2 \times E(T_1) - E(S_1)$).[44] Presumably, this lends itself to the efficiency of these systems. To gain detailed mechanistic insight into the role of chromophore coupling, however, it is helpful to operate in a regime where this driving force is nearly isoergic so that behavior is not dominated by thermodynamic considerations. This allows for the effects of orientation and symmetry to be considered with greater detail. An ideal parent chromophore, then, should be rigidly linked to facilitate conformational understanding, and have energetics nearing isoergicity which can be readily modified to be endoergic or exoergic.

The dimer platform studied in this chapter (BT1, Figure 3.1) is a bis(tetracene) with a bridging norbornane. The BT1 molecule derives its linker structure from the most strongly coupled (single-norbornyl bridged) among a series of naphthalene dimers studied by Paddon-Row and coworkers.[45] In that system (also shown in Figure 3.1), Davydov splitting in the ultraviolet (UV) $S_3 \leftarrow S_0$ region of the spectrum was monitored as one measure of interchromophore coupling, controllable through modification of the bridge length (BN1-BN3).

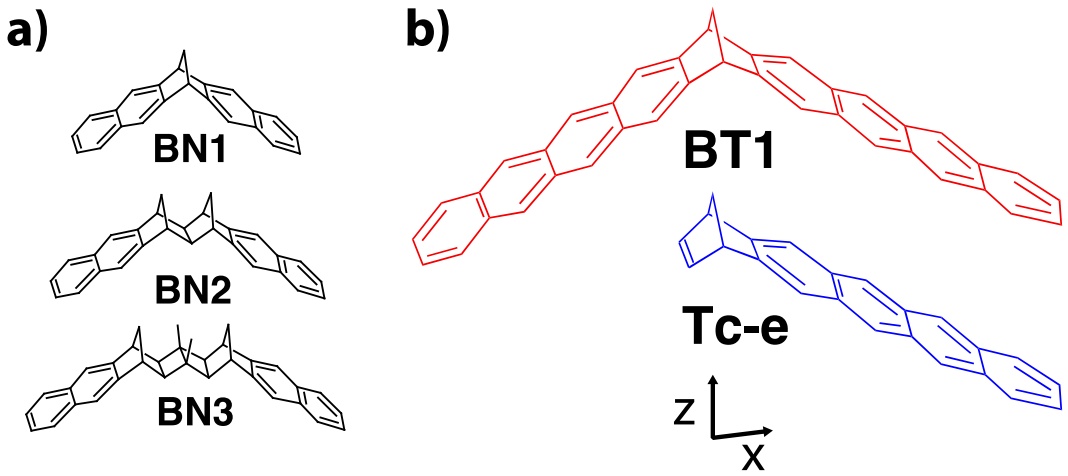

Figure 3.1. (a) The BNX (X = 1, 2, 3) series of molecules studied by Paddon-Row and coworkers.[45] (b) The bis-tetracene dimer BT1 (red) and its monomer analogue Tc-e (blue). The coordinate system depicted in (b) is used throughout this chapter, with the molecules oriented such that the long axis of the chromophore arms lies along the x-axis, while the short axis of the chromophores lies along the y-axis (not shown). The z-axis points through the molecules.

As a chemical platform, BT1 possess many of the desirable traits outlined above. The connectivity of the norbornane precludes rotation or significant twisting of the Tc chromophores, allowing calculations to access the role of symmetry and vibrations in interchromophore coupling.[41,46] Given the point-group symmetry of BT1's ground state (C_{2v}, with a symmetry plane passing through both chromophores) and the resulting symmetries of the frontier orbitals, it is expected that the diabatic electronic coupling leading from the S_1 excited state to the multiexcitonic

^{1}TT state should be zero.[41] This is true with or without a CT intermediary, such that one should expect slow SF that is allowed only through symmetry-breaking vibrations (the rate of which may be calculated using coupling gradients[41]). This in turn facilitates exploration of SF enhancement through pumping specific vibrational modes with shaped femtosecond laser pulses as was done for polycrystalline Tc.[43] Additionally, with the chromophore subunits orientationally constrained and partially co-facial, modifications to symmetry and/or energetics through atom substitution[42] or through alternate linking arrangements[46] are readily understood, with predicted substantial increases to the rate of SF. Taken together, these make BT1 an excellent platform upon which to build.

3.2 BT1 Synthetic Overview

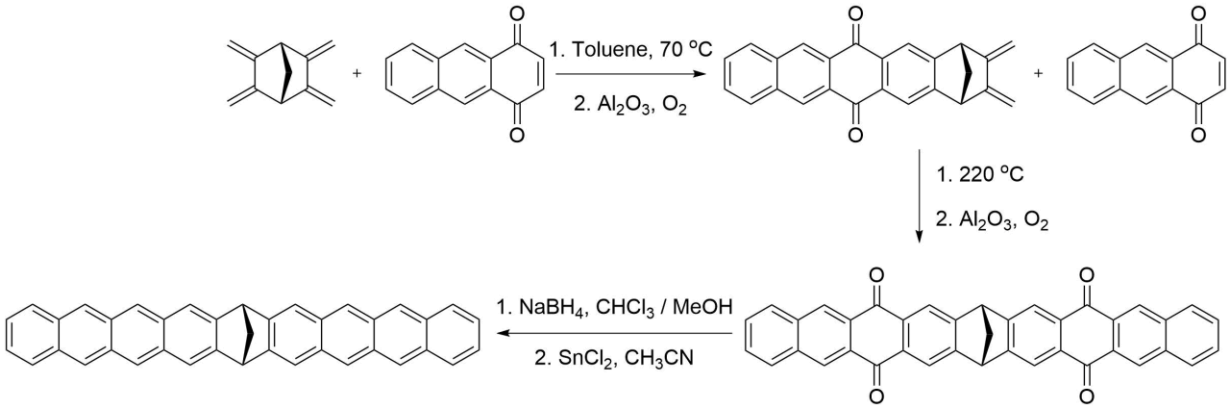

Figure 3.2. A summary of the synthetic method used to create the molecule BT1, consisting of: (a) a Diels-Alder cycloaddition to create one Tc arm; (b) a second Diels-Alder cycloaddtion to add the second Tc arm followed by an oxidation to yield the bisquinone; (c) a reduction of the quinone to obtain a tetraol and subsequent reduction of the tetraol and elimination to obtain BT1.

Synthesis of the dimer BT1 was carried out by fellow group member Thomas Carey as described elsewhere[47] and is summarized in Figure 3.2. Briefly: a Diels-Alder cycloaddition is employed to form one Tc arm from a quinone and a norbornyl tetraene; a second Diels-Alder cycloaddtion adds the second arm followed by oxidation to yield a bisquinone; the bisquinone is reduced with a hydride source to obtain a tetraol; and a final reduction and elimination yield BT1.

Tc-e was synthesized through a separate process by group member Jamie Snyder as described elsewhere.[48]

3.3 Steady-State Behavior

3.3.1 Methods

Electronic absorption measurements were performed using an Agilent Cary 5000 UV-Vis-NIR absorbance spectrophotometer operating in dual-beam mode. Steady-state photoluminescence measurements were performed on an Olis SLM 8000 spectrofluorimeter. High-purity spectrophotometric-grade solvents were purchased from Burdick & Jackson (toluene) or Sigma-Aldrich (chloroform) and used as received. All samples were prepared in dilute (~5 μM) solution using 1-cm quartz cuvettes. Cuvettes were capped using screw-top lids with polytetrafluoroethylene gaskets, and bubble-degassed with argon for 30 minutes prior to sealing under positive argon pressure. Experiments were carried out promptly after sample preparation, and sample integrity was verified before and after data acquisition via steady-state absorption spectroscopy.

3.3.2 Electronic Absorption in Chloroform

Steady-state measurements were carried out on Tc-e and BT1 in chloroform to preserve information in the ultraviolet (UV) region of the spectrum. The primary features found in Tc-e (spectrum in Figure 3.3) resemble those in solution-phase Tc,[11] exhibiting two prominent sets of absorption features: one in the visible (onset near 470 nm) and a second in the UV (onset near 300 nm). There is also a third, very weak set of features (onset near 402 nm, indicated by an arrow in the inset region of Figure 3.3) that is barely visible atop the latter vibronic peaks of the larger visible progression.

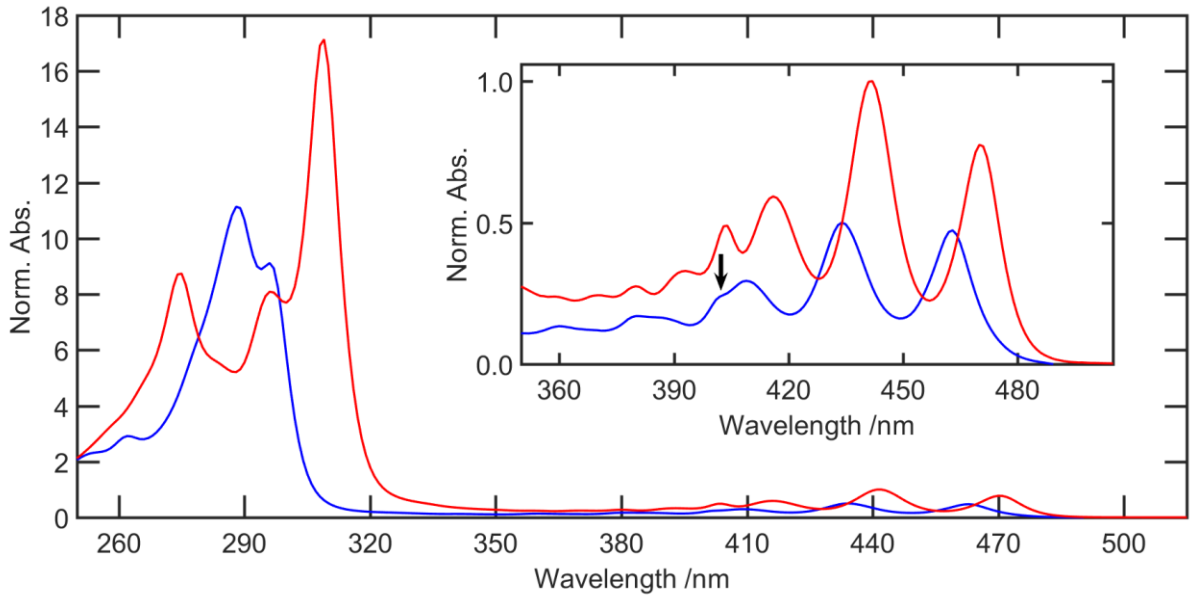

Figure 3.3. Electronic absorption spectra of Tc-e (blue) and BT1 (red) in $CHCl_3$. Tc-e has been scaled to have half the absorptivity of BT1 in the $S_1 \leftarrow S_0$ (inset) region to aid in interpreting the Davydov split (UV) region. The arrow highlights the onset of the $S_2 \leftarrow S_0$ absorption atop the latter vibronic peaks in the $S_1 \leftarrow S_0$ region in Tc-e.

The $S_1 \leftarrow S_0$ progression with onset near 470 nm is expected to arise from a highest occupied molecular orbital (HOMO) → lowest unoccupied molecular orbital (LUMO) transition dipole and would be known as the ^1L_a band in the notation of Platt.[49] The second and third absorption bands ($S_2 \leftarrow S_0$ and $S_3 \leftarrow S_0$) originate from out-of-phase and in-phase combinations (respectively) of the near-degenerate HOMO–1 → LUMO and HOMO → LUMO+1 transitions. These constitute the ^1L_b and B bands, respectively. This pattern is similar to what is found in porphyrin systems, where near-degeneracy of bands results in one strongly allowed band in the UV (Soret band) and second band of nearly forbidden transitions the visible (Q band).[50] The nature of these transitions in Tc-e, including their relative strengths and polarizations, is well-described by transition dipoles calculated in the space of four frontier orbitals (the HOMO–1, HOMO, LUMO, and LUMO+1 orbitals, depicted in Figure 3.4).

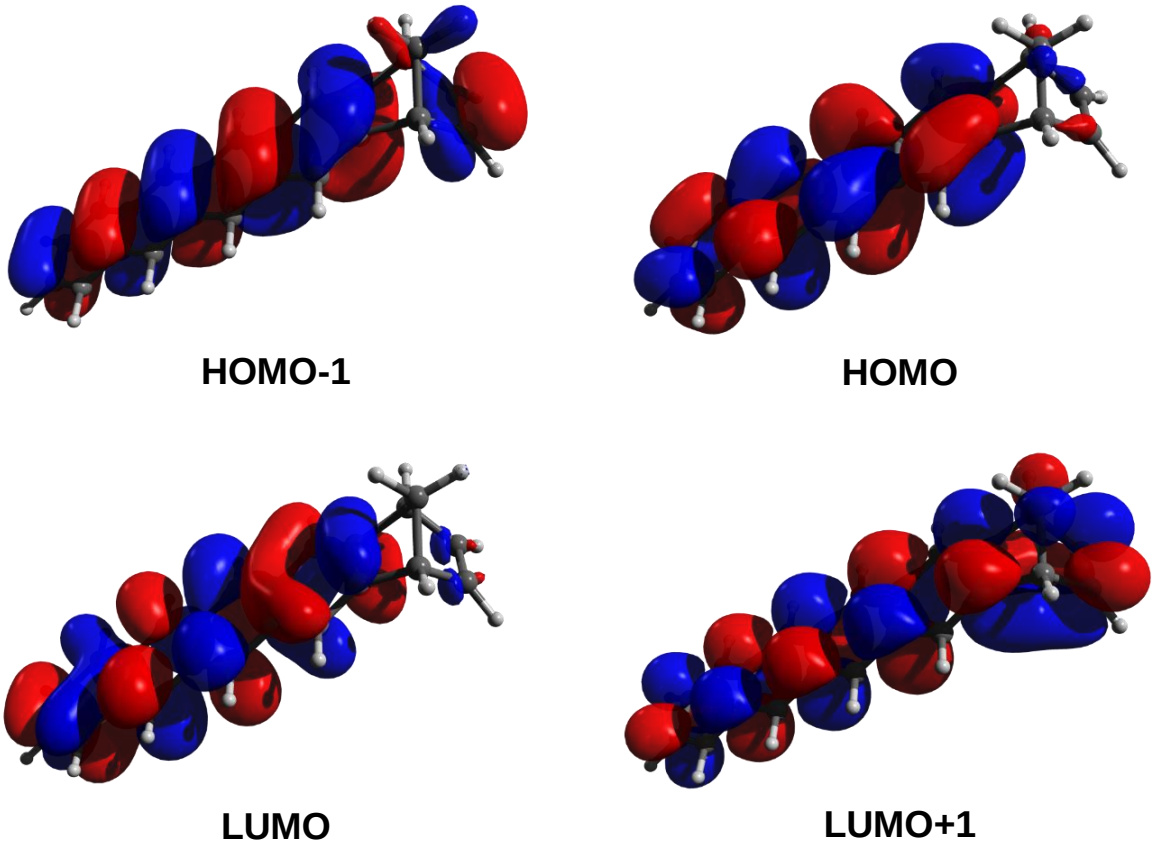

Figure 3.4. Frontier orbitals of Tc-e used in determining the transition dipole moments for the first three observed singlet transitions. These orbitals were obtained from previous work in our group[46] following geometry optimization of Tc-e with DFT using the range-corrected ω-B97XD density functional and the 6-31g(d) basis set.

The frontier orbitals considered (HOMO–1 to LUMO+1) here were previously obtained from geometry optimization of Tc-e (without symmetry constraints) via density functional theory (DFT) using the range-corrected ω-B97XD density functional and the 6-31g(d) basis set in the Gaussian 09 software package.[46,51] To describe the observed electronic transitions with regards to their intensity and orientation, transition dipole contributions were numerically calculated for their corresponding spatial directions ($D_{ij,x}$, $D_{ij,y}$, and $D_{ij,z}$ for $\hat{x}$, $\hat{y}$, and $\hat{z}$, respectively) to obtain the overall transition moment ($\overrightarrow{D}_{ij}$) between orbitals ($\boldsymbol{\Psi_i} \rightarrow \boldsymbol{\Psi_j}$) as detailed in Equations 1-4 (where the ○ operation denotes element by element multiplication).

$$D_{ij,x} = \Sigma_{x,y,z} (\mathbf{\Psi_i} \circ \mathbf{x} \circ \mathbf{\Psi_j}) \quad (1)$$

$$D_{ij,y} = \Sigma_{x,y,z} (\mathbf{\Psi_i} \circ \mathbf{y} \circ \mathbf{\Psi_j}) \quad (2)$$

$$D_{ij,z} = \Sigma_{x,y,z} (\mathbf{\Psi_i} \circ \mathbf{z} \circ \mathbf{\Psi_j}) \quad (3)$$

$$\vec{D}_{ij} = D_{ij,x}\,\hat{x} + D_{ij,y}\,\hat{y} + D_{ij,z}\,\hat{z} \quad (4)$$

The spatial matrices **x**, **y**, and **z** were generated by replicating the corresponding spatial vector ($\vec{x}$, $\vec{y}$, or $\vec{z}$) along the remaining two dimensions (e.g. $\vec{x}$ was replicated in the $\hat{y}$ and $\hat{z}$ directions to give **x** with dimensionality identical to $\mathbf{\Psi_i}$ and $\mathbf{\Psi_j}$). Output cube files were subsequently multiplied on an element-by-element basis with the corresponding space matrix element, scaled by the appropriate voxel volume (determined from the step sizes of $\vec{x}$, $\vec{y}$, and $\vec{z}$) and the results were summed. The transition dipoles $\vec{D}_{ij}$ computed in this way are summarized in Table 3.1 in units of elementary charge-angstroms, along with the relevant molecular axis along which the transition lies. The orientations found for these transitions are consistent with the symmetry of the orbitals from which they arise (A', A", A', and A" for the HOMO–1, HOMO, LUMO, and LUMO+1, respectively, in the C_s point group of Tc-e).

Table 3.1. Transition dipole moments calculated for the observed singlet transitions in Tc-e

Electronic Transition	Transition Name (Platt)	Orbital Origins	Transition Dipole /eÅ	Polarization Axis (Acene)
$S_1 \leftarrow S_0$	^1L_a	HOMO → LUMO	1.6	Short
None	None	HOMO–1 → LUMO	3.03	Long
None	None	HOMO → LUMO+1	2.95	Long
$S_2 \leftarrow S_0$	^1L_b	(HOMO–1 → LUMO) – (HOMO → LUMO+1)	0.08	Long
$S_3 \leftarrow S_0$	B	(HOMO–1 → LUMO) + (HOMO → LUMO+1)	5.98	Long

The relative strengths calculated for these transitions is in good agreement with the spectrum in Figure 3.3. The $S_1 \leftarrow S_0$ (HOMO → LUMO) band is allowed, but more weakly than the $S_3 \leftarrow S_0$ (HOMO–1 → LUMO + HOMO → LUMO+1) band. Using the relationship between oscillator strength f, frequency ν, and transition dipole moment ($f \sim \nu|\vec{D}_{ij}|^2$) yields a predicted ratio of ~22.5:1 for the relative strengths of the two allowed absorption features ($S_3 \leftarrow S_0$ vs. $S_1 \leftarrow S_0$). This is in very good agreement with the ~23.6:1 ratio observed in the spectrum. Finally, the $S_2 \leftarrow S_0$ (HOMO–1 → LUMO – HOMO → LUMO+1) band is very weak.

In BT1, the same approximate features are present, in the form of an allowed $S_1 \leftarrow S_0$ band, a weak $S_2 \leftarrow S_0$ band, and a strong $S_3 \leftarrow S_0$ band. An immediate question about this spectrum concerns why there is one set of features in the $S_1 \leftarrow S_0$ region rather than a split transition with two sets of features. This is explained by considering the corresponding monomeric transitions in Tc-e, which are short-axis in nature. Given the defined structure of the BT1 molecule (which precludes significant geometric distortion), the in-phase combination of the two monomer transition dipole moments (which lie side-by-side and parallel) should be enhanced, while the out-of-phase combination should be forbidden. This is typical behavior for transitions that are H-aggregate like.[52] In previous work,[46] these S_1 transitions were referred to as S_{1a} (forbidden) and S_{1b} (allowed), where Franck–Condon excitation from the A_1 (in the C_{2v} point group of BT1) ground state is allowed to the B_2-symmetric S_{1b} state and forbidden to the A_2-symmetric S_{1a} state. There is also a noticeable red-shift in the $S_1 \leftarrow S_0$ band relative to that in Tc-e (as predicted via time-dependent density functional theory (TD-DFT)[46]). This sort of behavior has been cited as indicative of electronic coupling,[31,33] and is consistent with H-aggregate behavior in the limit of weak interchromophore-coupling.[53]

The splitting that was invisible in the $S_1 \leftarrow S_0$ band of BT1 is readily evident in the strong UV $S_3 \leftarrow S_0$ transitions at 275 nm 309 nm. These features are split about the single transition in Tc-e, and are analogous to those seen in BN1[45] indicating interchromophore electronic coupling. To understand the intensity ratio of these Davydov-split peaks, the interaction of monomeric features from Tc-e is again considered. In Tc-e, the strong $S_3 \leftarrow S_0$ absorbance is long-axis polarized. Unlike the short-axis $S_1 \leftarrow S_0$ transition, this results in two allowed transitions in the dimer, where the interchromophore angle (end–bridgehead–end, or C9–C19–C9', as described by Vallett et al.[46]) is 113.1°. This slightly obtuse angle results in the out-of-phase combination of the monomeric features being more-strongly allowed (and at lower energy) than the in-phase combination. The redder feature at 309 nm (occurring to an excited state with B_1 symmetry, hereafter S_{3a}) is thus polarized along x, while the bluer feature at 275 nm (occurring to an excited state with A_1 symmetry, hereafter S_{3b}) is polarized along z (refer to Figure 3.1 for coordinate system).

The $S_2 \leftarrow S_0$ region in BT1 is expected to show weak dipole-allowed S_{2a} and S_{2b} features sitting atop the latter vibronic peaks of S_{1b}, as was the case for Tc-e. These should be related to S_{3a}/S_{3b} through configuration interaction, and indeed there are a number of weak features with onset near 405 nm evident in the electronic absorption spectrum, though their small amplitude and coincidence with the much larger S_{1b} precludes further analysis.

Calculated transition dipole moments for BT1 are summarized in Table 3.2. As in Tc-e, calculation of the expected ratio of transitions via $f \sim \nu|\vec{D}_{ij}|^2$ yields results in good agreement with the observed electronic absorption spectrum. For S_{3a}:S_{3b}, this analysis predicts a ratio of 2.0:1, in excellent agreement with the observed ratio of 1.9:1 from the electronic absorption spectrum and

2.6:1 predicted using TD-DFT results[46] (see also discussion below). For S_{3a}:S_{1b}, the predicted ratio is 15:1, again in good agreement with the observed ratio (~17:1).

Table 3.2. Transition dipole moments calculated for the first and third sets of singlet transitions in BT1 based on calculated transitions in Tc-e

Electronic Transition	Monomer Origins	Transition Dipole /eÅ	Polarization Axis
$S_{1a} \leftarrow S_0$	S_1(Tc-e) – S_1(Tc-e)	0.0	None
$S_{1b} \leftarrow S_0$	S_1(Tc-e) + S_1(Tc-e)	3.2	y
$S_{3a} \leftarrow S_0$	S_3(Tc-e) + S_3(Tc-e)	9.97	x
$S_{3b} \leftarrow S_0$	S_3(Tc-e) – S_3(Tc-e)	6.6	z

Indeed, the general character of the observed electronic absorption is in good agreement with the results from TD-DFT. Figure 3.5 shows the results of simulated electronic absorption in the region encompassing 240–550 nm based on the above discussed TD-DFT results (grey dotted line, in toluene) as compared to experimental results in chloroform (red; solvent chosen to preserve information in the UV), along with the energies for the most important frontier orbitals. Modeling of the spectra was accomplished by conversion of TD-DFT calculated oscillator strengths (f) for all relevant transitions into molar attenuation coefficient (ε) values using the relationship between ε and f[54] as follows (where n is the refractive index—1.50 for toluene—and ν refers to the transition frequency in wavenumbers):

$$f = \frac{1}{n} \, 4.319 \times 10^{-9} \int \varepsilon(\nu) \, d\nu \qquad (5)$$

A Gaussian line shape was assumed with a peak width chosen to qualitatively match the observed spectrum (full-width at half-maximum of 0.2 eV). Additionally, a red-shift of 0.35 eV was added to line up the onset of the 0–0 transition with the peak of the calculated TD-DFT transition. Both spectra are normalized to the amplitude of the $S_3 \leftarrow S_0$ transition in the UV.

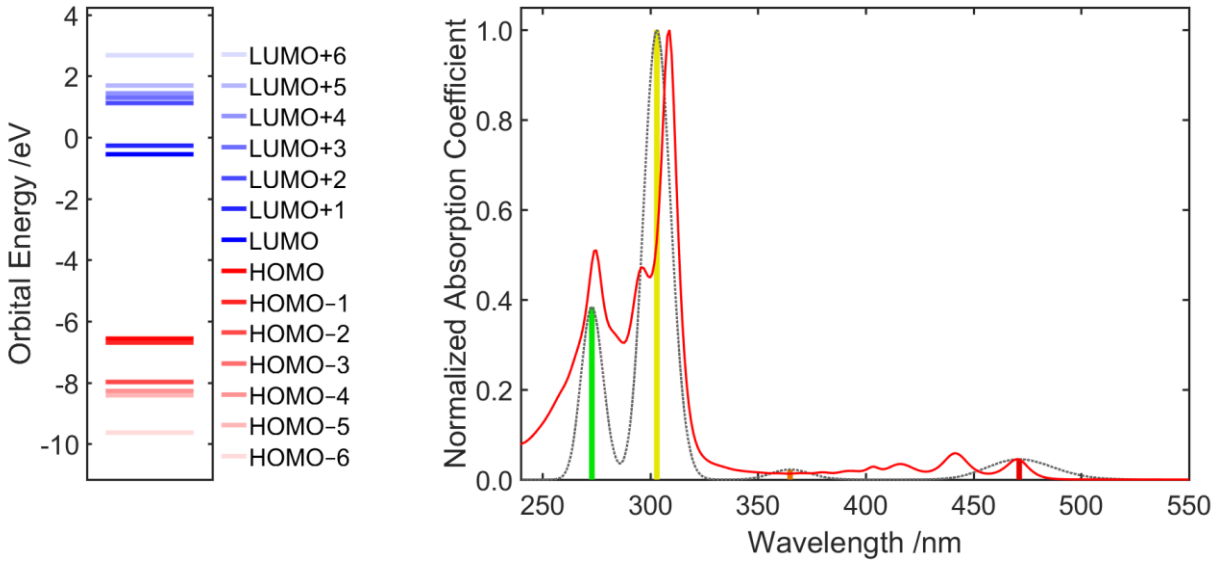

Figure 3.5. Left: frontier orbitals of BT1 calculated via DFT, with filled orbitals in red and unfilled orbitals in blue. Right: electronic absorption spectrum of BT1 obtained from experiment (red line, again in chloroform to preserve the information in the UV) and calculated from TD-DFT results (grey dotted line), with individual transitions shown as color-coded vertical lines.

Qualitatively, all of the observed features are reproduced well in the simulated spectrum, including their relative amplitudes. Both of the Davydov peaks ($S_{3a} \leftarrow S_0$ and $S_{3b} \leftarrow S_0$) are present, and their ratio is in good agreement with experiment. There is only a single $S_1 \leftarrow S_0$ peak, and a weak $S_2 \leftarrow S_0$ feature is apparent in the intervening spectral region. The location of the $S_2 \leftarrow S_0$ is somewhat different from the location observed in experiment (where its onset appears to be at the tail end of the $S_1 \leftarrow S_0$ progression, see Figure 3.3), but the weak nature of that transition is nonetheless correctly captured.

3.3.3 Electronic Absorption and Emission in Toluene

All subsequent measurements in this chapter are carried out in toluene to maintain consistency with computational efforts[41,46] and because toluene was found to increase solubility

(which proved problematic in many other solvents). No significant differences were found in the steady-state behavior of the system between toluene and chloroform (see Appendix A for comparative spectra).

Electronic absorption and emission spectra for Tc-e in toluene are shown in Figure 3.6 (blue). The observed shift between these spectra is small (~5 nm) and the average of their onsets lies at 2.66 eV, suggesting this is the true location of the S_1. This is in reasonable agreement with TD-DFT findings that predicted the S_1 would lie at 2.76 eV.[46] As was the case with its absorption, the emission spectrum of Tc-e shows a clear vibronic progression whose spacing is ~1400 cm^{-1}, essentially the same as in the electronic absorption data. The strength of the 0–0 peak in the emission suggests that the absorbing and emitting states are nested, and the absorption/emission having mirror-image character and clear vibronic structure suggests that emission occurs from the Franck–Condon state. In general, the behavior of Tc-e closely resembles that of solution-phase Tc.[55] This similarity carries through in the emission quantum yield (Φ_{em}), which was determined to be 0.14 ± 0.03 in Tc-e, compared with 0.11 for Tc (Burgdorff et al. report 0.16[56]). This and other quantum yield measurements in this chapter were made relative to coumarin 480 in methanol (Φ_{em} = 0.87[57]), with the quoted value coming from four independent measurements.

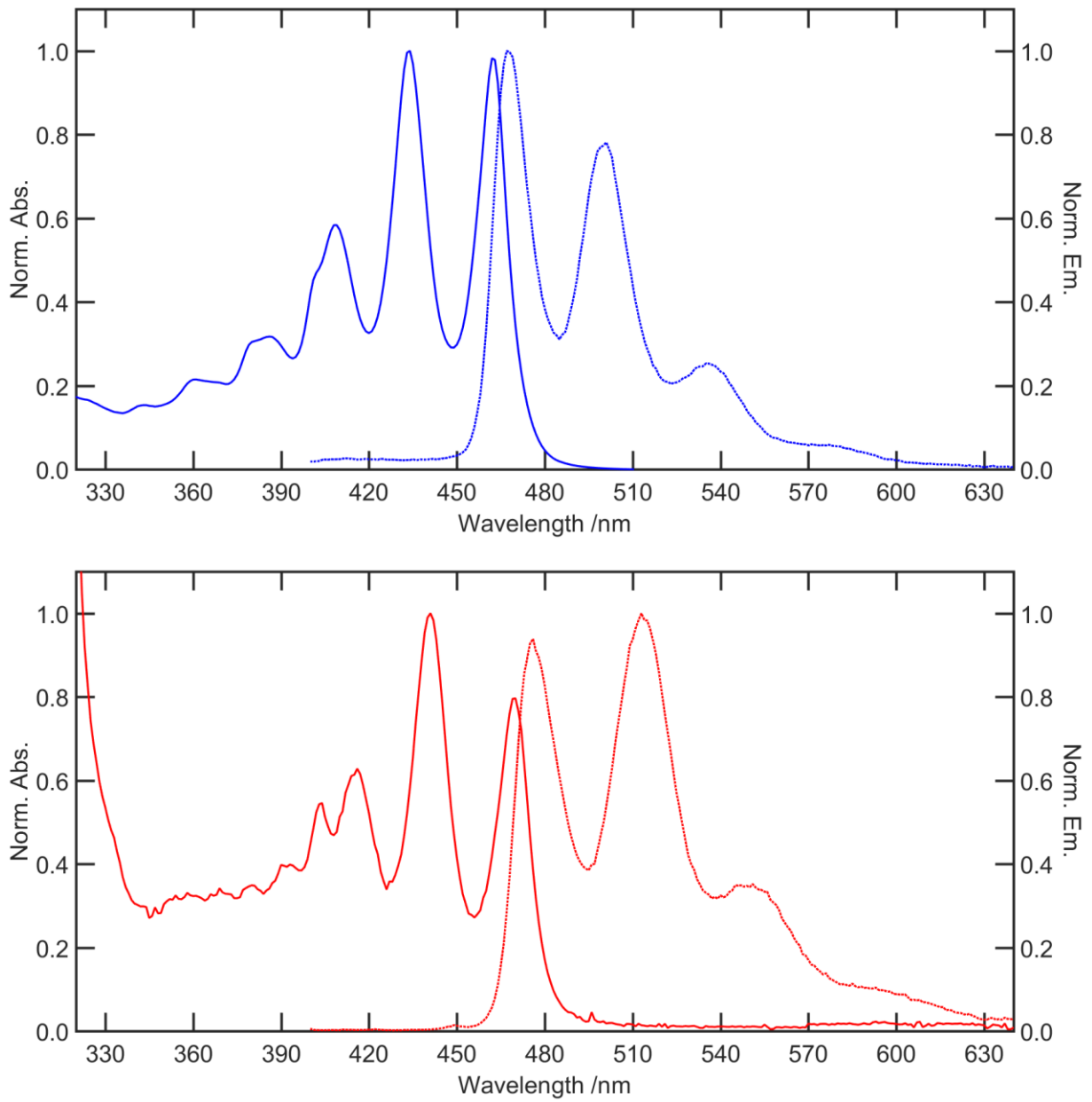

Figure 3.6. Normalized electronic absorption spectra (solid lines) and normalized emission spectra (dotted lines) of Tc-e (blue) and BT1 (red) in room-temperature toluene.

In BT1 (Figure 3.6, bottom), the observed shift between the absorption and emission onsets is again small (~6 nm), and using these energies to estimate the location of S_1 suggests it lies at 2.62 eV. TD-DFT again slightly overestimates this value by predicting 2.71 eV, but is nonetheless close.[46] Also, though it systematically overestimates the S_1 energies of the monomer and dimer

(by ~100 meV), TD-DFT correctly captures the magnitude of the observed red-shift. These results suggest that the method used (consisting of the ω-B97XD range-corrected functional and 6-31g(d) basis set) is generally well suited to this system.

With regards to emission, a vibronic progression (~1550 cm^{-1}) is evident in the emission spectra of BT1 which mirrors the electronic absorption. Unlike in Tc-e, the 0–0 feature in BT1 is smaller than the 0–1 feature (this is true in both the absorption and emission spectra), though this change is mirrored in both the absorption and the emission. This mirror-image character, combined with the small shift, suggests that emission does not occur from an excimer state. Given the rigidity of the norbornyl bridge, which should prevent large-amplitude motions, this is a reasonable explanation. The ratio of vibronic peaks, however, is somewhat unexpected given computational results that suggested localization of the lowest-energy singlet excited state onto one of the acene arms.[46] In such a scenario, it would be reasonable to expect the emission to follow the pattern present in Tc-e, with the 0–0 peak being the strongest emission feature. This is not the case, though the difference may be partially explained given the corresponding reduction of the 0–0 peak in the absorption spectrum of BT1. It is possible that, in the case of both absorption and emission, the 0–0 peak is reduced relative to the 0–1 peak due to coupling between the two chromophore subunits, similar to the origin of the red-shift present in BT1. This effect has been observed previously in molecular dimer systems.[32,58]

As a final note on the steady-state behavior of BT1, the value of Φ_{em} was determined to be 0.10 ± 0.02 (based on 11 independent measurements). This value is somewhat reduced relative to that of Tc-e or Tc (*vide supra*). Subsequent exploration of time-resolved behavior in Tc-e and BT1 allows the quantum yields of both molecules to be understood further.

3.4 Time-Resolved Emission

3.4.1 Time-Correlated Single-Photon Counting

Time-resolved emission measurements were performed via time-correlated single-photon counting (TCSPC), as described in Chapter 2. Emitted light (at magic angle polarization of 54.7°) was again passed through a monochromator (Oriel 77250), here set to an emission wavelength λ_{em} = 480 nm.

All samples were prepared in dilute (~5 μM) solution using 1-cm quartz cuvettes. Cuvettes were capped using screw-top lids with polytetrafluoroethylene gaskets, and bubble-degassed with argon for 30 minutes prior to sealing under positive argon pressure. Experiments were carried out promptly after sample preparation, and sample integrity was verified before and after data acquisition via steady-state absorption spectroscopy. The instrument response function (IRF) was measured by replacing the sample with a scattering medium to direct a portion of the 395 nm excitation light into the detector, while also adjusting the emission monochromator to obtain scattered 395 nm light.

3.4.2 Time-Resolved Fits

The results obtained for the time-resolved emission of Tc-e and BT1 are shown in Figure 3.7. In Tc-e, the TCSPC data (λ_{em} = 480 nm) is well described by a single-exponential decay (convolved with the IRF, also shown in Figure 3.7) with an observed lifetime $\tau_{obs} = 3.9 \pm 0.2$ ns (based on four independent measurements). Repeated measurements at other wavelengths between 465 and 540 nm suggested no wavelength dependence to this behavior. This allows for separation of the radiative and non-radiative components of Tc-e excited state decay using the relationship $\Phi_{em} = k_r/k_{obs} = k_r/(k_r + k_{nr}) = k_r \tau_{obs}$. Here, k_{nr} includes all non-radiative losses, including intersystem crossing (ISC) and internal conversion (IC). Using the value of Φ_{em} determined earlier,

the quantities $k_r = (3.5 \pm 0.7) \times 10^7\ s^{-1}$ and $k_{nr} = (2.2 \pm 0.6) \times 10^8\ s^{-1}$ are found. It is noted that the determined value of k_{nr} is somewhat large relative to that of other dye fluorophores (such as coumarin 153, where k_{nr} is of order $1 \times 10^7\ s^{-1}$, only reaches values near $1 \times 10^8\ s^{-1}$ in highly polar solvents like 2,2,2-trifluoroethanol). This is likely responsible for the small Φ_{em} observed for Tc-e, and presumably has origins similar to the similarly large k_{nr} in Tc ($1.9 \times 10^8\ s^{-1}$ in this work; $1.8 \times 10^8\ s^{-1}$ quoted by Burgdorff et al.[56]). In Tc system, which is electronically and structurally similar to Tc-e, the second triplet excited state (T_2) is known[59] to be energetically proximal to the S_1 such that intersystem crossing ($S_1 \rightarrow T_2$) is atypically fast.[56] Excited states that enter this loss channel are deactivated through fast internal conversion ($T_2 \rightarrow T_1$), which prevents appreciable recovery of the emissive singlet through $T_2 \rightarrow S_1$ reverse intersystem crossing. The triplet quantum yield in Tc is accordingly high (it has been reported as $\Phi_{ISC} = 0.62$[60]), a trait which Tc-e is expected to also possess.

In BT1, there is obvious deviation from the single-exponential behavior observed in Tc-e. A single-exponential fit (again convolved with the IRF) is shown in Figure 3.7a to emphasize this deviation, which begins when the signal has dropped to approximately 10% of its initial value. A second fit is also shown. This fit uses a sum of two exponentials [$\text{Signal}(t) = A_1 \exp(-t/\tau_1) + A_2 \exp(-t/\tau_2)$] for which the lifetimes $\tau_1 = 4.3 \pm 0.4$ ns ($92 \pm 5\%$) and $\tau_2 = 11 \pm 3$ ns ($9 \pm 5\%$) were found. This latter fit adequately reproduces the observed behavior.

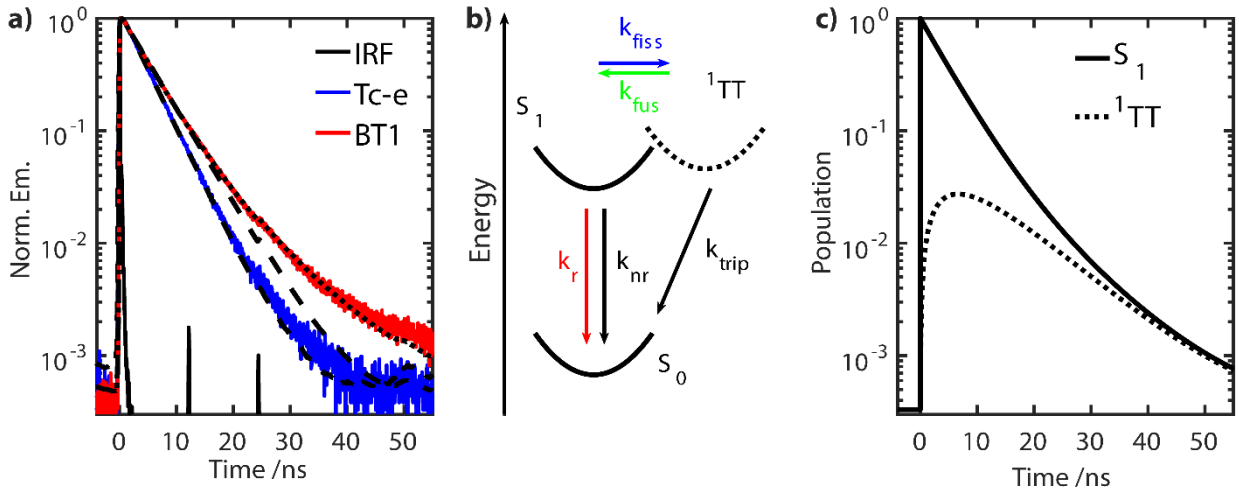

Figure 3.7. Time-resolved behavior of Tc-e and BT1 in toluene. **(a)** Raw data and exponential fits to Tc-e (blue) and BT1 (red) in toluene, including instrument response (black) with which fits were convolved. Dashed lines are fits to single exponential models, while the dotted line is a fit of emission in BT1 to a sum of two exponentials. **(b)** Schematic of the kinetic model used in describing the behavior of BT1 following excitation into its S_1 state, showing all included parameters. **(c)** Reconstructed populations of the S_1 and ^{1}TT states generated by evaluation of the kinetic model.

3.4.3 Modeling BT1 Kinetics

To understand the multiexponential behavior of BT1, a number of models were considered and ruled out. Intersystem crossing, as in Tc-e, is expected to be a significant loss pathway, but it is unable to account for the second observed lifetime. Any T_2 states formed through intersystem crossing from S_1 to T_2 would rapidly yield a single low-energy T_1 state (with $E(T_1) = 1.37$ eV via DFT[46]) as in Tc or Tc-e that is unable to regenerate S_1 population or phosphoresce in the wavelength region studied (~480 nm). Additionally, given the low fluences used and the dilute concentrations of the samples studied, collisional triplet-triplet annihilation leading to delayed fluorescence is extremely unlikely, though such behavior has been observed by others in highly concentrated solutions.[38] Reversible conversion to an excimer state has also been considered and ruled out for a few reasons. Firstly—as discussed in Section 3.3.3–the observed emission retains the vibronic progression of the absorbing state, and there is no evidence in the photoluminescence

spectrum in Figure 3.6 that an additional singlet excimer state exists near the emissive S_1. This is sensible given the structural rigidity of the norbornyl bridge, which should preclude any such low-lying excimer states. Computational results on BT1 and related systems[46] (using TD-DFT with gradients to identify adiabatic singlet excited states) likewise find no states with excimer character near the Franck–Condon singlet state. A dimer-delocalized singlet state was found—referred to as $S_{1\text{-deloc}}$—with energy ~140 meV above that of the arm-localized $S_{1\text{-loc}}$ ($E(S_{1\text{-loc}}) = 2.71$ eV). However, the interchromophore angle in $S_{1\text{-deloc}}$ was slightly larger than in $S_{1\text{-loc}}$, and it is expected that $S_{1\text{-deloc}}$ acts as a transition state between two degenerate (one-arm localized) S_1 states. Lastly, any conversion to or from $S_{1\text{-deloc}}$ (if it were an intermediate) should not be expected to occur on the slow (nanosecond) timescales observed in the emission of BT1. These same computational results did, however, identify a lowest-energy triplet (T_1, localized to one of the dimer arms) with $E(T_1) = 1.37$ eV (such that $2 \times E(T_1) = 2.74$ eV) and a lowest quintet state (Q) with $E(Q) = 2.76$ eV. The Q state is of particular interest because it closely approximates a state with one T_1 excitation localized to each of the Tc arms in BT1, and is therefore expected to be similar in energy to a multiexcitonic ^{1}TT state. Thus, with the energies of $2 \times T_1$ and Q most proximal to the adiabatic $S_{1\text{-loc}}$ and other explanations ruled out, the kinetic model in Figure 3.7b invokes singlet fission to explain the biexponential decay observed in the emission of BT1.

In the BT1 kinetic model, loss pathways for the S_1 state consist of radiative losses (k_r), non-radiative losses (k_{nr}, including ISC—likely through T_2 as was the case in Tc and Tc-e—and IC), and singlet fission (k_{fiss}) which produces the multiexcitonic state ^{1}TT. The ^{1}TT state in turn loses population through triplet fusion (k_{fus}, the microscopic reverse of SF), which repopulates S_1, or by irreversible relaxation to the S_0 ground state such as through formation of T_1 (summarized by k_{trip}). No modeling is done for the isolated triplet state T_1 since there is no evidence in the data for a third

exponential that would result from equilibrium between ^{1}TT and (T_1 + T_1). The model used here is analogous to the model used by Bardeen and coworkers in their studies of the first covalent Tc dimers.[25] From the model, coupled differential equations are derived for the populations of S_1 and ^{1}TT, respectively:

$$\frac{dS_1}{dt} = -(k_{loss}+k_{fiss})S_1 + k_{fus}\,{}^1TT \tag{6}$$

$$\frac{d{}^1TT}{dt} = -k_{fiss}S_1 - \left(\frac{k_{trip}}{2} + k_{fus}\right){}^1TT \tag{7}$$

In the above expressions, k_r and k_{nr} have been grouped together as k_{loss} for clarity, and the value of k_{trip} is halved to account for the formation of two triplet states from each relaxed ^{1}TT. These expressions are solved using matrix eigenanalysis to match the observed biexponential fit parameters (*vide supra*). First, the expression is rewritten in matrix form, where the matrix **K** holds the rate coefficients and the vector $\vec{N}$ and its time-derivative $\vec{N'}$ contain the populations of the states S_1 and ^{1}TT and their time derivatives, respectively:

$$\vec{N}'(t) = \mathbf{K}\,\vec{N}(t) = \begin{pmatrix} -(k_{loss}+k_{fiss}) & k_{fus} \\ k_{fiss} & -\left(\frac{k_{trip}}{2}+k_{fus}\right) \end{pmatrix} \begin{pmatrix} S_1(t) \\ {}^1TT(t) \end{pmatrix} \tag{8}$$

General solutions to this type of equation are well-known to be n-exponential (where n is the size of square matrix **K**; here n = 2) and in the two-exponential case follow the form:

$$\vec{N}(t) = c_1 \exp(\lambda_1 t)\vec{V_1} + c_2 \exp(\lambda_2 t)\vec{V_2} \tag{9}$$

In this expression, the scalars λ_i and vectors $\vec{V}_i$ are, respectively, the i^{th} eigenvalues and i^{th} eigenvectors of matrix **K**. This can be rewritten to consider only the TCSPC observable (the population of S_1, which is the element N_1 from $\vec{N}$) as:

$$S_1(t) = c_1V_{11}\exp(\lambda_1 t) + c_2V_{12}\exp(\lambda_2 t) = A_1\exp(-t/\tau_1) + A_2\exp(-t/\tau_2) \tag{10}$$

In this, the quantities V_{11} and V_{12} denote the first elements of eigenvectors $\vec{V}_1$ and $\vec{V}_2$, respectively, such that the observed lifetimes and amplitudes from TCSPC can be directly equated to parameters from eigenanalysis of **K**:

$$A_1 = c_1V_{11},\ A_2 = c_2V_{12},\ \tau_1 = \lambda_1^{-1},\ \tau_2 = \lambda_2^{-1} \tag{11}$$

Thus **K** is diagonalized and the observed lifetimes τ_i are found in terms of its eigenvalues λ_i:

$$\tau_{1,2} = \lambda_{1,2}^{-1} = \frac{-4}{-2\,k_{fiss} - 2\,k_{fus} - 2\,k_{loss} - k_{trip} \mp \sqrt{(2\,k_{fiss}+2\,k_{fus}+2\,k_{loss}+k_{trip})^2 - 8\,(2\,k_{fus}k_{loss}+k_{fiss}k_{trip}+k_{loss}k_{trip})}} \tag{12}$$

The eigenvectors $\vec{V}_i$ are likewise found when **K** is diagonalized:

$$\vec{V}_{1,2} = \begin{pmatrix} \dfrac{2\,k_{fiss} - 2\,k_{fus} + 2\,k_{loss} - k_{trip} \pm \sqrt{(2\,k_{fiss}+2\,k_{fus}+2\,k_{loss}+k_{trip})^2 - 8\,(2\,k_{fus}k_{loss}+k_{fiss}k_{trip}+k_{loss}k_{trip})}}{4\,k_{fiss}} \\ 1 \end{pmatrix} \tag{13}$$

Expressions for the amplitudes A_i additionally require the coefficients c_i. To obtain these, initial conditions are assumed and applied. The reasonable assumption is made that, given impulsive (~100 fs) excitation, all of the population is in the S_1 state at time zero. Thus the initial populations $S_1(t = 0) = 1$ and $^1TT(t = 0) = 0$ are used to find expressions for c_i:

$$\vec{N}(t = 0) = \begin{pmatrix} 1 \\ 0 \end{pmatrix} = c_1\vec{V_1} + c_2\vec{V_2} \Longrightarrow$$

$$c_{1,2} = \mp \frac{2k_{fiss}}{\sqrt{(2k_{fiss}+2k_{fus}+2k_{loss}+k_{trip})^2 - 8(2k_{fus}k_{loss}+k_{fiss}k_{trip}+k_{loss}k_{trip})}} \tag{14}$$

The system consisting of equations 11–13 was solved numerically (using the values of A_1, A_2, τ_1, and τ_2 retrieved from the TCSPC data of BT1) to obtain values for k_{fiss} ($1.4 \times 10^7\ s^{-1}$), k_{fus} ($1.1 \times 10^8\ s^{-1}$), and k_{loss} ($2.1 \times 10^8\ s^{-1}$). The value of k_{trip} was set at $1 \times 10^3\ s^{-1}$, which is justified by consideration of the probable loss pathways coupling ^1TT to the S_0 ground state. Any direct

electronic coupling between these states should be small (though not strictly zero by symmetry[3,41]) given the multiexcitonic nature of the ^{1}TT state as compared to the closed shell S_0. Deliberate overestimation of the diabatic coupling and reorganization energy (100 meV and 1 eV, respectively) yields Marcus transfer rates too slow to be relevant due to the massive free energy difference, which pushes this pathway far into the Marcus inverted region. Another possible contributor to k_{trip} is intersystem crossing from ^{1}TT to T_2, though (given that this process is multiexcitonic and spin-forbidden) this may also be ignored under the reasonable assumption that it is substantially slower (by a factor of ~10 or more) than ISC from S_1 to T_2. Lastly, dephasing of the coupled triplets (^{1}TT) into two T_1 states is considered, where both T_1 states then undergo ISC to irreversibly reform S_0. The rate of $T_1 \rightarrow S_0$ ISC in solid Tc is ~1×10^3 s^{-1}, and it is from this value that k_{trip} was approximated.[25,56] Because all of the aforementioned ^{1}TT $\rightarrow S_0$ relaxation pathways are quite slow, k_{trip} is considered generally unimportant, and changing its value substantially (by 3–4 orders of magnitude) had little effect on the results. With the assumption that k_{trip} is small, the radiative and non-radiative rate constants k_r and k_{nr} may be separated from k_{loss} using the measured Φ_{em} value for BT1 according to:

$$\Phi_{em} = \frac{k_r}{k_r + k_{nr}} = \frac{k_r}{k_{loss}} \tag{15}$$

This assumes that losses of S_1 population due to SF are largely regained by triplet fusion, which is reasonable in the limit that triplet fusion is faster than SF and that irreversible losses from ^{1}TT are minimal. No such assumption was necessary in the case of the monomer, where there was no evidence for ^{1}TT state (and k_{loss} was directly equal to k_{obs}). This analysis finds $k_r = (2.3 \pm 0.5) \times 10^7$ s^{-1} and $k_{nr} = (1.9 \pm 0.2) \times 10^8$ s^{-1}.

3.5 Discussion of Rates, Yields, and SF Energetics

The values for all determined rates, lifetimes, and yields are summarized in Table 3.3. In BT1, the non-radiative rate coefficient (k_{nr}) differs little from that found for Tc and Tc-e. As was the case in those systems, these non-radiative losses are likely dominated by $S_1 \rightarrow T_2$ ISC. The radiative decay coefficient k_r, however, sees a modest reduction relative to its value in Tc and Tc-e. This is presumably linked to the changes in Franck–Condon factors observed via the vibronic structure in the absorption and photoluminescence spectra of BT1 (especially the changes discussed previously for the 0–0 vs. 0–1 peak ratios).

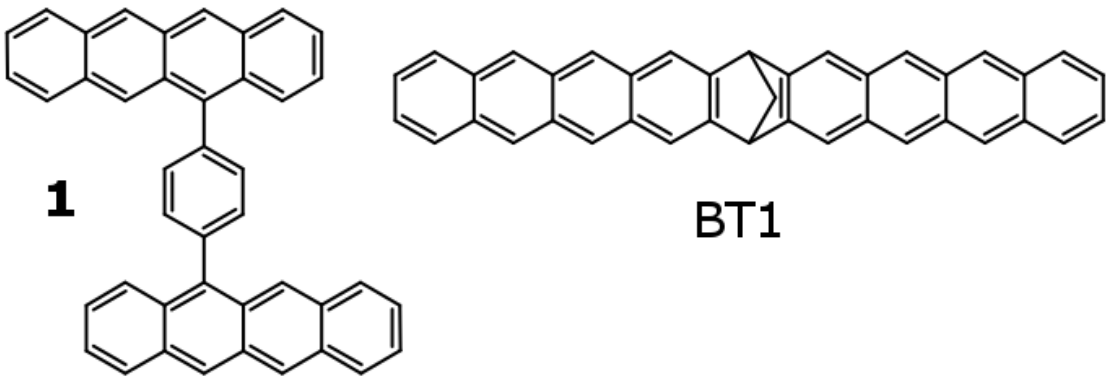

Figure 3.8. Structures of the phenyl-bridged Tc dimer (**1**) studied by Müller et al.[25] (left) and BT1 (right).

The SF rate coefficient (k_{fiss}) found for BT1 is $(1.4 \pm 0.3) \times 10^7$ s^{-1}. Though small, this is somewhat larger (by a factor of 5) than what was found for a phenylene-spaced Tc dimer (**1**, pictured in Figure 3.8 with kinetic details in Table 3.3) studied by Müller et al. in the first study of SF in solution-phase dimers.[25] The quantum yield of ^{1}TT formation in BT1 is found via the expression $\Phi_{fiss} = k_{fiss}/(k_{fiss} + k_r + k_{nr}) = 0.063$. Again, this compares favorably with **1**, where $\Phi_{fiss} = 0.029$.[25] Interestingly, k_{fus} (1.1×10^8 s^{-1}) is much larger in BT1 than in **1**, by a factor of 37, and

is additionally much larger than k_{fiss} in either molecule (8 times greater than k_{fiss} in BT1 and 39 times larger than k_{fiss} in **1**). This large $^1TT \rightarrow S_1$ rate coefficient should preclude formation of significant ^1TT population, as shown Figure 3.7c (the population of ^1TT peaks at around 3% of the initial excited state population, and rapidly falls off as S_1 decays).

Table 3.3. Rates, lifetimes, and yields in toluene solution

	Tc	Tc-e	BT1	**1**[a]
τ_{obs} /ns (amplitude)	4.6, 4.8[b]	3.9 ± 0.2	4.3 ± 0.4 (A_1: 0.92 ± 0.05) and 11 ± 3 (A_2: 0.09 ± 0.05)	6.13 ± 0.02 and >100
Φ_{em}	0.11[c], 0.16[b]	0.14 ± 0.03[c]	0.10 ± 0.02[c]	0.31 ± 0.01
$k_r \times s$	2.4×10^7, 3.3×10^{7b}	$(3.5 \pm 0.7) \times 10^7$	$(2.3 \pm 0.5) \times 10^7$	$(5.00 \pm 0.05) \times 10^7$
$k_{nr} \times s$	1.9×10^8, 1.8×10^{8b}	$(2.2 \pm 0.6) \times 10^8$	$(1.9 \pm 0.2) \times 10^8$	$(4.50 \pm 0.05) \times 10^7$
$k_{fiss} \times s$	-	-	$(1.4 \pm 0.3) \times 10^7$	$(2.8 \pm 0.2) \times 10^6$
$k_{fus} \times s$	-	-	$(1.1 \pm 0.3) \times 10^8$	$(3.0 \pm 0.2) \times 10^6$
Φ_{fiss}	-	-	0.063 ± 0.014	0.028 ± 0.002
ΔG_{fiss} /eV	-	-	0.052 ± 0.010	0.104 ± 0.006

[a]Molecule **1** from Müller et al.; amplitudes not specified.[25] [b]From Burgdorff et al.; experiments done in benzene.[56] [c]Φ_{em} measured relative to coumarin 480 in methanol (Φ_{em} = 0.87[57]).

Using the determined values of k_{fiss} and k_{fus} for BT1, the free energy difference between the S_1 and ^1TT states (ΔG_{fiss}) is estimated according to the standard Gibbs free energy expression (where k_B is the Boltzmann constant), $\Delta G_{fiss} = -k_B T \ln K_{eq} = -k_B T \ln(k_{fiss} / k_{fus})$. This gives a free energy difference of 52 meV that is overall endergonic for SF, in remarkably good agreement with the previously discussed computations (see discussion in Section 3.4.3)[46] that predict 30 meV for

the difference between $2 \times T_1$ and $S_{1\text{-loc}}$ or—in even better agreement—50 meV for the difference between Q (the proxy for ^{1}TT) and $S_{1\text{-loc}}$.

Similar calculation of ΔG_{fiss} for **1** leads to a value of ~2 meV, in disagreement with the 104 meV measured by temperature-dependent photoluminescence decay.[25] This disconnect can be understood by considering the structures of BT1 and **1** in Figure 3.8, with particular attention to the nature of the linkage between the two acene arms. In BT1, it is reasonable to expect the diabatic coupling between the S_1 and ^{1}TT states to be similar in either reaction direction given the well-defined structure of the dimer. As a result of this microscopic reversibility, ΔG_{fiss} should be readily understood in terms of the ratio of the fission and fusion rates (with $k_{fiss}/k_{fus} = 0.13$). In **1**, this is not the case due to the single-bond connectivity through the phenylene bridge, which allows modulation of the inter-ring dihedral angle between the acene arms and the bridge itself. The result is that **1** may exhibit behavior similar to a set of donor-bridge-acceptor systems[61–63] where twisting of a single-bond point of attachment upon photoexcitation slowed the rate of backward electron transfer relative to the forward process. For SF in **1**, this would manifest as two triplets, localized (one each) to the acene arms of **1**, whose recombination is slowed by a decrease in diabatic coupling between ^{1}TT and S_1 due to a change in the ring-bridge-ring dihedral angle. This elimination of microscopic reversibility would slow k_{fus} in **1** relative to k_{fiss} (explaining their observed ratio, $k_{fiss}/k_{fus} = 0.91$) while allowing the thermodynamic driving force ΔG_{fiss} to stay meaningfully endergonic (104 meV) as measured. The above discussion underscores the value of rigidity through facilitating direct comparison between computation and experiment.

Though the initial step of SF is faster in BT1 than in **1**, formation of ^{1}TT is still very slow, with a lifetime of 70 ns that is roughly 1000 times slower than in polycrystalline Tc films—despite that system being more endergonic than BT1 ($\Delta E_{fiss} \approx 100$ meV in Tc vs. 52 meV in BT1).[20,64,65]

The rate coefficient for SF (k_{fiss}) can be computed for both systems to aid in understanding this difference using the Marcus equation, which requires estimates for the diabatic coupling V between S_1 and ^{1}TT, reorganization energy λ, and reaction free energy ΔG_{fiss}:

$$k_{fiss} = \frac{2\pi}{\hbar} V^2 \frac{1}{\sqrt{4\pi\lambda k_B T}} \exp\left(-\frac{(\lambda+\Delta G_{fiss})^2}{4\lambda k_B T}\right) \quad (16)$$

For polycrystalline Tc films, the following literature values are used for these parameters: λ = 0.176 eV,[66] V = 7.3 meV[41] (using a nearest-neighbor non-covalent Tc dimer within a crystal), and $\Delta G_{fiss} \approx 100$ meV (an approximate value based on multiple reports[20,64,65]). This predicts a lifetime of 33 ps, which agrees well with experimental results (31–125 ps, depending on grain size[20]).

Obtaining this Marcus theory prediction for BT1 requires estimates for λ and for V. The value of λ for BT1 in solution is expected to be larger than that solid Tc in a solid, and was estimated using gas-phase single-point calculations by Niels Damrauer. These calculations started with previously-determined geometries from previous work (using TD-DFT with gradients, 6-31g(d) basis set, ω-B97XD range-corrected density functional, and toluene polarizable continuum model)[46] for the states $S_{1\text{-loc}}$ and Q (see Appendix A for nuclear coordinates). The lowest quintet state energy was calculated at the geometry single-points of the optimized $S_{1\text{-loc}}$ and the optimized Q, and the difference (0.431 eV) was taken to as the inner-sphere contribution to λ. The outer-sphere contribution is expected to be relatively small, and so the estimate λ = 0.5 eV is made for BT1 $S_1 \rightarrow {}^1$TT. Because of the C_{2v} ground state of BT1, the coupling V is ordinarily zero. Estimation of V is instead derived from diabatic coupling gradients by Alguire et al.[41] These gradients take into account coupling that emerges for $S_1 \rightarrow {}^1$TT due to symmetry-breaking vibrations, and instead give an effective coupling as a function of λ. In the case where λ = 0.5 eV (and ΔG_{fiss} = 52 meV), the coupling is estimated to be = 5 meV. From these values, the lifetime of

SF is determined to be 635 ps, or approximately 100 times too fast. Using a coupling of 0.5 meV (reducing the gradient-derived value by a factor of 10) gives a lifetime of 63.5 ns, which is much closer to the experimentally observed result (70 ns). This suggests that the computational technique for estimating coupling gradients needs refinement (to minimize overestimation of V) but also emphasizes the importance of considering non-equilibrium coupling for systems like BT1 where equilibrium coupling is formally zero.

3.6 Conclusion

With endergonic thermodynamics (ΔG_{fiss} = +52 meV), microscopic reversibility for $S_1 \leftrightarrow {}^1TT$, and unfavorable symmetry, BT1 undergoes SF slowly (70 ns) and in small quantities (Φ_{fiss} = 0.063), losing population to other loss pathways (in particular, $S_1 \rightarrow T_2$ ISC). However, the platform provided by BT1 is useful for building a comprehensive understanding of the relative importance of the aforementioned factors. Subsequent modifications to the rigid BT1 framework (such as those described in the following chapter) will provide more detailed insight into SF, allowing for individual exploration of energetics, kinetic competition, and symmetry. This should in principle aid in answering a multitude of SF-related questions. Through microscopic reversibility, it may be possible to reveal how heavily SF relies on favorable energetics, helping to understand the nature of SF in the endergonic Tc solid.[3,65] Also because of rigidity, questions about decoherence and relative energetics of the ${}^1TT$ into 2 × T_1 should be more accessible through techniques like transient absorption spectroscopy. Simple modifications which change symmetry[42] should allow substantial quantum mechanical control with significant macroscopic results—a derivative of BT1 with C2 symmetry, for example, is predicted to have a diabatic coupling between S_1 and ${}^1TT$ of 10 meV, for example, which exceeds the value for polycrystalline Tc used above. Importantly, this modification to coupling is accomplished without accompanying significant

changes to the energetics of the molecule, again highlighting the value of this framework for independent exploration of these parameters. Finally, experiments utilizing coherent control on molecular dimers—initial attempts are explored in the last chapter of this thesis—are possible to explore the role of symmetry-breaking vibrations in enabling SF where coupling is otherwise nonexistent. To begin this task, the following chapter considers a substituted derivative of BT1 known as TIPS-BT1 (where a pair of triisopropylsilylethynyl groups has been added to each arm) with the goal of extending the BT1 platform and analysis provided in this chapter.

3.7 Bibliography

1. Swenberg, C. E. & Stacy, W. T. Bimolecular radiationless transitions in crystalline tetracene. *Chem. Phys. Lett.* **2,** 327–328 (1968).
2. Merrifield, R. E., Avakian, P. & Groff, R. P. Fission of singlet excitons into pairs of triplet excitons in tetracene crystals. *Chem. Phys. Lett.* **3,** 155–157 (1969).
3. Smith, M. B. & Michl, J. Singlet Fission. *Chem. Rev.* **110,** 6891–6936 (2010).
4. Johnson, J. C., Nozik, A. J. & Michl, J. High triplet yield from singlet fission in a thin film of 1,3-diphenylisobenzofuran. *J. Am. Chem. Soc.* **132,** 16302–16303 (2010).
5. Burdett, J. J. & Bardeen, C. J. Quantum Beats in Crystalline Tetracene Delayed Fluorescence Due to Triplet Pair Coherences Produced by Direct Singlet Fission. *J. Am. Chem. Soc.* **134,** 8597–8607 (2012).
6. Wilson, M. W. B., Rao, A., Ehrler, B. & Friend, R. H. Singlet Exciton Fission in Polycrystalline Pentacene: From Photophysics toward Devices. *Acc. Chem. Res.* **46,** 1330–1338 (2013).
7. Swenberg, C. E. & Pope, M. *Electronic Processes in Organic Crystals and Polymers*. (Oxford University Press, 1999).
8. Dillon, R. J., Piland, G. B. & Bardeen, C. J. Different Rates of Singlet Fission in Monoclinic versus Orthorhombic Crystal Forms of Diphenylhexatriene. *J. Am. Chem. Soc.* **135,** 17278–17281 (2013).
9. Eaton, S. W., Shoer, L. E., Karlen, S. D., Dyar, S. M., Margulies, E. A., Veldkamp, B. S., Ramanan, C., Hartzler, D. A., Savikhin, S., Marks, T. J. & Wasielewski, M. R. Singlet Exciton Fission in Polycrystalline Thin Films of a Slip-Stacked Perylenediimide. *J. Am. Chem. Soc.* **135,** 14701–14712 (2013).

10. Eaton, S. W., Miller, S. a., Margulies, E. a., Shoer, L. E., Schaller, R. D. & Wasielewski, M. R. Singlet Exciton Fission in Thin Films of tert -Butyl-Substituted Terrylenes. *J. Phys. Chem. A* **119,** 4151–4161 (2015).

11. Burdett, J. J., Müller, A. M., Gosztola, D. & Bardeen, C. J. Excited state dynamics in solid and monomeric tetracene: The roles of superradiance and exciton fission. *J. Chem. Phys.* **133,** 144506 (2010).

12. Burdett, J. J., Gosztola, D. & Bardeen, C. J. The dependence of singlet exciton relaxation on excitation density and temperature in polycrystalline tetracene thin films: kinetic evidence for a dark intermediate state and implications for singlet fission. *J. Chem. Phys.* **135,** 214508 (2011).

13. Berkelbach, T. C., Hybertsen, M. S. & Reichman, D. R. Microscopic theory of singlet exciton fission. III. Crystalline pentacene. *J. Chem. Phys.* **141,** 0–12 (2014).

14. Teichen, P. E. & Eaves, J. D. Collective aspects of singlet fission in molecular crystals. *J. Chem. Phys.* **143,** 44118 (2015).

15. Feng, X., Kolomeisky, A. B. & Krylov, A. I. Dissecting the Effect of Morphology on the Rates of Singlet Fission: Insights from Theory. *J. Phys. Chem. C* **118,** 19608–19617 (2014).

16. Ryerson, J. L., Schrauben, J. N., Ferguson, A. J., Sahoo, S. C., Naumov, P., Havlas, Z., Michl, J., Nozik, A. J. & Johnson, J. C. Two Thin Film Polymorphs of the Singlet Fission Compound 1,3-Diphenylisobenzofuran. *J. Phys. Chem. C* **118,** 12121–12132 (2014).

17. Wan, Y., Guo, Z., Zhu, T., Yan, S., Johnson, J. & Huang, L. Cooperative singlet and triplet exciton transport in tetracene crystals visualized by ultrafast microscopy. *Nat. Chem.* **7,** 785–792 (2015).

18. Piland, G. B. & Bardeen, C. J. How Morphology Affects Singlet Fission in Crystalline

Tetracene. *J. Phys. Chem. Lett.* **6,** 1841–1846 (2015).

19. Hartnett, P. E., Margulies, E. A., Mauck, C. M., Miller, S. A., Wu, Y., Wu, Y.-L., Marks, T. J. & Wasielewski, M. R. Effects of Crystal Morphology on Singlet Exciton Fission in Diketopyrrolopyrrole Thin Films. *J. Phys. Chem. B* **120,** 1357–1366 (2016).
20. Arias, D. H., Ryerson, J. L., Cook, J. D., Damrauer, N. H. & Johnson, J. C. Polymorphism influences singlet fission rates in tetracene thin films. *Chem. Sci.* **7,** 1185–1191 (2016).
21. Bhattacharyya, K. & Datta, A. Polymorphism Controlled Singlet Fission in TIPS-Anthracene: Role of Stacking Orientation. *J. Phys. Chem. C* **121,** 1412–1420 (2017).
22. Hanna, M. C. & Nozik, A. J. Solar Conversion Efficiency of Photovoltaic and Photoelectrolysis Cells with Carrier Multiplication Absorbers. *J. Appl. Phys.* **100,** 74510 (2006).
23. Schrauben, J. N., Zhao, Y., Mercado, C., Dron, P. I., Ryerson, J. L., Michl, J., Zhu, K. & Johnson, J. C. Photocurrent Enhanced by Singlet Fission in a Dye-Sensitized Solar Cell. *ACS Appl. Mater. Interfaces* **7,** 2286–2293 (2015).
24. Lee, J., Jadhav, P., Reusswig, P. D., Yost, S. R., Thompson, N. J., Congreve, D. N., Hontz, E., Van Voorhis, T. & Baldo, M. a. Singlet Exciton Fission Photovoltaics. *Acc. Chem. Res.* **46,** 1300–1311 (2013).
25. Müller, A. M., Avlasevich, Y. S., Schoeller, W. W., Müllen, K. & Bardeen, C. J. Exciton Fission and Fusion in Bis(tetracene) Molecules with Different Covalent Linker Structures. *J. Am. Chem. Soc.* **129,** 14240–14250 (2007).
26. Johnson, J. C., Akdag, A., Zamadar, M., Chen, X., Schwerin, A. F., Paci, I., Smith, M. B., Havlas, Z. Z., Miller, J. R., Ratner, M. A., Nozik, A. J. & Michl, J. Toward designed singlet fission: Solution photophysics of two indirectly coupled covalent dimers of 1,3-

diphenylisobenzofuran. *J. Phys. Chem. B* **117,** 4680–4695 (2013).

27. Margulies, E. A., Shoer, L. E., Eaton, S. W. & Wasielewski, M. R. Excimer formation in cofacial and slip-stacked perylene-3,4:9,10-bis(dicarboximide) dimers on a redox-inactive triptycene scaffold. *Phys. Chem. Chem. Phys.* **16,** 23735–23742 (2014).

28. Liu, H., Nichols, V. M., Shen, L., Jahansouz, S., Chen, Y., Hanson, K. M., Bardeen, C. J. & Li, X. Synthesis and photophysical properties of a 'face-to-face' stacked tetracene dimer. *Phys. Chem. Chem. Phys.* **17,** 6523–6531 (2015).

29. Sanders, S. N., Kumarasamy, E., Pun, A. B., Trinh, M. T., Choi, B., Xia, J., Taffet, E. J., Low, J. Z., Miller, J. R., Roy, X., Zhu, X.-Y., Steigerwald, M. L., Sfeir, M. Y. & Campos, L. M. Quantitative Intramolecular Singlet Fission in Bipentacenes. *J. Am. Chem. Soc.* **137,** 8965–8972 (2015).

30. Zirzlmeier, J., Lehnherr, D., Coto, P. B., Chernick, E. T., Casillas, R., Basel, B. S., Thoss, M., Tykwinski, R. R. & Guldi, D. M. Singlet fission in pentacene dimers. *Proc. Natl. Acad. Sci.* **112,** 5325–5330 (2015).

31. Lukman, S., Musser, A. J., Chen, K., Athanasopoulos, S., Yong, C. K., Zeng, Z., Ye, Q., Chi, C., Hodgkiss, J. M., Wu, J., Friend, R. H. & Greenham, N. C. Tuneable Singlet Exciton Fission and Triplet-Triplet Annihilation in an Orthogonal Pentacene Dimer. *Adv. Funct. Mater.* **25,** 5452–5461 (2015).

32. Korovina, N. V., Das, S., Nett, Z., Feng, X., Joy, J., Haiges, R., Krylov, A. I., Bradforth, S. E. & Thompson, M. E. Singlet Fission in a Covalently Linked Cofacial Alkynyltetracene Dimer. *J. Am. Chem. Soc.* **138,** 617–627 (2016).

33. Sakuma, T., Sakai, H., Araki, Y., Mori, T., Wada, T., Tkachenko, N. V. & Hasobe, T. Long-Lived Triplet Excited States of Bent-Shaped Pentacene Dimers by Intramolecular Singlet

Fission. *J. Phys. Chem. A* **120,** 1867–1875 (2016).

34. Sanders, S. N., Kumarasamy, E., Pun, A. B., Steigerwald, M. L., Sfeir, M. Y. & Campos, L. M. Intramolecular Singlet Fission in Oligoacene Heterodimers. *Angew. Chemie Int. Ed.* **55,** 3373–3377 (2016).

35. Lukman, S., Chen, K., Hodgkiss, J. M., Turban, D. H. P., Hine, N. D. M., Dong, S., Wu, J., Greenham, N. C. & Musser, A. J. Tuning the role of charge-transfer states in intramolecular singlet exciton fission through side-group engineering. *Nat. Commun.* **7,** 13622 (2016).

36. Zirzlmeier, J., Casillas, R., Reddy, S. R., Coto, P. B., Lehnherr, D., Chernick, E. T., Papadopoulos, I., Thoss, M., Tykwinski, R. R. & Guldi, D. M. Solution-based intramolecular singlet fission in cross-conjugated pentacene dimers. *Nanoscale* **8,** 10113–10123 (2016).

37. Mukhopadhyay, T., Musser, A. J., Puttaraju, B., Dhar, J., Friend, R. H. & Patil, S. Is the Chemical Strategy for Imbuing 'Polyene' Character in Diketopyrrolopyrrole-Based Chromophores Sufficient for Singlet Fission? *J. Phys. Chem. Lett.* **8,** 984–991 (2017).

38. Walker, B. J., Musser, A. J., Beljonne, D. & Friend, R. H. Singlet exciton fission in solution. *Nat. Chem.* **5,** 1019–1024 (2013).

39. Stern, H. L., Musser, A. J., Gelinas, S., Parkinson, P., Herz, L. M., Bruzek, M. J., Anthony, J., Friend, R. H. & Walker, B. J. Identification of a triplet pair intermediate in singlet exciton fission in solution. *Proc. Natl. Acad. Sci.* **112,** 7656–7661 (2015).

40. Smith, M. B. & Michl, J. Recent Advances in Singlet Fission. *Annu. Rev. Phys. Chem.* **64,** 361–386 (2013).

41. Alguire, E. C., Subotnik, J. E. & Damrauer, N. H. Exploring Non-Condon Effects in a Covalent Tetracene Dimer: How Important Are Vibrations in Determining the Electronic

Coupling for Singlet Fission? *J. Phys. Chem. A* **119,** 299–311 (2015).

42. Damrauer, N. H. & Snyder, J. L. Symmetry-Directed Control of Electronic Coupling for Singlet Fission in Covalent Bis–Acene Dimers. *J. Phys. Chem. Lett.* **6,** 4456–4462 (2015).
43. Grumstrup, E., Johnson, J. & Damrauer, N. Enhanced Triplet Formation in Polycrystalline Tetracene Films by Femtosecond Optical-Pulse Shaping. *Phys. Rev. Lett.* **105,** 257403 1-4 (2010).
44. Johnson, J. C., Nozik, A. J. & Michl, J. The Role of Chromophore Coupling in Singlet Fission. *Acc. Chem. Res.* **46,** 1290–1299 (2013).
45. Scholes, G. D., Ghiggino, K. P., Oliver, A. M. & Paddon-Row, M. N. Through-space and through-bond effects on exciton interactions in rigidly linked dinaphthyl molecules. *J. Am. Chem. Soc.* **115,** 4345–4349 (1993).
46. Vallett, P. J., Snyder, J. L. & Damrauer, N. H. Tunable electronic coupling and driving force in structurally well-defined tetracene dimers for molecular singlet fission: a computational exploration using density functional theory. *J. Phys. Chem. A* **117,** 10824–38 (2013).
47. Carey, T. J., Snyder, J. L., Miller, E. G., Sammakia, T. & Damrauer, N. H. Synthesis of Geometrically Well-Defined Covalent Acene Dimers for Mechanistic Exploration of Singlet Fission. *J. Org. Chem.* acs.joc.7b00602 (2017).
48. Snyder, J. L. A Symmetry Exploration into Covalent Tetracene Dimers with Tunable Electronic Coupling for Singlet Fission. (University of Colorado, Boulder, 2015).
49. Platt, J. R. Classification of Spectra of Cata-Condensed Hydrocarbons. *J. Chem. Phys.* **17,** 484 (1949).
50. Gouterman, M. Spectra of porphyrins. *J. Mol. Spectrosc.* **6,** 138–163 (1961).
51. Frisch, M. J. *et al.* Gaussian 09, Revision A.1. (2009).

52. Davydov, A. S. The Theory of Molecular Excitons. *Sov. Phys. Uspekhi* **7,** 145–178 (1964).

53. Spano, F. C. The Spectral Signatures of Frenkel Polarons in H- and J-Aggregates. *Acc. Chem. Res.* **43,** 429–439 (2010).

54. Lakowicz, J. R. *Principles of Fluorescence Spectroscopy*. (Springer US, 2006).

55. Lim, S.-H., Bjorklund, T., Spano, F. & Bardeen, C. J. Exciton Delocalization and Superradiance in Tetracene Thin Films and Nanoaggregates. *Phys. Rev. Lett.* **92,** 107402 (2004).

56. Burgdorff, C., Ehrhardt, S. & Loehmannsroeben, H. G. Photophyslcal Properties of Tetracene Derivatives in Solution. 2. Halogenated Tetracene Derivatives. *J. Phys. Chem.* **95,** 4246–4249 (1991).

57. Fletcher, A. N. & Bliss, D. E. Laser dye stability. Part 5. *Appl. Phys.* **16,** 289–295 (1978).

58. Veldman, D., Chopin, S. M. A., Meskers, S. C. J., Groeneveld, M. M., Williams, R. M. & Janssen, R. A. J. Triplet Formation Involving a Polar Transition State in a Well-Defined Intramolecular Perylenediimide Dimeric Aggregate. *J. Phys. Chem. A* **112,** 5846–5857 (2008).

59. Pavlopoulos, T. G. Measurement of the Triplet-Triplet Absorption Spectrum of Tetracene Using cw Argon Laser Excitation. *J. Chem. Phys.* **56,** 227 (1972).

60. Birks, J. B. *Photophysics of Aromatic Molecules*. (Wiley-Interscience, 1970).

61. Meylemans, H. A., Lei, C.-F. & Damrauer, N. H. Ligand Structure, Conformational Dynamics, and Excited-State Electron Delocalization for Control of Photoinduced Electron Transfer Rates in Synthetic Donor-Bridge-Acceptor Systems. *Inorg. Chem.* **47,** 4060–4076 (2008).

62. Meylemans, H. A. & Damrauer, N. H. Controlling Electron Transfer through the

Manipulation of Structure and Ligand-Based Torsional Motions: A Computational Exploration of Ruthenium Donor−Acceptor Systems using Density Functional Theory. *Inorg. Chem.* **48,** 11161–11175 (2009).

63. Meylemans, H. A., Hewitt, J. T., Abdelhaq, M., Vallett, P. J. & Damrauer, N. H. Exploiting Conformational Dynamics To Facilitate Formation and Trapping of Electron-Transfer Photoproducts in Metal Complexes. *J. Am. Chem. Soc.* **132,** 11464–11466 (2010).

64. Burdett, J. J. & Bardeen, C. J. The Dynamics of Singlet Fission in Crystalline Tetracene and Covalent Analogs. *Acc. Chem. Res.* **46,** 1312–1320 (2013).

65. Wilson, M. W. B., Rao, A., Johnson, K., Gélinas, S., di Pietro, R., Clark, J. & Friend, R. H. Temperature-Independent Singlet Exciton Fission in Tetracene. *J. Am. Chem. Soc.* **135,** 16680–16688 (2013).

66. Yost, S. R., Lee, J., Wilson, M. W. B., Wu, T., McMahon, D. P., Parkhurst, R. R., Thompson, N. J., Congreve, D. N., Rao, A., Johnson, K., Sfeir, M. Y., Bawendi, M. G., Swager, T. M., Friend, R. H., Baldo, M. a. & Van Voorhis, T. A transferable model for singlet-fission kinetics. *Nat. Chem.* **6,** 492–497 (2014).

Chapter 4. Photophysics of the TIPS-BT1 Covalent Dimer

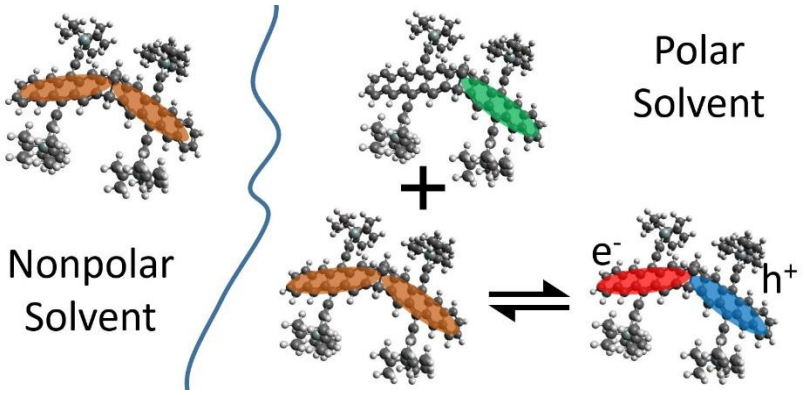

4.1 TIPS-BT1: Updating the BT1 Framework

Given our understanding of the BT1 parent dimer established in the previous chapter, and with the same goal of understanding singlet fission (SF) through its fundamental subunit of a dimer, we move to TIPS-BT1, shown below in Figure 4.1. TIPS-BT1 is a modification to BT1 in which four acetylene-linked triisopropylsilyl (TIPS) groups are added (two on each arm) in place of four corresponding hydrogens in BT1. This is accomplished by alkynylating with a Grignard reagent instead of reduction with a hydride source (see Chapter 3). As with BT1, this synthetic work was carried out by fellow group member Thomas Carey.[1] One could also imagine additional modifications to this framework, such as a pentacene (Pc) derived TIPS dimer.

The monomer bis(triisopropylsilylethynyl)tetracene (TIPS-Tc, shown in Figure 4.1) was studied alongside TIPS-BT1. Monomers that more closely resemble TIPS-acetylene analogues to Tc-e have been synthesized, but the quantities made were insufficient to perform all experiments described herein, and preliminary findings are instead provided in Appendix B. Those molecules, referred to as TIPS-Tc-es and TIPS-Tc-eu, are linear, norbornyl-fused TIPS-Tc molecules whose terminal norbornanes are saturated or unsaturated, respectively (where the latter is the closest analogue to Tc-e). As was the case when comparing Tc-e to Tc (see Chapter 3), the norbornyl

bridge appears to cause small perturbations to the energetics of the molecule while retaining the fundamental photophysics of the TIPS-Tc monomer (such as single-exponential emission decays of similar lifetime to TIPS-Tc and no evidence of splitting in the absorbance; discussed in this chapter for TIPS-Tc and in Appendix B for TIPS-Tc-es and TIPS-Tc-eu).

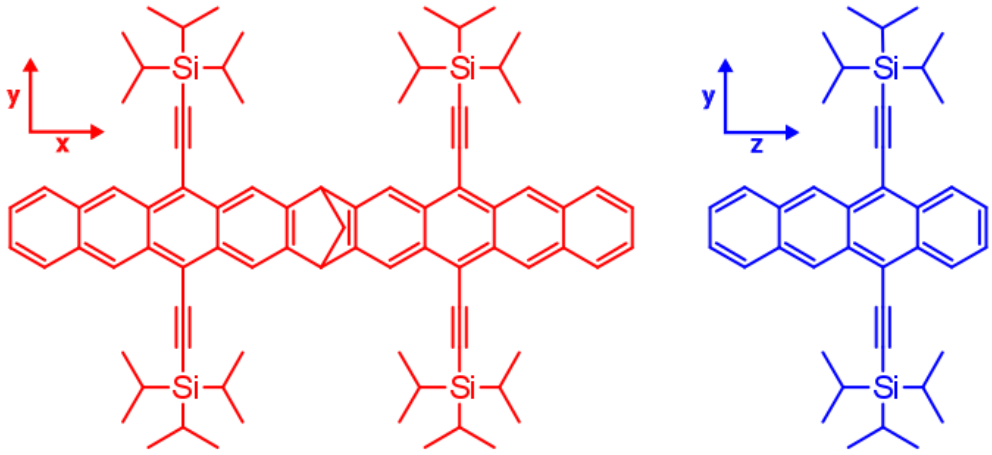

Figure 4.1. Stick structures of the TIPS-BT1 dimer (red) and its monomer counterpart TIPS-Tc (blue). Axes used for subsequent symmetry discussions are given beside the corresponding molecule. In TIPS-BT1 (C_{2v} point group), the principal C_2 axis (z-axis) points directly upwards through the center of the molecule, the y-axis lies parallel to the short axis of the chromophore arms, and the x-axis points from one arm to the other. In TIPS-Tc (also C_{2v}), the principal C_2 axis (z-axis) is the long axis of the tetracene parent, and the y-axis is again parallel to the short axis of the chromophore.

Logistically, the addition of TIPS-acetylene groups to the BT1 backbone facilitates the photophysical studies described in this chapter. Specifically, this modification provides improved resistance to oxidation (primarily due to the acetylene linkers)[2] and improved solubility (due to the triisopropylsilyl groups) over BT1, allowing for studies in polar solvents. As a result, the experiments described in this chapter have been significantly expanded upon relative to those on BT1 and include a set of two solvents (toluene and benzonitrile), electrochemical behavior, and more in-depth photophysical measurements like transient absorption (TA).

4.2 Steady-State Electronic Absorption and Photoluminescence

4.2.1 Instrumentation and Sample Preparation

Steady-state electronic absorption measurements were performed using an Agilent Cary 5000 UV-Vis-NIR absorbance spectrophotometer operating in dual-beam mode. Steady-state photoluminescence measurements were performed on an Olis SLM 8000 spectrophotometer. High-purity solvents were purchased from Burdick & Jackson (toluene) or Sigma-Aldrich (chloroform and benzonitrile) and used as received. Dilute (~5 μM) samples for fluorescence spectroscopy were prepared in 1-cm quartz cuvettes (equipped with Kontes HI-VAC® vacuum-valves) and bubble-degassed with argon for 30 minutes prior to sealing. Sample integrity was verified before and after photoluminescence experiments via steady-state absorption spectroscopy.

4.2.2 Computational Details

All orbitals, state energies, and nuclear coordinates in this chapter, unless otherwise noted, were obtained from density functional theory (DFT) or time-dependent DFT (TD-DFT) as specified. Calculations were done in the Gaussian 09 software package[3] by Niels Damrauer using the range-corrected ω-B97XD density functional, 6-31g(d) basis set, and toluene polarizable continuum model. This maintains consistency with the calculations for BT1[4] referenced in Chapter 3. Nuclear coordinates for TIPS-Tc and TIPS-BT1 are provided in Appendix B.

4.2.3 Electronic Absorption in Chloroform

Electronic absorption spectra of TIPS-Tc and TIPS-BT1 in chloroform are shown in Figure 4.2, and peak molar attenuation coefficient values for the first three electronic transitions are summarized in Table 4.1. Chloroform was used in order to preserve information in the ultraviolet (UV), as was done for BT1 and Tc-e in the previous chapter. Similar to those molecules (and Tc[5]), TIPS-Tc has two sets of prominent absorption features—one in the visible (peaked at

535 nm with a strong 1370 cm^{-1} vibronic progression) and a second in the ultraviolet (peaked at 292 nm)—with a third weak progression in the middle of the spectrum (peaked at 418 nm).

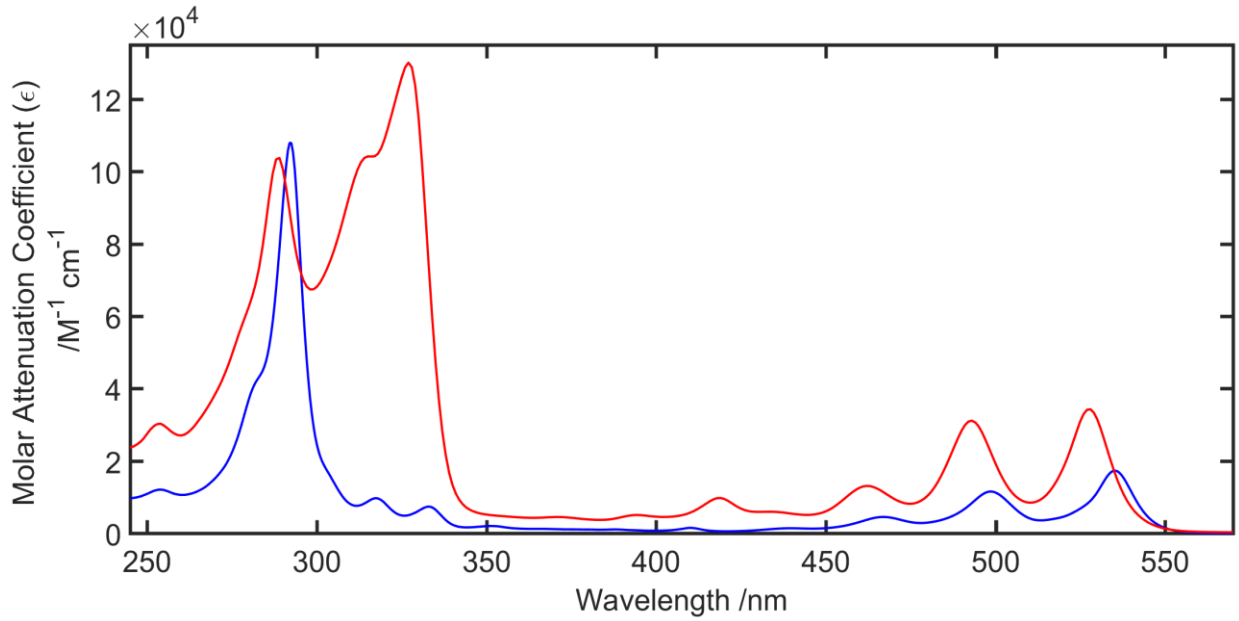

Figure 4.2. Electronic absorption spectra of TIPS-Tc (blue) and TIPS-BT1 (red) in $CHCl_3$, showing features in the UV region.

Table 4.1. Peak molar attenuation coefficients for TIPS-Tc and TIPS-BT1 in chloroform solution

Transition	Peak ε (TIPS-Tc) /$M^{-1}cm^{-1}$	Peak ε (TIPS-BT1) /$M^{-1}cm^{-1}$
$S_1 \leftarrow S_0$	17,300 @ 535 nm	34,200 @ 528 nm
$S_2 \leftarrow S_0$	1,500 @ 410 nm	9,700 @ 419 nm
$S_3 \leftarrow S_0$	108,000 @ 292 nm	S_{3a}: 130,000 @ 327 nm S_{3b}: 104,000 @ 289 nm

As was the case for Tc-e, these observed transitions are well described using a basis set of only four frontier orbitals (shown in Figure 4.3). Here, the relevant orbitals consist of the highest

occupied molecular orbital (HOMO), lowest unoccupied molecular orbital (LUMO), HOMO–2, and LUMO+2. Also shown are the HOMO–1 and LUMO+1. All of these orbitals were calculated following geometry optimization of TIPS-Tc via DFT. For computational expediency, each of the isopropyl constituents on the TIPS groups was replaced with a hydrogen atom in these calculations. This is expected to have very little effect on the results, given that others have found minimal frontier orbital character derived from the alkyl substituents in TIPS-substituted acenes.[6–11] Transition dipole moments were calculated in an identical manner to that described for Tc-e in Chapter 3.

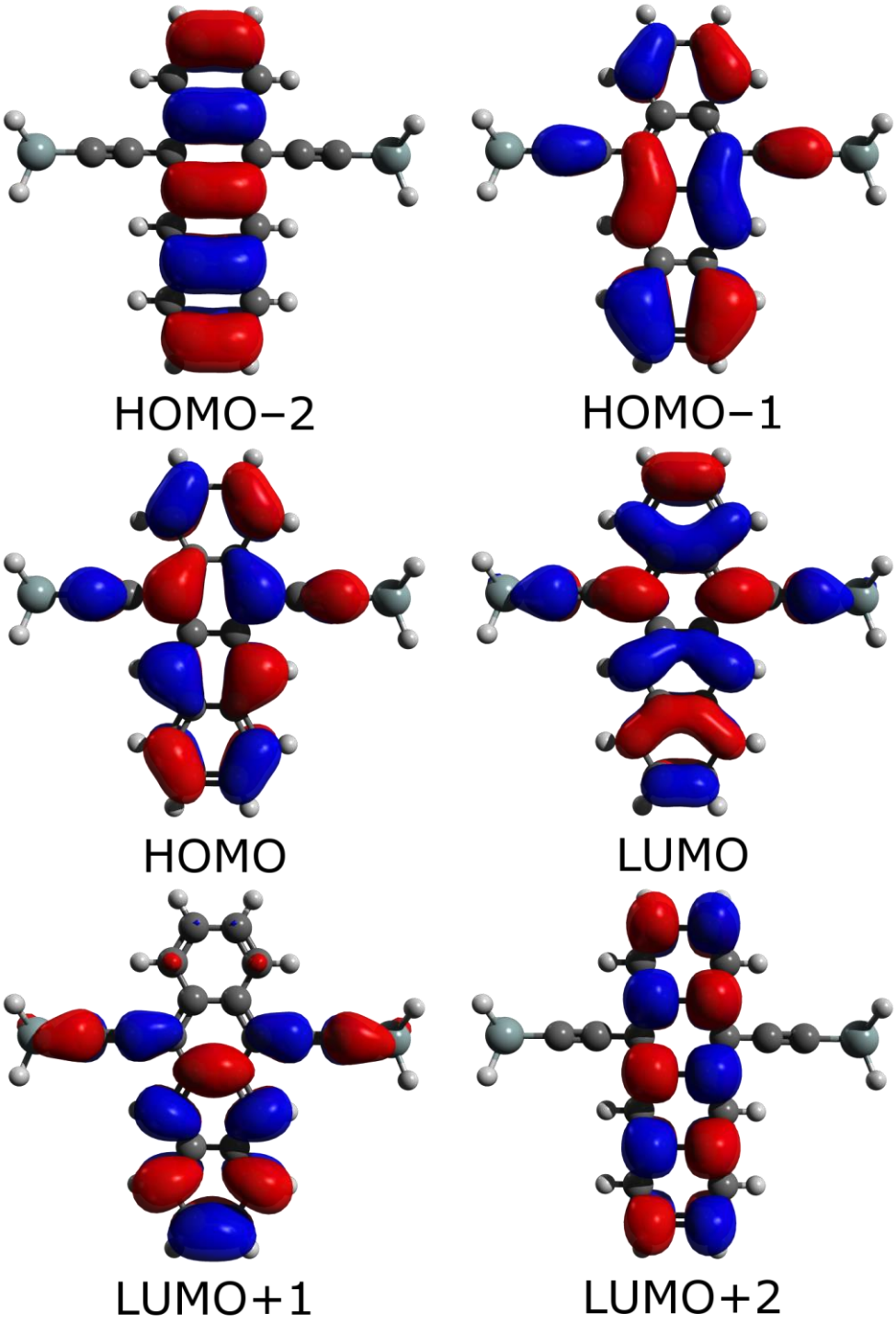

Figure 4.3. Frontier orbitals of TIPS-Tc obtained following geometry optimization with DFT. Isopropyl constituents of the TIPS groups have been replaced with hydrogen atoms for computational expediency.

As in Tc and Tc-e, the TIPS-Tc visible $S_1 \leftarrow S_0$ vibronic progression (peaks between 450–550 nm) is expected to have primarily HOMO → LUMO character. Calculation of the transition dipole between these orbitals finds an allowed, short-axis (with regards to the acene parent) transition, just as with Tc-e. This is consistent with the symmetry of the TIPS-Tc HOMO and LUMO orbitals (A_2 and B_1 in the C_{2v} point group of TIPS-Tc, respectively). There is a substantial red-shift to this feature in TIPS-Tc relative to Tc, however, with the $S_1 \leftarrow S_0$ onset moving from 470 nm in tetracene[5] (Tc) to 535 nm in TIPS-Tc. Though some computational work[8] suggests that this effect arises due to lowering of the LUMO in the TIPS-substituted molecules (with effectively no change to the HOMO), combined theoretical and experimental work[6] on adiabatic ionization energies of TIPS-acenes instead suggests that the change in optical gap is equally attributable to an increase in the energy of the HOMO. By this shrinking of the HOMO–LUMO gap, the $S_1 \leftarrow S_0$ transition is red-shifted by around 300 meV in TIPS-Tc relative to Tc.

The higher energy TIPS-Tc electronic transitions (the weak $S_2 \leftarrow S_0$ at 410 nm and the strong $S_3 \leftarrow S_0$ at 292 nm) again result from out-of-phase and in-phase combinations (respectively) of staggered frontier orbital transitions, in this case the HOMO–2 → LUMO and HOMO → LUMO+2. As in Tc-e, these transitions are near-degenerate and strong, but their orbital origins differ from those in Tc-e. In that system, the transition dipole moments for $S_2 \leftarrow S_0$ and $S_3 \leftarrow S_0$ result from out-of-phase and in-phase combinations of the HOMO–1 → LUMO and HOMO → LUMO+1 (respectively) that are similarly long-axis, strong, and of nearly equal magnitude. The HOMO–1 → LUMO and HOMO → LUMO+1 transitions in TIPS-Tc are instead short-axis, weak, and have magnitudes differing by a factor of ~2 from one another. This difference can be understood by inspection of the character of the TIPS-Tc frontier orbitals in the C_{2v} point group of the molecule. The TIPS-Tc HOMO–1 and LUMO+1 have symmetries (A_2 and B_1, respectively)

that do not match the LUMO and HOMO orbitals (B_1 and A_2, respectively), such that the HOMO–1 → LUMO and HOMO → LUMO+1 transitions lie along y and are short-axis polarized. Meanwhile, the TIPS-Tc HOMO–2 and LUMO+2 orbitals share obvious visual similarity with their HOMO–1 and LUMO+1 counterparts in Tc-e (shown in Chapter 3). The TIPS-Tc HOMO–2 and LUMO also share symmetry character (both are B_1), as do the TIPS-Tc LUMO+2 and HOMO (both are A_2). This is analogous to the shared symmetry between the Tc-e HOMO–1 and LUMO (both A' in the C_s point group of Tc-e) and between the Tc-e HOMO and LUMO+1 (both A"). This shared symmetry causes the aforementioned transitions to be long-axis (z) in nature. Furthermore, their near-degeneracy with their staggered counterparts (e.g. HOMO–2 → LUMO and HOMO → LUMO+2 in TIPS-Tc) explains the relative strengths of the observed $S_2 \leftarrow S_0$ and $S_3 \leftarrow S_0$ transitions in their respective molecules, with the out-of-phase and in-phase combinations responsible for creating a weak $S_2 \leftarrow S_0$ and a strong $S_3 \leftarrow S_0$ (respectively). Calculated transition dipole moments for all of the transitions discussed are summarized in Table 4.2.

Table 4.2. Calculated transition dipole moments for the observed singlet transitions in TIPS-Tc

Electronic Transition	Transition Name (Platt)	Orbital Origins	Transition Dipole /eÅ	Polarization Axis (Acene)
$S_1 \leftarrow S_0$	^1L_a	HOMO → LUMO	2.41	Short
None	None	HOMO–1 → LUMO	0.77	Short
None	None	HOMO → LUMO+1	0.35	Short
None	None	HOMO–2 → LUMO	2.82	Long
None	None	HOMO → LUMO+2	2.80	Long
$S_2 \leftarrow S_0$	^1L_b	(HOMO–2 → LUMO) – (HOMO → LUMO+2)	0.02	Long
$S_3 \leftarrow S_0$	B	(HOMO–2 → LUMO) + (HOMO → LUMO+2)	5.62	Long

It is important to note that the energy of the HOMO–2 is close to that of the HOMO–1, and the energy of the LUMO+2 is likewise close to the LUMO+1, while the energies of the next closest frontier orbitals (the HOMO–3 and LUMO+3) are significantly different from the orbitals involved here. The energies of these TIPS-Tc orbitals (as calculated via DFT) are shown in Figure 4.4 at left. It is therefore reasonable to expect that the $S_2 \leftarrow S_0$ and $S_3 \leftarrow S_0$ have orbital origins significantly drawn from the HOMO–2 and LUMO+2 orbitals, but that contributions from the next nearest orbitals (the HOMO–3 and LUMO+3) are negligible as the resulting orbital-to-orbital gaps become too large. The energies of these TIPS-Tc orbitals (as calculated via DFT) are shown in Figure 4.4. We now turn to simulated transitions, calculated from the results of time-dependent DFT (TD-DFT) for comparison with the simple vector model described above.

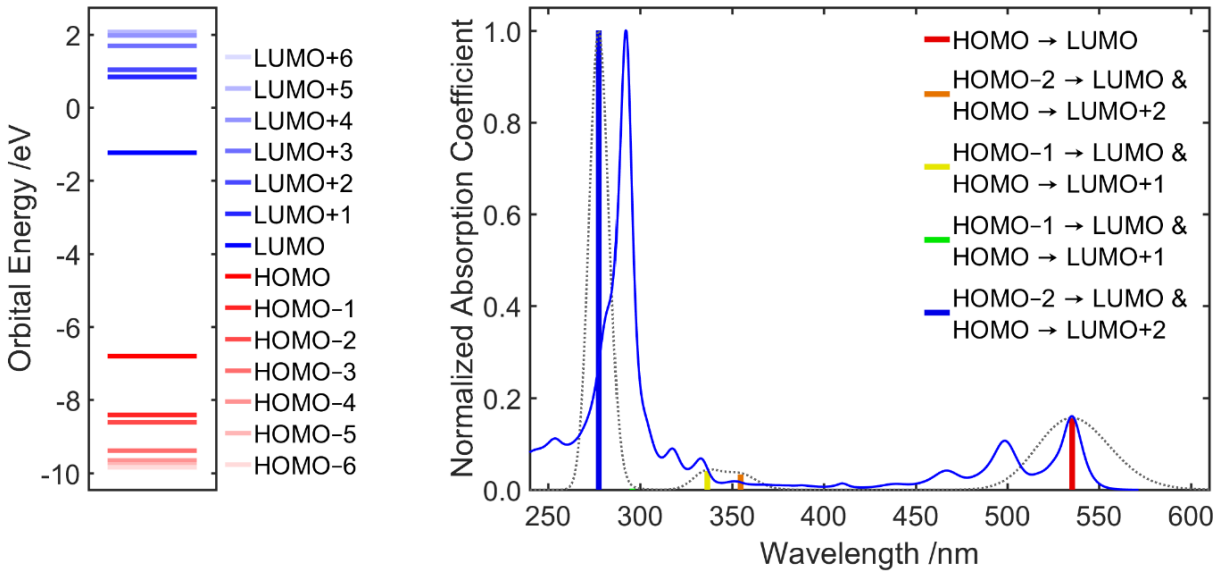

Figure 4.4. Electronic structure of TIPS-Tc. Left: frontier orbital energies of TIPS-Tc calculated via DFT, with filled orbitals in red and unfilled orbitals in blue. Right: electronic absorption spectra obtained from experiment (blue line) and calculated from TD-DFT results (grey dotted line), with individual transitions shown as color-coded vertical lines (with TD-DFT orbital origins shown in legend).

The simulated electronic absorption spectrum of TIPS-Tc in toluene, overlaid with the experimental electronic absorption spectrum in chloroform (again chosen so that the UV $S_3 \leftarrow S_0$ feature could be observed), is shown in Figure 4.4 at right. The simulated spectrum uses the first 5 transitions for TIPS-Tc calculated with TD-DFT. Transitions are shown as vertical lines and color-coded according to their TD-DFT orbital origins (listed in the legend at right). The methodology used to compute this spectrum is described in Chapter 3; it again consists of conversion from computed oscillator strength f to molar attenuation coefficient ε, incorporating a red-shift to the computed transitions of 0.155 eV (in order to align the $S_1 \leftarrow S_0$ transitions of the experimental and TD-DFT results) and a line full-width at half-maximum of 0.2 eV.

The TD-DFT simulated spectrum is in reasonable agreement with the simple DFT transition-dipole arguments presented above, with the TD-DFT $S_1 \leftarrow S_0$ transition (the red line at 535 nm) having HOMO → LUMO character and the strong $S_3 \leftarrow S_0$ (the blue line at 278 nm) having HOMO–2 → LUMO and HOMO → LUMO+2 character. It is unclear if the TD-DFT transitions near 350 nm are associated with the experimental peaks near 418 nm or near 325 nm. The redder of the TD-DFT peaks has HOMO–2 → LUMO and HOMO → LUMO+2 character (the orange line at 355 nm) while the higher-energy (yellow) line at 337 nm is derived from the HOMO–1 → LUMO and HOMO → LUMO+1 transitions. There is also a very small transition with HOMO–1 → LUMO and HOMO → LUMO+1 character (the green line at 296 nm) that may instead be responsible for the small set of peaks at the red edge of the $S_3 \leftarrow S_0$ feature.

The overall behavior of the electronic absorption of TIPS-Tc is once again related to that of porphyrins, where one band is strongly allowed at the expense of another.[12] Using Platt's polarization diagrams,[13] the observed transitions would be categorized as follows: the $S_1 \leftarrow S_0$ is

^1L_a (with nodes bisecting the bonds), the weak $S_2 \leftarrow S_0$ is ^1L_b (with nodes on the atoms), and the strong $S_3 \leftarrow S_0$ is B. These assignments are identical to those in Tc-e.

In the electronic absorption of the TIPS-BT1 dimer (Figure 4.2), the behavior is broadly similar to that in TIPS-Tc (including a strong 1340 cm^{-1} progression in the visible) excepting three immediately obvious differences: a general blue-shift in the visible region of the spectrum, a near-doubling of the molar attenuation coefficient in the $S_1 \leftarrow S_0$ region, and the emergence of a split feature in the UV (250–350 nm). The blue-shift in the $S_1 \leftarrow S_0$ region of TIPS-BT1 relative that in TIPS-Tc contrasts with observations for BT1 relative to Tc-e,[14] where there was instead a red-shift in the dimer. This difference is due the presence of a norbornyl bridge in TIPS-BT1 which is missing from TIPS-Tc. When coupled linearly to the acene parent, the norbornyl group destabilizes the S_1 through electron donation.[4] Accordingly, the $S_1 \leftarrow S_0$ transition in TIPS-BT1 is blue-shifted relative to that in TIPS-Tc, where the norbornyl group is not present. As expected, this blue-shift is found in TIPS-Tc-eu and TIPS-Tc-es relative to TIPS-Tc (see Appendix B). The approximately doubled molar attenuation coefficient in the $S_1 \leftarrow S_0$ region of TIPS-BT1 (34,200 $M^{-1}cm^{-1}$ at the peak of the 0–0 transition) relative to that in TIPS-Tc (17,300 $M^{-1}cm^{-1}$) is consistent with two weakly-coupled absorbing chromophore arms,[15] and has been observed by others.[16–21] The assignment of weak coupling is based on a 0–0 to 0–1 absorption ratio that is very similar to that of the monomer. The small amount of 0–0 peak suppression evident in TIPS-BT1 is a consequence of H-aggregate excitonic coupling between the short-axis $S_1 \leftarrow S_0$ transitions on the TIPS-Tc arms, with its extent determined by coupling strength (which, in the strong coupling limit, would lead to a completely suppressed 0–0 transition).[15] It is additionally evident that coupling in TIPS-BT1 is slightly weaker than in BT1 (for which the 0–0 peak was more suppressed relative to the 0–1 peak; refer to Chapter 3). By contrast, Lukman et al. observed a decrease in ε for a series of Pc dimers

that they attributed to strong J-aggregate type dipole-dipole coupling (and in which the 0–0 transition was enhanced).[10,22]

That the $S_1 \leftarrow S_0$ transition is alone in TIPS-BT1 (not accompanied by a second Davydov-split transition) may also be thought of in the context of interacting TIPS-Tc monomer transitions from Table 4.2 (as was done for BT1 with transitions from Tc-e). The $S_1 \leftarrow S_0$ transitions on each arm of TIPS-BT1 should interact as H-aggregates, and accordingly have one active transition (the higher-energy, in-phase combination) with doubled intensity and one inactive transition (the lower-energy, out-of-phase combination). As with BT1 (and the BN1 series[23]), a Davydov-split $S_3 \leftarrow S_0$ feature is observed in the UV absorption of TIPS-BT1. This splitting between these transitions is nearly identical here to its value in BT1 (both are ~500 meV). This is again understood through considering interacting long-axis monomer transitions at an angle of 112.7° (measured, as for BT1[4], between three carbon atoms in the DFT-optimized ground state geometry: one at the end of each chromophore with the third being the bridgehead carbon). This gives two transitions whose relative intensity is predicted to be 2.0:1 (as compared to the 1.3:1 ratio of peak heights observed in the electronic absorption spectrum), with the more intense lower-energy transition polarized along x and the less intense higher-energy transition polarized along z. Each of these Davydov-split peaks has intensity comparable to that of the $S_3 \leftarrow S_0$ feature in the monomer. These results for TIPS-BT1 are summarized in Table 4.3.

Table 4.3. Calculated transition dipole moments for the first and third singlet transitions in TIPS-BT1 based on calculated transitions in TIPS-Tc

Electronic Transition	Monomer Origins	Transition Dipole /eÅ	Polarization Axis
$S_{1a} \leftarrow S_0$	S_1(TIPS-Tc) – S_1(TIPS-Tc)	0	None
$S_{1b} \leftarrow S_0$	S_1(TIPS-Tc) + S_1(TIPS-Tc)	4.82	y
$S_{3a} \leftarrow S_0$	S_3(TIPS-Tc) + S_3(TIPS-Tc)	9.36	x
$S_{3b} \leftarrow S_0$	S_3(TIPS-Tc) – S_3(TIPS-Tc)	6.23	z

As a final comment on the basic electronics of TIPS-BT1, it is noted that its ground state molecular structure should have C_{2v} symmetry, just as BT1 did[4] (see Appendix B for the DFT-optimized ground state geometry of TIPS-BT1). Meanwhile, the relevant TIPS-Tc monomer orbitals (HOMO and LUMO) carry the same behavior upon σ_{xz} reflection as those from Tc-e, and their linkage (end-to-end) in the dimer remains the same. Thus, as was the case in BT1, the diabatic electronic couplings between the dimer (AB) singlet excitonic states (S_0S_1/S_1S_0) and the multiexcitonic SF product (^{1}TT) should be zero by symmetry. There is still expected to be some coupling enabled through symmetry-breaking vibrations,[24] but fast SF is not to be expected.

4.2.4 Solvent-Dependent Changes in Absorption and Photoluminescence

The solvents toluene and benzonitrile were chosen to give representative nonpolar and polar environments, respectively. The preliminary solvent-dependent steady-state findings discussed here will inform discussions that follow on more complex behavior. Figure 4.5 shows the solvent dependent changes observed in the steady-state electronic spectra (absorption and emission) of TIPS-Tc and TIPS-BT1. The TIPS-Tc monomer is shown in blue, while the TIPS-BT1 dimer is shown in red.

As was the case in the chloroform electronic absorbance, the toluene electronic absorbance shows a blue-shift in moving from the TIPS-Tc monomer (S_1 onset at 535 nm) to the norbornyl-

bridged TIPS-BT1 dimer (S_1 onset at 528 nm) due to electronic destabilization from the bridge.[4] Both samples experience noticeable absorption solvatochromism in the form of a bathochromic shift (red-shift) when moving from toluene to the more polar benzonitrile (535 nm in the monomer becomes 539 nm, and 528 nm in the dimer becomes 532 nm). This observation suggests that there is some charge-transfer character to the S_1 state[25]. This effect is unlikely to be caused by polarizability effects, as toluene and benzonitrile have similar polarizabilities.[26] Excepting this solvatochromism, little changes in the structure of the electronic absorption of either molecule when switching between toluene and benzonitrile.

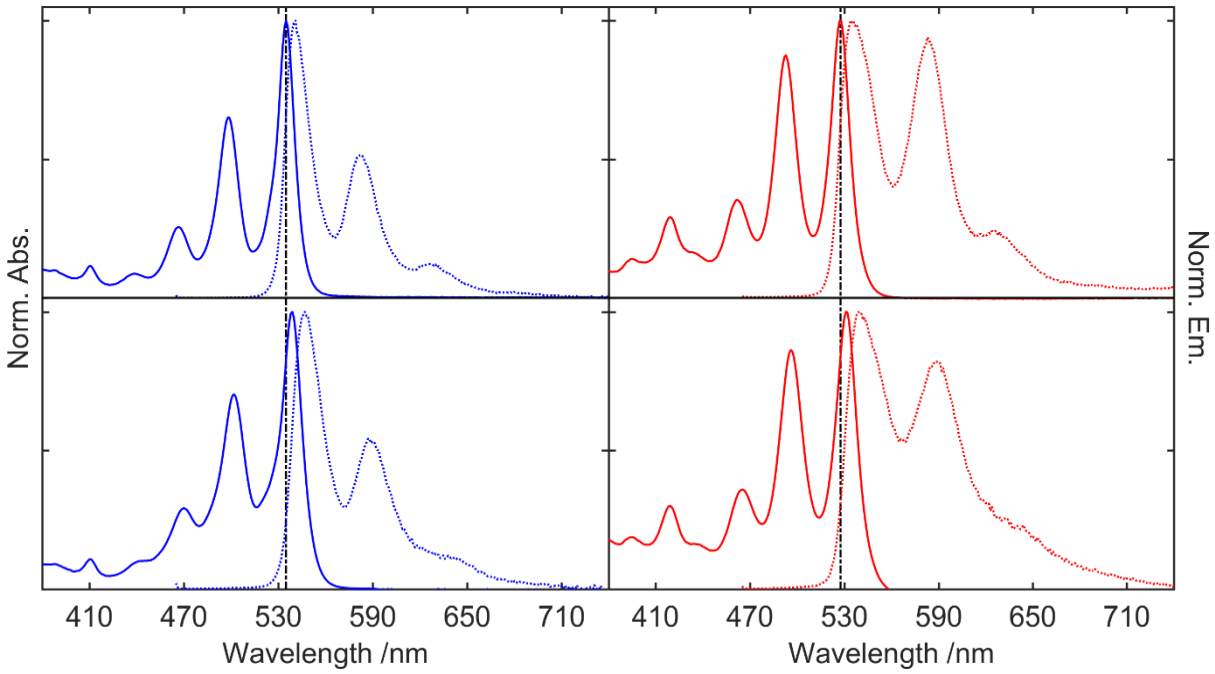

Figure 4.5. Electronic absorption spectra (solid lines) and emission spectra (dashed lines) of TIPS-Tc (blue) and TIPS-BT1 (red) in toluene (top) and benzonitrile (bottom). Vertical dashed lines (black) highlight the S_1 absorption onsets in toluene, showing slight solvatochromism.

In the emission, a bathochromic shift is again evident in both molecules with increased solvent polarity, again indicating differential stabilization between the ground and excited state.

Specifically, the emissive state appears to have some degree of charge-separation (being stabilized by the polar benzonitrile) in both the monomer and the dimer. This is consistent with the current understanding of the S_1 state in polyacenes, which has been described as having "hidden" charge-transfer character.[27] Thus the monomer emission maximum of 541 nm in toluene red-shifts to 547 nm in benzonitrile, while the dimer maximum similarly red-shifts from 535 nm to 540 nm. In both solvents, TIPS-Tc appears to emit from the state accessed during the Franck–Condon absorption event, as does TIPS-BT1 in toluene, with the emission having strong mirror symmetry in those cases. There are however noticeable structural changes in the emission spectrum of the dimer moving to benzonitrile; the reasons for this are explained in subsequent time-resolved measurements. For the moment, it is noted that there is a substantial solvent-dependence on the relative amplitudes of the 0–0 and 0–1 emission peaks for TIPS-BT1. In TIPS-Tc, these emission peaks have a ratio of 1:0.52 in toluene that is approximately preserved (1:0.55) in benzonitrile. In the dimer this ratio is 1:0.94 in toluene and becomes 1:0.82 in benzonitrile. The dimer additionally loses some of its defined structure (e.g. the clearly distinguishable 0–2 peak) and its spectrum broadens overall. Subsequent time-resolved measurements indicate that this behavior is due to the creation of multiple emissive species with distinct spectra (*vide infra*).

Photoluminescence quantum yields (Φ_{em}) were measured for these molecules using coumarin 153/540A (Φ_{em} = 0.45) in methanol as a reference.[28] In toluene, Φ_{em} is nearly the same for TIPS-Tc and TIPS-BT1: 0.74 ± 0.08 for the monomer and 0.72 ± 0.09 for the dimer (determined from four independent measurements for each molecule). When changing solvents to benzonitrile, the emission of TIPS-Tc is increased to 0.90 ± 0.02, while TIPS-BT1 has a significantly lower emission quantum yield in benzonitrile of 0.52 ± 0.04. The decrease in TIPS-BT1 photoluminescence instead suggests the enhancement of existing non-radiative loss pathways, or

the introduction of new ones. Given the polar nature of benzonitrile, it is reasonable to posit the emergence of an intramolecular charge transfer (CT) state as the underlying cause for this change, however this state does not appear to be accessed by vertical excitation in absorbance given the absence of any new CT bands in the absorption spectrum of TIPS-BT1 in benzonitrile. The existence of a CT state gives a competitive relaxation pathway from the initially excited Franck–Condon state. Such a CT state should have a different emission spectrum and a different (typically much lower, given ordinarily weak oscillator strengths[29]) photoluminescence yield vs. the Franck–Condon accessible S_1. There is literature precedent for multiple dimeric systems[10,19,21,30] that shows increasing solvent polarity induces substantial changes to observed photophysics; in those systems, the authors implicate a CT state. Subsequent time-resolved experiments indeed identify such a state (*vide infra*).

It is worthwhile at this juncture to comment on the SF-relevant state energies for TIPS-BT1 in toluene and benzonitrile. In TIPS-Tc, one experimental study suggests T_1 lies near 1.25 eV (assigned from a broad emission feature in a polymer matrix)[31]; this may be taken as a first-order estimate of the T_1 energy in TIPS-BT1. Separate DFT results in our group place the TIPS-BT1 T_1 energy at 1.1 eV (relaxed T_1 nuclear coordinates available in Appendix B). With the aforementioned values, the energy difference for SF ($\Delta E_{SF} = 2 \times E(T_1) - E(S_1)$) may be as favorable as –130 meV or as unfavorable as +170 meV in toluene (where $E(S_1)$ is derived from the 2.33 eV mean of the 0–0 absorption and emission energies). In benzonitrile, where S_1 lies near 2.31 eV (using the same 0–0 absorption and emission average), ΔE_{SF} should lie between –110 and +190 meV (if the triplet energy is not solvent dependent) or between –150 and +150 meV (if the triplet energy is solvent dependent and experiences the same 20 meV red-shift as the singlet). This range is large, but not dissimilar to the ΔE_{SF} often discussed for Tc (~100 meV).[32–34]

4.3 Time-Resolved Photoluminescence at Ambient Temperature

4.3.1 Methods

Time-resolved photoluminescence (TRPL) measurements were performed by exciting samples with the output of a Fianium SC400-2-PP supercontinuum tunable fiber laser (with wavelength selection accomplished using an acousto-optic tunable filter) and detected with a Hamamatsu ORCA-R2 C10600 visible streak camera. High-purity solvents were purchased from Burdick & Jackson (toluene) or Sigma-Aldrich (benzonitrile) and used as received. Dilute (~5 μM) samples were prepared in 1-cm quartz cuvettes (equipped with Kontes HI-VAC® vacuum-valves) and bubble-degassed with argon for 30 minutes prior to sealing. Sample integrity was verified before and after data acquisition via steady-state absorption spectroscopy. Global fitting was performed in MATLAB using a fitting algorithm written by our group to a sum of exponentially modified Gaussians (obtained by convolving a sum of exponential decays with a Gaussian function) for which the Gaussian standard deviation was ~0.7–1.3 ns, depending on time window. Spectral slices with corresponding fits are shown in Appendix B for all data sets. All basis spectra shown are decay associated spectra[35] (DAS); these are expected to represent the true species associated spectra (SAS) unless otherwise noted, and all amplitude information is contained in the spectra (that is, all corresponding species kinetics are normalized). These and other TRPL measurements were conducted with substantial assistance from Dr. Justin Johnson and Dr. Dylan Arias at the National Renewable Energy Laboratory. Retrieved photophysical constants determined from steady-state and time-resolve emission data at room temperature (with comparative data from Chapter 3 for Tc-e and BT1) are compiled in Table 4.4 at the end of this section.

4.3.2 Time-Resolved Photoluminescence in Toluene at Ambient Temperature

TIPS-Tc in toluene has a photoluminescence that is well-described by a single, globally fit decay with a lifetime (τ_{obs}) of 12.5 ns. The emission basis spectrum from this fit and the complete spectral data are shown in Figure 4.6. This time-resolved spectrum agrees with the spectrum observed in steady-state measurements and is expected to be the only species in TIPS-Tc (and thus constitute the SAS for the TIPS-Tc $S_1 \rightarrow S_0$ emission).

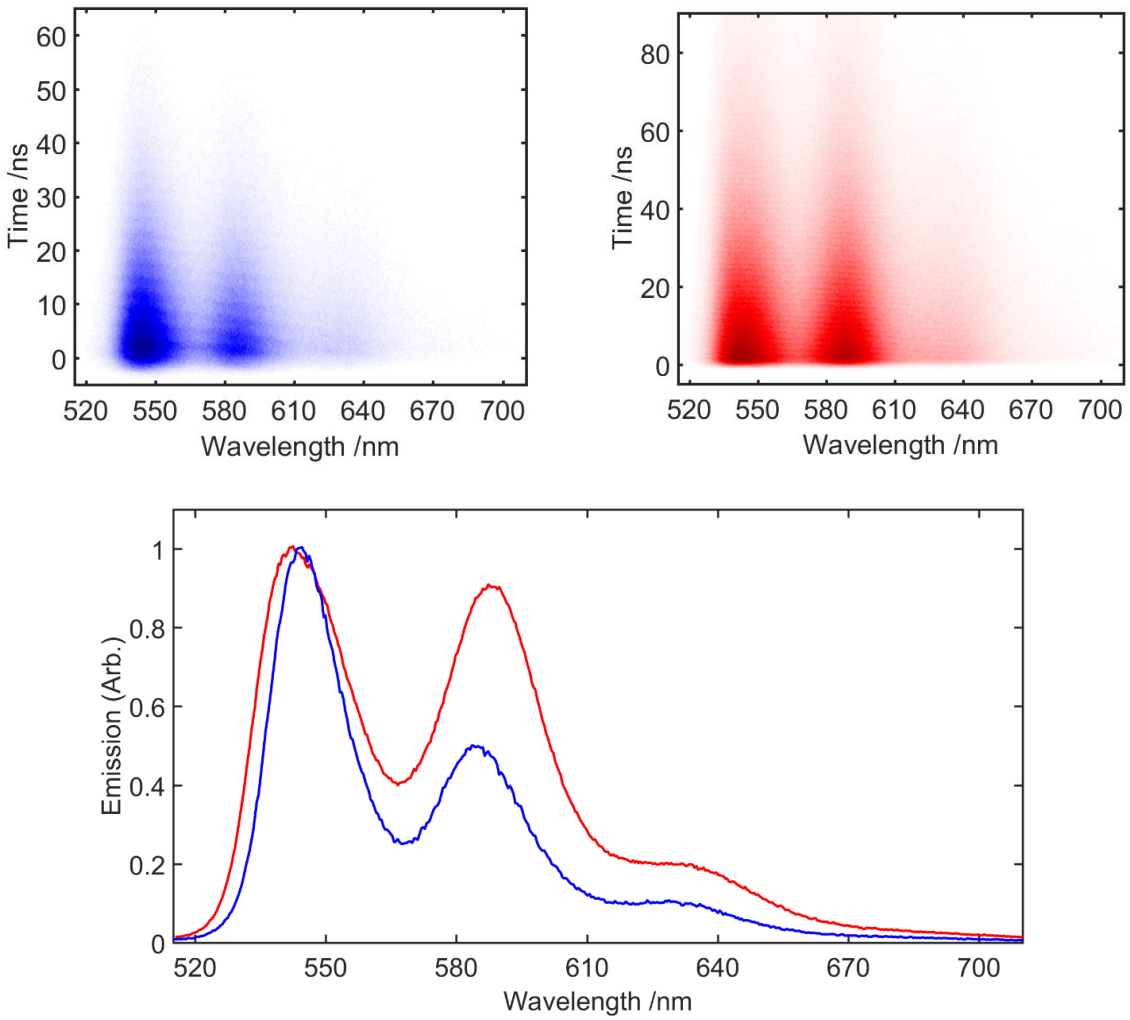

Figure 4.6. Photoluminescence of TIPS-Tc (blue) and TIPS-BT1 (red) in toluene after excitation at 493 nm (intensity of color signifies emission intensity). Top: full spectral decays (normalized). Bottom: normalized basis spectra retrieved from mono-exponential global fits with lifetimes of 12.5 ns (TIPS-Tc, blue) and 25.1 ns (TIPS-BT1, red).

From the observed TIPS-Tc emission lifetime and the previously discussed quantum yield, radiative (k_r) and non-radiative (k_{nr}) rate coefficients from the emissive S_1 state are determined according to the expression $\Phi_{em} = k_r/k_{obs} = k_r/(k_r + k_{nr}) = k_r \times \tau_{obs}$. This gives the values $k_r = (5.9 \pm 0.7) \times 10^7$ s^{-1} and $k_{nr} = (2.1 \pm 0.2) \times 10^7$ s^{-1}. The value of k_r in TIPS-Tc is slightly more than doubled relative to that in Tc ($k_r = 2.4 \times 10^7$ s^{-1}), while k_{nr} is smaller by an order of magnitude ($k_{nr} = 1.9 \times 10^8$ s^{-1} in Tc; see Chapter 3 for the determination of k_r and k_{nr} in Tc). This decrease in k_{nr} compared to the parent acene is likely dominated by a reduction in contributions to k_{nr} from singlet → triplet intersystem crossing (ISC). That process is thought to have a small yield (<6%) in TIPS-Tc,[31] as compared to a substantial (10 times greater at 62%) yield in Tc[36].

TIPS-BT1 in toluene exhibits mono-exponential behavior just as TIPS-Tc does, with the caveat that the observed lifetime is significantly longer (the lifetime is found to be 24.3 ns, as determined from two independent measurements of 23.4 ns and 25.1 ns). The globally fit basis spectrum (presumed to be the SAS for the TIPS-BT1 S_1 state and again consistent with steady-state measurements) and full spectrally resolved decay for TIPS-BT1 are shown in Figure 4.6 with their TIPS-Tc counterparts. TIPS-BT1 has a significantly smaller k_{nr} than its non-TIPS counterpart, BT1, just as was observed for TIPS-Tc relative to Tc (and presumably also because of a decrease in ISC). However, there is only a minimal difference in the radiative rate k_r between TIPS-BT1 and BT1. In TIPS-BT1, the values found are $k_r = (3.0 \pm 0.4) \times 10^7$ s^{-1} and $k_{nr} = (1.2 \pm 0.2) \times 10^7$ s^{-1}, as compared to $k_r = 2.3 \times 10^7$ s^{-1} and $k_{nr} = 1.9 \times 10^8$ s^{-1} for BT1.

The substantially longer lifetime of TIPS-BT1 relative to TIPS-Tc is due to a near-halving of both k_r and k_{nr} in the dimer. The observed reduction to k_r may be related to an increase in charge-transfer character in the S_1 emission of the dimer relative to that of the monomer, which would

reduce coupling to the ground state and in turn yield a slower radiative rate for $S_1 \rightarrow S_0$. A similar decrease to k_r was observed in BT1 relative to Tc-e (its value is 34% smaller in BT1). The origin of the accompanying decrease in k_{nr} may be explained through the energy gap law, assuming similar origins for k_{nr} between the dimer and monomer[37–39] (k_{nr} in both molecules should be dominated by internal conversion rather than ISC). Given the absorption-emission mirror symmetry and small stokes shifts evident in Figure 4.5, expressions for the weak coupling limit are employed.[39] This assumes the 30 meV blue-shift in the dimer is the only relevant difference between the non-radiative losses in TIPS-Tc and those in TIPS-BT1. From this analysis, k_{nr} for TIPS-BT1 is expected (according to equation 10 from the work of Caspar and Meyer[38]) to be 0.5–0.6 times its value in TIPS-Tc. These values were computed assuming a γ parameter of 1-1.3 (typical for $S_1 \rightarrow S_0$ relaxation in hydrocarbons in the weak coupling limit[39]) along with an acceptor vibration $\omega_M = 3000\ cm^{-1}$ (the high-frequency C–H stretching mode typical for aromatic systems[39]). This analysis neglects $S_1 \rightarrow T_n$ relaxation, which is not thought to be a dominant process in TIPS-Tc[31] (this assumption is borne out in subsequent TA measurements of TIPS-Tc and TIPS-BT1, *vide infra*).

An alternative explanation for the observed halving of both k_r and k_{nr} in the dimer (with a single emissive species) invokes a nearly iso-energetic (with S_1) dark state such as the SF-produced multiexcitonic ^{1}TT state formed in an ultrafast equilibration step preceding the observed S_1 emission. This step would yield S_1 in equilibrium with said dark state, resulting in an approximately halved S_1 population at all times. This would cause an accompanying near-halving of the effective decay rate of S_1, and in turn halve the calculated k_r and k_{nr}. This interpretation is revisited and discussed further in subsequent sections (*vide infra*).

4.3.3 Time-Resolved Photoluminescence in Benzonitrile at Ambient Temperature

The behavior of TIPS-Tc in benzonitrile, shown in Figure 4.7, varies little from its behavior in toluene, again having one globally-fit decay component with a (slightly longer) lifetime of 13.4 ns. From this information the radiative and non-radiative loss rates in benzonitrile are found, respectively, to be $k_r = (6.7 \pm 0.2) \times 10^7\ s^{-1}$ and $k_{nr} = (7.8 \pm 0.2) \times 10^6\ s^{-1}$. The lengthening of the lifetime (and accompanying increase in quantum yield, *vide supra*) is thus primarily due to a decrease in non-radiative losses contributing to k_{nr}, rather than an increase in k_r, in moving to benzonitrile. It is worth noting here that the non-radiative component k_{nr} does not distinguish between ISC (e.g. singlet → triplet decay pathways) and internal conversion, though as discussed for toluene, internal conversion is presumed to be the dominant component of k_{nr}.

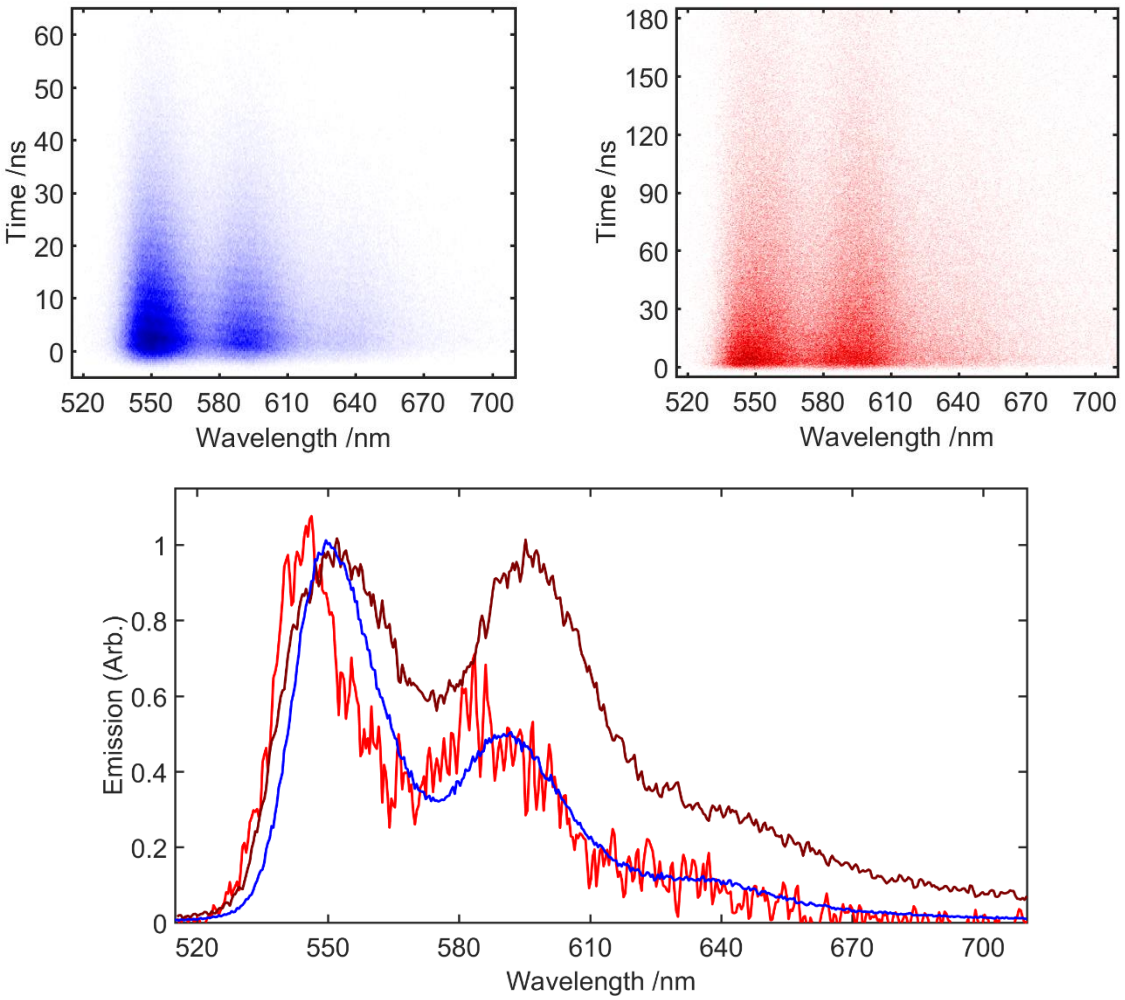

Figure 4.7. Photoluminescence of TIPS-Tc (blue) and TIPS-BT1 (red) in benzonitrile after excitation at 493 nm (intensity of color signifies greater emission intensity). Top: full spectral decays (normalized). Bottom: normalized basis spectra retrieved from global fits, with the sole component (lifetime of 13.4 ns) in TIPS-Tc shown in blue and the two decay-associated spectra from TIPS-BT1 shown in light red (component with lifetime of 12.6 ns) and dark red (component with lifetime of 68.2 ns). The decay associated spectra shown for TIPS-BT1 have been smoothed using a Savitzky-Golay filter (span of 5 points) for clarity. All analysis used raw (unsmoothed) spectra.

While the behavior of TIPS-Tc changes minimally switching from toluene to benzonitrile, that of TIPS-BT1 differs drastically. The dimer exhibits a shift in emission spectrum over time, and global analysis reveals two distinct emissive lifetimes of 12.6 ns and 68.2 ns, with associated spectral characteristics. The obtained decay associated spectra are shown in Figure 4.7. Pictured spectra have been normalized; their true amplitude ratio is 0.98/1 at the peak for the early/late

components, respectively. Neither basis spectrum is a mirror image of the absorption spectrum, suggesting that emission does not occur from the state accessed by the Franck–Condon transition in the absorption. The spectrum of the early decay component (12.5 ns) closely resembles that of the monomer TIPS-Tc in both shape and lifetime, suggesting its character is arm localized; this state is henceforth referred to as $S_{1\text{-loc}}$. The 0–0 to 0–1 peak ratio in this spectrum indicates a significant decrease in the H-aggregate coupling of the chromophore pair relative to the TIPS-BT1 S_1 in toluene.[15] The other, late-time spectrum is instead red-shifted (by 30 meV), broadened (the 0-0 peak, for example, has a full-width at half-maximum of ~130 meV in contrast to 70 meV for the same feature in the $S_{1\text{-loc}}$ component) and has a strikingly different ratio of 0–0 to 0–1 emission peaks from the absorption, indicating an increase in coupling between the chromophores.[15] All of these traits (broadening, red-shifting, and a change in structure/coupling) are consistent with a dimer-delocalized singlet state, and this state is therefore referred to as $S_{1\text{-dim}}$. Given its emergence in a polar solvent, one may posit that $S_{1\text{-dim}}$ is a CT state. This is unlikely given that this CT state appears to be optically dark (no new CT band emerges in the absorption, suggesting that a hypothetical CT state should have weak coupling to S_0) while Φ_{em} remains relatively high (0.52). Experimentally, both $S_{1\text{-loc}}$ and $S_{1\text{-dim}}$ show significant emission (though analysis reveals that the majority of emission comes from $S_{1\text{-dim}}$, *vide infra*). Given the shortening of the $S_{1\text{-loc}}$ component lifetime (τ_{loc} = 12.6 ns) and lengthening of the $S_{1\text{-dim}}$ component lifetime (τ_{dim} = 68.2 ns) relative to the single emissive component in in toluene (24.3 ns), it is presumed that the emissive singlet in toluene (which is expected to have some CT character as is typical of polyacenes[27]) has been split into two separate states by interaction with the polar benzonitrile solvent environment and/or due to interaction with a now-accessible CT state. To further investigate the dual emission

observed in benzonitrile, temperature dependent measurements were made on the emissive behavior of TIPS-BT1.

Table 4.4. Summary of photophysical constants for TIPS-Tc and TIPS-BT1 emission in solution,[a] with comparative Tc-e and BT1 data reproduced from Chapter 3

	Tc-e	BT1	TIPS-Tc	TIPS-BT1
Φ_{em}[b]	0.14 ± 0.03	0.10 ± 0.02	0.74 ± 0.08 **0.90 ± 0.02**	0.72 ± 0.09 **0.52 ± 0.04**
τ_{obs} /ns	3.9 ± 0.2	4.3 ± 0.4, 11 ± 3	12.5 **13.4**	24.3 **12.6 (τ_{loc}), 68.2 (τ_{dim})**
$k_r \times s$	$(3.5 \pm 0.7) \times 10^7$	$(2.3 \pm 0.5) \times 10^7$	$(5.9 \pm 0.7) \times 10^7$ **$(6.7 \pm 0.2) \times 10^7$**	$(3.1 \pm 0.4) \times 10^7$
$k_{nr} \times s$	$(2.2 \pm 0.6) \times 10^8$	$(1.9 \pm 0.2) \times 10^8$	$(2.1 \pm 0.2) \times 10^7$ **$(0.76 \pm 0.02) \times 10^7$**	$(1.2 \pm 0.2) \times 10^7$

[a]Unbolded values are from toluene solution and bolded values are from benzonitrile solution. [b]Tc-e and BT1 measured relative to coumarin 480 in methanol[40]; TIPS-Tc and TIPS-BT1 measured relative to coumarin 540A (coumarin 153) in methanol.[28]

4.4 Changes in Photoluminescence with Temperature

4.4.1 Temperature-Dependent Steady-State Photoluminescence

Steady-state photoluminescence measurements were carried out on TIPS-Tc and TIPS-BT1 in toluene and benzonitrile at temperatures between 275 and 315 K, and the results are shown in Figure 4.8. Plotted relative emission values (Φ_{rel}) were obtained by computing the emission quantum yield at each temperature (relative to coumarin 540A in room temperature methanol[28]) and dividing the result by Φ_{em} at 293 K (20 °C). Linear fits are given as solid and dashed lines to guide the eye. The emission spectra of TIPS-BT1 at each temperature are also shown, where each individual spectrum has been scaled to reflect the measured Φ_{em} at the indicated temperature relative to Φ_{em} at 20 °C in the corresponding solvent.

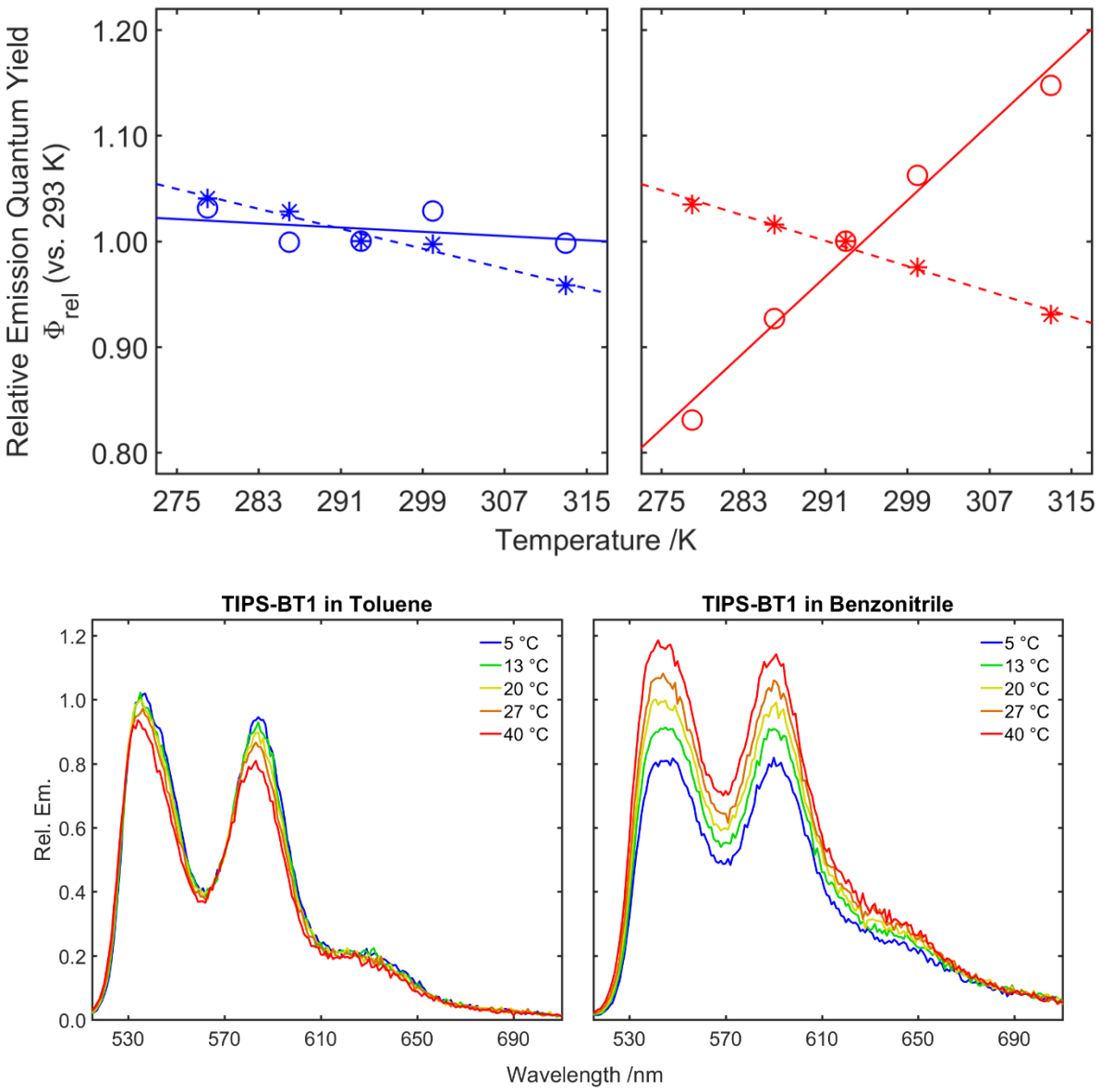

Figure 4.8. Top: temperature-dependence of Φ_{em} for TIPS-Tc (blue) and TIPS-BT1 (red) in toluene (asterisks, fits as dashed lines) and benzonitrile (open circles, fits as solid lines) between 275 K and 315 K. Values of Φ_{rel} for each solvent were obtained by scaling Φ_{em} at each temperature to its value at 293 K (20 °C). Bottom: emission spectra of TIPS-BT1 in toluene and benzonitrile at each temperature, scaled to the spectrum at 20 °C in the corresponding solvent.

In TIPS-Tc, there is very little change observed for Φ_{em} in either solvent with increasing temperature. In toluene, deviation from the reference (20 °C) emission signal is small (~4%) and shows an overall systematic decrease with temperature. In benzonitrile, changes are again small

(~4%) and again suggest a systematic decrease (though this decrease is much less pronounced than in toluene). These subtle findings are presumably due to small increases in k_{nr} with increasing temperature, likely dominated by vibrationally-driven (e.g. thermally activated) internal conversion or intersystem crossing.

The behavior of TIPS-BT1 in toluene is similar to that of TIPS-Tc, with a small systematic decrease in Φ_{em} as the temperature increases (not exceeding ~7% of the initial value). The reason for the slightly increased strength of the observed temperature effect is unclear, though it is possibly due to an increase in the number of vibrational degrees of freedom available to TIPS-BT1 relative to TIPS-Tc. Spectral changes upon heating and cooling are minimal, with a minor increase in the ratio of 0–0 to 0–1 peak heights evident as temperature is increased (further consistent with the behavior of a weak H-aggregate upon heating, for which this is the expected behavior due to thermally activated 0–0 emission as the coherence size of the aggregate is reduced[15]).

In benzonitrile, TIPS-BT1 again exhibits changes to its spectrum with temperature in the form of a subtle (even less pronounced than in toluene) increase in the ratio of 0–0 to 0–1 peak heights as temperature is increased. This is paired with a startling increase in emission quantum yield with temperature that exceeds 15% of the reference (20 °C) value at the extremes of the temperature range investigated. A potential explanation for this behavior is through a change in the emission quantum yield of either individual state. For example, an increase to the radiative rate k_r for either $S_{1\text{-loc}}$ or $S_{1\text{-dim}}$ would result in an increased emission quantum yield for TIPS-BT1, in addition to a change in the steady-state spectrum favoring the emission of that state. The value of k_r is generally thought to be temperature independent and determined only by the electronic coupling (e.g. Franck–Condon factors) between the ground and excited states. There are known cases where k_r varies with temperature, but these are typically cases where the emissive state

exhibits significant conformational flexibility, such as a twisted intramolecular charge transfer (TICT) state, and where emission from otherwise unstable molecular configurations is thermally activated.[41] Given the norbornane backbone of TIPS-BT1 and its accompanying rigidity, such a TICT state is unlikely to exist at reasonable energies in this system. Furthermore, it is reiterated that $S_{1\text{-dim}}$ is unlikely to be a CT state, and this mechanism is thus unlikely (albeit not impossible).

Alternatively, an exchange of population between states (such as $S_{1\text{-loc}}$ and $S_{1\text{-dim}}$) could change the overall emission quantum yield (Φ_{em}). This will occur if the emission quantum yields of the individual states ($\Phi_{em,n}$, where n denotes the specific state from which emission occurs) are different. For a set of n states (here n = {loc, dim} to denote $S_{1\text{-loc}}$ and $S_{1\text{-dim}}$, respectively), Φ_{em} is given by the following sum (for which the state populations P_n are normalized to give $\Sigma_n [P_n] = 1$):

$$\Phi_{em} = \Sigma_n [\Phi_{em,n} \times P_n] \quad (1)$$

Whether through an initial partitioning step (e.g. with $S_{1\text{-loc}}$ and $S_{1\text{-dim}}$ created from a hot Franck–Condon state promptly following excitation) or over the course of electronic relaxation (e.g. with $S_{1\text{-loc}}$ and $S_{1\text{-dim}}$ in temperature-dependent equilibrium throughout the reaction), any mechanism that relies on a transfer of population between $S_{1\text{-loc}}$ and $S_{1\text{-dim}}$ is unlikely to be due to the magnitude of observed changes in Φ_{em}. To rationalize this, the fractional contributions to the observed emission (denoted $E_{frac,n}$, for which $\Sigma_n [E_{frac,n}] = 1$, and where n again specifies the emissive state) from each state are considered. $E_{frac,n}$ may be understood simply given the definitions of Φ_{em}, $\Phi_{em,n}$, and P_n:

$$E_{frac,n} = \frac{\text{photons emitted by n}}{\text{photons emitted}} = \frac{\text{(photons emitted by n) / (excited n)}}{\text{(photons emitted) / (excited states)}} \times \frac{\text{excited n}}{\text{excited states}} = \frac{\Phi_{em,n}}{\Phi_{em}} \times P_n \quad (2)$$

These fractions are thus defined for each state in terms of P_n, $\Phi_{em,n}$, and Φ_{em}, and are found by normalizing Equation 1 to the overall emission quantum yield:

$$\Sigma_n [(\Phi_{em,n} \times P_n) / \Phi_{em}] = \Sigma_n [E_{frac,n}] = 1 \quad (3)$$

$$E_{frac,n} = (\Phi_{em,n} \times P_n) / \Phi_{em} \quad (4)$$

$E_{frac,n}$ is found experimentally by integrating the photons emitted by a state, then normalizing to the total photons observed. The TRPL contribution from each state is numerically obtained by multiplication of its un-normalized basis spectrum from Figure 4.7 by the appropriate exponentially modified Gaussian decay, while the total emission is obtained by summation of the full TRPL signal. At room temperature (23 °C), this method reveals that 90% of detected light is emitted by $S_{1\text{-}dim}$ (that is, $E_{frac,dim} = [\Phi_{em,dim} \times P_{dim}] / \Phi_{em}$, = 0.90) while only 10% is emitted by $S_{1\text{-}loc}$ (for which $E_{frac,loc} = [\Phi_{em,loc} \times P_{loc}] / \Phi_{em} = 0.10$). Thus, in the hypothetical case of complete population transfer from $S_{1\text{-}loc}$ to $S_{1\text{-}dim}$ at cold temperatures (giving $P_{loc} = 0$ and $P_{dim} = 1$), a reduction to Φ_{em} of (at most) 10% is achievable. This assumes temperature-independent $\Phi_{em,n}$ values, though $\Phi_{em,n}$ is expected to *increase* at lower temperatures (as observed for the monomer in both solvents and for the dimer in toluene), resulting in an *increase* in the observed emission, and in turn reducing the magnitude of a real decrease (that is, to less than 10%). This is inconsistent with the 17% decrease to Φ_{em} observed when the sample is cooled to 5 °C. Meanwhile, the significant spectral changes that would accompany this transfer of population between $S_{1\text{-}loc}$ and $S_{1\text{-}dim}$ (as required to produce 15% more photons at 40 °C and 17% fewer at 5 °C relative to 20 °C) are absent in the steady-state spectra in Figure 4.8 (for which there is no significant spectral evolution with temperature). Direct transfer of population between $S_{1\text{-}loc}$ and $S_{1\text{-}dim}$ is conclusively ruled out by time-resolved experiments (*vide infra*) that show the quantity of $S_{1\text{-}loc}$ emission to be temperature-independent.

In the absence of inter-state population transfer, the observed increase to Φ_{em} may be explained by thermally-activated re-population of either $S_{1\text{-}loc}$ or $S_{1\text{-}dim}$ from a lower-lying dark

state such as a multiexcitonic ^{1}TT state or CT. This would require a fast equilibration step to occur prior to the timescale of the TRPL experiment so as to be non-detectable, but would allow for an increase in emission without transfer of population between $S_{1\text{-loc}}$ and $S_{1\text{-dim}}$. Subsequent ultrafast experiments (*vide infra*) show fast evolution that is consistent with this hypothesis.

4.4.2 Temperature-Dependent Time-Resolved Photoluminescence

The temperature-dependence of the TIPS-BT1 TRPL signal was measured as described in Section 4.3.1, with the addition of a cryostat around the sample to allow for temperature control. This allows for discrimination between the mechanisms proposed above for the temperature-dependent changes to Φ_{em} observed for TIPS-BT1 in benzonitrile. Solution-phase samples of TIPS-BT1 in toluene and benzonitrile were allowed to equilibrate at temperatures of 0, 23, and 50 °C for 15 minutes prior to measurement. Resulting TRPL data was fitted globally in an identical manner to that in Section 4.3.1 (23 °C measurements are reproduced here, but are identical to those discussed Section 4.3), and the resulting TRPL basis spectra from these global fits are given in Figure 4.9. The corresponding lifetimes for each temperature and extracted per-state emission yields are summarized in Table 4.5 (tabulated values are explained in the text). Full TRPL data and spectral slices with corresponding fits are shown in Appendix B for all data sets discussed. The color scheme in this section deviates from that in the rest of this chapter, with blue used for measurements at 0 °C, black for measurements at 23 °C, and red for measurements 50 °C.

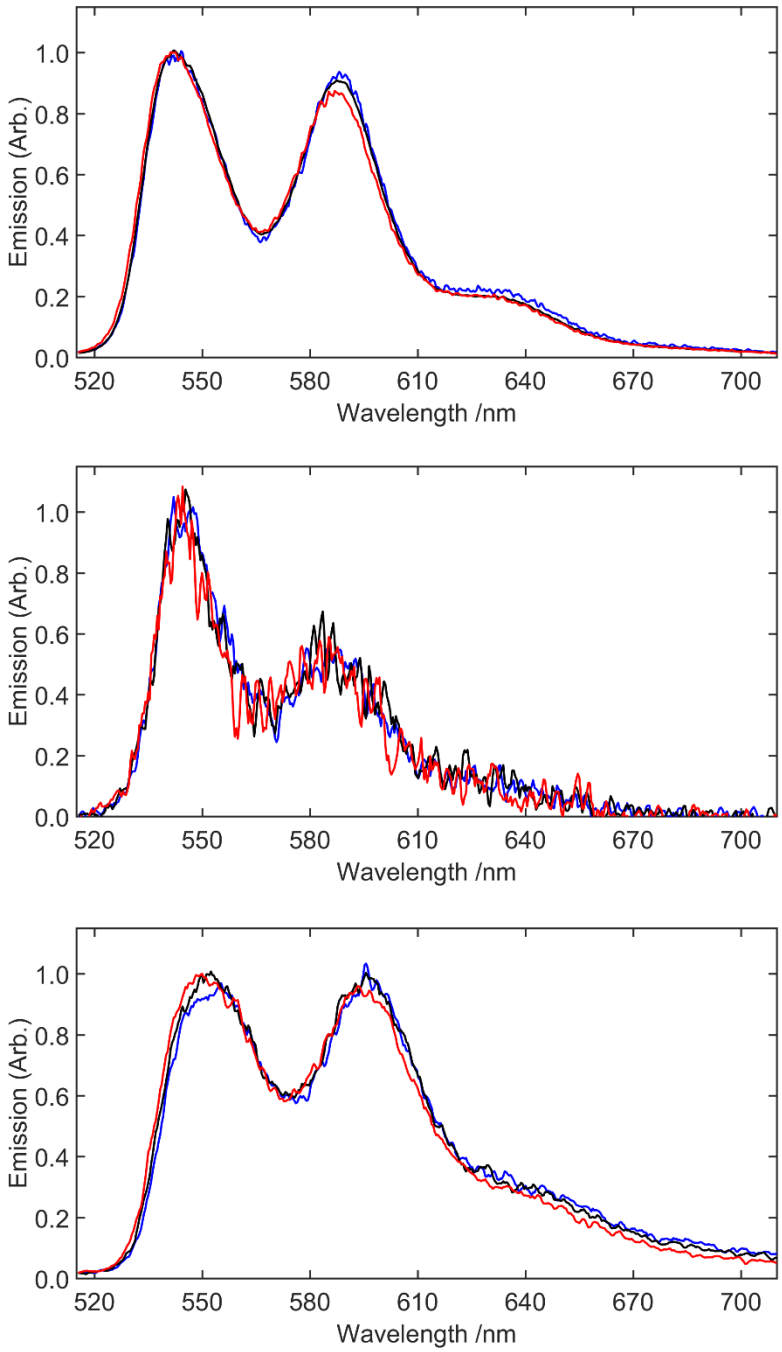

Figure 4.9. Temperature-dependent basis spectra (normalized) in TIPS-BT1 at 0 °C (blue), 23 °C (black), and 50 °C (red). Top: toluene S_1, with lifetimes of 25.3 ns, 25.1 ns, and 26.0 ns (at 0 °C, 23 °C, and 50 °C, respectively). Middle: benzonitrile $S_{1\text{-loc}}$ with lifetimes of 13.4 ns, 12.6 ns, and 13.0 ns (at 0 °C, 23 °C, and 50 °C). Bottom: benzonitrile $S_{1\text{-dim}}$ with lifetimes of 75.0 ns, 68.2 ns, and 57.0 ns (at 0 °C, 23 °C, and 50 °C). Before normalization, the relative amplitudes for $S_{1\text{-loc}}/S_{1\text{-dim}}$ in benzonitrile were 1.26/1, 0.99/1, and 0.62/1 at 0°C, and 23°C, and 50 °C, respectively.

TIPS-BT1 in toluene exhibits mono-exponential behavior at all temperatures (lifetimes of 25.3 ns, 25.1 ns, and 26.0 ns at 0 °C, 23 °C, and 50 °C, respectively) with no systematic changes in the observed lifetime vs. temperature. Spectral changes to the S_1 basis spectrum suggest a minor shift towards monomer-like emission as the temperature is increased (consistent with the steady-state behavior shown in Figure 4.8, and expected for H-like aggregates with increasing temperature[15] as discussed for the steady-state spectra).

Table 4.5. Temperature-dependent data from TRPL of TIPS-BT1, including emissive lifetimes and relative emission of individual states, color-coded by temperature

Component (solvent)	Temperature /°C	State Lifetime, τ_n /ns	Emission Fraction, $E_{frac,n}(T)$	Relative Emission $E_{rel,n}(T)$
S_1 (toluene)	0	25.3	1	1.05
	23	25.1	1	0.99
	50	26.0	1	0.90
$S_{1\text{-loc}}$ (benzonitrile)	0	13.4	0.13	0.10
	23	12.6	0.10	0.11
	50	13.0	0.08	0.10
$S_{1\text{-dim}}$ (benzonitrile)	0	75.0	0.87	0.70
	23	68.2	0.90	0.91
	50	57.0	0.92	1.15

Findings for TIPS-BT1 in benzonitrile are yet again markedly different from those in toluene. Bi-exponential global fitting reveals the same two spectral components ($S_{1\text{-loc}}$ and $S_{1\text{-dim}}$) at all temperatures, but their behavior with temperature differs drastically. The $S_{1\text{-loc}}$ component appears to have no systematic temperature-dependence on shape (see Figure 4.9), or lifetime (τ_{loc}

was 13.4 ns, 12.6 ns, and 13.0 ns at 0 °C, 23 °C, and 50 °C, respectively). The $S_{1\text{-dim}}$ component (shown in Figure 4.9) shifts towards a more monomer-like emission profile at higher temperatures (indicative again of H-aggregate behavior[15]) while its lifetime becomes systematically shorter. Lifetimes found for $S_{1\text{-dim}}$ (τ_{dim}) were 75.0 ns at 0 °C, 68.2 ns at 23 °C, and 57.0 ns at 50 °C.

The temperature-dependence of the $S_{1\text{-dim}}$ lifetime (τ_{dim}) shows that high-temperature increases to Φ_{em} do not stem from a decrease to k_{nr}. Given that $\Phi_{em} = k_r/[k_r + k_{nr}] = k_r \times \tau_{obs}$, any decrease to k_{nr} (for the dimer) will increase τ_{dim} and in turn increase Φ_{em}. Experimental findings, however, show an increase in emission as τ_{dim} decreases. With an increase to k_r unlikely for the reasons listed previously (see Section 4.4.1), we instead attempt to access the populations of $S_{1\text{-mon}}$ and $S_{1\text{-dim}}$ to search for evidence of thermal repopulation from a lower-lying dark state.

The emission contributions for both $S_{1\text{-loc}}$ and $S_{1\text{-dim}}$ in benzonitrile were calculated at each temperature in the same manner described for the room temperature TRPL data (*vide supra*) to provide a proxy for the populations of these states. The temperature-dependent fraction of observed emission from each state n, denoted $E_{frac,n}(T)$, was determined (using the appropriate basis spectrum from Figure 4.9 with associated kinetics) for both states at each temperature. This value is defined in terms of $\Phi_{em,n}$, P_n, and temperature T in Equation 5.

$$E_{frac,n}(T) = [\Phi_{em,n}(T) \times P_n(T)] / \Phi_{em}(T) \quad (5)$$

This is identical to the definition of $E_{frac,n}$ in Equation 4, except that the temperature dependence has been explicitly included. It is now possible to define a temperature-dependent, state-specific relative emission (denoted $E_{rel,n}(T)$ for state n at temperature T) by scaling $E_{frac,n}(T)$ by the temperature-dependent relative emission $\Phi_{rel}(T)$ estimated from Figure 4.8 for each TRPL measurement. This is given in Equation 6. The result is an effective fraction of emitting states that is scaled to the emission observed at 20 °C.

$$E_{rel,n}(T) = \Phi_{rel}(T) \times E_{frac,n}(T) \quad (6)$$

This may be thought of as follows (rephrasing Equation 6):

$$E_{rel,n}(T) = \frac{\text{photons emitted at T}}{\text{photons emitted at 20 °C}} \times \frac{\text{photons emitted by n at T}}{\text{photons emitted at T}} = \frac{\text{photons emitted by n at T}}{\text{photons emitted at 20 °C}} \quad (7)$$

Use of this metric is helpful without an independent measure of $\Phi_{em,n}$ or P_n for either $S_{1\text{-loc}}$ or $S_{1\text{-dim}}$. The findings from this analysis nonetheless rule out thermally-driven population transfer between $S_{1\text{-loc}}$ and $S_{1\text{-dim}}$, as the quantity of emission from $S_{1\text{-loc}}$ (given by $\Phi_{em,loc} \times P_{loc}$) remains approximately constant with temperature (0.10, 0.11, and 0.10 at 0 °C, 23 °C, and 50 °C, respectively) while emission from $S_{1\text{-dim}}$ (given by $P_{dim} \times \Phi_{em,dim}$) changes drastically (0.70, 0.91, and 1.15 at 0 °C, 23 °C, and 50 °C, respectively). The result is that the overwhelming majority of the observed changes in the emission of TIPS-BT1 in benzonitrile are from changes to the emission of $S_{1\text{-dim}}$, which changes by a factor of 1.26 at the highest temperature and 0.77 at the lowest temperature.

Given the findings presented thus far, the most probable explanation for the temperature-dependent emission of TIPS-BT1 in benzonitrile is that a lower-energy non-emissive state (such as ^{1}TT or CT) exists in equilibrium with the emissive $S_{1\text{-dim}}$, and that the equilibrium between these states is thermally controlled. That is, under the constraint that the total population of these states is conserved (dark state plus $S_{1\text{-dim}}$) the rate of emission may be increased by redistributing the population to favor the emissive state. This increases the probability of emission at all times, thereby increasing the decay rate. As an aside, two decay lifetimes arise from this behavior (the first determined by prompt loss of the emissive state into the dark state as equilibrium is established), though the fast lifetime may be undetectable by nanosecond techniques like TRPL. The fast timescale necessary to observe this equilibration is accessed by subsequent ultrafast

measurements (*vide infra*), and the results are consistent with this picture. Finally, this equilibrium exists concurrently with and isolated from the faster mono-exponential decay of $S_{1\text{-loc}}$.

4.5 Cyclic Voltammetry and Spectroelectrochemistry: Energetics and Spectral Signatures of the Charge-Transfer State

To access the energies of the HOMO and LUMO of TIPS-Tc and TIPS-BT1 and accordingly assess the viability of accessing CT states, cyclic voltammetry (CV) was performed on TIPS-Tc and TIPS-BT1. An electrochemical analyzer (CH Instruments 601C) with a three-electrode setup in benzonitrile was used, consisting of: a platinum disk working electrode (3 mm diameter); a 0.5 mm platinum wire counter-electrode; and a 0.01 M $Ag/AgNO_3$ reference electrode prepared immediately before use. All samples incorporated 0.1 M tetrabutylammonium hexafluorophosphate (TBAPF) as a supporting electrolyte in solution with the chosen TIPS-acene chromophore, and potential was scanned at a rate of 100 mV/s (scans are shown in Appendix B). Potentials ($E_{1/2}$, average of cathodic and anodic peaks) are given in Table 4.6. Values were adjusted using a ferrocene internal standard ($Fc^{+/0}$, subtraction of 0.0592 V) in benzonitrile. The separation between cathodic and anodic peaks is also provided. Literature values were used to convert to $Fc^{+/0}$ in acetonitrile[42,43], SHE in acetonitrile[43], and finally from SHE to vacuum[44].

Additional spectroelectrochemical measurements in benzonitrile again used a three-electrode setup, but substituted a platinum mesh working electrode in the optical path for the platinum disk electrode used for CV. This system was placed inside of a 2 mm optical cell and bubble-degassed with argon prior to—and kept under an argon blanket during—measurements. Substantial recovery of the initial absorbance was observed for reductive spectroelectrochemistry upon applying a null potential, while only minimal recovery was observed for oxidative measurements. Absorption difference spectra from spectroelectrochemical measurements are

shown in Figure 4.10. The author acknowledges Steven Fatur for his assistance in conducting and interpreting these measurements.

Table 4.6. Cyclic voltammetry findings for TIPS-Tc and TIPS-BT1 vs. optical gap from electronic absorption measurements

	TIPS-Tc, benzonitrile	TIPS-BT1, benzonitrile
$E_{1/2}$ /V, +/0	0.59 (0.09), **–5.82**	0.59 (0.07), **–5.83**
$E_{1/2}$ /V, 0/–	–1.66 (0.07), **–3.58**	–1.67 (0.06), **–3.57**
E_{gap} /V	2.25	2.26
$E_{optical}$ /eV	2.28	2.31

Non-bolded values are relative to $Fc^{+/0}$ in benzonitrile. Bolded values have been corrected to vacuum using literature values.[42–44] Numbers in parentheses are the separation values for anodic vs. cathodic peaks. The optical gap ($E_{optical}$) is estimated as the average of the absorption and emission peaks in benzonitrile.

The TIPS-Tc CV findings show that the optical gap ($E_{optical}$; estimated from the average of the absorption and emission peaks to be 2.28 eV) is larger than the combined gap between one-electron oxidation and one-electron reduction events (E_{gap} = 2.25 V). The latter combination should be a proxy for the energy of an intermolecular charge transfer state consisting of two transiently associated TIPS-Tc molecules, neglecting coulombic stabilization (which would serve to shrink the measured 2.25 V gap). An intramolecular CT state in TIPS-BT1, where an electron is transferred from one acene arm to the other, should be similar in nature to an intermolecular CT state composed of two TIPS-Tc molecules, which suggests that—even neglecting coulombic stabilization—such a state should be accessible upon optical excitation in a polar environment such as benzonitrile. In comparing the tabulated TIPS-Tc oxidation and reduction potentials to those in TIPS-BT1, there is very little difference, suggesting that the one-electron oxidation and reduction events measured in the dimer are localized to one arm (as is necessarily the case in the

monomer). The electrochemistry of TIPS-Tc is therefore expected to be a reasonable proxy for that of TIPS-BT1 in subsequent spectroelectrochemical measurements. In TIPS-BT1, the optical gap is at 2.31 eV, while the redox gap is again smaller at 2.26 V. This should give a lower limit to the energy difference between an intramolecular CT state and S_1. A reasonable estimate of coulombic stabilization via Coulomb's law in a benzonitrile environment (using a 10.5 Å separation taken from the center-to-center distance of the acene arms and the literature[26] relative permittivity of benzonitrile, 25.9) suggests that the redox gap is approximately an additional 50 meV lower. This places the CT state at an estimated 100 meV beneath the optical S_1 in the event of a one-electron excitation, which supports the notion that a low-lying CT state is involved in the temperature-dependent behavior of TIPS-BT1 in benzonitrile.

Given the similarity between the redox behavior of the monomer and dimer, spectroelectrochemical measurements on the TIPS-Tc monomer were made to provide a qualitative estimate of the corresponding absorption features of the dimer CT state. Results in benzonitrile are shown in Figure 4.10, in which both the absorptive and reductive components have been normalized.

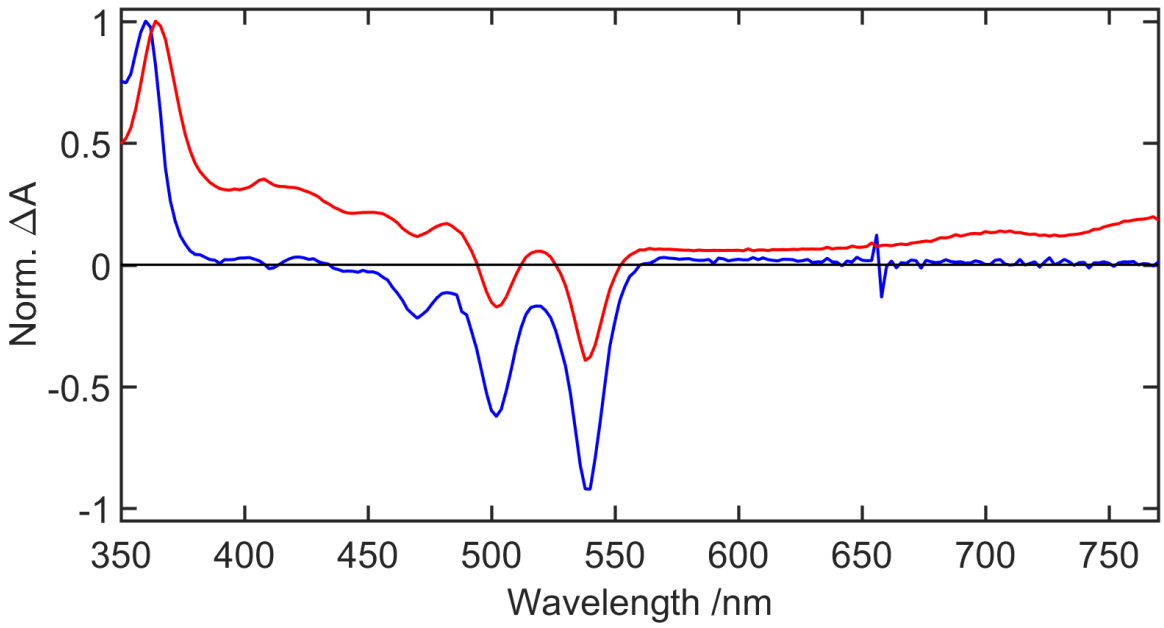

Figure 4.10. Absorption difference spectra (normalized) of TIPS-Tc in benzonitrile from oxidative (blue) and reductive (red) spectroelectrochemistry. The small feature at 650 nm (oxidative component) is an instrument-related artifact and does not originate from TIPS-Tc.

The most prominent feature evident in the absorption difference spectra of TIPS-Tc is an absorptive feature peaked in the UV that is present (albeit shifted slightly) in both the oxidized (blue) and reduced (red) species that continues into the visible until between 450–500 nm. Also prominent (in both the oxidized and reduced species) is a decrease in absorbance in the region of $S_1 \leftarrow S_0$ features (the appearance of a ground state bleach). Lastly, there is an additional broad and relatively weak absorption increase present only in the reduced species with an onset near 560 nm which extends into the red. Though these spectra are purely qualitative (e.g. no effort was made to quantify the relative magnitude of the absorptive and reductive components), the features identified above will facilitate identification of transient species in the TA data in the following section.

4.6 Transient Absorption

To access the behavior of TIPS-BT1 in the femtosecond to microsecond regime, and in particular to look for direct evidence of the dark (by emission) TIPS-BT1 CT state, TA experiments were carried out (again using TIPS-Tc for reference) in both solvent systems (toluene and benzonitrile). First, behavior between ~200 fs and 1.5 ns is accessed with femtosecond TA (fsTA), before moving to nanosecond–microsecond TA (nsTA) to study the long-time behavior of the dimer.

4.6.1 Ultrafast Transient Absorption Spectrometer: Data Acquisition and Analysis

The methods employed for fsTA experiments in this chapter differ from those detailed in Chapter 2, particularly with regards to the detection method. The second harmonic of a CW Nd:YVO_4 laser (Coherent Verdi) is used to pump a Ti:sapphire oscillator (~800 nm, ~50 fs pulses at 94 MHz, K&M Labs), the output of which is directed into a multi-pass amplifier (Quantronix Odin). Amplified ~800 nm pulses (~1 mJ/pulse at 1 kHz) are primarily directed into a home-built non-collinear optical parametric amplifier (NOPA). NOPA output pulses (center wavelength near 530 nm, full-width at half-maximum (FWHM) of ~15 nm) are passed through a prism compressor to give pulses with 35–50 fs temporal FWHM, characterized using second harmonic generation frequency resolved optical gating (SHG-FROG). Pump pulses are mechanically chopped at 500 Hz and directed through a home-built zero-dispersion 4-f grating compressor with a CRi 640 liquid crystal spatial light modulator (SLM) at its center in the frequency domain. The SLM was set during these experiments to provide no phase modulation (refer to Chapter 2 for a diagram of the shaper and operating principles). Excitation fluences were kept low (50–200 μJ/cm^2, with pump diameter near 200 μm FWHM) and power-dependent measurements showed no dependence on excitation fluence.

All measurements were done at magic angle polarization (54.7°) relative to the probe. Probe white light is generated from a small portion of 800 nm amplifier output that is routed onto a delay stage before being focused into a circularly-translated (to prevent burning) CaF_2 crystal. After exiting the sample, residual 800 nm fundamental is filtered from the probe light using a short-pass filter and coupled into a Chromex 250 IS spectrograph and detected at 1 kHz with an Andor Newton camera operating in full-vertical-binning mode. This enables detection with adequate signal/noise between ~350–700 nm. This experiment is controlled using home-built software written in LabVIEW (National Instruments). Dilute solution-phase samples (absorbance at 530 nm pump wavelength of 0.1, typically ~5 µm concentration) were prepared in 2 mm quartz cuvettes (equipped with Kontes HI-VAC® vacuum-valves) using high-purity solvents. Samples were bubble-degassed with argon for 30 minutes prior to sealing. Sample integrity was verified before and after data acquisition via steady-state absorption spectroscopy.

Data sets were chirp corrected and fitted in MATLAB using code written by our group. Global fitting to a single or to a sum of exponential decays (the number of exponentials is indicated in the text; fits start at 3 ps to avoid coherent artifacts and any remaining chirp) was performed on fsTA surfaces, while fits to a sum of exponentially modified Gaussian functions were performed on single-feature kinetics (generated by averaging together of ~5 nm regions of full fsTA surfaces) for which the retrieved Gaussian FWHM was 380 fs.

4.6.2 Findings on the Ultrafast Timescale

Data and fits covering a time window between 3 and 1400 ps for TIPS-Tc in toluene and benzonitrile are shown in Figure 4.11. It is evident from the pictured mono-exponential global fits that the only evolution in these systems is the slow S_1 relaxation that was observed in TRPL. The lifetime found here in toluene is 10 ns. While this lies far outside the 1.4 ns window of the fsTA

experiment, it does not conflict with the TRPL lifetime of 12.5 ns and suggests that no early-time behavior is present in the monomer. In benzonitrile, the behavior is effectively unchanged (again consistent with observations in TRPL). The determined lifetime of 10 ns (similarly outside the window of the fsTA experiment) does not conflict with the 13.4 ns lifetime found via TRPL, and no sub-nanosecond evolution is apparent. The spectrum in both solvents consists of three primary features: a broad $S_1 \rightarrow S_n$ excited-state absorption (ESA) near 423 nm that (beginning at 450 nm) exhibits structure derived from overlapping ground-state bleach (GSB) features, a second ESA with onset near 550 nm that overlaps with stimulated emission (SE) until ~600 nm, and a GSB near 500 nm corresponding to the 0–1 peak in the electronic absorption.

For TIPS-BT1 in toluene (Figure 4.12, again over a time window of 3 to 1500 ps), as with TRPL, a mono-exponential fit adequately describes the behavior of the system. There is evidence for a single component with a many-nanosecond lifetime (approximately 20 ns, similarly too long to obtain a meaningful lifetime from a 1.4 ns window) that is consistent with the lifetime found from TRPL measurements. The features present largely match those of the monomer: there is a broad ESA (here centered at 429 nm, and extending somewhat further into the UV than seen in the monomer) with overlapping vibronic structure from the GSB, an ESA in the red (onset 550 nm) that is stronger than the corresponding feature in the monomer (again with structure derived from SE), and the same GSB near 500 nm. The extension of the blue ESA into the UV (relative to the TIPS-Tc monomer) and the increase in the ESA from 550 nm onwards are consistent with a subtle increase in charge-transfer character of the S_1 state in the dimer, as these features match those from the spectroelectrochemistry changes in Figure 4.10. This is hardly conclusive, however, and the state present in these fsTA measurements does not exhibit any other changes over the length of the 1.4 ns delay in the fsTA experiment (excepting a single sub-picosecond feature discussed below).

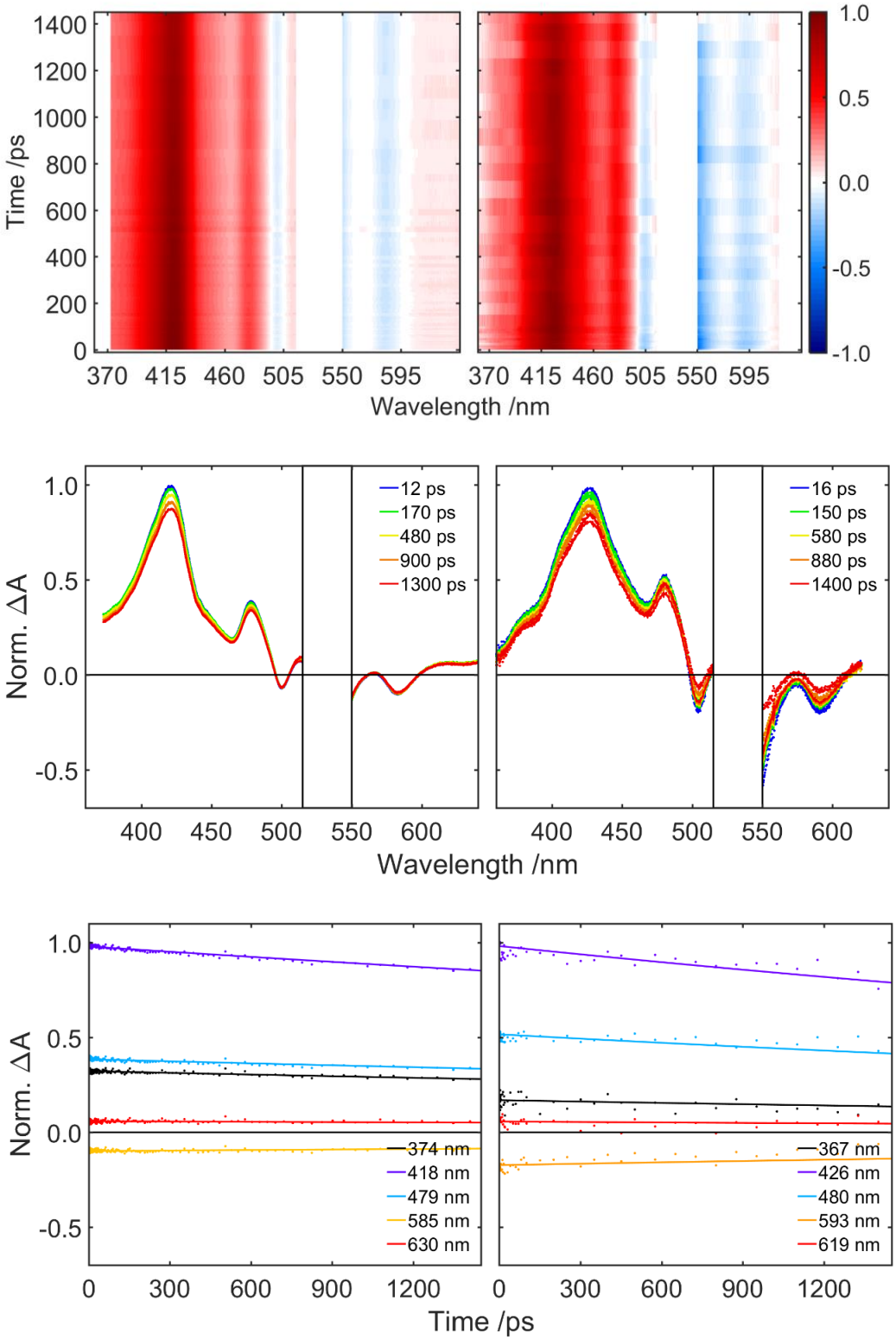

Figure 4.11. TIPS-Tc fsTA surfaces (top), spectra (middle), and kinetics (bottom) in toluene (left) and benzonitrile (right). Spectra and kinetics are extracted from the data (points) and from the global fit (lines). Pump scatter has been removed.

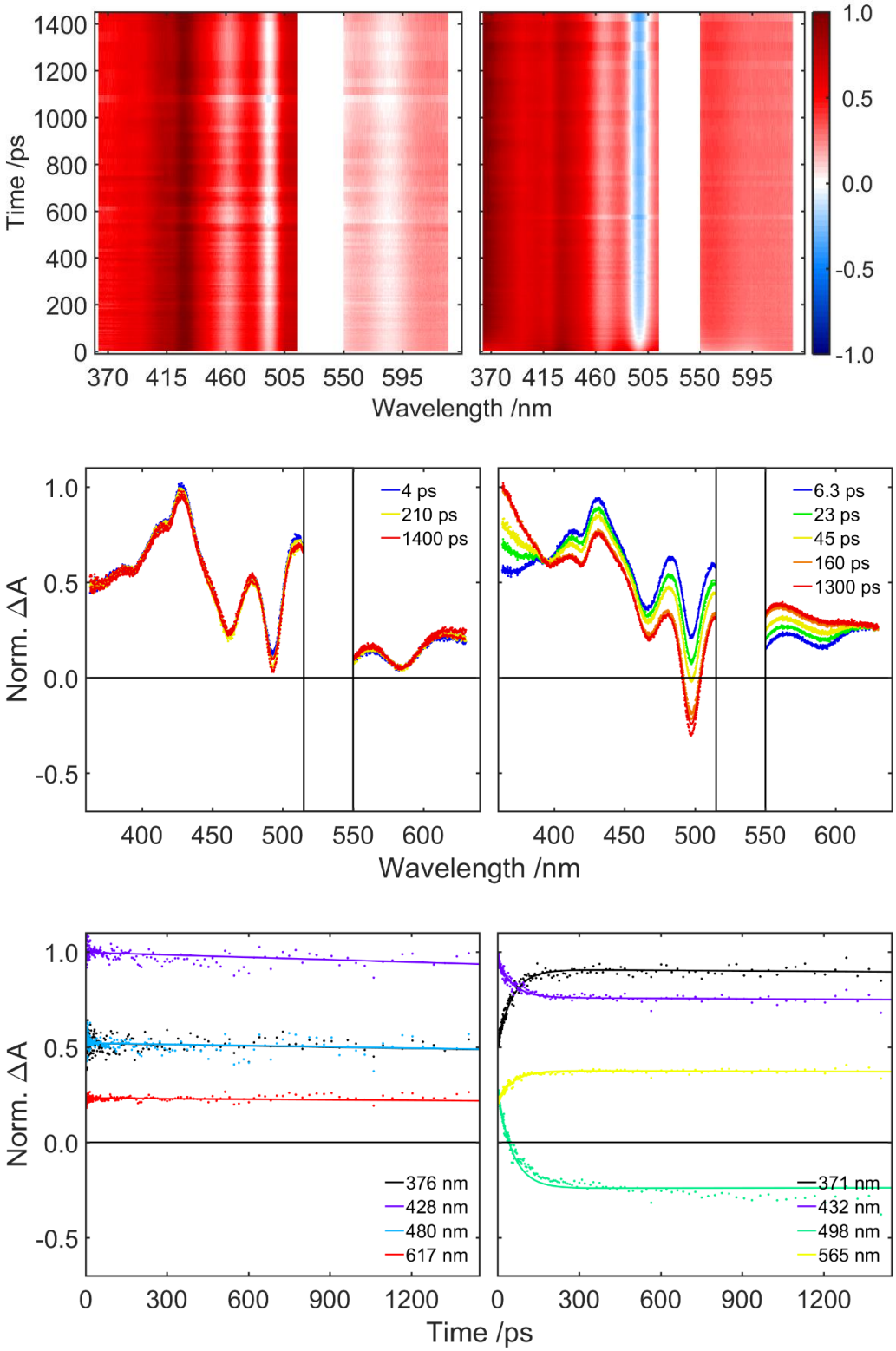

Figure 4.12. TIPS-BT1 fsTA surfaces (top), spectra (middle), and kinetics (bottom) in toluene (left) and benzonitrile (right). Spectra and kinetics are extracted from the data (points) and from the global fit (lines). Pump scatter has been removed for clarity.

In benzonitrile, TIPS-BT1 undergoes substantial evolution with a 50 ps lifetime (Figure 4.12). A new ESA feature emerges with its peak in UV (the feature begins near 390 nm and continues outside of the 360 nm window of the experiment) and a second ESA appears with onset near 550 nm. There is a concurrent loss of ESA throughout the region between 400 nm and 550 nm where a singlet ESA is present in the monomer (in both solvents, see Figure 4.11) and the dimer (in toluene, see Figure 4.12), and where the singlets $S_{1\text{-dim}}$ and/or $S_{1\text{-loc}}$ could thus reasonably be expected to absorb. There is an additional loss of stimulated emission to the red of 550 nm, further signifying a loss of singlet population. All of these characteristics are consistent with the formation of an intermolecular CT state (as determined via spectroelectrochemistry; see Figure 4.10) at the expense of an emissive singlet-like state. A rapid (47 ps lifetime) loss of emission is also observed in preliminary picosecond fluorescence measurements in support of this conclusion (see Appendix B). The CT formation timescale τ_{CT} = 50 ps suggests that the coupling between the emissive singlet and CT is fairly strong, while a lack of complete conversion (singlet features are still present after the 50 ps process has completed) suggests that multiple states exist in equilibrium. The emission data showed no evidence of any state in equilibrium with $S_{1\text{-loc}}$, while there was strong evidence for a buried dark state in equilibrium with $S_{1\text{-dim}}$; for that reason, we conclude that CT is coupled to $S_{1\text{-dim}}$ (not $S_{1\text{-loc}}$), and that this coupling persists for the duration of the $S_{1\text{-dim}}$ decay. This is confirmed by subsequent long-time TA measurements (*vide infra*). Finally, the relative energies of CT and $S_{1\text{-dim}}$ (that CT lies below $S_{1\text{-dim}}$) are evident from the observed temperature-dependence of Φ_{em} and τ_{dim} (increasing with temperature and decreasing with temperature, respectively, *vide supra*). It is reasonable to expect that the 50 ps lifetime of this process would not be evident in the TRPL experiment, and thus the model presented here to explain the fsTA findings is fully consistent with a thermally-controlled equilibrium between a bright $S_{1\text{-dim}}$ and a dark CT.

As a final observation in the fsTA, the dimer exhibits a small amount of sub-picosecond decay in both solvents. This behavior is highlighted in Figure 4.13, which shows single-feature kinetics (and accompanying fits) for TIPS-Tc and TIPS-BT1 in toluene and benzonitrile. Fits are also shown, derived from a single exponentially modified Gaussian in the case of the monomer (lifetime ~10 ns) and a sum of two exponentially-modified Gaussians in the dimer (for which the longer component was ~20 ns). On this timescale (which occurs well before CT formation in benzonitrile), the dimer exhibits a small relaxation (behavior near 430 nm is shown) in both solvents and with similar lifetimes τ_{rel}. In toluene, τ_{rel} = 850 fs (kinetics shown at 429 nm, the peak of the blue ESA) while in benzonitrile, τ_{rel} = 675 fs (kinetics shown at 433 nm, the same ESA peak). There are no such early relaxation kinetics evident in TIPS-Tc (additional early kinetics for both molecules are provided in Appendix B), suggesting that this feature is unique to the interaction of the chromophore arms in the dimer.

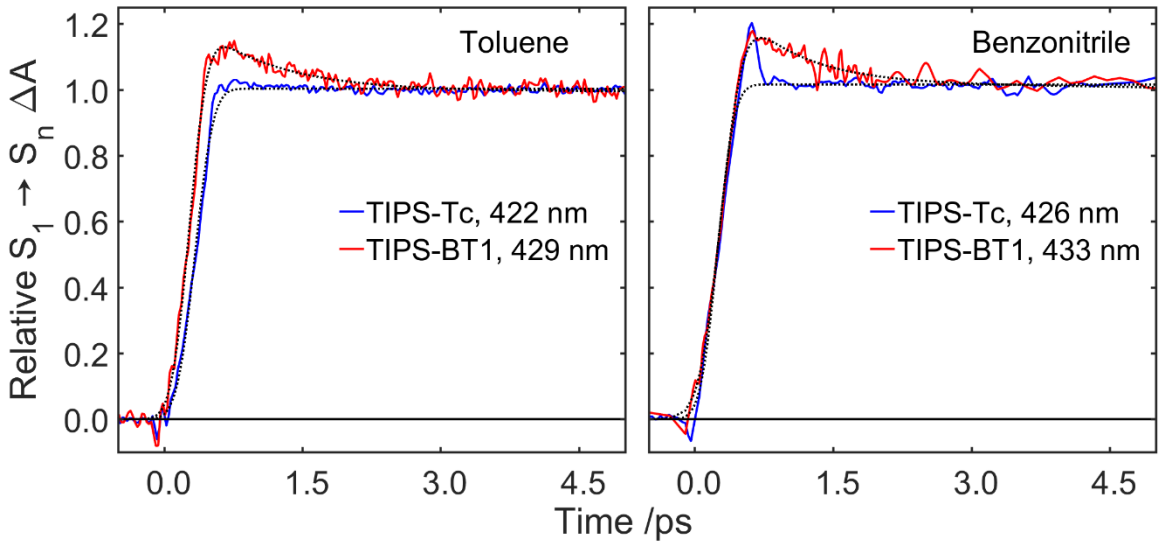

Figure 4.13. Single-feature kinetics extracted from the fsTA data of TIPS-Tc (blue) and TIPS-BT1 (red). These kinetics show the early behavior of an $S_1 \rightarrow S_n$ ESA after excitation at 530 nm. Fits to a single (sum of two) exponentially modified Gaussian function(s) are shown as dashed lines for TIPS-Tc (TIPS-BT1). The rapid spike (~100 fs) in the benzonitrile data for TIPS-Tc is ascribed to a coherent artifact rather than an ultrafast process in the TIPS-Tc.

One possible explanation for this sub-picosecond behavior is the establishment of a solvent shell around the excited state that is slowed in the dimer (relative to the monomer) due to solvent molecules interacting with both arms of the dimer. A second, unlikely possibility is that the first step of ultrafast SF occurs in the dimer to give the multiexcitonic ^{1}TT state in equilibrium with the emissive singlet in less than 1 ps. The reactant state in toluene would be the S_1 (no other emissive state was observed), explaining the apparent halving of k_r and k_{nr}, while the reactant would be $S_{1\text{-}dim}$ in benzonitrile (since the lifetime of $S_{1\text{-}loc}$ matches that of the monomer, ruling out an equilibrium between that state and ^{1}TT, and subsequent nanosecond measurements do not implicate a fourth transient species with a distinct lifetime, *vide infra*). In this picture, the spectral character of the triplet pair would need to be similar to that of the singlet in the visible, a claim that has been made in the literature for related Tc- and Pc-derived dimers.[18,19,21,22] Given the C_{2v} symmetry of TIPS-BT1, ultrafast SF on a sub-picosecond is unexpected,[24,45] but not impossible. To confirm that the CT character is uniquely linked to the longer-lived $S_{1\text{-}dim}$ and to rule out long-lived non-emissive transients such as the ^{1}TT state and/or T_1, nsTA measurements were performed on TIPS-BT1 in both toluene and benzonitrile.

4.6.3 Nanosecond Transient Absorption Experiment

The following nsTA measurements were carried out on two distinct Ultrafast Systems EOS Sub-Nanosecond TA Spectrometers. Experiments at the National Renewable Energy Laboratory (for which the author acknowledges the assistance of Dr. Dylan Arias and Dr. Justin Johnson) used a Coherent Libra amplified Ti:sapphire laser, while experiments at the University of Colorado (for which the author acknowledges the assistance of James Utterback and Orion Pearce) used a Spectra-Physics Solstice amplified Ti:sapphire laser. In both cases, excitation pulses were derived from a TOPAS-C optical parametric amplifier (100nJ pulse energy, 1 kHz repetition rate, ~100 fs

pulse duration, 530 nm center wavelength). Excitation spot size was 270 μm (full-width at half maximum), with fluences of ~500uJ/cm^3. Samples were prepared in 2-mm quartz cuvettes (with Kontes HI-VAC® vacuum-valves) and bubble-degassed with argon for 30 minutes prior to sealing. Sample integrity was verified before and after data acquisition via steady-state absorption spectroscopy. Finally, data was background-subtracted and chirp-corrected using Ultrafast Systems Surface Xplorer software before global fitting in Matlab.

4.6.4 Nanosecond Behavior and Triplet Yield

Findings from nsTA measurements are shown in Figure 4.14 as normalized TA surfaces, followed by spectra extracted from the data and from the global fit. In toluene, S_1 forms during the instrument rise and survives alone for 23.4 ns (consistent with the 25.1 ns lifetime from TRPL) before apparently returning to the ground state without any formation of long-lived species (such as isolated triplets). In benzonitrile, two species (with lifetimes of 13.7 ns and 67.4 ns) are identified by global fitting to a sum of two exponentials. The lifetimes here agree with those from TRPL, and their assignments are therefore retained, with the faster component corresponding directly to $S_{1\text{-loc}}$ and the slower-decaying component assigned to the equilibrium between $S_{1\text{-dim}}$ and CT (with the dark CT state now visible in the nsTA). Their transient spectra are shown in Figure 4.15

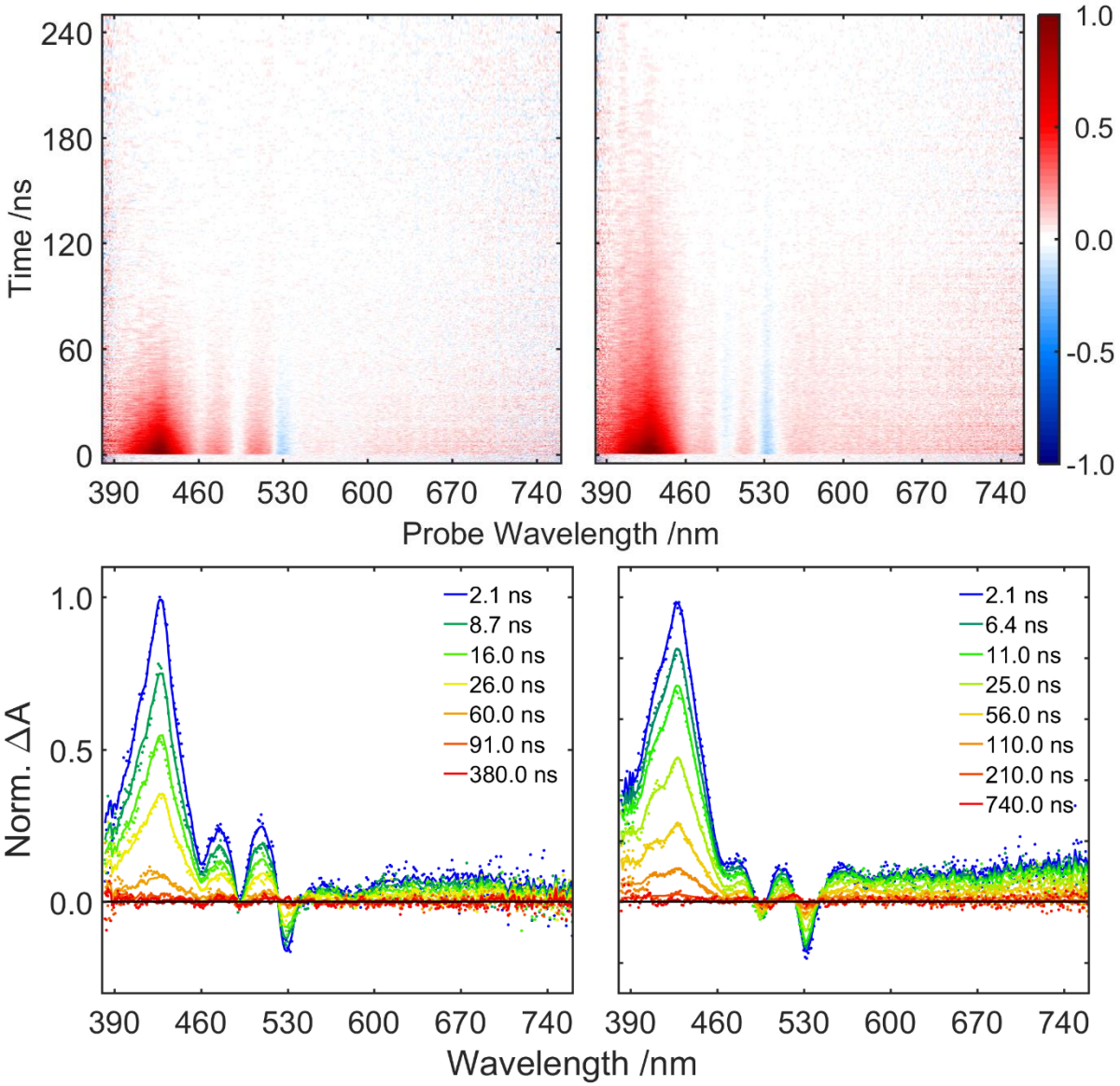

Figure 4.14. Top: full nsTA surfaces showing the normalized TA behavior of TIPS-BT1 in toluene (left) and benzonitrile (right) following 530 nm excitation over the first 240 ns. Bottom: spectra extracted from the data (points) and from the global fit (lines) at the indicated times.

Comparative spectra are shown in Figure 4.15 from fits to the fsTA and nsTA data, and the constituent species for each spectrum are labeled. For the nsTA, the DAS are given since the two components do not interconvert (as determined from the temperature-dependent TRPL and photoluminescence measurements, *vide supra*). For the fsTA, an early-time and a late time spectrum (taken from the start and end of the global fit) are shown, since the DAS do not directly

correspond to species. The spectral characteristics present are consistent between the two experiments. The CT character that is developed in the fsTA regime (the growth features whose formation occurred in τ_{CT} = 50 ps in the fsTA) is evident in the long-lifetime $S_{1\text{-dim}}$ + CT component of the nsTA, but absent from the short-lifetime $S_{1\text{-loc}}$ component, in which neither the UV ESA nor the 560 nm ESA are present. The fact that these CT features persist for the full lifetime of the long-lived spectral component (whose lifetime matches the emissive $S_{1\text{-dim}}$) confirms that the temperature-sensitive equilibrium is between CT and $S_{1\text{-dim}}$. Finally, both $S_{1\text{-loc}}$ and $S_{1\text{-dim}}$ + CT appear to return to the ground state without creation of significant long-lived population (such as isolated triplets).

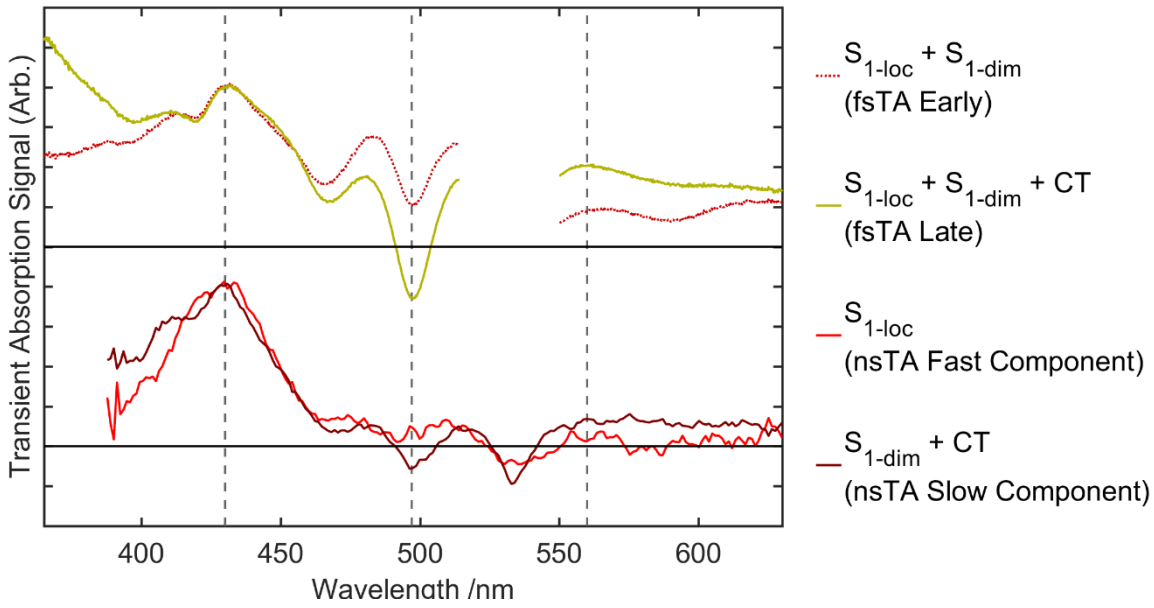

Figure 4.15. Normalized (to the ~430 nm ESA) spectra from global fits of TIPS-BT1 in benzonitrile. Top: fsTA spectra extracted from the beginning (red dotted line, contains contributions from $S_{1\text{-loc}}$ and $S_{1\text{-dim}}$) and end (yellow solid line, contains contributions from $S_{1\text{-loc}}$, $S_{1\text{-dim}}$, and CT) of the global fit. Bottom: nsTA basis spectra for the short-lifetime component (red, pure $S_{1\text{-loc}}$) and long-lifetime component (dark red, $S_{1\text{-dim}}$ + CT) from the nsTA experiment. Vertical dashed lines show alignment of 433 nm ESA, 498 nm GSB, and 560 nm ESA between species (as applicable).

To estimate the ISC triplet yield, and thus confirm that no substantial triplet formation occurs in either solvent, a sensitized triplet spectrum for the TIPS-BT1 triplet (T_1) was obtained with accompanying transient molar attenuation coefficient. Triplet sensitization[46] was performed by doping a sample with anthracene, for which the triplet energy $E(T_{1,An}) \approx 1.8$ eV[47] should be ample for enabling $T_{1,An} \rightarrow T_1$ energy transfer on a collisional (microsecond) timescale. The anthracene-doped TIPS-BT1 sample was excited at 360 nm, resulting in minimal excited TIPS-BT1 (which was accounted for during fitting). The resulting spectral evolution was globally fit to a sum of 4 exponentials for which the associated processes are: efficient intersystem crossing in anthracene[48] from the initially excited singlet ($S_{1,An}$) to the triplet ($T_{1,An}$) in 3.4 ns; co-excited TIPS-BT1 S_1 decay to the ground state in 21 ns; $T_{1,An}$ triplet-to-triplet energy transfer to form TIPS-BT1 T_1 (7.52 μs); and decay of the TIPS-BT1 T_1 to the ground state (~960 μs, outside the window of the experiment). Full spectral data and the global fit are shown in Appendix B, while the retrieved basis spectrum for the TIPS-BT1 T_1 with associated molar attenuation coefficient is shown in Figure 4.16.

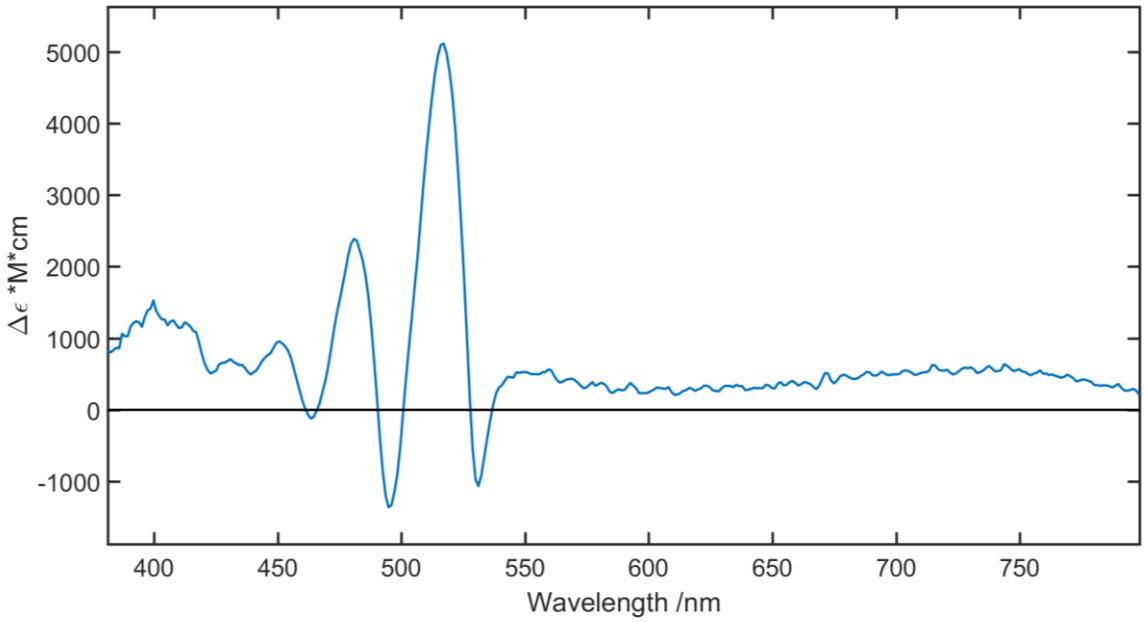

Figure 4.16. Sensitized transient spectrum of T_1 for TIPS-BT1 in toluene with accompanying ground-state bleach features (that is, this spectrum includes contributions from ground state bleach, as expected for a T_1 state formed through SF or ISC).

The triplet features identified by sensitization are essentially absent in the nsTA data of TIPS-BT1 in toluene and benzonitrile at long times. Estimation based on the signal-to-noise ratio and the initially excited singlet population in the TA suggests that the overall triplet yield (Φ_{Trip}) is at most 6% in both solvents. This rules out appreciable singlet → triplet ISC as well as significant T_1 formation from the final step of SF (the breakdown of the multiexcitonic ^{1}TT state into two separate triplets). The results from these and the previously discussed TA measurements are summarized in Table 4.7. With this information, it is now possible to assemble a complete model for the photophysics of TIPS-BT1 in both solvents.

Table 4.7. Transient lifetimes and yields for TIPS-Tc and TIPS-BT1 in solution[a]

	TIPS-Tc	TIPS-BT1
$1/\tau_{CT} \times s$	None	None **2.0×10^{10}**
τ_{rel} /fs	None	850 **675**
Φ_{Trip}	< 6%[b]	< 6% **< 6%**

[a]Unbolded values are from toluene solution and bolded values are from benzonitrile solution.
[b]Value from chloroform solution, estimated by Stern et al.[31]

4.7 Photophysical Model for TIPS-BT1

From the experiments summarized in this chapter, the following model is proposed based on consistency with observed behavior. TIPS-BT1 in toluene absorbs into and subsequently emits from a single electronic state that is accessed by a Franck–Condon absorption, and this occurs with minimal competition from other non-radiative processes like internal conversion. There is only one emissive species (with a high quantum yield) that shows no apparent temperature dependence to indicate either a buried or a high-energy dark state (like the ^{1}TT), so that any dark state would need to be isoergic or nearly isoergic (and also have negligible loss pathways). In the TA data (on the femtosecond to nanosecond timescale) only two processes are observed: a small sub-picosecond relaxation and a long-lifetime decay that tracks the observed emission. The sub-picosecond feature is unlikely to be derived from SF for two important reasons: first, the driving force must be near zero as stated above; second, the diabatic coupling for SF should be poor (zero at the equilibrium geometry) due to the symmetry of TIPS-BT1, which it shares with BT1. As in BT1 (see Chapter 3), a nodal plane in the monomer orbitals is shared between the two chromophore arms such that the diabatic electronic coupling matrix elements that link S_1 and ^{1}TT (whether

directly or through use of a CT state) vanish.[24] Thus TIPS-BT1 in toluene does not undergo any measureable SF in solution, and behaves with photophysics that are otherwise very similar to those of the TIPS-Tc monomer.

In benzonitrile, the polar solvent environment lowers the energy of the TIPS-BT1 intramolecular CT state and enables the formation of two distinct emissive singlet states: the arm-localized and monomer-like $S_{1\text{-loc}}$ and the dimer-delocalized $S_{1\text{-dim}}$. The monomer-like $S_{1\text{-loc}}$ decays independently to the ground state with a monomer-like lifetime and emission spectrum, and has no apparent communication with any other state after its formation. The delocalized emissive state ($S_{1\text{-dim}}$) is strongly coupled to a lower-energy CT state, and accordingly an equilibrium is established between the two on a 50 ps timescale (fully independent of $S_{1\text{-loc}}$ as determined from combined fsTA and nsTA measurements in addition to temperature-dependent TRPL measurements). Thermal repopulation of $S_{1\text{-dim}}$ from CT is readily allowed, and the two states decay together with a lifetime that is separate from $S_{1\text{-loc}}$. As in toluene, formation of long-lived triplets does not occur in benzonitrile whether from ISC or any SF (determined based on triplet sensitization measurements).

Figure 4.17 shows a cartoon of proposed potential energy curves for TIPS-BT1 in benzonitrile, where two separate emissive singlets coexist with a CT trap state (as observed experimentally). The pictured coordinate $q_{F\text{-}C}$ is the Franck–Condon active displacement evident in the absorption and emission spectra of the dimer. The two emissive singlet states $S_{1\text{-dim}}$ (dark red) and $S_{1\text{-loc}}$ (light red) are shown at their approximate experimental energies (taken from their emission spectra), while CT has been placed ~100 meV below their average, estimated using CV (see Section 4.5). The curvature and vibrational levels were estimated from the vibronic progression in the experimental absorption, with the potential well of the delocalized $S_{1\text{-dim}}$

adjusted to be slightly wider than that of the monomer-like $S_{1\text{-loc}}$. The potential minima for $S_{1\text{-loc}}$ and $S_{1\text{-dim}}$ were estimated based on their emission shapes, with $S_{1\text{-dim}}$ slightly more displaced than $S_{1\text{-mon}}$, based on the 0–0 and 0–1 ratios in those emission spectra. Finally, the curvature of CT was broadened to reflect the fact that both monomer arms have reduced bonding character (due to filling of an antibonding orbital in the reduced arm and due to removal of an electron from a bonding orbital in the oxidized arm). CT need not be accessed along $q_{F\text{-}C}$ (e.g. it may instead be accessed along a separate, primarily solvent-related coordinate in the polar benzonitrile environment), though it is shown here to emphasize its nesting with $S_{1\text{-dim}}$. These potential curves reproduce the behavior observed experimentally, with $S_{1\text{-dim}}$ and $S_{1\text{-loc}}$ weakly coupled to one another (and thus not able to interconvert) while CT is connected only to $S_{1\text{-dim}}$. Equilibrium between $S_{1\text{-dim}}$ and CT is thus possible independent of relatively fast $S_{1\text{-loc}}$ decay to S_0.

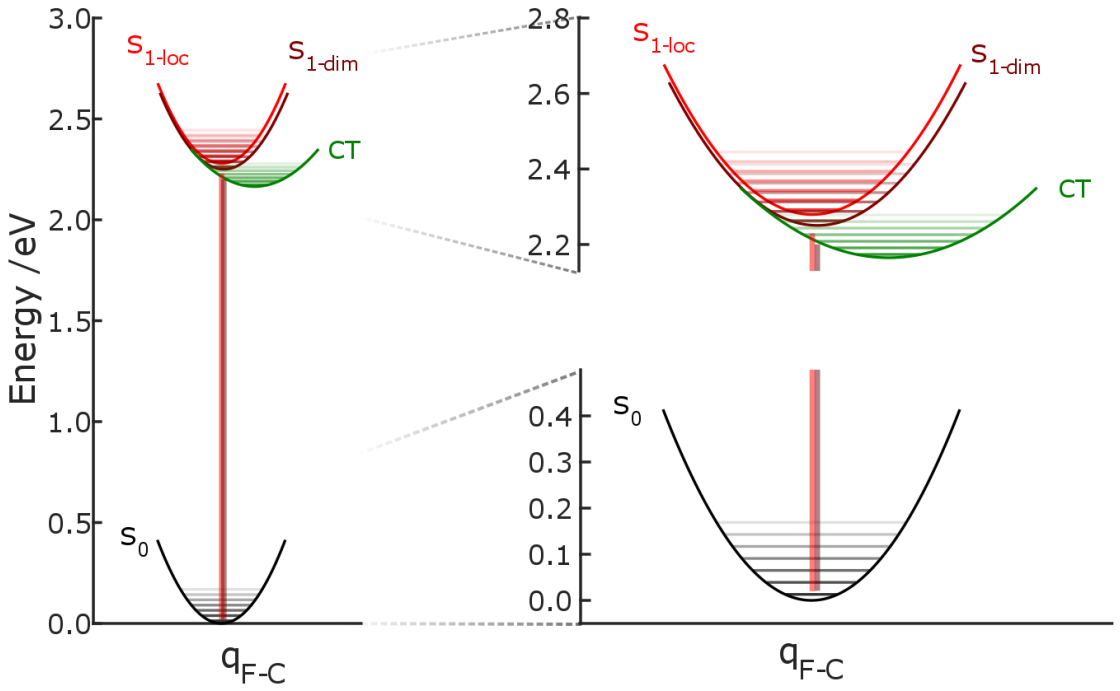

Figure 4.17. Proposed potential energy curves for TIPS-BT1 in benzonitrile, along the Franck–Condon active coordinate. Energetics, curvature and vibrational spacing were estimated from experimental emission and absorption measurements (see text). Very weak coupling between $S_{1\text{-loc}}$ and $S_{1\text{-dim}}$ (evident from their close spacing, as determined from emission data) prevents appreciable interconversion, while CT is readily accessible from $S_{1\text{-dim}}$. The ground (S_0) state is shown in black.

4.8 Conclusion and Future Directions

Independent of the mechanism, TIPS-BT1 returns to its ground state rather quickly (<70 ns) in both solvents with no evidence for triplet formation at long times. Lowering the energy of the CT state by moving to a polar solvent does not appear to have enabled SF in TIPS-BT1, and instead appears to have create a trap state (others have variously observed trapping or SF enhancement by changing CT energetics in Pc and terrylene bis(dicarboximide) dimers[10,19,21,30]). This contributes to the growing body of evidence that the specific energy of CT plays a major role in enabling or preventing SF. Here, when the energy of CT is too high, SF is forbidden due to weak coupling, but when its energy is lowered too far, it instead becomes a trap, preventing SF in a different

manner. Perhaps through exploration of additional solvent environments of intermediate polarity, or in mixed solvent systems, it may be possible to find an ideal CT state energy that enables SF, in the event that the energy of ^{1}TT is appropriate.

As a platform for informing future studies, TIPS-BT1 has extensive promise. As a parent chromophore, it is far more extensible than BT1 due to its improved solubility and stability. This, in combination with a significantly slower non-radiative loss rate (in contrast to unsubstituted BT1, for which ISC in particular is quite fast) makes TIPS-BT1 a useful advance over BT1 as a parent molecule for subsequent studies. TIPS-BT1 is thus a better control molecule against which to compare subsequent species. Interesting motifs for subsequent investigations include three main categories: symmetric Pc dimers (e.g. dimers whose symmetry prevents large diabatic coupling); dimers with asymmetry derived from either changes in bridge connectivity or substitution of carbon atoms with nitrogen (for which the diabatic coupling between S_1 and ^{1}TT can be significantly greater than the transient couplings available here[4,45]); and asymmetric Pc dimers, for which energetic driving force and efficient coupling should work in concert to provide highly efficient SF.

Individually, each of these motifs is interesting, but their analysis as a set provides a more comprehensive picture. That is the true purpose of these studies on TIPS-BT1. Through comparison with TIPS-BT1, symmetric Pc dimers should isolate the role of energetics in facilitating otherwise forbidden (by symmetry) SF, an area which (given the conformational flexibility present in other dimer systems[10,17–22,30,49–53]) is largely unexplored. Studies of asymmetric Tc dimers will allow for comparison of predicted SF rates against experiment, testing theories about diabatic coupling in the absence of statistical effects like entropy that complicate behavior in solid materials.[54,55] Finally, asymmetric Pc dimers should give rise to very fast and

efficient SF and allow for testing of the limits of efficient SF in the solution phase, informing future work on dye-sensitized solar cells (and other motifs) that aim to harness the energy-generation potential of SF.

4.9 Bibliography

1. Carey, T. J., Snyder, J. L., Miller, E. G., Sammakia, T. & Damrauer, N. H. Synthesis of Geometrically Well-Defined Covalent Acene Dimers for Mechanistic Exploration of Singlet Fission. *J. Org. Chem.* acs.joc.7b00602 (2017).
2. Fudickar, W. & Linker, T. Why Triple Bonds Protect Acenes from Oxidation and Decomposition. *J. Am. Chem. Soc.* **134,** 15071–15082 (2012).
3. Frisch, M. J. *et al.* Gaussian 09, Revision A.1. (2009).
4. Vallett, P. J., Snyder, J. L. & Damrauer, N. H. Tunable electronic coupling and driving force in structurally well-defined tetracene dimers for molecular singlet fission: a computational exploration using density functional theory. *J. Phys. Chem. A* **117,** 10824–38 (2013).
5. Burdett, J. J., Müller, A. M., Gosztola, D. & Bardeen, C. J. Excited state dynamics in solid and monomeric tetracene: The roles of superradiance and exciton fission. *J. Chem. Phys.* **133,** 144506 (2010).
6. Griffith, O. L., Jones, A. G., Anthony, J. E. & Lichtenberger, D. L. Intermolecular Effects on the Hole States of Triisopropylsilylethynyl-Substituted Oligoacenes. *J. Phys. Chem. C* **114,** 13838–13845 (2010).
7. Lobanova Griffith, O., Gruhn, N. E., Anthony, J. E., Purushothaman, B. & Lichtenberger, D. L. Electron Transfer Parameters of Triisopropylsilylethynyl-Substituted Oligoacenes. *J. Phys. Chem. C* **112,** 20518–20524 (2008).
8. Maliakal, A., Raghavachari, K., Katz, H., Chandross, E. & Siegrist, T. Photochemical Stability of Pentacene and a Substituted Pentacene in Solution and in Thin Films. *Chem. Mater.* **16,** 4980–4986 (2004).
9. Bhattacharyya, K. & Datta, A. Polymorphism Controlled Singlet Fission in TIPS-

Anthracene: Role of Stacking Orientation. *J. Phys. Chem. C* **121,** 1412–1420 (2017).

10. Lukman, S., Chen, K., Hodgkiss, J. M., Turban, D. H. P., Hine, N. D. M., Dong, S., Wu, J., Greenham, N. C. & Musser, A. J. Tuning the role of charge-transfer states in intramolecular singlet exciton fission through side-group engineering. *Nat. Commun.* **7,** 13622 (2016).
11. Fuemmeler, E. G., Sanders, S. N., Pun, A. B., Kumarasamy, E., Zeng, T., Miyata, K., Steigerwald, M. L., Zhu, X.-Y., Sfeir, M. Y., Campos, L. M. & Ananth, N. A Direct Mechanism of Ultrafast Intramolecular Singlet Fission in Pentacene Dimers. *ACS Cent. Sci.* **2,** 316–324 (2016).
12. Gouterman, M. Spectra of porphyrins. *J. Mol. Spectrosc.* **6,** 138–163 (1961).
13. Platt, J. R. Classification of Spectra of Cata-Condensed Hydrocarbons. *J. Chem. Phys.* **17,** 484 (1949).
14. Cook, J. D., Carey, T. J. & Damrauer, N. H. Solution-Phase Singlet Fission in a Structurally Well-Defined Norbornyl-Bridged Tetracene Dimer. *J. Phys. Chem. A* **120,** 4473–4481 (2016).
15. Spano, F. C. The Spectral Signatures of Frenkel Polarons in H- and J-Aggregates. *Acc. Chem. Res.* **43,** 429–439 (2010).
16. Johnson, J. C., Nozik, A. J. & Michl, J. The Role of Chromophore Coupling in Singlet Fission. *Acc. Chem. Res.* **46,** 1290–1299 (2013).
17. Sanders, S. N., Kumarasamy, E., Pun, A. B., Trinh, M. T., Choi, B., Xia, J., Taffet, E. J., Low, J. Z., Miller, J. R., Roy, X., Zhu, X.-Y., Steigerwald, M. L., Sfeir, M. Y. & Campos, L. M. Quantitative Intramolecular Singlet Fission in Bipentacenes. *J. Am. Chem. Soc.* **137,** 8965–8972 (2015).
18. Korovina, N. V., Das, S., Nett, Z., Feng, X., Joy, J., Haiges, R., Krylov, A. I., Bradforth, S.

E. & Thompson, M. E. Singlet Fission in a Covalently Linked Cofacial Alkynyltetracene Dimer. *J. Am. Chem. Soc.* **138,** 617–627 (2016).

19. Zirzlmeier, J., Lehnherr, D., Coto, P. B., Chernick, E. T., Casillas, R., Basel, B. S., Thoss, M., Tykwinski, R. R. & Guldi, D. M. Singlet fission in pentacene dimers. *Proc. Natl. Acad. Sci.* **112,** 5325–5330 (2015).

20. Sakuma, T., Sakai, H., Araki, Y., Mori, T., Wada, T., Tkachenko, N. V. & Hasobe, T. Long-Lived Triplet Excited States of Bent-Shaped Pentacene Dimers by Intramolecular Singlet Fission. *J. Phys. Chem. A* **120,** 1867–1875 (2016).

21. Zirzlmeier, J., Casillas, R., Reddy, S. R., Coto, P. B., Lehnherr, D., Chernick, E. T., Papadopoulos, I., Thoss, M., Tykwinski, R. R. & Guldi, D. M. Solution-based intramolecular singlet fission in cross-conjugated pentacene dimers. *Nanoscale* **8,** 10113–10123 (2016).

22. Lukman, S., Musser, A. J., Chen, K., Athanasopoulos, S., Yong, C. K., Zeng, Z., Ye, Q., Chi, C., Hodgkiss, J. M., Wu, J., Friend, R. H. & Greenham, N. C. Tuneable Singlet Exciton Fission and Triplet-Triplet Annihilation in an Orthogonal Pentacene Dimer. *Adv. Funct. Mater.* **25,** 5452–5461 (2015).

23. Scholes, G. D., Ghiggino, K. P., Oliver, A. M. & Paddon-Row, M. N. Through-space and through-bond effects on exciton interactions in rigidly linked dinaphthyl molecules. *J. Am. Chem. Soc.* **115,** 4345–4349 (1993).

24. Alguire, E. C., Subotnik, J. E. & Damrauer, N. H. Exploring Non-Condon Effects in a Covalent Tetracene Dimer: How Important Are Vibrations in Determining the Electronic Coupling for Singlet Fission? *J. Phys. Chem. A* **119,** 299–311 (2015).

25. Reichardt, C. Solvatochromic Dyes as Solvent Polarity Indicators. *Chem. Rev.* **94,** 2319–

2358 (1994).

26. Haynes, W. M. *CRC Handbook of Chemistry and Physics, 97th Edition (Internet Version 2017)*. (CRC Press/Taylor & Francis).

27. Yang, Y., Davidson, E. R. & Yang, W. Nature of ground and electronic excited states of higher acenes. *Proc. Natl. Acad. Sci.* **113,** E5098–E5107 (2016).

28. Lewis, J. E. & Maroncelli, M. On the (uninteresting) dependence of the absorption and emission transition moments of coumarin 153 on solvent. *Chem. Phys. Lett.* **282,** 197–203 (1998).

29. Swenberg, C. E. & Pope, M. *Electronic Processes in Organic Crystals and Polymers*. (Oxford University Press, 1999).

30. Margulies, E. A., Miller, C. E., Wu, Y., Ma, L., Schatz, G. C., Young, R. M. & Wasielewski, M. R. Enabling singlet fission by controlling intramolecular charge transfer in π-stacked covalent terrylenediimide dimers. *Nat. Chem.* **8,** 1120–1125 (2016).

31. Stern, H. L., Musser, A. J., Gelinas, S., Parkinson, P., Herz, L. M., Bruzek, M. J., Anthony, J., Friend, R. H. & Walker, B. J. Identification of a triplet pair intermediate in singlet exciton fission in solution. *Proc. Natl. Acad. Sci.* **112,** 7656–7661 (2015).

32. Wilson, M. W. B., Rao, A., Johnson, K., Gélinas, S., di Pietro, R., Clark, J. & Friend, R. H. Temperature-Independent Singlet Exciton Fission in Tetracene. *J. Am. Chem. Soc.* **135,** 16680–16688 (2013).

33. Burdett, J. J. & Bardeen, C. J. The Dynamics of Singlet Fission in Crystalline Tetracene and Covalent Analogs. *Acc. Chem. Res.* **46,** 1312–1320 (2013).

34. Smith, M. B. & Michl, J. Singlet Fission. *Chem. Rev.* **110,** 6891–6936 (2010).

35. van Stokkum, I. H. M., Larsen, D. S. & van Grondelle, R. Global and target analysis of

time-resolved spectra. *Biochim. Biophys. Acta* **1657,** 82–104 (2004).

36. Burgdorff, C., Ehrhardt, S. & Loehmannsroeben, H. G. Photophyslcal Properties of Tetracene Derivatives in Solution. 2. Halogenated Tetracene Derivatives. *J. Phys. Chem.* **95,** 4246–4249 (1991).
37. Lakowicz, J. R. *Principles of Fluorescence Spectroscopy*. (Springer US, 2006).
38. Caspar, J. V & Meyer, T. J. Application of the Energy Gap Law to Excited-State Decay. *J. Phys. Chem.* **87,** 952–957 (1983).
39. Englman, R. & Jortner, J. The energy gap law for radiationless transitions in large molecules. *Mol. Phys.* **18,** 145–164 (1970).
40. Fletcher, A. N. & Bliss, D. E. Laser dye stability. Part 5. *Appl. Phys.* **16,** 289–295 (1978).
41. Van der Auweraer, M., Grabowski, Z. R. & Rettig, W. Molecular structure and the temperature-dependent radiative rates in Twisted Intramolecular Charge-Transfer and exciplex systems. *J. Phys. Chem.* **95,** 2083–2092 (1991).
42. Noviandri, I., Brown, K. N., Fleming, D. S., Gulyas, P. T., Lay, P. a, Masters, A. F. & Phillips, L. The Decamethylferrocenium/Decamethylferrocene Redox Couple: A Superior Redox Standard to the Ferrocenium/Ferrocene Redox Couple for Studying Solvent Effects on the Thermodynamics of Electron Transfer. *J. Phys. Chem. B* **103,** 6713–6722 (1999).
43. Pavlishchuk, V. V. & Addison, A. W. Conversion constants for redox potentials measured versus different reference electrodes in acetonitrile solutions at 25°C. *Inorganica Chim. Acta* **298,** 97–102 (2000).
44. Trasatti, S. The absolute electrode potential: an explanatory note (Recommendations 1986). *Pure Appl. Chem.* **58,** (1986).
45. Damrauer, N. H. & Snyder, J. L. Symmetry-Directed Control of Electronic Coupling for

Singlet Fission in Covalent Bis–Acene Dimers. *J. Phys. Chem. Lett.* **6,** 4456–4462 (2015).

46. Bonneau, R., Carmichael, I. & Hug, G. L. Molar absorption coefficients of transient species in solution. *Pure Appl. Chem.* **63,** 289–299 (1991).

47. Mcglynn, S. P., Padhye, M. R. & Kasha, M. Lowest Triplet Levels of the Polyacenes. *J. Chem. Phys.* **23,** 593 (1955).

48. Nijegorodov, N., Vasilenko, V., Monowe, P. & Masale, M. Systematic investigation of the influence of methyl groups upon fluorescence parameters and the intersystem crossing rate constant of aromatic molecules. *Spectrochim. Acta. A. Mol. Biomol. Spectrosc.* **74,** 188–94 (2009).

49. Müller, A. M., Avlasevich, Y. S., Schoeller, W. W., Müllen, K. & Bardeen, C. J. Exciton Fission and Fusion in Bis(tetracene) Molecules with Different Covalent Linker Structures. *J. Am. Chem. Soc.* **129,** 14240–14250 (2007).

50. Johnson, J. C., Akdag, A., Zamadar, M., Chen, X., Schwerin, A. F., Paci, I., Smith, M. B., Havlas, Z. Z., Miller, J. R., Ratner, M. A., Nozik, A. J. & Michl, J. Toward designed singlet fission: Solution photophysics of two indirectly coupled covalent dimers of 1,3-diphenylisobenzofuran. *J. Phys. Chem. B* **117,** 4680–4695 (2013).

51. Walker, B. J., Musser, A. J., Beljonne, D. & Friend, R. H. Singlet exciton fission in solution. *Nat. Chem.* **5,** 1019–1024 (2013).

52. Margulies, E. A., Shoer, L. E., Eaton, S. W. & Wasielewski, M. R. Excimer formation in cofacial and slip-stacked perylene-3,4:9,10-bis(dicarboximide) dimers on a redox-inactive triptycene scaffold. *Phys. Chem. Chem. Phys.* **16,** 23735–23742 (2014).

53. Varnavski, O., Abeyasinghe, N., Aragó, J., Serrano-Pérez, J. J., Ortí, E., López Navarrete, J. T., Takimiya, K., Casanova, D., Casado, J. & Goodson, T. High Yield Ultrafast

Intramolecular Singlet Exciton Fission in a Quinoidal Bithiophene. *J. Phys. Chem. Lett.* **6,** 1375–1384 (2015).

54. Teichen, P. E. & Eaves, J. D. Collective aspects of singlet fission in molecular crystals. *J. Chem. Phys.* **143,** 44118 (2015).

55. Kolomeisky, A. B., Feng, X. & Krylov, A. I. A Simple Kinetic Model for Singlet Fission: A Role of Electronic and Entropic Contributions to Macroscopic Rates. *J. Phys. Chem. C* **118,** 5188–5195 (2014).

Chapter 5. Towards Coherent Control of the TIPS-BT1 Covalent Dimer

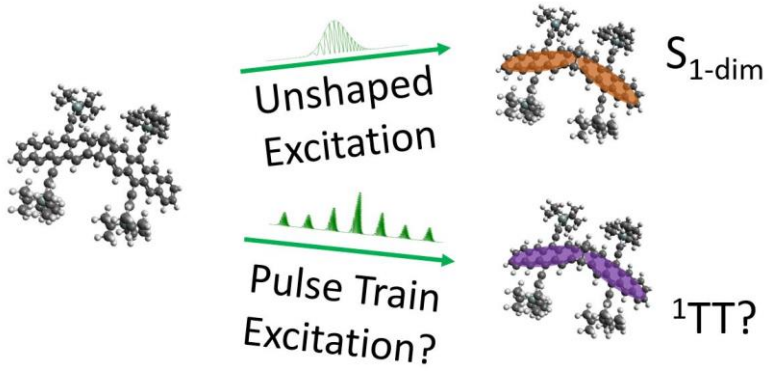

5.1 Extending Control to a Molecular Dimer

In Chapter 4, it was determined that TIPS-BT1 does not form significant triplet (T_1) population at long times. Given that $2 \times T_1$ is the desired product of singlet fission (SF), it would be desirable to better understand why this is the case. The first likely culprit is the relative orientation of the chromophores in TIPS-BT1, which (given the individual arm orbital symmetries and its close relationship to BT1; see also Chapter 3) should cause the diabatic coupling for SF to be statically zero[1,2]. This would imply that SF does not occur to any measurable extent in our experiments due to a slow rate, but that if it were enabled, T_1 population could be created. A second possibility is that the energetics for SF (that is, the difference in energy between the product $2 \times T_1$ and the reactant singlet state) are unfavorable in TIPS-BT1; as it stands, these values are indeterminate due to ambiguity in the energy of the TIPS-BT1 triplet (see Chapter 4). If the reaction is endoergic, strong coupling may give an equilibrium between the product ($2 \times T_1$) and reactant (the initial singlet) that favors the reactant and which decays without obvious spectral evidence for T_1, even if the first step of SF is fast. Here, the first possibility is investigated (that is, the possibility that symmetry gives rise to a zero diabatic coupling) by studying the potential of intermolecular vibrations to break this symmetry and thereby enable coupling. In separate

theoretical work on a closely related system (BT1; see Chapter 3 for discussion of this molecule) Alguire, Subotnik, and Damrauer[2] showed that it was possible for some vibrational modes (those that break the symmetry plane shared between two chromophore arms) to contribute to effective diabatic couplings even in cases where this coupling is zero at the equilibrium geometry. Breaking this symmetry in an active manner (e.g. by driving these vibrations[3]) may be able to substantially increase the rate of SF, and this could in turn alter the emission quantum yield (Φ_{em}), an observable which is readily measured (see below). This was attempted through pulse shaping experiments similar to those in Chapter 2 (but in which a few important modifications were made to mitigate the effects of the SLM-related problems discussed there).

The coherent control experiments here study TIPS-BT1 in toluene (with TIPS-Tc, the monomer discussed alongside TIPS-BT1 in Chapter 4, as a reference system). The observable tracked in these experiments is Φ_{em}, whose value may decrease in the event that initially excited singlets can be directed into a pathway leading to T_1 (such as SF) if the diabatic coupling between these two states can be increased. As discussed at the outset of control efforts in Chapter 2, changing excited state branching ratios through excitation with pulse trains (including for SF[3]) is known in the literature,[3–6] and pulse trains were again explored here. For a more in-depth discussion of control and this choice of pulse shape, refer to Chapter 2. As discussed in Chapter 2, our shaper exhibits changes in both pump power and spot size during phase-only shaping, and only pump power may be readily measured during the experiment (and is in principle correctable simply by normalization if measured simultaneously). To circumvent this problem, the observable Φ_{em} is used here in place of transient absorption signal due to its dependence only on overall pump power (where transient absorption signal, due to pump-probe overlap, depends on spot size as well).

5.1.1 Methods

The method for generating excitation pulses used here was described in Section 4.6.1. Near-transform-limited (35 fs temporal FWHM), 521 ± 18 nm laser pulses (30 nJ/pulse) were shaped using the method that was described in Chapter 2 (using approximately 200 SLM pixels to give a resolution of ~0.3 nm per pixel; see Chapter 2 for further information). Briefly, shaping involved phase-only modulation of input pulses with sinusoidal phase functions whose form is shown in Equation 1.

$$\Phi(\omega_i) = A\cos(\omega_i\tau + \phi) \quad (1)$$

This gives pulse trains for which the parameter A determines the envelope (fixed here at 2.5), ϕ gives the spectral phase of sub-pulses (fixed here at 0) and τ controls the interpulse spacing. These choices were made for reasons described in Chapter 2 based on the work of Grumstrup et al.[3]

Fluorescence was measured using a Thor Labs Amplified Photodiode PDA36A coupled to a Stanford Research SR810 lock-in amplifier synced to the 500 Hz chopper frequency. This was placed immediately behind the sample to detect fluorescence. The detector has a relatively large area (13 mm^2) that was found to be largely insensitive to alignment behind the sample. Pump light was filtered out with a 580 nm band pass filter in a 1” filter tube directly connected to the detector (this resulted in a transmitted pump background signal that was approximately one part in 1000 of the fluorescence signal). A second large-area photodiode (Thor Labs PDA55) coupled to a second identical lock-in amplifier simultaneously measured pump power using a reflection of the pump light from a thin glass cover slip placed immediately before the sample. This light was fully directed onto the photodiode active area using a lens placed at a distance shorter than its focal point to give a smaller, but unfocused beam. Both photodiode signals were tested for linear behavior

with pump power by attenuating unshaped pulses, and both were insensitive to small translations in space.

5.1.2 Findings

Observed emission in toluene is shown as a function of τ (varied between 0 and 700 fs) in Figure 5.1. This should include modes with frequencies as low as 48 cm^{-1}. Data for the monomer TIPS-Tc and the dimer TIPS-BT1 is shown in toluene. Power is also shown in green. As expected (see discussion in Chapter 2), the overall excitation power decreases with increasing interpulse spacing, while the overall emission remains largely unchanged in both molecules, varying by at most ~2% (perhaps due to imperfect power normalization). No significant differences are observed in the dimer relative to the monomer, suggesting that the small phase-dependence is not derived from coherent modulation of inter-chromophore interactions (which are obviously not possible in the dilute monomer solution), but rather due to an experimental source of error such as imperfect power correction. The observed changes are nonetheless quite small and hardly attributable to significant control of the order observed for SF in tetracene films.[3] Repeated experiments with smaller τ spacing likewise gave null results. Additional experiments were attempted using algorithmic control in a search space of random phases (where pixels are grouped together into small blocks to reduce the number of parameters) and these likewise showed no evidence that Φ_{em} could be controlled through phase-shaped excitation.

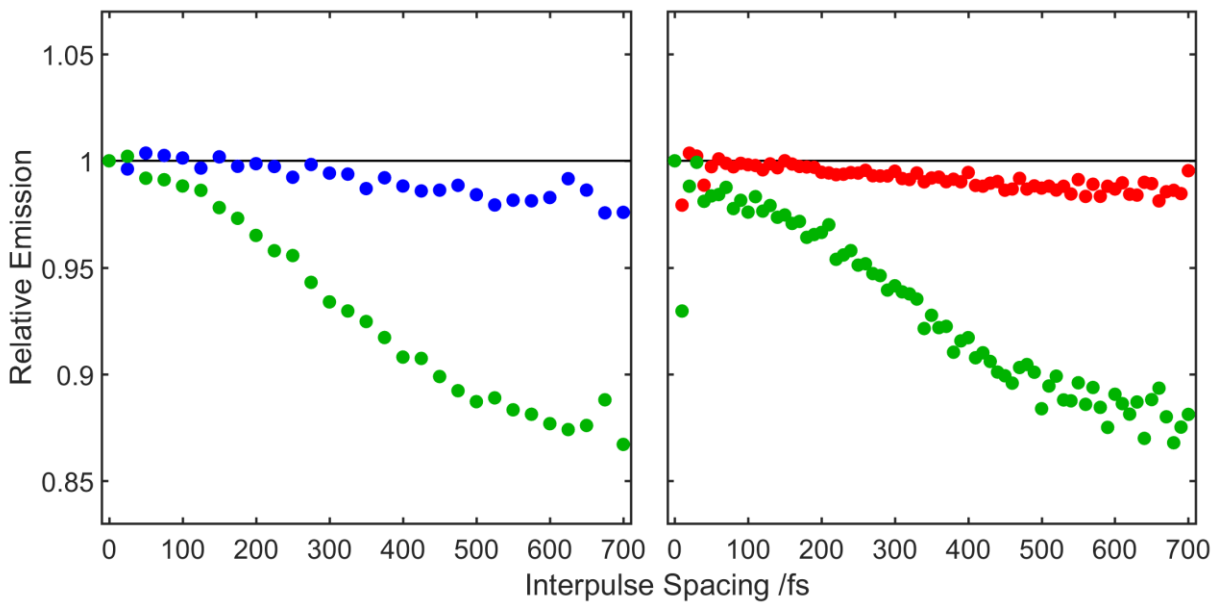

Figure 5.1. Emission (relative to TL pulse excitation) of TIPS-Tc and TIPS-BT1 upon excitation with pulse trains of various interpulse spacings. The power-normalized emission is shown in blue (for TIPS-Tc at left) or red (for TIPS-BT1 at right), while the pump power (relative to a zero-phase pump) is shown in green for both data sets. A line at one shows the reference emission value as a guide.

5.2 Conclusion and Future Directions

Though these laser fields were intended to modulate the interchromophore coupling between the acene arms, the null results here (TIPS-BT1 exhibits the same behavior as the TIPS-Tc monomer) do not preclude control. It should be mentioned here that significant coherent oscillations were not observed in the transient absorption signals of TIPS-BT1 (shown in Chapter 4 for TIPS-BT1 and TIPS-Tc), and it is possible that the 35 fs pulses used here simply do not have access to the frequencies necessary to induce symmetry breaking (significantly shorter pulses, for example, may be better suited to this task). A vibrational analysis of the various modes in TIPS-BT1 and their role in enabling diabatic coupling for SF has not been performed, and the appropriate frequencies for enabling said coupling are therefore not known. This analysis for BT1[2] found multiple coupling-relevant normal modes with frequencies below 480 cm^{-1} (the approximate

frequency limit for the 35 fs excitation pulses used here), however, so it would be somewhat surprising if there were no similarly low-frequency modes in TIPS-BT1 (especially given the addition of the bulky TIPS-acetylene groups). It is possible that a pair of T_1 states is in fact generated by the shaped pulses in these experiments, but that this pair subsequently recombines (with near unity quantum yield) to regenerate the emissive singlet. This would give null results as seen here. This is reasonable behavior if the triplet pair is able to quickly annihilate (since diffusion is not an option) and/or if the energetics favor the singlet state (the former point in particular is important even for non-rigid covalent dimers[7–11]). Finally, it is not inconceivable that there are unexpected consequences to the amplitude shaping that occurs upon attempting phase-only shaping (see Chapter 2) that could preclude otherwise possible control. An interesting extension to this experiment would involve carrying out these same measurements in benzonitrile with the goal of controlling the branching ratio of $S_{1\text{-loc}}$ and $S_{1\text{-dim}}$ in that system, for which a significant change in emission may be possible. These findings nonetheless show that power correction can be applied with steady-state emission to partially circumvent the problems evident in this shaper, and may allow future efforts to explore similar questions in other systems.

5.3 Bibliography

1. Vallett, P. J., Snyder, J. L. & Damrauer, N. H. Tunable electronic coupling and driving force in structurally well-defined tetracene dimers for molecular singlet fission: a computational exploration using density functional theory. *J. Phys. Chem. A* **117,** 10824–38 (2013).
2. Alguire, E. C., Subotnik, J. E. & Damrauer, N. H. Exploring Non-Condon Effects in a Covalent Tetracene Dimer: How Important Are Vibrations in Determining the Electronic Coupling for Singlet Fission? *J. Phys. Chem. A* **119,** 299–311 (2015).
3. Grumstrup, E., Johnson, J. & Damrauer, N. Enhanced Triplet Formation in Polycrystalline Tetracene Films by Femtosecond Optical-Pulse Shaping. *Phys. Rev. Lett.* **105,** 257403 1-4 (2010).
4. Herek, J. L., Wohlleben, W., Cogdell, R. J., Zeidler, D. & Motzkus, M. Quantum control of energy flow in light harvesting. *Nature* **417,** 533–5 (2002).
5. Brüggemann, B., Organero, J. A., Pascher, T., Pullerits, T. & Yartsev, A. Control of Electron Transfer Pathways in a Dye-Sensitized Solar Cell. *Phys. Rev. Lett.* **97,** 208301 (2006).
6. Prokhorenko, V. I., Nagy, A. M., Waschuk, S. a, Brown, L. S., Birge, R. R. & Miller, R. J. D. Coherent control of retinal isomerization in bacteriorhodopsin. *Science* **313,** 1257–61 (2006).
7. Lukman, S., Chen, K., Hodgkiss, J. M., Turban, D. H. P., Hine, N. D. M., Dong, S., Wu, J., Greenham, N. C. & Musser, A. J. Tuning the role of charge-transfer states in intramolecular singlet exciton fission through side-group engineering. *Nat. Commun.* **7,** 13622 (2016).
8. Zirzlmeier, J., Casillas, R., Reddy, S. R., Coto, P. B., Lehnherr, D., Chernick, E. T., Papadopoulos, I., Thoss, M., Tykwinski, R. R. & Guldi, D. M. Solution-based

intramolecular singlet fission in cross-conjugated pentacene dimers. *Nanoscale* **8,** 10113–10123 (2016).

9. Sanders, S. N., Kumarasamy, E., Pun, A. B., Appavoo, K., Steigerwald, M. L., Campos, L. M. & Sfeir, M. Y. Exciton Correlations in Intramolecular Singlet Fission. *J. Am. Chem. Soc.* **138,** 7289–7297 (2016).

10. Margulies, E. A., Miller, C. E., Wu, Y., Ma, L., Schatz, G. C., Young, R. M. & Wasielewski, M. R. Enabling singlet fission by controlling intramolecular charge transfer in π-stacked covalent terrylenediimide dimers. *Nat. Chem.* **8,** 1120–1125 (2016).

11. Korovina, N. V., Das, S., Nett, Z., Feng, X., Joy, J., Haiges, R., Krylov, A. I., Bradforth, S. E. & Thompson, M. E. Singlet Fission in a Covalently Linked Cofacial Alkynyltetracene Dimer. *J. Am. Chem. Soc.* **138,** 617–627 (2016).

Bibliography

Chapter 1

1. IPCC. *Climate Change 2013 - The Physical Science Basis*. (Cambridge University Press, 2014).
2. Cook, T. R., Dogutan, D. K., Reece, S. Y., Surendranath, Y., Teets, T. S. & Nocera, D. G. Solar Energy Supply and Storage for the Legacy and Nonlegacy Worlds. *Chem. Rev.* **110,** 6474–6502 (2010).
3. Lewis, N. S., Crabtree, G., Nozik, A. J., Wasielewski, M. R., Alivisatos, P., Kung, H., Tsao, J., Chandler, E., Walukiewicz, W., Spitler, M., Ellingson, R., Overend, R., Mazer, J., Gress, M., Horwitz, J., Ashton, C., Herndon, B., Shapard, L. & Nault, R. M. *Basic Research Needs for Solar Energy Utilization. Report of the Basic Energy Sciences Workshop on Solar Energy Utilization, April 18-21, 2005*. *Basic Energy Sciences Workshop on Solar Energy Utilization* (2005).
4. Bleich, K. & Guimaraes, R. D. *Renewable Infrastructure Investment Handbook: A Guide for Institutional Investors*. (2016).
5. Shockley, W. & Queisser, H. J. Detailed Balance Limit of Efficiency of p-n Junction Solar Cells. *J. Appl. Phys.* **32,** 510 (1961).
6. Green, M. A. Third generation photovoltaics: Ultra-high conversion efficiency at low cost. *Prog. Photovoltaics Res. Appl.* **9,** 123–135 (2001).
7. Hanna, M. C. & Nozik, A. J. Solar Conversion Efficiency of Photovoltaic and Photoelectrolysis Cells with Carrier Multiplication Absorbers. *J. Appl. Phys.* **100,** 74510 (2006).
8. Zhu, X. Exceeding the Limit in Solar Energy Conversion with Multiple Excitons. *Acc.*

Chem. Res. **46,** 1239–1241 (2013).

9. De Vos, A. & Desoete, B. On the ideal performance of solar cells with larger-than-unity quantum efficiency. *Sol. Energy Mater. Sol. Cells* **51,** 413–424 (1998).
10. Smith, M. B. & Michl, J. Singlet Fission. *Chem. Rev.* **110,** 6891–6936 (2010).
11. Greyson, E. C., Stepp, B. R., Chen, X., Schwerin, A. F., Paci, I., Smith, M. B., Akdag, A., Johnson, J. C., Nozik, A. J., Michl, J. & Ratner, M. A. Singlet Exciton Fission for Solar Cell Applications: Energy Aspects of Interchromophore Coupling. *J. Phys. Chem. B* **114,** 14223–32 (2010).
12. Xia, J., Sanders, S. N., Cheng, W., Low, J. Z., Liu, J., Campos, L. M. & Sun, T. Singlet Fission: Progress and Prospects in Solar Cells. *Adv. Mater.* **28,** 1601652 (2016).
13. Jadhav, P. J., Mohanty, A., Sussman, J., Lee, J. & Baldo, M. a. Singlet Exciton Fission in Nanostructured Organic Solar Cells. *Nano Lett.* **11,** 1495–1498 (2011).
14. Congreve, D. N., Lee, J., Thompson, N. J., Hontz, E., Yost, S. R., Reusswig, P. D., Bahlke, M. E., Reineke, S., Van Voorhis, T. & Baldo, M. A. External Quantum Efficiency Above 100% in a Singlet-Exciton-Fission-Based Organic Photovoltaic Cell. *Science.* **340,** 334–337 (2013).
15. Pazos-Outón, L. M., Lee, J. M., Futscher, M. H., Kirch, A., Tabachnyk, M., Friend, R. H. & Ehrler, B. A Silicon–Singlet Fission Tandem Solar Cell Exceeding 100% External Quantum Efficiency with High Spectral Stability. *ACS Energy Lett.* **2,** 476–480 (2017).
16. Pavlopoulos, T. G. Measurement of the Triplet-Triplet Absorption Spectrum of Tetracene Using cw Argon Laser Excitation. *J. Chem. Phys.* **56,** 227 (1972).
17. Smith, M. B. & Michl, J. Recent Advances in Singlet Fission. *Annu. Rev. Phys. Chem.* **64,** 361–386 (2013).

18. Le, A. K., Bender, J. A. & Roberts, S. T. Slow Singlet Fission Observed in a Polycrystalline Perylenediimide Thin Film. *J. Phys. Chem. Lett.* **7,** 4922–4928 (2016).

19. Margulies, E. A., Shoer, L. E., Eaton, S. W. & Wasielewski, M. R. Excimer formation in cofacial and slip-stacked perylene-3,4:9,10-bis(dicarboximide) dimers on a redox-inactive triptycene scaffold. *Phys. Chem. Chem. Phys.* **16,** 23735–23742 (2014).

20. Eaton, S. W., Miller, S. a., Margulies, E. a., Shoer, L. E., Schaller, R. D. & Wasielewski, M. R. Singlet Exciton Fission in Thin Films of tert -Butyl-Substituted Terrylenes. *J. Phys. Chem. A* **119,** 4151–4161 (2015).

21. Ryerson, J. L., Schrauben, J. N., Ferguson, A. J., Sahoo, S. C., Naumov, P., Havlas, Z., Michl, J., Nozik, A. J. & Johnson, J. C. Two Thin Film Polymorphs of the Singlet Fission Compound 1,3-Diphenylisobenzofuran. *J. Phys. Chem. C* **118,** 12121–12132 (2014).

22. Johnson, J. C., Akdag, A., Zamadar, M., Chen, X., Schwerin, A. F., Paci, I., Smith, M. B., Havlas, Z. Z., Miller, J. R., Ratner, M. A., Nozik, A. J. & Michl, J. Toward designed singlet fission: Solution photophysics of two indirectly coupled covalent dimers of 1,3-diphenylisobenzofuran. *J. Phys. Chem. B* **117,** 4680–4695 (2013).

23. Piland, G. B., Burdett, J. J., Kurunthu, D. & Bardeen, C. J. Magnetic field effects on singlet fission and fluorescence decay dynamics in amorphous rubrene. *J. Phys. Chem. C* **117,** 1224–1236 (2013).

24. Stern, H. L., Musser, A. J., Gelinas, S., Parkinson, P., Herz, L. M., Bruzek, M. J., Anthony, J., Friend, R. H. & Walker, B. J. Identification of a triplet pair intermediate in singlet exciton fission in solution. *Proc. Natl. Acad. Sci.* **112,** 7656–7661 (2015).

25. Walker, B. J., Musser, A. J., Beljonne, D. & Friend, R. H. Singlet exciton fission in solution. *Nat. Chem.* **5,** 1019–1024 (2013).

26. Burdett, J. J. & Bardeen, C. J. The Dynamics of Singlet Fission in Crystalline Tetracene and Covalent Analogs. *Acc. Chem. Res.* **46,** 1312–1320 (2013).

27. Wan, Y., Guo, Z., Zhu, T., Yan, S., Johnson, J. & Huang, L. Cooperative singlet and triplet exciton transport in tetracene crystals visualized by ultrafast microscopy. *Nat. Chem.* **7,** 785–792 (2015).

28. Arias, D. H., Ryerson, J. L., Cook, J. D., Damrauer, N. H. & Johnson, J. C. Polymorphism influences singlet fission rates in tetracene thin films. *Chem. Sci.* **7,** 1185–1191 (2016).

29. Jundt, C., Klein, G., Sipp, B. & Moigne, J. Le. Exciton Dynamics in Pentacene Thin Films Studied by Pump-Probe Spectroscopy. *Chem. Phys. Lett.* **2614,** (1995).

30. Wright, G. Absolute Quantum Efficiency of Photofluorescence of Anthracene Crystals. *Proc. Phys. Soc. B* **241,** (1955).

31. Swenberg, C. E. & Stacy, W. T. Bimolecular radiationless transitions in crystalline tetracene. *Chem. Phys. Lett.* **2,** 327–328 (1968).

32. Tomkiewicz, Y., Groff, R. P. & Avakian, P. Spectroscopic Approach to Energetics of Exciton Fission and Fusion in Tetracene Crystals. *J. Chem. Phys.* **54,** 4504–4507 (1971).

33. Nijegorodov, N., Ramachandran, V. & Winkoun, D. P. The dependence of the absorption and fluorescence parameters, the intersystem crossing and internal conversion rate constants on the number of rings in polyacene molecules. *Spectrochim. Acta Part A Mol. Biomol. Spectrosc.* **53,** 1813–1824 (1997).

34. Lim, S.-H., Bjorklund, T., Spano, F. & Bardeen, C. J. Exciton Delocalization and Superradiance in Tetracene Thin Films and Nanoaggregates. *Phys. Rev. Lett.* **92,** 107402 (2004).

35. Singh, S., Jones, W. J., Siebrand, W., Stoicheff, B. P. & Schneider, W. G. Laser Generation

of Excitons and Fluorescence in Anthracene Crystals. *J. Chem. Phys.* **42,** 330 (1965).

36. Johnson, R. & Merrifield, R. Effects of Magnetic Fields on the Mutual Annihilation of Triplet Excitons in Anthracene Crystals. *Phys. Rev. B* **1,** 896–902 (1970).

37. Wilson, M. W. B., Rao, A., Johnson, K., Gélinas, S., di Pietro, R., Clark, J. & Friend, R. H. Temperature-Independent Singlet Exciton Fission in Tetracene. *J. Am. Chem. Soc.* **135,** 16680–16688 (2013).

38. Wilson, M. W. B., Rao, A., Clark, J., Kumar, R. S. S., Brida, D., Cerullo, G. & Friend, R. H. Ultrafast dynamics of exciton fission in polycrystalline pentacene. *J. Am. Chem. Soc.* **133,** 11830–3 (2011).

39. Grumstrup, E., Johnson, J. & Damrauer, N. Enhanced Triplet Formation in Polycrystalline Tetracene Films by Femtosecond Optical-Pulse Shaping. *Phys. Rev. Lett.* **105,** 257403 1-4 (2010).

40. Brif, C., Chakrabarti, R. & Rabitz, H. Control of Quantum Phenomena: Past, Present and Future. *New J. Phys.* **12,** 75008 (2010).

41. Alguire, E. C., Subotnik, J. E. & Damrauer, N. H. Exploring Non-Condon Effects in a Covalent Tetracene Dimer: How Important Are Vibrations in Determining the Electronic Coupling for Singlet Fission? *J. Phys. Chem. A* **119,** 299–311 (2015).

42. Berkelbach, T. C., Hybertsen, M. S. & Reichman, D. R. Microscopic theory of singlet exciton fission. II. Application to pentacene dimers and the role of superexchange. *J. Chem. Phys.* **138,** 114103 (2013).

43. Teichen, P. E. & Eaves, J. D. A microscopic model of singlet fission. *J. Phys. Chem. B* **116,** 11473–81 (2012).

44. Vallett, P. J., Snyder, J. L. & Damrauer, N. H. Tunable electronic coupling and driving force

in structurally well-defined tetracene dimers for molecular singlet fission: a computational exploration using density functional theory. *J. Phys. Chem. A* **117,** 10824–38 (2013).

45. Ayed, O., Bernard, E. & Silvi, B. On the Mulliken approximation of multicentre integrals. *J. Mol. Struct. THEOCHEM* **135,** 159–168 (1986).

Chapter 2

1. Burdett, J. J., Müller, A. M., Gosztola, D. & Bardeen, C. J. Excited state dynamics in solid and monomeric tetracene: The roles of superradiance and exciton fission. *J. Chem. Phys.* **133,** 144506 (2010).
2. Berkelbach, T. C., Hybertsen, M. S. & Reichman, D. R. Microscopic theory of singlet exciton fission. III. Crystalline pentacene. *J. Chem. Phys.* **141,** 0–12 (2014).
3. Teichen, P. E. & Eaves, J. D. Collective aspects of singlet fission in molecular crystals. *J. Chem. Phys.* **143,** 44118 (2015).
4. Piland, G. B. & Bardeen, C. J. How Morphology Affects Singlet Fission in Crystalline Tetracene. *J. Phys. Chem. Lett.* **6,** 1841–1846 (2015).
5. Ryerson, J. L., Schrauben, J. N., Ferguson, A. J., Sahoo, S. C., Naumov, P., Havlas, Z., Michl, J., Nozik, A. J. & Johnson, J. C. Two Thin Film Polymorphs of the Singlet Fission Compound 1,3-Diphenylisobenzofuran. *J. Phys. Chem. C* **118,** 12121–12132 (2014).
6. Wan, Y., Guo, Z., Zhu, T., Yan, S., Johnson, J. & Huang, L. Cooperative singlet and triplet exciton transport in tetracene crystals visualized by ultrafast microscopy. *Nat. Chem.* **7,** 785–792 (2015).
7. Hartnett, P. E., Margulies, E. A., Mauck, C. M., Miller, S. A., Wu, Y., Wu, Y.-L., Marks, T. J. & Wasielewski, M. R. Effects of Crystal Morphology on Singlet Exciton Fission in Diketopyrrolopyrrole Thin Films. *J. Phys. Chem. B* **120,** 1357–1366 (2016).

8. Kolata, K., Breuer, T., Witte, G. & Chatterjee, S. Molecular Packing Determines Singlet Exciton Fission in Organic Semiconductors. *ACS Nano* **8,** 7377–7383 (2014).

9. Smith, M. B. & Michl, J. Singlet Fission. *Chem. Rev.* **110,** 6891–6936 (2010).

10. Greyson, E. C., Stepp, B. R., Chen, X., Schwerin, A. F., Paci, I., Smith, M. B., Akdag, A., Johnson, J. C., Nozik, A. J., Michl, J. & Ratner, M. a. Singlet Exciton Fission for Solar Cell Applications: Energy Aspects of Interchromophore Coupling. *J. Phys. Chem. B* **114,** 14223–32 (2010).

11. Smith, M. B. & Michl, J. Recent Advances in Singlet Fission. *Annu. Rev. Phys. Chem.* **64,** 361–386 (2013).

12. Johnson, J. C., Nozik, A. J. & Michl, J. The Role of Chromophore Coupling in Singlet Fission. *Acc. Chem. Res.* **46,** 1290–1299 (2013).

13. Alguire, E. C., Subotnik, J. E. & Damrauer, N. H. Exploring Non-Condon Effects in a Covalent Tetracene Dimer: How Important Are Vibrations in Determining the Electronic Coupling for Singlet Fission? *J. Phys. Chem. A* **119,** 299–311 (2015).

14. Eaton, S. W., Miller, S. a., Margulies, E. a., Shoer, L. E., Schaller, R. D. & Wasielewski, M. R. Singlet Exciton Fission in Thin Films of tert -Butyl-Substituted Terrylenes. *J. Phys. Chem. A* **119,** 4151–4161 (2015).

15. Dillon, R. J., Piland, G. B. & Bardeen, C. J. Different Rates of Singlet Fission in Monoclinic versus Orthorhombic Crystal Forms of Diphenylhexatriene. *J. Am. Chem. Soc.* **135,** 17278–17281 (2013).

16. Voigt, M., Langner, a, Schouwink, P., Lupton, J. M., Mahrt, R. F. & Sokolowski, M. Picosecond time resolved photoluminescence spectroscopy of a tetracene film on highly oriented pyrolytic graphite: dynamical relaxation, trap emission, and superradiance. *J.*

Chem. Phys. **127,** 114705 (2007).

17. Burdett, J. J. & Bardeen, C. J. The Dynamics of Singlet Fission in Crystalline Tetracene and Covalent Analogs. *Acc. Chem. Res.* **46,** 1312–1320 (2013).
18. Wilson, M. W. B., Rao, A., Johnson, K., Gélinas, S., di Pietro, R., Clark, J. & Friend, R. H. Temperature-Independent Singlet Exciton Fission in Tetracene. *J. Am. Chem. Soc.* **135,** 16680–16688 (2013).
19. Holmes, D., Kumaraswamy, S., Matzger, A. J. & Vollhardt, K. P. C. On the Nature of Nonplanarity in the [N]Phenylenes. *Chem. Eur. J.* **5,** 3399–3412 (1999).
20. Venuti, E., Della Valle, R. G., Farina, L., Brillante, A., Masino, M. & Girlando, A. Phonons and structures of tetracene polymorphs at low temperature and high pressure. *Phys. Rev. B* **70,** 104106 (2004).
21. Milita, S., Santato, C. & Cicoira, F. Structural investigation of thin tetracene films on flexible substrate by synchrotron X-ray diffraction. *Appl. Surf. Sci.* **252,** 8022–8027 (2006).
22. Milita, S., Servidori, M., Cicoira, F., Santato, C. & Pifferi, A. Synchrotron X-ray investigation of tetracene thin films grown at different deposition fluxes. *Nucl. Instruments Methods Phys. Res. Sect. B Beam Interact. with Mater. Atoms* **246,** 101–105 (2006).
23. Brillante, A., Bilotti, I., Della Valle, R. G., Venuti, E. & Girlando, A. Probing polymorphs of organic semiconductors by lattice phonon Raman microscopy. *CrystEngComm* **10,** 937 (2008).
24. Schatschneider, B., Monaco, S., Tkatchenko, A. & Liang, J.-J. Understanding the Structure and Electronic Properties of Molecular Crystals Under Pressure: Application of Dispersion Corrected DFT to Oligoacenes. *J. Phys. Chem. A* **117,** 8323–8331 (2013).
25. Sebastian, L., Weiser, G. & Bässler, H. Charge transfer transitions in solid tetracene and

pentacene studied by electroabsorption. *Chem. Phys.* **61,** 125–135 (1981).

26. Burdett, J. J., Gosztola, D. & Bardeen, C. J. The dependence of singlet exciton relaxation on excitation density and temperature in polycrystalline tetracene thin films: kinetic evidence for a dark intermediate state and implications for singlet fission. *J. Chem. Phys.* **135,** 214508 (2011).
27. Arias, D. H., Ryerson, J. L., Cook, J. D., Damrauer, N. H. & Johnson, J. C. Polymorphism influences singlet fission rates in tetracene thin films. *Chem. Sci.* **7,** 1185–1191 (2016).
28. Ryerson, J. L. Structural and photophysical considerations of singlet fission organic thin films for solar photochemistry. (University of Colorado, Boulder, 2016).
29. Grumstrup, E., Johnson, J. & Damrauer, N. Enhanced Triplet Formation in Polycrystalline Tetracene Films by Femtosecond Optical-Pulse Shaping. *Phys. Rev. Lett.* **105,** 257403 1-4 (2010).
30. Trebino, R. *Frequency-Resolved Optical Gating: The Measurement of Ultrashort Laser Pulses*. (Springer US, 2000).
31. Lehnig, R. & Slenczka, A. Spectroscopic investigation of the solvation of organic molecules in superfluid helium droplets. *J. Chem. Phys.* **122,** 244317 (2005).
32. Weinberg-Wolf, J. R., McNeil, L. E., Liu, S. & Kloc, C. Evidence of low intermolecular coupling in rubrene single crystals by Raman scattering. *J. Phys. Condens. Matter* **19,** 276204 (2007).
33. Weiner, A. M. Ultrafast optical pulse shaping: A tutorial review. *Opt. Commun.* **284,** 3669–3692 (2011).
34. Brif, C., Chakrabarti, R. & Rabitz, H. Control of Quantum Phenomena: Past, Present and Future. *New J. Phys.* **12,** 75008 (2010).

35. Prokhorenko, V. I., Nagy, A. M., Waschuk, S. a, Brown, L. S., Birge, R. R. & Miller, R. J. D. Coherent control of retinal isomerization in bacteriorhodopsin. *Science* **313,** 1257–61 (2006).

36. Herek, J. L., Wohlleben, W., Cogdell, R. J., Zeidler, D. & Motzkus, M. Quantum control of energy flow in light harvesting. *Nature* **417,** 533–5 (2002).

37. Weiner, A. M., Leaird, D. E., Wiederrecht, G. P. & Nelson, K. A. Femtosecond Pulse Sequences Used for Optical Manipulation of Molecular Motion. *Science (80-.).* **247,** 1317–1319 (1990).

38. Weiner, A. M. Femtosecond optical pulse shaping and processing. *Prog. Quantum ...* **19,** 161–237 (1995).

39. Weiner, A. M. Femtosecond pulse shaping using spatial light modulators. *Rev. Sci. Instrum.* **71,** 1929 (2000).

40. Monmayrant, A., Weber, S. & Chatel, B. A newcomer's guide to ultrashort pulse shaping and characterization. *J. Phys. B At. Mol. Opt. Phys.* **43,** 103001 (2010).

41. Judson, R. S. & Rabitz, H. Teaching lasers to control molecules. *Phys. Rev. Lett.* **68,** 1500–1503 (1992).

42. Brüggemann, B., Organero, J. A., Pascher, T., Pullerits, T. & Yartsev, A. Control of Electron Transfer Pathways in a Dye-Sensitized Solar Cell. *Phys. Rev. Lett.* **97,** 208301 (2006).

Chapter 3

1. Swenberg, C. E. & Stacy, W. T. Bimolecular radiationless transitions in crystalline tetracene. *Chem. Phys. Lett.* **2,** 327–328 (1968).

2. Merrifield, R. E., Avakian, P. & Groff, R. P. Fission of singlet excitons into pairs of triplet

excitons in tetracene crystals. *Chem. Phys. Lett.* **3,** 155–157 (1969).

3. Smith, M. B. & Michl, J. Singlet Fission. *Chem. Rev.* **110,** 6891–6936 (2010).
4. Johnson, J. C., Nozik, A. J. & Michl, J. High triplet yield from singlet fission in a thin film of 1,3-diphenylisobenzofuran. *J. Am. Chem. Soc.* **132,** 16302–16303 (2010).
5. Burdett, J. J. & Bardeen, C. J. Quantum Beats in Crystalline Tetracene Delayed Fluorescence Due to Triplet Pair Coherences Produced by Direct Singlet Fission. *J. Am. Chem. Soc.* **134,** 8597–8607 (2012).
6. Wilson, M. W. B., Rao, A., Ehrler, B. & Friend, R. H. Singlet Exciton Fission in Polycrystalline Pentacene: From Photophysics toward Devices. *Acc. Chem. Res.* **46,** 1330–1338 (2013).
7. Swenberg, C. E. & Pope, M. *Electronic Processes in Organic Crystals and Polymers*. (Oxford University Press, 1999).
8. Dillon, R. J., Piland, G. B. & Bardeen, C. J. Different Rates of Singlet Fission in Monoclinic versus Orthorhombic Crystal Forms of Diphenylhexatriene. *J. Am. Chem. Soc.* **135,** 17278–17281 (2013).
9. Eaton, S. W., Shoer, L. E., Karlen, S. D., Dyar, S. M., Margulies, E. A., Veldkamp, B. S., Ramanan, C., Hartzler, D. A., Savikhin, S., Marks, T. J. & Wasielewski, M. R. Singlet Exciton Fission in Polycrystalline Thin Films of a Slip-Stacked Perylenediimide. *J. Am. Chem. Soc.* **135,** 14701–14712 (2013).
10. Eaton, S. W., Miller, S. a., Margulies, E. a., Shoer, L. E., Schaller, R. D. & Wasielewski, M. R. Singlet Exciton Fission in Thin Films of tert -Butyl-Substituted Terrylenes. *J. Phys. Chem. A* **119,** 4151–4161 (2015).
11. Burdett, J. J., Müller, A. M., Gosztola, D. & Bardeen, C. J. Excited state dynamics in solid

and monomeric tetracene: The roles of superradiance and exciton fission. *J. Chem. Phys.* **133,** 144506 (2010).

12. Burdett, J. J., Gosztola, D. & Bardeen, C. J. The dependence of singlet exciton relaxation on excitation density and temperature in polycrystalline tetracene thin films: kinetic evidence for a dark intermediate state and implications for singlet fission. *J. Chem. Phys.* **135,** 214508 (2011).
13. Berkelbach, T. C., Hybertsen, M. S. & Reichman, D. R. Microscopic theory of singlet exciton fission. III. Crystalline pentacene. *J. Chem. Phys.* **141,** 0–12 (2014).
14. Teichen, P. E. & Eaves, J. D. Collective aspects of singlet fission in molecular crystals. *J. Chem. Phys.* **143,** 44118 (2015).
15. Feng, X., Kolomeisky, A. B. & Krylov, A. I. Dissecting the Effect of Morphology on the Rates of Singlet Fission: Insights from Theory. *J. Phys. Chem. C* **118,** 19608–19617 (2014).
16. Ryerson, J. L., Schrauben, J. N., Ferguson, A. J., Sahoo, S. C., Naumov, P., Havlas, Z., Michl, J., Nozik, A. J. & Johnson, J. C. Two Thin Film Polymorphs of the Singlet Fission Compound 1,3-Diphenylisobenzofuran. *J. Phys. Chem. C* **118,** 12121–12132 (2014).
17. Wan, Y., Guo, Z., Zhu, T., Yan, S., Johnson, J. & Huang, L. Cooperative singlet and triplet exciton transport in tetracene crystals visualized by ultrafast microscopy. *Nat. Chem.* **7,** 785–792 (2015).
18. Piland, G. B. & Bardeen, C. J. How Morphology Affects Singlet Fission in Crystalline Tetracene. *J. Phys. Chem. Lett.* **6,** 1841–1846 (2015).
19. Hartnett, P. E., Margulies, E. A., Mauck, C. M., Miller, S. A., Wu, Y., Wu, Y.-L., Marks, T. J. & Wasielewski, M. R. Effects of Crystal Morphology on Singlet Exciton Fission in Diketopyrrolopyrrole Thin Films. *J. Phys. Chem. B* **120,** 1357–1366 (2016).

20. Arias, D. H., Ryerson, J. L., Cook, J. D., Damrauer, N. H. & Johnson, J. C. Polymorphism influences singlet fission rates in tetracene thin films. *Chem. Sci.* **7,** 1185–1191 (2016).

21. Bhattacharyya, K. & Datta, A. Polymorphism Controlled Singlet Fission in TIPS-Anthracene: Role of Stacking Orientation. *J. Phys. Chem. C* **121,** 1412–1420 (2017).

22. Hanna, M. C. & Nozik, A. J. Solar Conversion Efficiency of Photovoltaic and Photoelectrolysis Cells with Carrier Multiplication Absorbers. *J. Appl. Phys.* **100,** 74510 (2006).

23. Schrauben, J. N., Zhao, Y., Mercado, C., Dron, P. I., Ryerson, J. L., Michl, J., Zhu, K. & Johnson, J. C. Photocurrent Enhanced by Singlet Fission in a Dye-Sensitized Solar Cell. *ACS Appl. Mater. Interfaces* **7,** 2286–2293 (2015).

24. Lee, J., Jadhav, P., Reusswig, P. D., Yost, S. R., Thompson, N. J., Congreve, D. N., Hontz, E., Van Voorhis, T. & Baldo, M. a. Singlet Exciton Fission Photovoltaics. *Acc. Chem. Res.* **46,** 1300–1311 (2013).

25. Müller, A. M., Avlasevich, Y. S., Schoeller, W. W., Müllen, K. & Bardeen, C. J. Exciton Fission and Fusion in Bis(tetracene) Molecules with Different Covalent Linker Structures. *J. Am. Chem. Soc.* **129,** 14240–14250 (2007).

26. Johnson, J. C., Akdag, A., Zamadar, M., Chen, X., Schwerin, A. F., Paci, I., Smith, M. B., Havlas, Z. Z., Miller, J. R., Ratner, M. A., Nozik, A. J. & Michl, J. Toward designed singlet fission: Solution photophysics of two indirectly coupled covalent dimers of 1,3-diphenylisobenzofuran. *J. Phys. Chem. B* **117,** 4680–4695 (2013).

27. Margulies, E. A., Shoer, L. E., Eaton, S. W. & Wasielewski, M. R. Excimer formation in cofacial and slip-stacked perylene-3,4:9,10-bis(dicarboximide) dimers on a redox-inactive triptycene scaffold. *Phys. Chem. Chem. Phys.* **16,** 23735–23742 (2014).

28. Liu, H., Nichols, V. M., Shen, L., Jahansouz, S., Chen, Y., Hanson, K. M., Bardeen, C. J. & Li, X. Synthesis and photophysical properties of a ‘face-to-face’ stacked tetracene dimer. *Phys. Chem. Chem. Phys.* **17,** 6523–6531 (2015).

29. Sanders, S. N., Kumarasamy, E., Pun, A. B., Trinh, M. T., Choi, B., Xia, J., Taffet, E. J., Low, J. Z., Miller, J. R., Roy, X., Zhu, X.-Y., Steigerwald, M. L., Sfeir, M. Y. & Campos, L. M. Quantitative Intramolecular Singlet Fission in Bipentacenes. *J. Am. Chem. Soc.* **137,** 8965–8972 (2015).

30. Zirzlmeier, J., Lehnherr, D., Coto, P. B., Chernick, E. T., Casillas, R., Basel, B. S., Thoss, M., Tykwinski, R. R. & Guldi, D. M. Singlet fission in pentacene dimers. *Proc. Natl. Acad. Sci.* **112,** 5325–5330 (2015).

31. Lukman, S., Musser, A. J., Chen, K., Athanasopoulos, S., Yong, C. K., Zeng, Z., Ye, Q., Chi, C., Hodgkiss, J. M., Wu, J., Friend, R. H. & Greenham, N. C. Tuneable Singlet Exciton Fission and Triplet-Triplet Annihilation in an Orthogonal Pentacene Dimer. *Adv. Funct. Mater.* **25,** 5452–5461 (2015).

32. Korovina, N. V., Das, S., Nett, Z., Feng, X., Joy, J., Haiges, R., Krylov, A. I., Bradforth, S. E. & Thompson, M. E. Singlet Fission in a Covalently Linked Cofacial Alkynyltetracene Dimer. *J. Am. Chem. Soc.* **138,** 617–627 (2016).

33. Sakuma, T., Sakai, H., Araki, Y., Mori, T., Wada, T., Tkachenko, N. V. & Hasobe, T. Long-Lived Triplet Excited States of Bent-Shaped Pentacene Dimers by Intramolecular Singlet Fission. *J. Phys. Chem. A* **120,** 1867–1875 (2016).

34. Sanders, S. N., Kumarasamy, E., Pun, A. B., Steigerwald, M. L., Sfeir, M. Y. & Campos, L. M. Intramolecular Singlet Fission in Oligoacene Heterodimers. *Angew. Chemie Int. Ed.* **55,** 3373–3377 (2016).

35. Lukman, S., Chen, K., Hodgkiss, J. M., Turban, D. H. P., Hine, N. D. M., Dong, S., Wu, J., Greenham, N. C. & Musser, A. J. Tuning the role of charge-transfer states in intramolecular singlet exciton fission through side-group engineering. *Nat. Commun.* **7,** 13622 (2016).

36. Zirzlmeier, J., Casillas, R., Reddy, S. R., Coto, P. B., Lehnherr, D., Chernick, E. T., Papadopoulos, I., Thoss, M., Tykwinski, R. R. & Guldi, D. M. Solution-based intramolecular singlet fission in cross-conjugated pentacene dimers. *Nanoscale* **8,** 10113–10123 (2016).

37. Mukhopadhyay, T., Musser, A. J., Puttaraju, B., Dhar, J., Friend, R. H. & Patil, S. Is the Chemical Strategy for Imbuing 'Polyene' Character in Diketopyrrolopyrrole-Based Chromophores Sufficient for Singlet Fission? *J. Phys. Chem. Lett.* **8,** 984–991 (2017).

38. Walker, B. J., Musser, A. J., Beljonne, D. & Friend, R. H. Singlet exciton fission in solution. *Nat. Chem.* **5,** 1019–1024 (2013).

39. Stern, H. L., Musser, A. J., Gelinas, S., Parkinson, P., Herz, L. M., Bruzek, M. J., Anthony, J., Friend, R. H. & Walker, B. J. Identification of a triplet pair intermediate in singlet exciton fission in solution. *Proc. Natl. Acad. Sci.* **112,** 7656–7661 (2015).

40. Smith, M. B. & Michl, J. Recent Advances in Singlet Fission. *Annu. Rev. Phys. Chem.* **64,** 361–386 (2013).

41. Alguire, E. C., Subotnik, J. E. & Damrauer, N. H. Exploring Non-Condon Effects in a Covalent Tetracene Dimer: How Important Are Vibrations in Determining the Electronic Coupling for Singlet Fission? *J. Phys. Chem. A* **119,** 299–311 (2015).

42. Damrauer, N. H. & Snyder, J. L. Symmetry-Directed Control of Electronic Coupling for Singlet Fission in Covalent Bis–Acene Dimers. *J. Phys. Chem. Lett.* **6,** 4456–4462 (2015).

43. Grumstrup, E., Johnson, J. & Damrauer, N. Enhanced Triplet Formation in Polycrystalline

Tetracene Films by Femtosecond Optical-Pulse Shaping. *Phys. Rev. Lett.* **105,** 257403 1-4 (2010).

44. Johnson, J. C., Nozik, A. J. & Michl, J. The Role of Chromophore Coupling in Singlet Fission. *Acc. Chem. Res.* **46,** 1290–1299 (2013).

45. Scholes, G. D., Ghiggino, K. P., Oliver, A. M. & Paddon-Row, M. N. Through-space and through-bond effects on exciton interactions in rigidly linked dinaphthyl molecules. *J. Am. Chem. Soc.* **115,** 4345–4349 (1993).

46. Vallett, P. J., Snyder, J. L. & Damrauer, N. H. Tunable electronic coupling and driving force in structurally well-defined tetracene dimers for molecular singlet fission: a computational exploration using density functional theory. *J. Phys. Chem. A* **117,** 10824–38 (2013).

47. Carey, T. J., Snyder, J. L., Miller, E. G., Sammakia, T. & Damrauer, N. H. Synthesis of Geometrically Well-Defined Covalent Acene Dimers for Mechanistic Exploration of Singlet Fission. *J. Org. Chem.* acs.joc.7b00602 (2017).

48. Snyder, J. L. A Symmetry Exploration into Covalent Tetracene Dimers with Tunable Electronic Coupling for Singlet Fission. (University of Colorado, Boulder, 2015).

49. Platt, J. R. Classification of Spectra of Cata-Condensed Hydrocarbons. *J. Chem. Phys.* **17,** 484 (1949).

50. Gouterman, M. Spectra of porphyrins. *J. Mol. Spectrosc.* **6,** 138–163 (1961).

51. Frisch, M. J. *et al.* Gaussian 09, Revision A.1. (2009).

52. Davydov, A. S. The Theory of Molecular Excitons. *Sov. Phys. Uspekhi* **7,** 145–178 (1964).

53. Spano, F. C. The Spectral Signatures of Frenkel Polarons in H- and J-Aggregates. *Acc. Chem. Res.* **43,** 429–439 (2010).

54. Lakowicz, J. R. *Principles of Fluorescence Spectroscopy*. (Springer US, 2006).

55. Lim, S.-H., Bjorklund, T., Spano, F. & Bardeen, C. J. Exciton Delocalization and Superradiance in Tetracene Thin Films and Nanoaggregates. *Phys. Rev. Lett.* **92,** 107402 (2004).

56. Burgdorff, C., Ehrhardt, S. & Loehmannsroeben, H. G. Photophyslcal Properties of Tetracene Derivatives in Solution. 2. Halogenated Tetracene Derivatives. *J. Phys. Chem.* **95,** 4246–4249 (1991).

57. Fletcher, A. N. & Bliss, D. E. Laser dye stability. Part 5. *Appl. Phys.* **16,** 289–295 (1978).

58. Veldman, D., Chopin, S. M. A., Meskers, S. C. J., Groeneveld, M. M., Williams, R. M. & Janssen, R. A. J. Triplet Formation Involving a Polar Transition State in a Well-Defined Intramolecular Perylenediimide Dimeric Aggregate. *J. Phys. Chem. A* **112,** 5846–5857 (2008).

59. Pavlopoulos, T. G. Measurement of the Triplet-Triplet Absorption Spectrum of Tetracene Using cw Argon Laser Excitation. *J. Chem. Phys.* **56,** 227 (1972).

60. Birks, J. B. *Photophysics of Aromatic Molecules*. (Wiley-Interscience, 1970).

61. Meylemans, H. A., Lei, C.-F. & Damrauer, N. H. Ligand Structure, Conformational Dynamics, and Excited-State Electron Delocalization for Control of Photoinduced Electron Transfer Rates in Synthetic Donor-Bridge-Acceptor Systems. *Inorg. Chem.* **47,** 4060–4076 (2008).

62. Meylemans, H. A. & Damrauer, N. H. Controlling Electron Transfer through the Manipulation of Structure and Ligand-Based Torsional Motions: A Computational Exploration of Ruthenium Donor−Acceptor Systems using Density Functional Theory. *Inorg. Chem.* **48,** 11161–11175 (2009).

63. Meylemans, H. A., Hewitt, J. T., Abdelhaq, M., Vallett, P. J. & Damrauer, N. H. Exploiting

Conformational Dynamics To Facilitate Formation and Trapping of Electron-Transfer Photoproducts in Metal Complexes. *J. Am. Chem. Soc.* **132,** 11464–11466 (2010).

64. Burdett, J. J. & Bardeen, C. J. The Dynamics of Singlet Fission in Crystalline Tetracene and Covalent Analogs. *Acc. Chem. Res.* **46,** 1312–1320 (2013).

65. Wilson, M. W. B., Rao, A., Johnson, K., Gélinas, S., di Pietro, R., Clark, J. & Friend, R. H. Temperature-Independent Singlet Exciton Fission in Tetracene. *J. Am. Chem. Soc.* **135,** 16680–16688 (2013).

66. Yost, S. R., Lee, J., Wilson, M. W. B., Wu, T., McMahon, D. P., Parkhurst, R. R., Thompson, N. J., Congreve, D. N., Rao, A., Johnson, K., Sfeir, M. Y., Bawendi, M. G., Swager, T. M., Friend, R. H., Baldo, M. a. & Van Voorhis, T. A transferable model for singlet-fission kinetics. *Nat. Chem.* **6,** 492–497 (2014).

Chapter 4

1. Carey, T. J., Snyder, J. L., Miller, E. G., Sammakia, T. & Damrauer, N. H. Synthesis of Geometrically Well-Defined Covalent Acene Dimers for Mechanistic Exploration of Singlet Fission. *J. Org. Chem.* acs.joc.7b00602 (2017).

2. Fudickar, W. & Linker, T. Why Triple Bonds Protect Acenes from Oxidation and Decomposition. *J. Am. Chem. Soc.* **134,** 15071–15082 (2012).

3. Frisch, M. J. *et al.* Gaussian 09, Revision A.1. (2009).

4. Vallett, P. J., Snyder, J. L. & Damrauer, N. H. Tunable electronic coupling and driving force in structurally well-defined tetracene dimers for molecular singlet fission: a computational exploration using density functional theory. *J. Phys. Chem. A* **117,** 10824–38 (2013).

5. Burdett, J. J., Müller, A. M., Gosztola, D. & Bardeen, C. J. Excited state dynamics in solid and monomeric tetracene: The roles of superradiance and exciton fission. *J. Chem. Phys.*

133, 144506 (2010).

6. Griffith, O. L., Jones, A. G., Anthony, J. E. & Lichtenberger, D. L. Intermolecular Effects on the Hole States of Triisopropylsilylethynyl-Substituted Oligoacenes. *J. Phys. Chem. C* **114,** 13838–13845 (2010).
7. Lobanova Griffith, O., Gruhn, N. E., Anthony, J. E., Purushothaman, B. & Lichtenberger, D. L. Electron Transfer Parameters of Triisopropylsilylethynyl-Substituted Oligoacenes. *J. Phys. Chem. C* **112,** 20518–20524 (2008).
8. Maliakal, A., Raghavachari, K., Katz, H., Chandross, E. & Siegrist, T. Photochemical Stability of Pentacene and a Substituted Pentacene in Solution and in Thin Films. *Chem. Mater.* **16,** 4980–4986 (2004).
9. Bhattacharyya, K. & Datta, A. Polymorphism Controlled Singlet Fission in TIPS-Anthracene: Role of Stacking Orientation. *J. Phys. Chem. C* **121,** 1412–1420 (2017).
10. Lukman, S., Chen, K., Hodgkiss, J. M., Turban, D. H. P., Hine, N. D. M., Dong, S., Wu, J., Greenham, N. C. & Musser, A. J. Tuning the role of charge-transfer states in intramolecular singlet exciton fission through side-group engineering. *Nat. Commun.* **7,** 13622 (2016).
11. Fuemmeler, E. G., Sanders, S. N., Pun, A. B., Kumarasamy, E., Zeng, T., Miyata, K., Steigerwald, M. L., Zhu, X.-Y., Sfeir, M. Y., Campos, L. M. & Ananth, N. A Direct Mechanism of Ultrafast Intramolecular Singlet Fission in Pentacene Dimers. *ACS Cent. Sci.* **2,** 316–324 (2016).
12. Gouterman, M. Spectra of porphyrins. *J. Mol. Spectrosc.* **6,** 138–163 (1961).
13. Platt, J. R. Classification of Spectra of Cata-Condensed Hydrocarbons. *J. Chem. Phys.* **17,** 484 (1949).
14. Cook, J. D., Carey, T. J. & Damrauer, N. H. Solution-Phase Singlet Fission in a Structurally

Well-Defined Norbornyl-Bridged Tetracene Dimer. *J. Phys. Chem. A* **120,** 4473–4481 (2016).

15. Spano, F. C. The Spectral Signatures of Frenkel Polarons in H- and J-Aggregates. *Acc. Chem. Res.* **43,** 429–439 (2010).

16. Johnson, J. C., Nozik, A. J. & Michl, J. The Role of Chromophore Coupling in Singlet Fission. *Acc. Chem. Res.* **46,** 1290–1299 (2013).

17. Sanders, S. N., Kumarasamy, E., Pun, A. B., Trinh, M. T., Choi, B., Xia, J., Taffet, E. J., Low, J. Z., Miller, J. R., Roy, X., Zhu, X.-Y., Steigerwald, M. L., Sfeir, M. Y. & Campos, L. M. Quantitative Intramolecular Singlet Fission in Bipentacenes. *J. Am. Chem. Soc.* **137,** 8965–8972 (2015).

18. Korovina, N. V., Das, S., Nett, Z., Feng, X., Joy, J., Haiges, R., Krylov, A. I., Bradforth, S. E. & Thompson, M. E. Singlet Fission in a Covalently Linked Cofacial Alkynyltetracene Dimer. *J. Am. Chem. Soc.* **138,** 617–627 (2016).

19. Zirzlmeier, J., Lehnherr, D., Coto, P. B., Chernick, E. T., Casillas, R., Basel, B. S., Thoss, M., Tykwinski, R. R. & Guldi, D. M. Singlet fission in pentacene dimers. *Proc. Natl. Acad. Sci.* **112,** 5325–5330 (2015).

20. Sakuma, T., Sakai, H., Araki, Y., Mori, T., Wada, T., Tkachenko, N. V. & Hasobe, T. Long-Lived Triplet Excited States of Bent-Shaped Pentacene Dimers by Intramolecular Singlet Fission. *J. Phys. Chem. A* **120,** 1867–1875 (2016).

21. Zirzlmeier, J., Casillas, R., Reddy, S. R., Coto, P. B., Lehnherr, D., Chernick, E. T., Papadopoulos, I., Thoss, M., Tykwinski, R. R. & Guldi, D. M. Solution-based intramolecular singlet fission in cross-conjugated pentacene dimers. *Nanoscale* **8,** 10113–10123 (2016).

22. Lukman, S., Musser, A. J., Chen, K., Athanasopoulos, S., Yong, C. K., Zeng, Z., Ye, Q., Chi, C., Hodgkiss, J. M., Wu, J., Friend, R. H. & Greenham, N. C. Tuneable Singlet Exciton Fission and Triplet-Triplet Annihilation in an Orthogonal Pentacene Dimer. *Adv. Funct. Mater.* **25,** 5452–5461 (2015).

23. Scholes, G. D., Ghiggino, K. P., Oliver, A. M. & Paddon-Row, M. N. Through-space and through-bond effects on exciton interactions in rigidly linked dinaphthyl molecules. *J. Am. Chem. Soc.* **115,** 4345–4349 (1993).

24. Alguire, E. C., Subotnik, J. E. & Damrauer, N. H. Exploring Non-Condon Effects in a Covalent Tetracene Dimer: How Important Are Vibrations in Determining the Electronic Coupling for Singlet Fission? *J. Phys. Chem. A* **119,** 299–311 (2015).

25. Reichardt, C. Solvatochromic Dyes as Solvent Polarity Indicators. *Chem. Rev.* **94,** 2319–2358 (1994).

26. Haynes, W. M. *CRC Handbook of Chemistry and Physics, 97th Edition (Internet Version 2017)*. (CRC Press/Taylor & Francis).

27. Yang, Y., Davidson, E. R. & Yang, W. Nature of ground and electronic excited states of higher acenes. *Proc. Natl. Acad. Sci.* **113,** E5098–E5107 (2016).

28. Lewis, J. E. & Maroncelli, M. On the (uninteresting) dependence of the absorption and emission transition moments of coumarin 153 on solvent. *Chem. Phys. Lett.* **282,** 197–203 (1998).

29. Swenberg, C. E. & Pope, M. *Electronic Processes in Organic Crystals and Polymers*. (Oxford University Press, 1999).

30. Margulies, E. A., Miller, C. E., Wu, Y., Ma, L., Schatz, G. C., Young, R. M. & Wasielewski, M. R. Enabling singlet fission by controlling intramolecular charge transfer in π-stacked

covalent terrylenediimide dimers. *Nat. Chem.* **8,** 1120–1125 (2016).

31. Stern, H. L., Musser, A. J., Gelinas, S., Parkinson, P., Herz, L. M., Bruzek, M. J., Anthony, J., Friend, R. H. & Walker, B. J. Identification of a triplet pair intermediate in singlet exciton fission in solution. *Proc. Natl. Acad. Sci.* **112,** 7656–7661 (2015).
32. Wilson, M. W. B., Rao, A., Johnson, K., Gélinas, S., di Pietro, R., Clark, J. & Friend, R. H. Temperature-Independent Singlet Exciton Fission in Tetracene. *J. Am. Chem. Soc.* **135,** 16680–16688 (2013).
33. Burdett, J. J. & Bardeen, C. J. The Dynamics of Singlet Fission in Crystalline Tetracene and Covalent Analogs. *Acc. Chem. Res.* **46,** 1312–1320 (2013).
34. Smith, M. B. & Michl, J. Singlet Fission. *Chem. Rev.* **110,** 6891–6936 (2010).
35. van Stokkum, I. H. M., Larsen, D. S. & van Grondelle, R. Global and target analysis of time-resolved spectra. *Biochim. Biophys. Acta* **1657,** 82–104 (2004).
36. Burgdorff, C., Ehrhardt, S. & Loehmannsroeben, H. G. Photophyslcal Properties of Tetracene Derivatives in Solution. 2. Halogenated Tetracene Derivatives. *J. Phys. Chem.* **95,** 4246–4249 (1991).
37. Lakowicz, J. R. *Principles of Fluorescence Spectroscopy*. (Springer US, 2006).
38. Caspar, J. V & Meyer, T. J. Application of the Energy Gap Law to Excited-State Decay. *J. Phys. Chem.* **87,** 952–957 (1983).
39. Englman, R. & Jortner, J. The energy gap law for radiationless transitions in large molecules. *Mol. Phys.* **18,** 145–164 (1970).
40. Fletcher, A. N. & Bliss, D. E. Laser dye stability. Part 5. *Appl. Phys.* **16,** 289–295 (1978).
41. Van der Auweraer, M., Grabowski, Z. R. & Rettig, W. Molecular structure and the temperature-dependent radiative rates in Twisted Intramolecular Charge-Transfer and

exciplex systems. *J. Phys. Chem.* **95,** 2083–2092 (1991).

42. Noviandri, I., Brown, K. N., Fleming, D. S., Gulyas, P. T., Lay, P. a, Masters, A. F. & Phillips, L. The Decamethylferrocenium/Decamethylferrocene Redox Couple: A Superior Redox Standard to the Ferrocenium/Ferrocene Redox Couple for Studying Solvent Effects on the Thermodynamics of Electron Transfer. *J. Phys. Chem. B* **103,** 6713–6722 (1999).

43. Pavlishchuk, V. V. & Addison, A. W. Conversion constants for redox potentials measured versus different reference electrodes in acetonitrile solutions at 25°C. *Inorganica Chim. Acta* **298,** 97–102 (2000).

44. Trasatti, S. The absolute electrode potential: an explanatory note (Recommendations 1986). *Pure Appl. Chem.* **58,** (1986).

45. Damrauer, N. H. & Snyder, J. L. Symmetry-Directed Control of Electronic Coupling for Singlet Fission in Covalent Bis–Acene Dimers. *J. Phys. Chem. Lett.* **6,** 4456–4462 (2015).

46. Bonneau, R., Carmichael, I. & Hug, G. L. Molar absorption coefficients of transient species in solution. *Pure Appl. Chem.* **63,** 289–299 (1991).

47. Mcglynn, S. P., Padhye, M. R. & Kasha, M. Lowest Triplet Levels of the Polyacenes. *J. Chem. Phys.* **23,** 593 (1955).

48. Nijegorodov, N., Vasilenko, V., Monowe, P. & Masale, M. Systematic investigation of the influence of methyl groups upon fluorescence parameters and the intersystem crossing rate constant of aromatic molecules. *Spectrochim. Acta. A. Mol. Biomol. Spectrosc.* **74,** 188–94 (2009).

49. Müller, A. M., Avlasevich, Y. S., Schoeller, W. W., Müllen, K. & Bardeen, C. J. Exciton Fission and Fusion in Bis(tetracene) Molecules with Different Covalent Linker Structures. *J. Am. Chem. Soc.* **129,** 14240–14250 (2007).

50. Johnson, J. C., Akdag, A., Zamadar, M., Chen, X., Schwerin, A. F., Paci, I., Smith, M. B., Havlas, Z. Z., Miller, J. R., Ratner, M. A., Nozik, A. J. & Michl, J. Toward designed singlet fission: Solution photophysics of two indirectly coupled covalent dimers of 1,3-diphenylisobenzofuran. *J. Phys. Chem. B* **117,** 4680–4695 (2013).

51. Walker, B. J., Musser, A. J., Beljonne, D. & Friend, R. H. Singlet exciton fission in solution. *Nat. Chem.* **5,** 1019–1024 (2013).

52. Margulies, E. A., Shoer, L. E., Eaton, S. W. & Wasielewski, M. R. Excimer formation in cofacial and slip-stacked perylene-3,4:9,10-bis(dicarboximide) dimers on a redox-inactive triptycene scaffold. *Phys. Chem. Chem. Phys.* **16,** 23735–23742 (2014).

53. Varnavski, O., Abeyasinghe, N., Aragó, J., Serrano-Pérez, J. J., Ortí, E., López Navarrete, J. T., Takimiya, K., Casanova, D., Casado, J. & Goodson, T. High Yield Ultrafast Intramolecular Singlet Exciton Fission in a Quinoidal Bithiophene. *J. Phys. Chem. Lett.* **6,** 1375–1384 (2015).

54. Teichen, P. E. & Eaves, J. D. Collective aspects of singlet fission in molecular crystals. *J. Chem. Phys.* **143,** 44118 (2015).

55. Kolomeisky, A. B., Feng, X. & Krylov, A. I. A Simple Kinetic Model for Singlet Fission: A Role of Electronic and Entropic Contributions to Macroscopic Rates. *J. Phys. Chem. C* **118,** 5188–5195 (2014).

Chapter 5

1. Vallett, P. J., Snyder, J. L. & Damrauer, N. H. Tunable electronic coupling and driving force in structurally well-defined tetracene dimers for molecular singlet fission: a computational exploration using density functional theory. *J. Phys. Chem. A* **117,** 10824–38 (2013).

2. Alguire, E. C., Subotnik, J. E. & Damrauer, N. H. Exploring Non-Condon Effects in a

Covalent Tetracene Dimer: How Important Are Vibrations in Determining the Electronic Coupling for Singlet Fission? *J. Phys. Chem. A* **119,** 299–311 (2015).

3. Grumstrup, E., Johnson, J. & Damrauer, N. Enhanced Triplet Formation in Polycrystalline Tetracene Films by Femtosecond Optical-Pulse Shaping. *Phys. Rev. Lett.* **105,** 257403 1-4 (2010).
4. Herek, J. L., Wohlleben, W., Cogdell, R. J., Zeidler, D. & Motzkus, M. Quantum control of energy flow in light harvesting. *Nature* **417,** 533–5 (2002).
5. Brüggemann, B., Organero, J. A., Pascher, T., Pullerits, T. & Yartsev, A. Control of Electron Transfer Pathways in a Dye-Sensitized Solar Cell. *Phys. Rev. Lett.* **97,** 208301 (2006).
6. Prokhorenko, V. I., Nagy, A. M., Waschuk, S. a, Brown, L. S., Birge, R. R. & Miller, R. J. D. Coherent control of retinal isomerization in bacteriorhodopsin. *Science* **313,** 1257–61 (2006).
7. Lukman, S., Chen, K., Hodgkiss, J. M., Turban, D. H. P., Hine, N. D. M., Dong, S., Wu, J., Greenham, N. C. & Musser, A. J. Tuning the role of charge-transfer states in intramolecular singlet exciton fission through side-group engineering. *Nat. Commun.* **7,** 13622 (2016).
8. Zirzlmeier, J., Casillas, R., Reddy, S. R., Coto, P. B., Lehnherr, D., Chernick, E. T., Papadopoulos, I., Thoss, M., Tykwinski, R. R. & Guldi, D. M. Solution-based intramolecular singlet fission in cross-conjugated pentacene dimers. *Nanoscale* **8,** 10113–10123 (2016).
9. Sanders, S. N., Kumarasamy, E., Pun, A. B., Appavoo, K., Steigerwald, M. L., Campos, L. M. & Sfeir, M. Y. Exciton Correlations in Intramolecular Singlet Fission. *J. Am. Chem. Soc.* **138,** 7289–7297 (2016).

10. Margulies, E. A., Miller, C. E., Wu, Y., Ma, L., Schatz, G. C., Young, R. M. & Wasielewski, M. R. Enabling singlet fission by controlling intramolecular charge transfer in π-stacked covalent terrylenediimide dimers. *Nat. Chem.* **8,** 1120–1125 (2016).

11. Korovina, N. V., Das, S., Nett, Z., Feng, X., Joy, J., Haiges, R., Krylov, A. I., Bradforth, S. E. & Thompson, M. E. Singlet Fission in a Covalently Linked Cofacial Alkynyltetracene Dimer. *J. Am. Chem. Soc.* **138,** 617–627 (2016).

Appendix A

1. Frisch, M. J. *et al.* Gaussian 09, Revision A.1. (2009).

2. Vallett, P. J., Snyder, J. L. & Damrauer, N. H. Tunable electronic coupling and driving force in structurally well-defined tetracene dimers for molecular singlet fission: a computational exploration using density functional theory. *J. Phys. Chem. A* **117,** 10824–38 (2013).

Appendix B

1. Frisch, M. J. *et al.* Gaussian 09, Revision A.1. (2009).

2. Nijegorodov, N., Ramachandran, V. & Winkoun, D. P. The dependence of the absorption and fluorescence parameters, the intersystem crossing and internal conversion rate constants on the number of rings in polyacene molecules. *Spectrochim. Acta Part A Mol. Biomol. Spectrosc.* **53,** 1813–1824 (1997).

Appendix A. Supporting Information for Chapter 3

A.1 Comparative Spectrum of BT1 in Toluene and Chloroform

Figure A.1 shows a normalized absorption spectrum of BT1 in toluene and chloroform, showing the minimal changes observed between the two solvents. The difference in absorbance in the UV is likely due to the onset of the toluene solvent window.

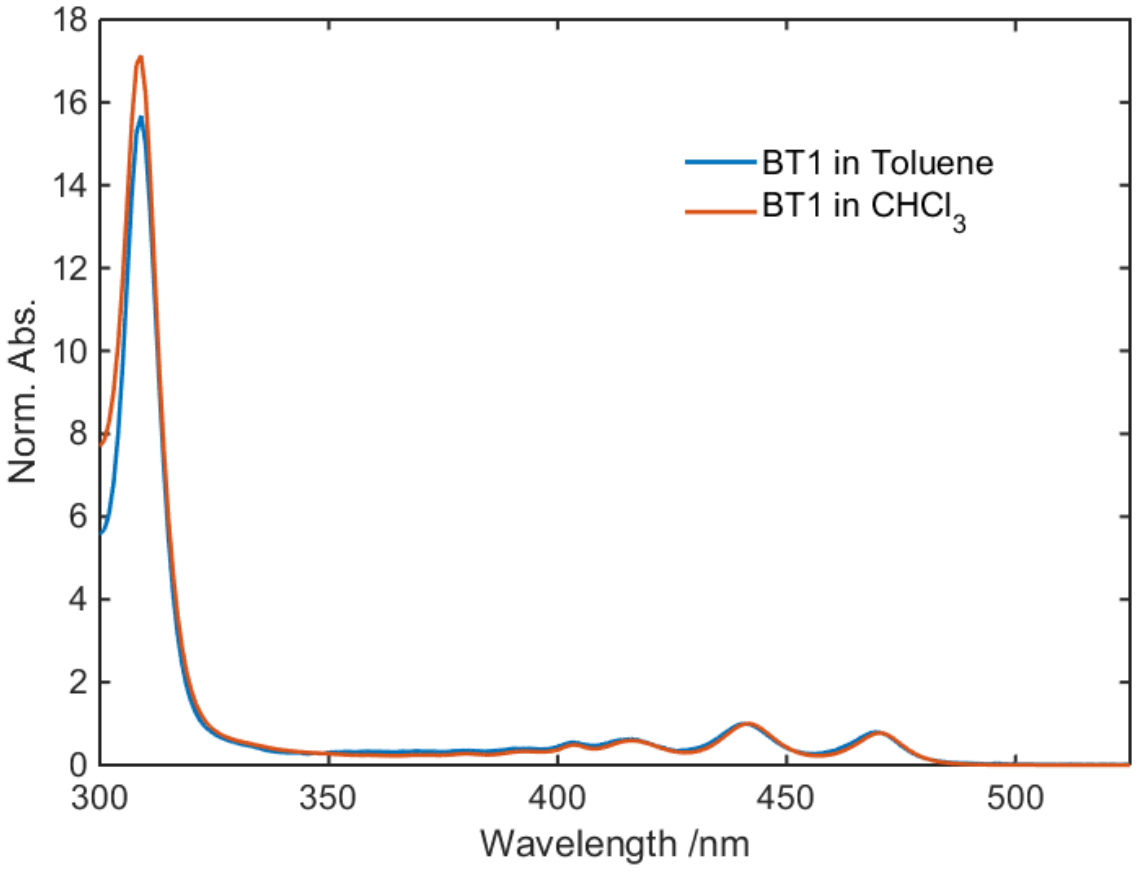

Figure A.1. Comparative electronic absorption spectra of BT1 in toluene and chloroform.

A.2 Nuclear Coordinates for $S_{1\text{-loc}}$ and Q

Single-point calculations (6-31g(d) basis, the ω-B97XD range corrected density functional, and gas phase) were carried out using the Gaussian 09 software package running on the National Energy Research Super Computer (NERSC) facility (www.NERSC.gov).[1] The energy of the lowest quintet state (Q) was calculated at two previously determined (using ΔSCF and TD-DFT with gradients, 6-31g(d) basis, the ω-B97XD range corrected density functional, and a polarizable continuum model parameterized for toluene)[2] geometries: $S_{1\text{-loc}}$ and Q. The difference in these energies was taken as an estimate of the inner sphere reorganization energy λ_i. The energies are given in Table A.1, while the coordinates for $S_{1\text{-loc}}$ and Q are given in Table A.2 and Table A.3, respectively.

Table A.1. Lowest energy quintet (Q) state energies (gas-phase calculations; 6-31g(d) and ω-B97XD range corrected density functional) at the indicated geometries, as used to estimate the inner sphere reorganization energy λ_i for SF

Geometry	Energy/ Hartree	λ_i / Hartree	λ_i / eV
$S_{1\text{-loc}}$	-1500.02590004		
		0.015826	0.431
Q	-1500.04172621		

Table A.2. Cartesian coordinates for optimized geometry of $S_{1\text{-loc}}$

C	-1.1986460000	2.4627510000	0.7050730000
C	0.0150310000	3.2705080000	1.1405210000
C	0.0150300000	3.2705080000	-1.1405210000
C	0.0362420000	4.3261200000	0.0000000000
H	0.9456420000	4.9351820000	0.0000000000
H	-0.8489760000	4.9689340000	0.0000000000
C	1.2188140000	2.4355370000	0.7223160000
C	1.2188130000	2.4355360000	-0.7223170000
H	0.0145070000	3.6303630000	2.1697000000
H	0.0145060000	3.6303620000	-2.1697010000
C	-2.1594540000	1.7760300000	-1.4169530000
C	-2.1594530000	1.7760300000	1.4169530000
C	-3.1737370000	1.0816150000	-0.7188350000
H	-2.1587570000	1.7685280000	-2.5042210000
C	-3.1737370000	1.0816160000	0.7188340000
H	-2.1587570000	1.7685290000	2.5042210000
C	-4.2039270000	0.3856410000	-1.3967680000
C	-4.2039270000	0.3856400000	1.3967680000
C	-5.2258050000	-0.2988280000	-0.7256540000
H	-4.2018190000	0.3862570000	-2.4848690000
C	-5.2258050000	-0.2988270000	0.7256550000
H	-4.2018190000	0.3862580000	2.4848690000
C	-6.2460460000	-0.9795260000	-1.3992620000
C	-6.2460460000	-0.9795260000	1.3992620000
C	-7.2827400000	-1.6675930000	-0.7173620000
H	-6.2476430000	-0.9813840000	-2.4873380000
C	-7.2827400000	-1.6675920000	0.7173630000
H	-6.2476430000	-0.9813820000	2.4873380000
H	-8.3094580000	-2.3472840000	2.4833750000
C	-8.3097410000	-2.3472500000	1.3962760000
C	-9.3140190000	-3.0108650000	0.6989110000
C	-9.3140190000	-3.0108650000	-0.6989100000
H	-10.0987250000	-3.5289020000	1.2415790000
C	-8.3097410000	-2.3472500000	-1.3962760000
H	-10.0987250000	-3.5289020000	-1.2415790000
H	-8.3094580000	-2.3472850000	-2.4833750000
C	-1.1986460000	2.4627510000	-0.7050740000
C	5.2233120000	-0.3096680000	-0.7201030000
C	4.1981630000	0.3828420000	-1.4001830000
C	5.2233130000	-0.3096670000	0.7201030000
C	6.2446400000	-0.9942610000	-1.4014830000
C	3.1990870000	1.0604370000	-0.7243760000
H	4.1991480000	0.3833230000	-2.4882000000
C	4.1981640000	0.3828420000	1.4001820000
C	6.2446410000	-0.9942610000	1.4014830000
C	7.2519830000	-1.6664560000	-0.7208650000
H	6.2449110000	-0.9944350000	-2.4895090000
C	3.1990870000	1.0604390000	0.7243760000
C	2.1611950000	1.7751670000	-1.4289170000
H	4.1991490000	0.3833260000	2.4881990000
H	6.2449090000	-0.9944400000	2.4895090000
C	7.2519830000	-1.6664560000	0.7208640000
C	2.1611950000	1.7751670000	1.4289170000
H	2.1671390000	1.7756540000	-2.5161830000
H	2.1671400000	1.7756560000	2.5161830000
H	10.0673740000	-3.5357920000	1.2469190000
C	9.2782550000	-3.0126100000	0.7151350000
C	8.3013490000	-2.3640700000	1.4061860000
C	9.2782550000	-3.0126110000	-0.7151340000
H	8.2999750000	-2.3631520000	2.4932140000
C	8.3013480000	-2.3640710000	-1.4061860000
H	10.0673730000	-3.5357920000	-1.2469180000
H	8.2999710000	-2.3631570000	-2.4932140000

Table A.3. Cartesian coordinates for optimized geometry of Q

C	1.2155930000	2.4283490000	-0.7034970000
C	-0.0000020000	3.2406590000	-1.1380430000
C	-0.0000020000	3.2406590000	1.1380440000
C	-0.0000300000	4.3009420000	0.0000000000
H	-0.8978210000	4.9265960000	0.0000000000
H	0.8977290000	4.9266410000	0.0000000000
C	-1.2155780000	2.4283120000	-0.7035070000
C	-1.2155780000	2.4283120000	0.7035070000
H	-0.0000070000	3.5974840000	-2.1684800000
H	-0.0000070000	3.5974840000	2.1684800000
C	2.1855360000	1.7552480000	1.4131850000
C	2.1855360000	1.7552480000	-1.4131850000
C	3.1989120000	1.0718430000	0.7113490000
H	2.1887690000	1.7508500000	2.5006310000
C	3.1989120000	1.0718430000	-0.7113490000
H	2.1887690000	1.7508500000	-2.5006300000
C	4.2477970000	0.3739440000	1.4009320000
C	4.2477970000	0.3739450000	-1.4009320000
C	5.2681480000	-0.2992520000	0.7311980000
H	4.2417890000	0.3770030000	2.4885870000
C	5.2681480000	-0.2992520000	-0.7311980000
H	4.2417890000	0.3770030000	-2.4885870000
C	6.2946010000	-0.9738720000	1.4056180000
C	6.2946010000	-0.9738720000	-1.4056180000
C	7.3491410000	-1.6629580000	0.7125590000
H	6.2994730000	-0.9777470000	2.4930730000
C	7.3491410000	-1.6629570000	-0.7125590000
H	6.2994730000	-0.9777460000	-2.4930730000
H	8.3726550000	-2.3299900000	-2.4797550000
C	8.3726600000	-2.3300110000	-1.3925840000
C	9.3848620000	-2.9890500000	-0.6959740000
C	9.3848620000	-2.9890500000	0.6959740000
H	10.1716720000	-3.5008430000	-1.2417350000
C	8.3726600000	-2.3300110000	1.3925840000
H	10.1716720000	-3.5008430000	1.2417350000
H	8.3726470000	-2.3300020000	2.4797550000
C	1.2155930000	2.4283490000	0.7034980000
C	-5.2681320000	-0.2992470000	0.7311960000
C	-4.2477930000	0.3739350000	1.4009290000
C	-5.2681320000	-0.2992470000	-0.7311960000
C	-6.2946040000	-0.9738740000	1.4056210000
C	-3.1989070000	1.0718260000	0.7113420000
H	-4.2417820000	0.3769970000	2.4885840000
C	-4.2477930000	0.3739350000	-1.4009290000
C	-6.2946040000	-0.9738740000	-1.4056210000
C	-7.3491480000	-1.6629550000	0.7125640000
H	-6.2994710000	-0.9777450000	2.4930750000
C	-3.1989070000	1.0718260000	-0.7113420000
C	-2.1855190000	1.7552340000	1.4131880000
H	-4.2417820000	0.3769970000	-2.4885840000
H	-6.2994710000	-0.9777440000	-2.4930750000
C	-7.3491480000	-1.6629550000	-0.7125650000
C	-2.1855190000	1.7552340000	-1.4131870000
H	-2.1887660000	1.7508330000	2.5006330000
H	-2.1887660000	1.7508330000	-2.5006330000
H	-10.1716840000	-3.5008300000	-1.2417390000
C	-9.3848780000	-2.9890430000	-0.6959670000
C	-8.3726620000	-2.3300000000	-1.3925830000
C	-9.3848780000	-2.9890430000	0.6959670000
H	-8.3726640000	-2.3299850000	-2.4797530000
C	-8.3726620000	-2.3300010000	1.3925820000
H	-10.1716830000	-3.5008310000	1.2417390000
H	-8.3726560000	-2.3299970000	2.4797530000

A.3 Bibliography

1. Frisch, M. J. *et al.* Gaussian 09, Revision A.1. (2009).

2. Vallett, P. J., Snyder, J. L. & Damrauer, N. H. Tunable electronic coupling and driving force in structurally well-defined tetracene dimers for molecular singlet fission: a computational exploration using density functional theory. *J. Phys. Chem. A* **117,** 10824–38 (2013).

Appendix B. Supporting Information for Chapter 4

B.1 Electronic Absorption and Emission of TIPS-Tc-es and TIPS-Tc-eu in Chloroform

The below are normalized absorption and emission spectra of TIPS-Tc-es (pink) and TIPS-Tc-eu (blue) in chloroform, showing similarity to TIPS-Tc. The absorbance to the left of the vertical line (below 400 nm) has been scaled to 15% of its true value for clarity. Both have a single feature in the ultraviolet. Note the contamination peak in the emission of TIPS-Tc-es near 450 nm.

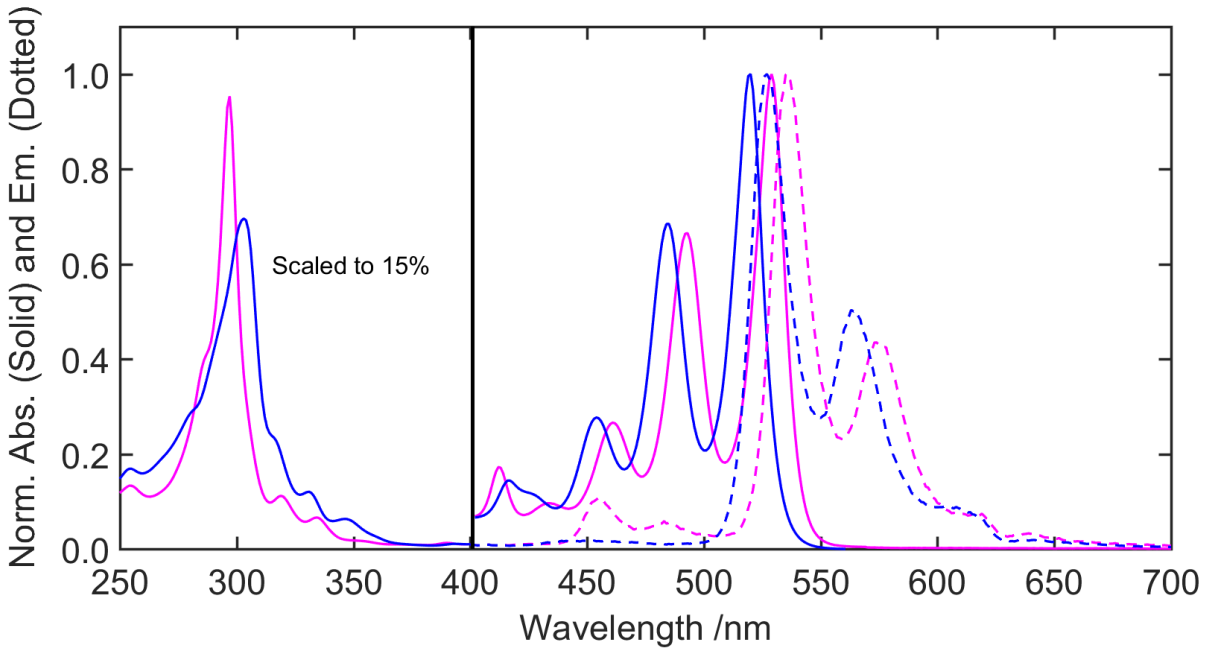

Figure B.1. Electronic absorption (solid lines) and emission (dotted lines) spectra of TIPS-Tc-es and TIPS-Tc-eu in chloroform solution.

In addition to the pictured steady-state spectra, time-correlated single-photon counting measurements (see Chapter 3 for details; emission wavelength was 580 nm for these experiments) were performed on TIPS-Tc-es and TIPS-Tc-eu in chloroform (Figure B.2).

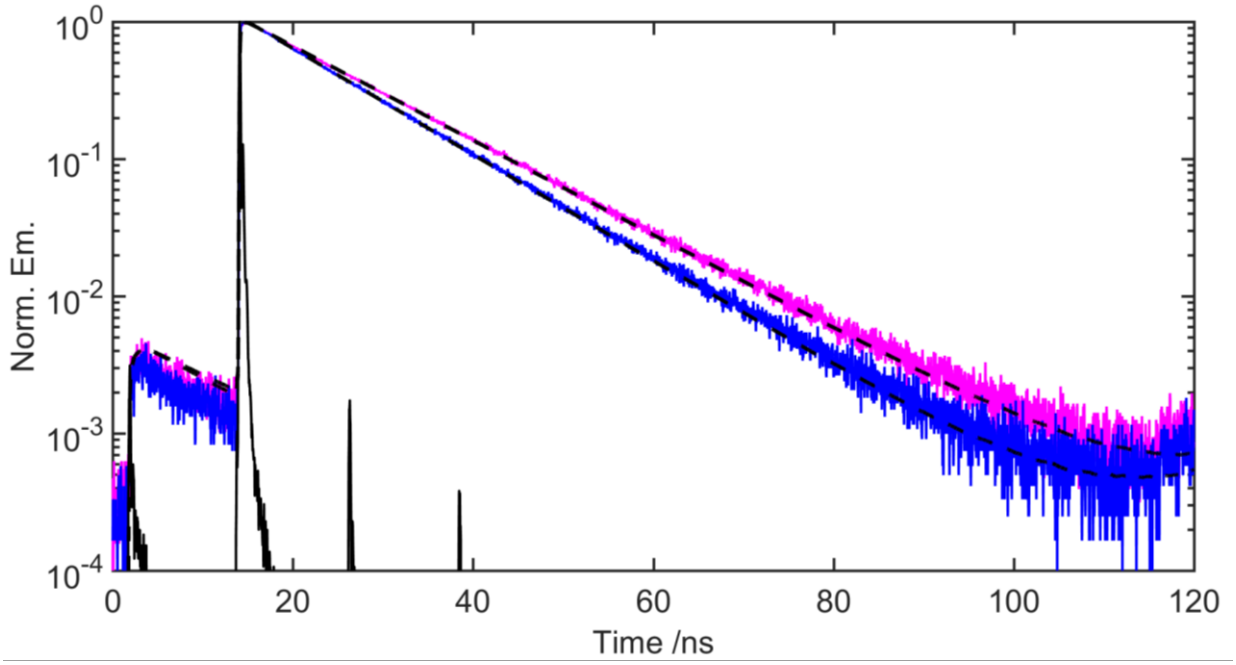

Figure B.2. TCSPC decays (solid lines) and fits (dashed lines) for TIPS-Tc-es (pink) and TIPS-Tc-eu (blue) in chloroform. IRF is shown in black.

Fitting (dashed lines in the above fiture) was accomplished by convolving the IRF (pictured) with an exponential decay. Lifetimes retrieved by this method were 12.6 ns for TIPS-Tc-es and 11.1 ns for TIPS-Tc-eu. The observed mono-exponential behavior and lifetimes are consistent with the behavior of TIPS-Tc.

B.2 Nuclear Coordinates for TIPS-Tc and TIPS-BT1

Coordinates were calculated by Niels Damrauer by geometry optimization of TIPS-Tc and TIPS-BT1 (after replacing the isopropyl constituents with hydrogen atoms) via density functional theory (DFT) using the Gaussian 09 software package[1] (ω-B97XD density functional, 6-31g(d) basis set, and toluene polarizable continuum model. Coordinates are given in Table B.1 for the TIPS-Tc ground state, Table B.2 for the TIPS-BT1 ground state, and Table B.3 for the TIPS-BT1 lowest energy triplet. See also Figure B.3 for a graphical representation of the TIPS-BT1 geometry

optimized structure in which the isopropyl groups have been manually added following optimization to show the overall structure).

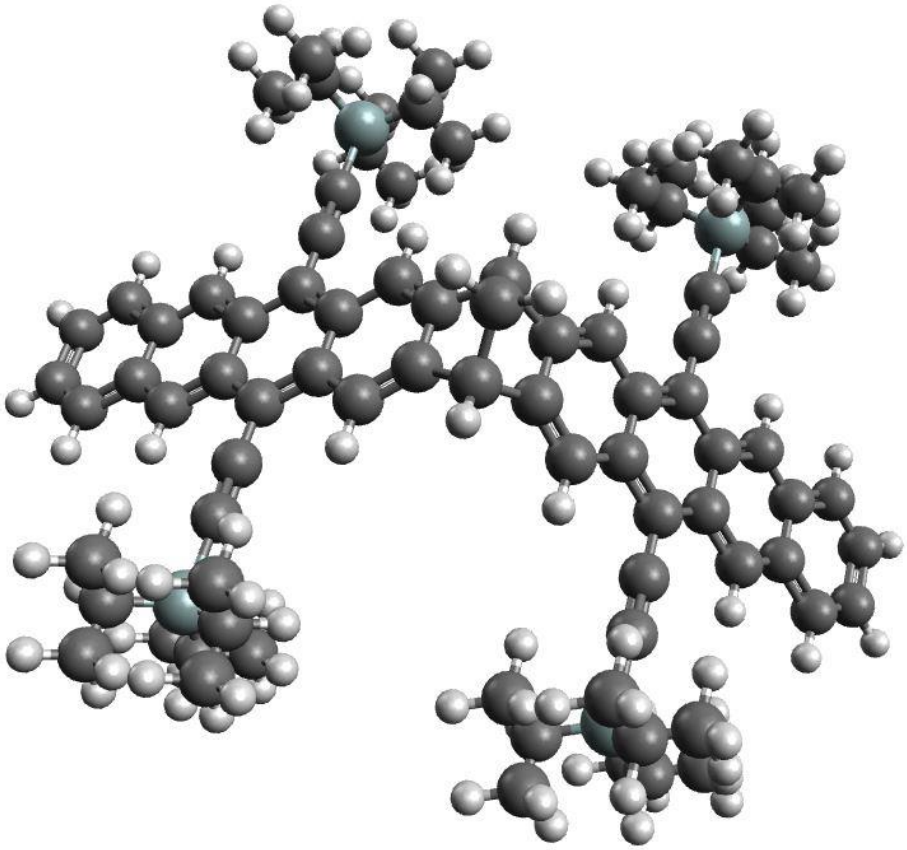

Figure B.3. TIPS-BT1 geometry optimized structure (the isopropyl groups shown here were added manually after optimization to show relative size and were not considered in the geometry optimization).

Table B.1. Cartesian coordinates for optimized geometry of the TIPS-Tc ground state

Atom #	Atom	ID	x /Å	y /Å	z /Å
1	C	6	0.713562	-4.495017	0.008293
2	C	6	-0.713945	-4.494957	0.008285
3	C	6	-0.718640	0.397939	0.004891
4	C	6	-1.414724	-0.845024	0.005115
5	C	6	0.718675	0.397879	0.004898
6	C	6	-1.398906	1.628029	0.004211
7	C	6	-0.718890	-2.063295	0.006538
8	C	6	-2.841410	-0.843698	0.002047
9	C	6	1.414653	-0.845143	0.005129
10	C	6	1.399045	1.627911	0.004226
11	C	6	-0.719590	2.837224	0.003645
12	H	1	-2.484978	1.627593	0.004370
13	C	6	0.718714	-2.063355	0.006545
14	C	6	-1.403386	-3.322592	0.007380
15	C	6	2.841339	-0.843945	0.002080
16	H	1	2.485117	1.627380	0.004396
17	C	6	0.719833	2.837164	0.003653
18	C	6	1.403103	-3.322711	0.007394
19	H	1	-2.488328	-3.319660	0.007497
20	H	1	2.488044	-3.319875	0.007522
21	H	1	1.245584	6.214696	0.002047
22	C	6	0.716169	5.266839	0.002526
23	C	6	1.408316	4.096188	0.003061
24	C	6	-0.715724	5.266898	0.002518
25	H	1	2.494996	4.091990	0.002983
26	C	6	-1.407969	4.096305	0.003046
27	H	1	-1.245058	6.214799	0.002033
28	H	1	-2.494649	4.092198	0.002956
29	C	6	-4.058193	-0.837657	-0.001474
30	Si	14	-5.883314	-0.828991	-0.016903
31	C	6	4.058123	-0.838005	-0.001444
32	Si	14	5.883244	-0.829354	-0.016922
33	H	1	-6.401717	-1.204932	1.320414
34	H	1	-6.377179	-1.799869	-1.022583
35	H	1	-6.367913	0.528287	-0.364631
36	H	1	6.367851	0.527828	-0.365011
37	H	1	6.377069	-1.800498	-1.022366
38	H	1	6.401678	-1.204961	1.320477
39	H	1	1.247585	-5.440058	0.009044
40	H	1	-1.248050	-5.439952	0.009031

Table B.2. Cartesian coordinates for optimized geometry of the TIPS-BT1 ground state

Atom #	Atomic #	x /Å	y /Å	z /Å
1	6	-1.212332	-0.719970	2.295301
2	6	-0.005829	-1.143747	3.117859
3	6	-0.005688	1.143800	3.117995
4	6	-0.006489	-0.000042	4.171886
5	1	0.889654	-0.000123	4.799256
6	1	-0.903529	-0.000046	4.797975
7	6	1.201778	-0.720116	2.296818
8	6	1.201980	0.720110	2.297060
9	1	-0.006150	-2.172172	3.478067
10	1	-0.005897	2.172176	3.478336
11	6	-2.161321	1.425216	1.642676
12	6	-2.161530	-1.424900	1.642839
13	6	-3.205204	0.721579	0.941817
14	1	-2.165181	2.510367	1.639198
15	6	-3.205353	-0.721249	0.941963
16	1	-2.165450	-2.510040	1.639413
17	6	-4.219387	1.412648	0.268334
18	6	-4.219611	-1.412327	0.268567
19	6	-5.259662	0.717886	-0.419560
20	6	-4.220311	2.839732	0.266662
21	6	-5.259800	-0.717575	-0.419377
22	6	-4.220516	-2.839413	0.267609
23	6	-6.285415	1.398451	-1.094147
24	6	-6.285624	-1.398210	-1.093788
25	6	-7.298723	0.719092	-1.757530
26	1	-6.285257	2.484503	-1.094309
27	6	-7.298834	-0.718888	-1.757362
28	1	-6.285500	-2.484272	-1.093745
29	1	-8.349099	-2.494031	-2.442439
30	6	-8.352515	-1.407323	-2.444898
31	6	-9.333915	-0.715314	-3.084681
32	6	-9.333786	0.715550	-3.084873
33	1	-10.128239	-1.245255	-3.601511
34	6	-8.352272	1.407541	-2.445252
35	1	-10.127991	1.245505	-3.601871
36	1	-8.348621	2.494251	-2.443124
37	6	-1.212240	0.720241	2.295302
38	6	5.253121	0.717534	-0.412187
39	6	4.212244	1.412369	0.274820
40	6	5.252361	-0.717861	-0.413250
41	6	6.280038	1.398143	-1.085056
42	6	3.196996	0.721371	0.946651
43	6	4.215067	2.839451	0.272224

44	6	4.210940	-1.412610	0.273022
45	6	6.278460	-1.398552	-1.087281
46	6	7.293596	0.718734	-1.748013
47	1	6.280788	2.484204	-1.084196
48	6	3.196471	-0.721527	0.945940
49	6	2.152328	1.424995	1.646211
50	6	4.212309	-2.839689	0.268361
51	1	6.277970	-2.484613	-1.088190
52	6	7.292743	-0.719230	-1.749216
53	6	2.151627	-1.425067	1.645313
54	1	2.156806	2.510131	1.643168
55	1	2.155616	-2.510204	1.641672
56	1	10.123539	-1.245769	-3.591168
57	6	9.329113	-0.715788	-3.074534
58	6	8.346604	-1.407750	-2.436405
59	6	9.330002	0.715083	-3.073278
60	1	8.342308	-2.494460	-2.435135
61	6	8.348318	1.407147	-2.433990
62	1	10.125108	1.244974	-3.588955
63	1	8.345397	2.493857	-2.430785
64	6	4.224041	4.056203	0.265493
65	14	4.243446	5.880614	0.240760
66	6	4.220000	-4.056438	0.259665
67	14	4.237338	-5.880810	0.231703
68	6	-4.223553	4.056528	0.263559
69	14	-4.214146	5.881159	0.262289
70	6	-4.222454	-4.056213	0.265683
71	14	-4.208825	-5.880834	0.273601
72	1	-4.205879	6.384313	-1.132240
73	1	-3.003134	6.368163	0.965610
74	1	-5.420885	6.391923	0.956455
75	1	4.595628	6.400644	1.584157
76	1	2.905558	6.392121	-0.142300
77	1	5.248636	6.348627	-0.743328
78	1	-3.201981	-6.359934	1.250952
79	1	-3.863231	-6.390822	-1.074980
80	1	-5.546643	-6.391431	0.658611
81	1	5.238385	-6.348206	-0.756829
82	1	2.897487	-6.390187	-0.147353
83	1	4.593768	-6.403635	1.572960

Table B.3. Cartesian coordinates for optimized geometry of the first TIPS-BT1 triplet

Atom #	Atom	x /Å	y /Å	z /Å
1	C	1.2240610000	2.4383790000	-0.4999610000
2	C	1.2223920000	2.3037200000	0.9348300000
3	C	2.1718360000	1.8521930000	-1.2612780000
4	C	2.1665630000	1.5834180000	1.5758330000
5	H	2.1720450000	1.4799400000	2.6559180000
6	H	2.1817630000	1.9552120000	-2.3413770000
7	C	3.2090860000	1.0763950000	-0.6264710000
8	C	3.2049750000	0.9380460000	0.8106590000
9	C	4.2166370000	0.4635990000	-1.3776900000
10	C	4.2266510000	0.6016180000	-2.8013880000
11	C	4.2407180000	0.7157560000	-4.0038530000
12	H	4.2524270000	0.8181470000	-5.0665320000
13	C	4.2066660000	0.1908310000	1.4374790000
14	C	4.2051380000	0.0504730000	2.8610010000
15	C	4.2103090000	-0.0721000000	4.0627140000
16	H	4.2124220000	-0.1830720000	5.1245940000
17	C	5.2394700000	-0.4400610000	0.6805680000
18	C	5.2454660000	-0.2999210000	-0.7481900000
19	C	6.2663550000	-0.9182710000	-1.4874410000
20	H	6.2708150000	-0.8106110000	-2.5680450000
21	C	6.2535330000	-1.1919790000	1.2947130000
22	H	6.2471060000	-1.2992360000	2.3753060000
23	C	7.2609570000	-1.8003280000	0.5574740000
24	C	7.2680570000	-1.6584700000	-0.8732640000
25	C	8.3159030000	-2.2899190000	-1.6217680000
26	H	8.3184880000	-2.1792530000	-2.7028810000
27	C	8.3013370000	-2.5675770000	1.1787330000
28	H	8.2913370000	-2.6736530000	2.2602700000
29	C	9.2775300000	-3.1502120000	0.4309390000
30	C	9.2852470000	-3.0084450000	-0.9927710000
31	C	-1.1946230000	2.3376230000	0.9153860000
32	C	0.0205200000	3.0968110000	1.4298870000
33	C	0.0217740000	3.3078100000	-0.8426490000
34	C	0.0460520000	4.2552240000	0.3915510000
35	H	0.9566700000	4.8594720000	0.4479720000
36	H	-0.8378570000	4.8967730000	0.4501230000
37	H	0.0198270000	3.3561180000	2.4885870000
38	H	0.0222740000	3.7591820000	-1.8346470000
39	C	-2.1629770000	1.8497960000	-1.2449980000
40	C	-2.1602900000	1.5871270000	1.5567180000
41	C	-3.1699720000	1.1018270000	-0.6133850000
42	H	-2.1637800000	1.9432520000	-2.3264710000
43	C	-3.1673180000	0.9676910000	0.7993090000

44	H	-2.1579000000	1.4754310000	2.6364550000
45	C	-4.2236850000	0.4617540000	-1.3941440000
46	C	-4.2153870000	0.1898420000	1.4513290000
47	C	-5.2642620000	-0.2986170000	-0.7570790000
48	C	-4.2208660000	0.5977600000	-2.7959120000
49	C	-5.2592360000	-0.4382460000	0.6883120000
50	C	-4.2008410000	0.0531800000	2.8530050000
51	C	-6.2720550000	-0.9028220000	-1.4828500000
52	C	-6.2615720000	-1.1712130000	1.2926680000
53	C	-7.3127850000	-1.6597630000	-0.8637180000
54	H	-6.2801790000	-0.8004020000	-2.5642190000
55	C	-7.3070890000	-1.7972410000	0.5482640000
56	H	-6.2609900000	-1.2800450000	2.3733760000
57	H	-8.3198600000	-2.6448000000	2.2534440000
58	C	-8.3277950000	-2.5403800000	1.1716370000
59	C	-9.3259320000	-3.1307900000	0.4203480000
60	C	-9.3318800000	-2.9945250000	-0.9775520000
61	C	-8.3392720000	-2.2702830000	-1.6095800000
62	H	-8.3415740000	-2.1624030000	-2.6910490000
63	C	-1.1948310000	2.4674390000	-0.4773680000
64	C	-4.2197150000	0.7152220000	-4.0039820000
65	H	-4.2170630000	0.8184390000	-5.0666100000
66	C	-4.1907340000	-0.0660450000	4.0608530000
67	H	-4.1787900000	-0.1745280000	5.1228910000
68	H	10.0613940000	-3.7284600000	0.9107010000
69	H	10.0749140000	-3.4819680000	-1.5682600000
70	H	-10.1088840000	-3.7009390000	0.9109150000
71	H	-10.1192850000	-3.4605550000	-1.5619580000

B.3 Spectral Slices and Global Fits for all TRPL Data

The following are spectral slices with accompanying fits for TRPL data on TIPS-Tc and TIPS-BT1. All fitting was done globally to either a single or a sum of two exponentially modified Gaussian functions, as described in the text. Spectral slices correspond to the indicated time relative to the onset of the laser pulse, while TRPL surfaces indicate raw photon counts as a function of time and wavelength.

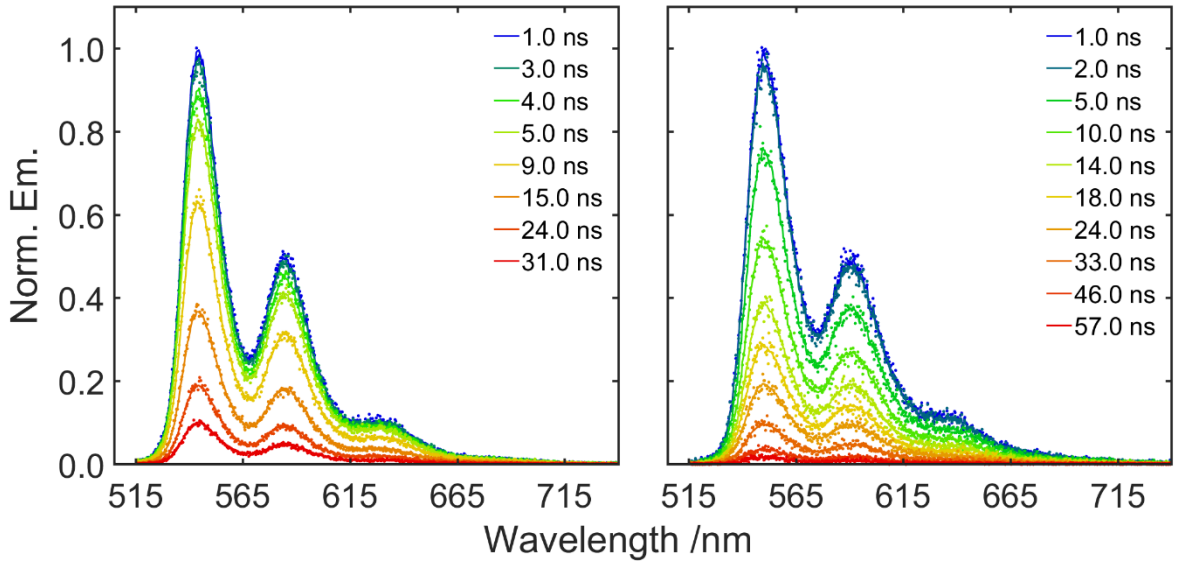

Figure B.4. TRPL spectra at the indicated times extracted from the data (points) and from the global fit (lines) for TIPS-Tc in toluene (left) and benzonitrile (right) at ambient temperature.

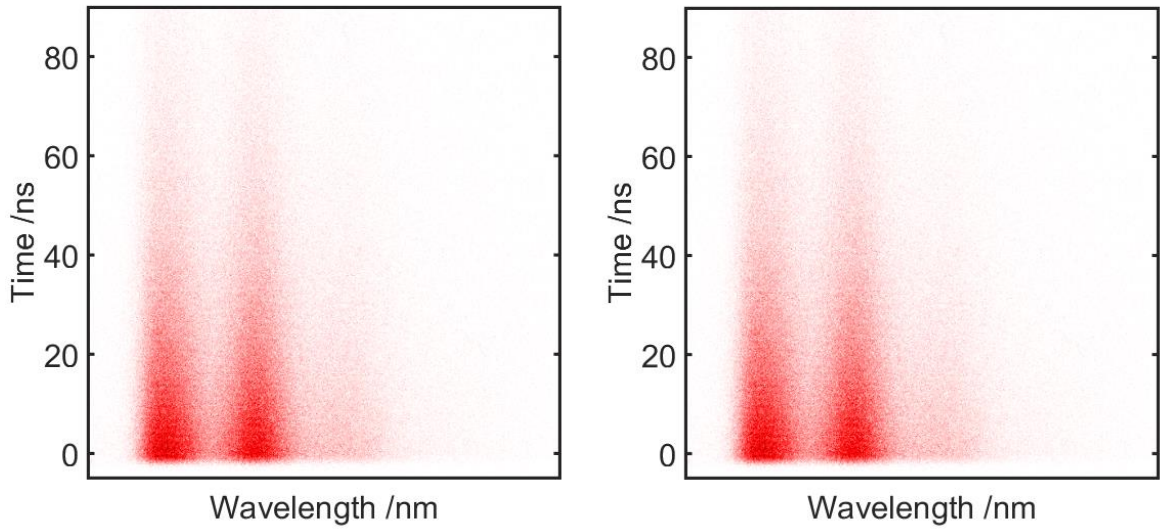

Figure B.5. TRPL surfaces for TIPS-BT1 in toluene at 0 °C (left) and 50 °C (right). Data at 23 °C is given in the main text. Intensity of color signifies greater emission intensity.

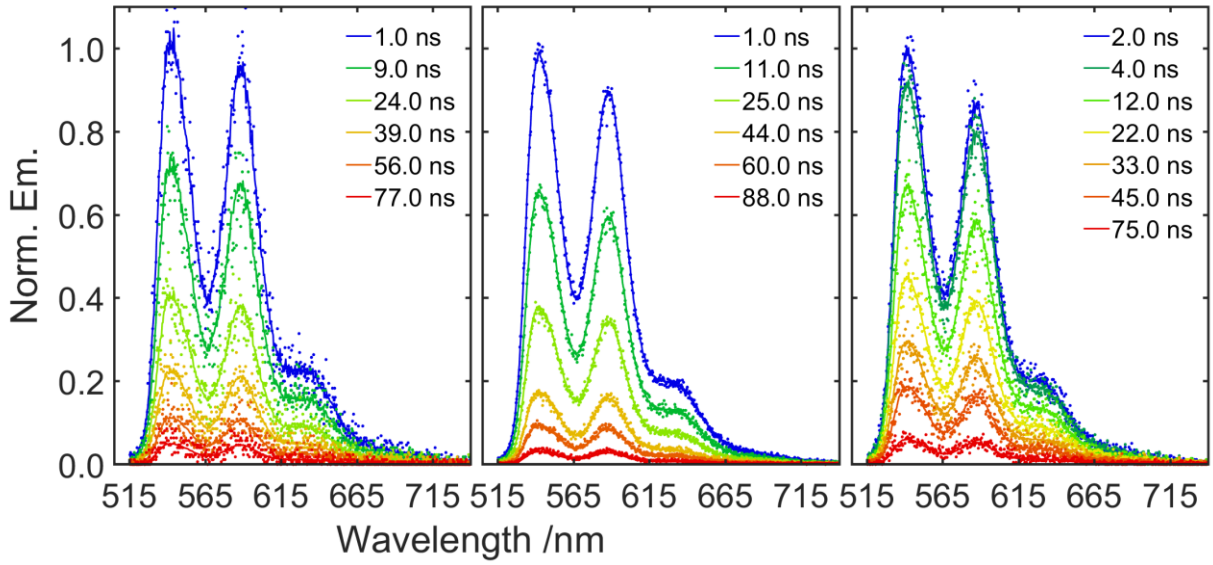

Figure B.6. TRPL spectra at the indicated times extracted from the data (points) and from the global fit (lines) for TIPS-BT1 in toluene at (left to right) 0 °C, 23 °C, and 50 °C.

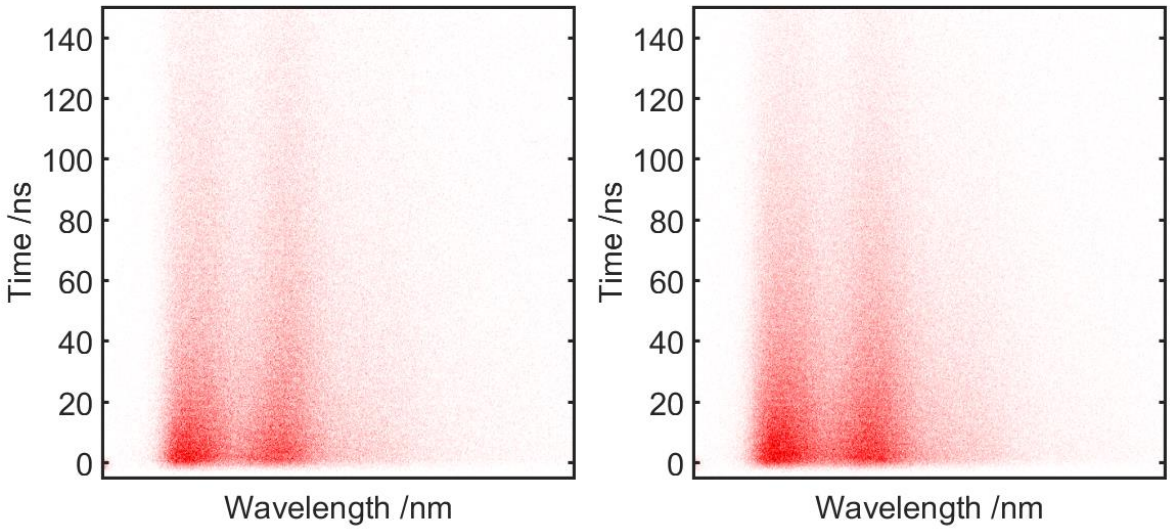

Figure B.7. TRPL surfaces for TIPS-BT1 in benzonitrile at 0 °C (left) and 50 °C (right). Data at 23 °C is given in the main text. Intensity of color signifies greater emission intensity.

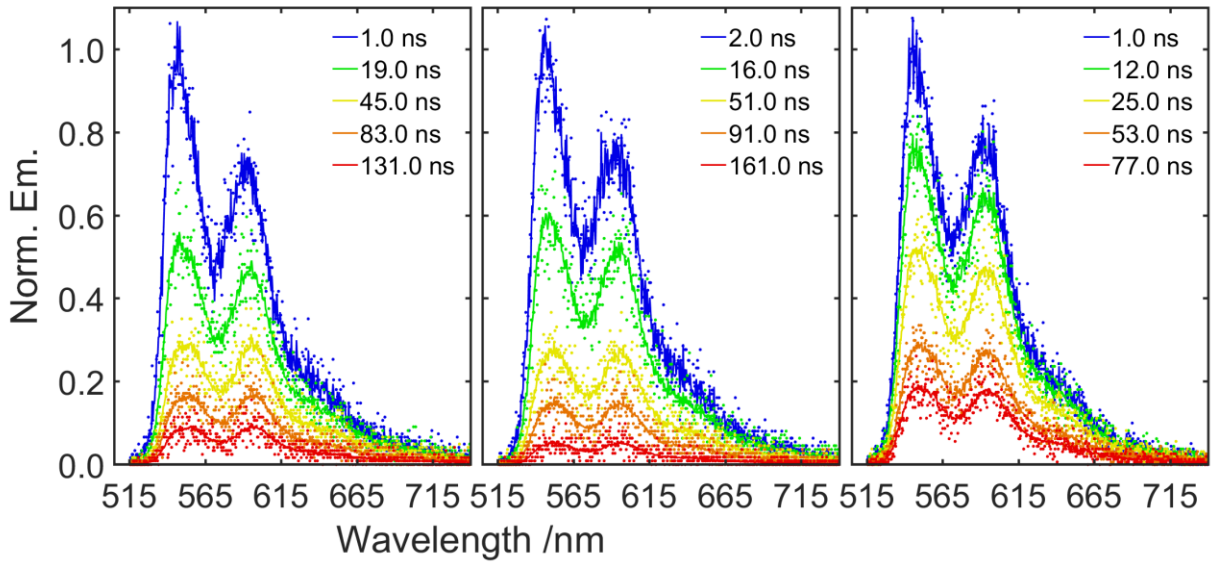

Figure B.8. TRPL spectra at the indicated times extracted from the data (points) and from the global fit (lines) for TIPS-BT1 in benzonitrile at (left to right) 0 °C, 23 °C, and 50 °C.

B.4 Cyclic Voltammetry Curves for TIPS-Tc and TIPS-BT1

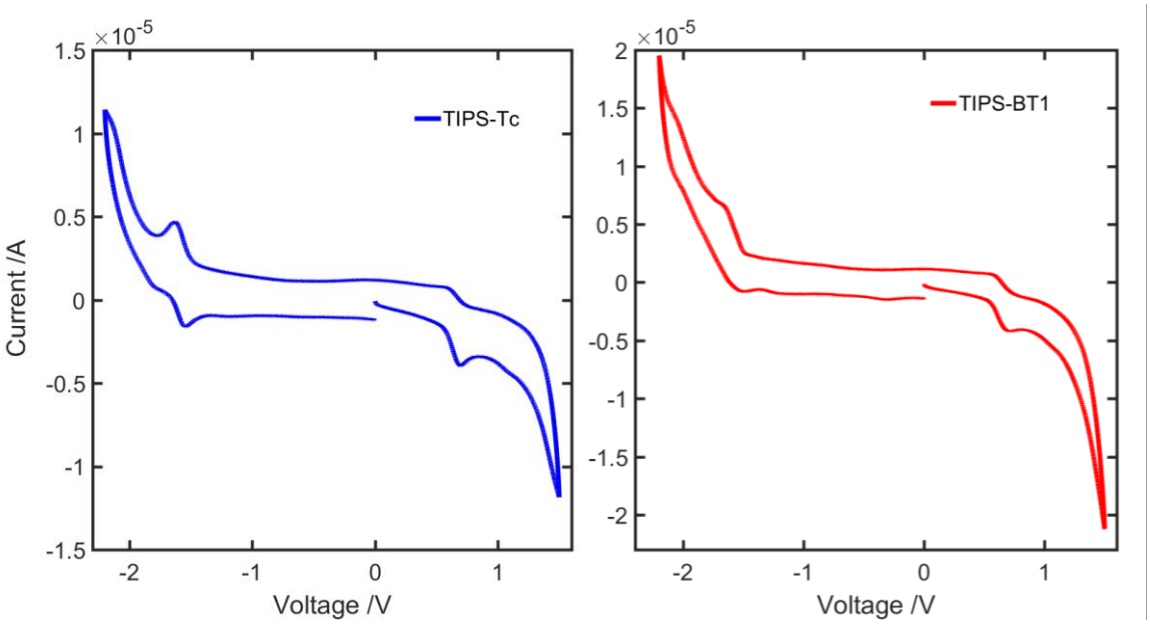

Figure B.9. Raw cyclic voltammograms for TIPS-Tc (blue, left) and TIPS-BT1 (red, right) in benzonitrile. See Chapter 4 for experiment details.

B.5 Picosecond Photoluminescence Measurements of TIPS-Tc and TIPS-BT1

B.5.1 Methods

Excitation light in the photoluminescence upconversion (PLU) experiment uses a TOPAS-C optical parametric amplifier driven with a Spectra-Physics Solstice amplified Ti:sapphire laser (1 kHz repetition rate, ~100 fs pulse duration, 493 nm center wavelength for these experiments). This (along with the additional fundamental at ~800 nm from the amplifier) is coupled into an Ultrafast Systems Halcyone Femtosecond Fluorescence Spectrometer. The excitation spot size was approximately 60 µm, with a pump fluence of 100 nJ/pulse. Orion Pearce was instrumental in acquiring this data, and this experiment could not have been done without his assistance. Data was processed using Ultrafast Systems Surface Xplorer to accomplish background correction and outlier removal before fitting in MATLAB.

B.5.2 Results

Measurements were taken on TIPS-Tc in benzonitrile, TIPS-BT1 in toluene, and TIPS-BT1 in benzonitrile exciting at 493 nm to match the excitation wavelength in TRPL. Spectral slices show no spectral evolution with time in all samples.

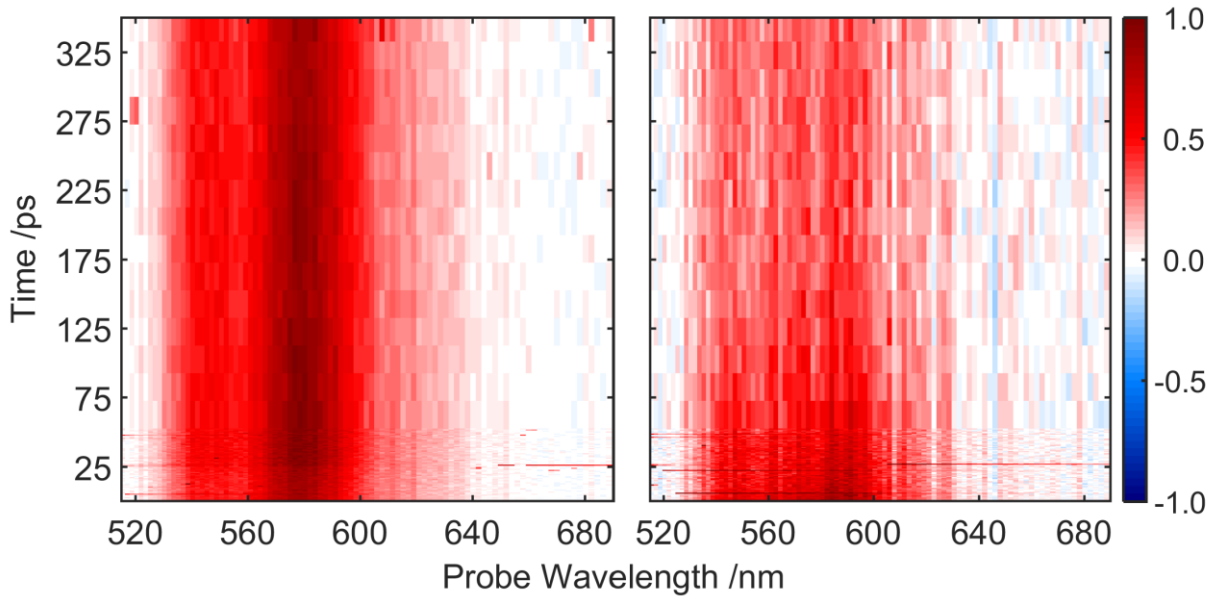

Figure B.10. Full PLU data for TIPS-BT1 in toluene (left) and benzonitrile (right) over 300 ps.

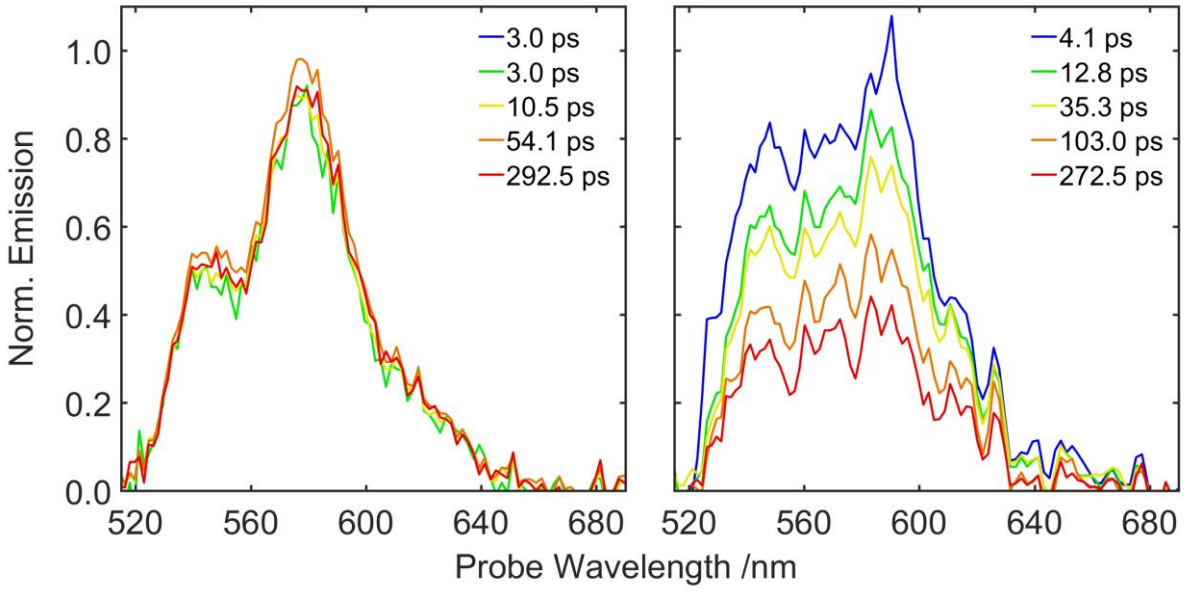

Figure B.11. Averaged PLU spectra (normalized at time = 0) centered at the indicated times for TIPS-BT1 in toluene (left) and benzonitrile (right) over 300 ps. Spectral features in benzonitrile do not shift discernibly with time.

An excitation leakage pulse in the instrument results in a re-excitation at ~25 ps in the data (see Figure B.12 evident in all 3 data sets). Fits to TIPS-Tc in benzonitrile and TIPS-BT1 in toluene are shown at left, for which the behavior cannot be described by an exponential rise or decay (example fits to a sum of two exponentials are shown). To correct for the re-excitation behavior, the decay for TIPS-BT1 in benzonitrile was divided by the TIPS-BT1 in toluene decay to give the bottom curves in the middle and right plots in Figure B.12. TIPS-Tc before fitting. Fits before and after application of this correction are shown. Given that no spectral shifts occurred, fits to the integrated spectra are shown in. Fits to an exponential decay before correction are of poor quality (giving an 89 ps lifetime), while fitting after correction gives an improved fit and a 47 ps lifetime.

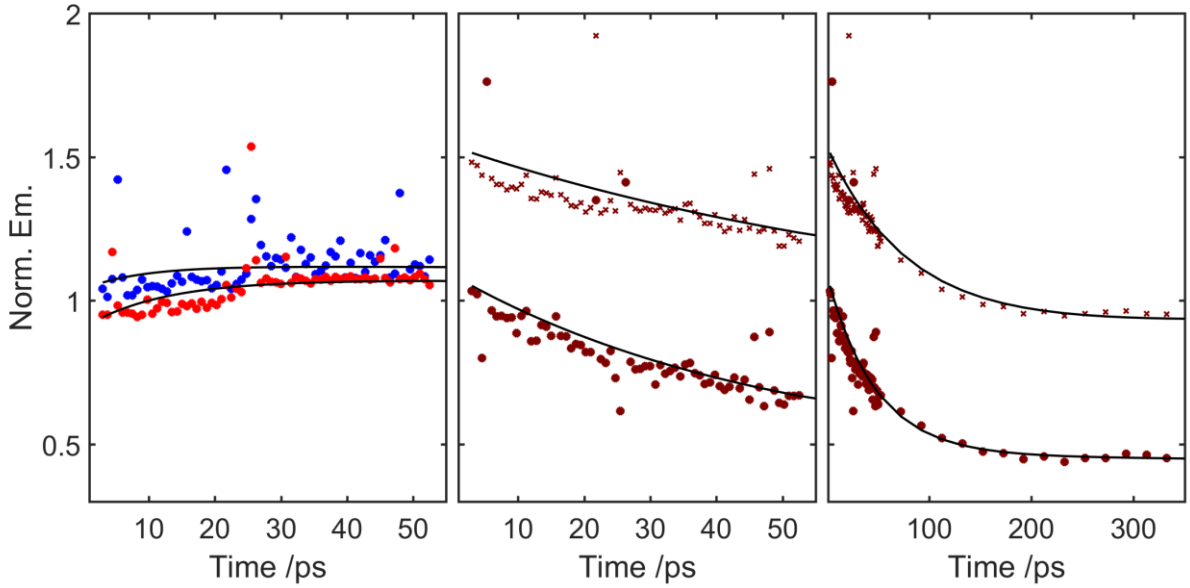

Figure B.12. Integrated PLU kinetics (normalized at time = 0) at the indicated times. Left: TIPS-Tc in benzonitrile (blue) and TIPS-BT1 in toluene (red), showing re-excitation at ~25 ps. Middle: early data for TIPS-BT1 in benzonitrile, with uncorrected (top, crosses, offset by 0.5) and corrected (bottom, circles, after division by TIPS-BT1 in toluene data) decays shown. Fits start at 1 ps to avoid scattered pump light. Right: identical to middle plot, but inclusive of remaining times.

B.6 Single-Feature Kinetics of TIPS-Tc and TIPS-BT1 in Toluene and Benzonitrile

The following figures (Figure B.13–Figure B.16) show single-feature kinetics for the indicated molecules in the indicated solvents. Surfaces are additionally shown at left for reference.

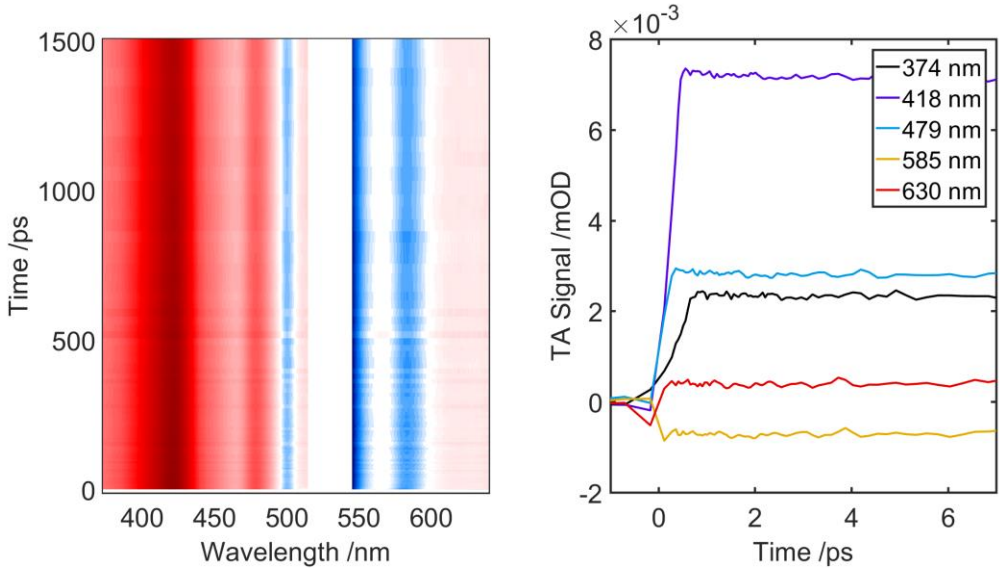

Figure B.13. Surface (for reference) and single-feature kinetics for TIPS-Tc in toluene at the indicated wavelengths ±2 nm. Pump scatter has been removed.

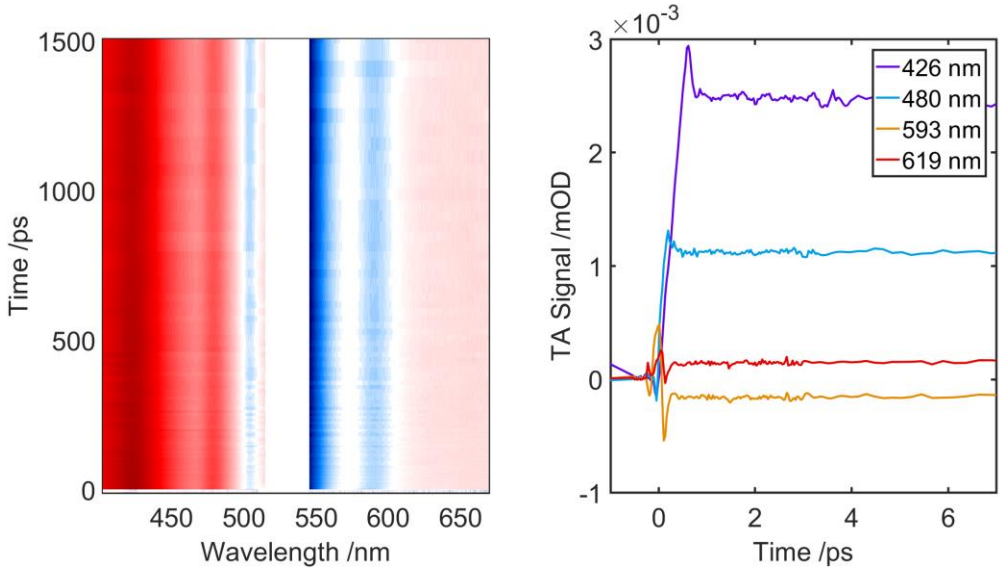

Figure B.14. Surface (for reference) and single-feature kinetics for TIPS-Tc in benzonitrile at the indicated wavelengths ±2 nm. Pump scatter has been removed.

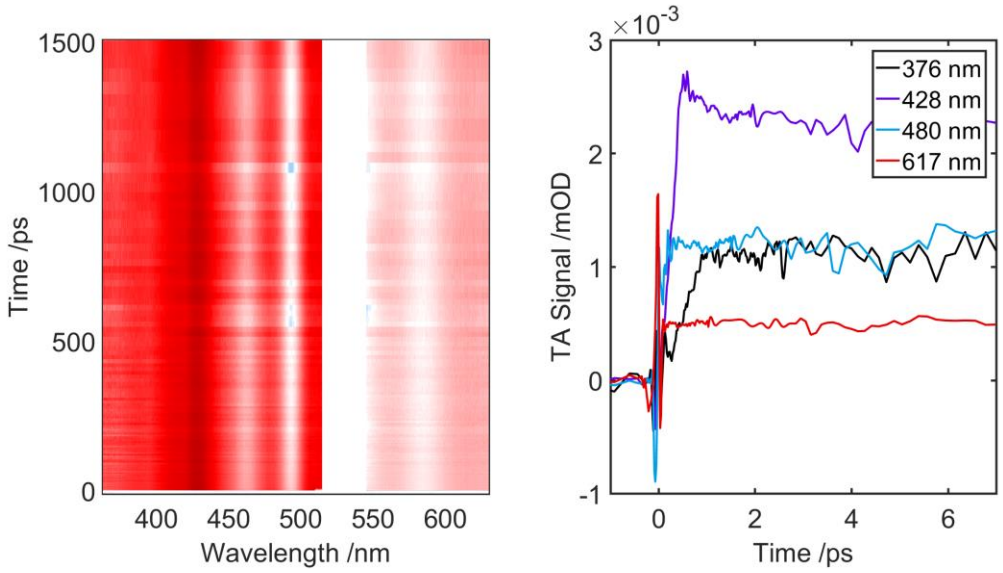

Figure B.15. Surface (for reference) and single-feature kinetics for TIPS-BT1 in toluene at the indicated wavelengths ±2 nm. Pump scatter has been removed.

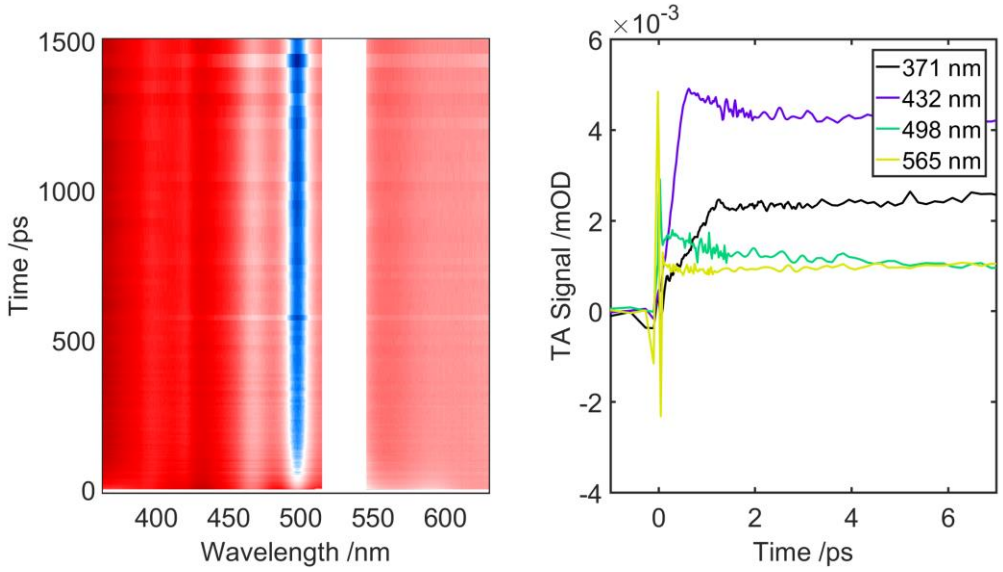

Figure B.16. Surface (for reference) and single-feature kinetics for TIPS-BT1 in benzonitrile at the indicated wavelengths ±2 nm. Pump scatter has been removed.

B.7 Triplet Sensitization of TIPS-BT1 with Anthracene

Nanosecond transient absorption (nsTA) measurements were performed as described in the main text of Chapter 4. Global fitting to a sum of four exponentially modified Gaussian functions gave the DAS which were converted to the basis spectra in Figure B.17 by assuming a model $S_{1,An} \rightarrow T_{1,An} \rightarrow T_{1,}$ $S_1 \rightarrow 0$. The identities of these states are: initially excited anthracene singlet ($S_{1,An}$), TIPS-BT1 initially excited singlet (S_1), anthracene triplet ($T_{1,An}$) created by ISC from $S_{1,An}$, and TIPS-BT1 triplet (T_1). The resulting anthracene triplet lifetime was τ_{sens} 7.51 μs (compared to anthracene in toluene, for which τ = 58.2 μs was measured).

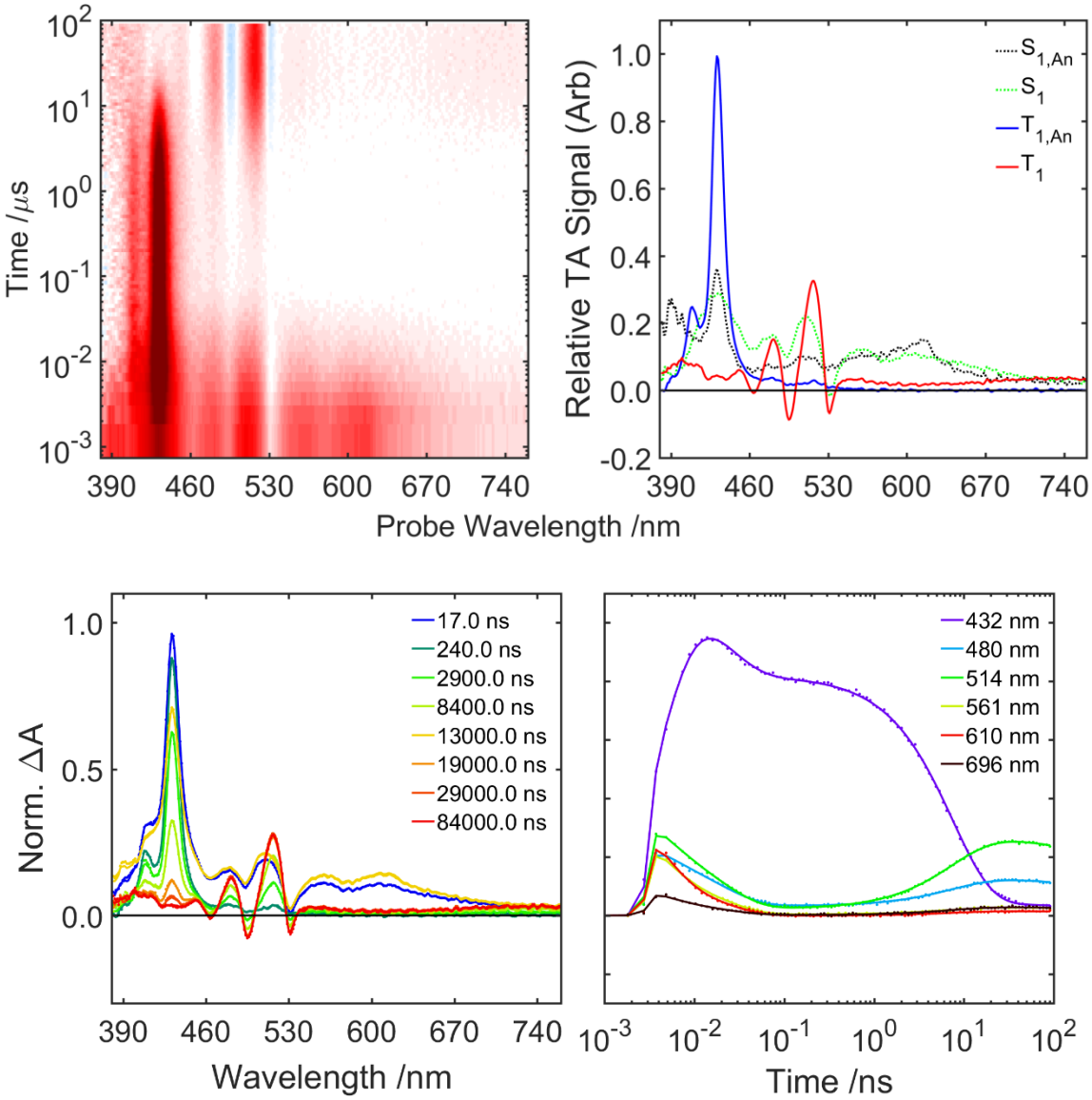

Figure B.17. Triplet sensitization of TIPS-BT1 with anthracene. Top left: full nsTA surface; top right: basis spectra (and identities) retrieved from a global fit; bottom left: spectra at the indicated times extracted from the data (points) and from the global fit (lines); Bottom right: kinetics at the indicated wavelengths extracted from the data (points) and from the global fit (lines).

From the pictured data, the number of excited TIPS-BT1 triplets (N_T) and in turn transient triplet molar attenuation coefficient ε were determined based on the excitation fluence (E_{pump} = 310 nJ/pulse), pump photon energy ($E_{phot} = 5.52 \times 10^{-19}$ J), pump spot full-width at half-maximum (d = 203 μm), anthracene absorption in the sample at the 360 nm excitation wavelength (A = 0.121), intersystem crossing quantum yield[2] Φ_{ISC} = 0.7 and the change in the observed anthracene

triplet lifetime relative to a reference anthracene sample in toluene (τ_{sens} and τ, respectively). This was done according to the following expressions:

$$N_T = \left(1\text{-}10^{-A}\right) \frac{E_{pump}}{E_{phot}} \Phi_{ISC} \frac{1/\tau_{sens}}{1/\tau + 1/\tau_{sens}} \quad (1)$$

$$\varepsilon(\lambda) = \Delta A(\lambda) \left(\frac{N_T/N_A}{V}\right)^{-1} L^{-1} \quad (2)$$

In the above, ΔA is the measured transient triplet spectrum, N_A is Avogadro's number, L is the cuvette path length (2 mm), and V is the excitation volume ($V = \pi(d/2)^2 L$). The result was the molar attenuation coefficient obtained for the triplet spectrum as pictured in the main text.

B.8 Bibliography

1. Frisch, M. J. *et al.* Gaussian 09, Revision A.1. (2009).

2. Nijegorodov, N., Ramachandran, V. & Winkoun, D. P. The dependence of the absorption and fluorescence parameters, the intersystem crossing and internal conversion rate constants on the number of rings in polyacene molecules. *Spectrochim. Acta Part A Mol. Biomol. Spectrosc.* **53,** 1813–1824 (1997).